

ALMA MATER STUDIORUM · UNIVERSITÀ DI BOLOGNA

---

SCUOLA DI INGEGNERIA E ARCHITETTURA

DEI – Dipartimento di Ingegneria dell’Energia Elettrica e dell’Informazione

In co-tutela con University of Leuven (KU Leuven), Lovanio, Belgio

Dottorato di Ricerca in Ingegneria Elettronica, Informatica e delle  
Telecomunicazioni – Ciclo XVII

Settore Concorsuale di Afferenza: 09/E3 – ELETTRONICA

Settore Scientifico Disciplinare: ING-INF/01 – ELETTRONICA

**NONLINEAR CHARACTERIZATION  
AND MODELING OF RADIO-FREQUENCY  
DEVICES AND POWER AMPLIFIERS  
WITH MEMORY EFFECTS**

Presentata da:

**GIAN PIERO GIBIINO**

Coordinatore Dottorato:

**Prof. A. VANELLI-CORALLI**

Relatori:

**Prof. F. FILICORI**

**Prof. D. SCHREURS**

**Esame Finale Anno 2016**



ALMA MATER STUDIORUM · UNIVERSITÀ DI BOLOGNA

---

SCUOLA DI INGEGNERIA E ARCHITETTURA

DEI – Dipartimento di Ingegneria dell’Energia Elettrica e dell’Informazione

In co-tutela con University of Leuven (KU Leuven), Lovanio, Belgio

Dottorato di Ricerca in Ingegneria Elettronica, Informatica e delle  
Telecomunicazioni – Ciclo XVII

Settore Concorsuale di Afferenza: 09/E3 – ELETTRONICA

Settore Scientifico Disciplinare: ING-INF/01 – ELETTRONICA

**NONLINEAR CHARACTERIZATION  
AND MODELING OF RADIO-FREQUENCY  
DEVICES AND POWER AMPLIFIERS  
WITH MEMORY EFFECTS**

Presentata da:

**GIAN PIERO GIBIINO**

Coordinatore Dottorato:

**Prof. A. VANELLI-CORALLI**

Relatori:

**Prof. F. FILICORI**

**Prof. D. SCHREURS**

**Esame Finale Anno 2016**

© 2015 Alma Mater Studiorum AD 1088, University of Bologna – School of Engineering  
Autopubblicato, Gian Piero Gibiino, Viale Risorgimento 2, 40136 Bologna (Italy)

© 2015 KU Leuven – Faculty of Engineering Science  
Uitgegeven in eigen beheer, Gian Piero Gibiino, Kasteelpark Arenberg 10 box 2444, B-3001 Heverlee (Belgium)

All rights reserved. No part of the publication may be reproduced in any form by print, photoprint, microfilm, electronic or any other means without written permission from the publisher.

Tutti i diritti riservati. Nessuna parte della pubblicazione può essere riprodotta in qualsiasi forma per mezzo stampa, stampa fotografica, microfilm, elettronica o qualsiasi altro mezzo senza il permesso scritto dell'editore.

Alle rechten voorbehouden. Niets uit deze uitgave mag worden vermenigvuldigd en/of openbaar gemaakt worden door middel van druk, fotokopie, microfilm, elektronisch of op welke andere wijze ook zonder voorafgaande schriftelijke toestemming van de uitgever.

# Preface

This manuscript reports the research results obtained under a collaboration between the University of Bologna and KU Leuven, which was formalized in November 2012 through a mutual agreement for the co-tutorship of the Ph.D. thesis. The work has been developed within the Electronic Design and Measurement for RF and Industrial Applications (EDM) research group of the Department of Electrical Engineering (DEI) of the University of Bologna, and the TELEcommunications and MICrowaves (TELEMIC) research group of the Department of Electrical Engineering (ESAT) of KU Leuven.

After three years and a half, I can finally acknowledge the people who helped me out reaching these results. My first thoughts are for my supervisors, Prof. Filicori and Prof. Schreurs, as they managed to build a common ground for cooperation. It has been an honor to experience their scientific insights and to have their encouragement through this journey. Moreover, I would like to thank them for their flexibility in the organization of the exchange periods, and for being extremely proactive to financially funding the activity. With respect to this, I also acknowledge CIRI-MAM (Interdepartmental Center for Industrial Research of the University of Bologna - Advanced Applications in Mechanical Engineering and Materials Technology) and FWO (Research Foundation Flanders).

I wish to express my special thanks to Prof. Santarelli - formally an assessor, but practically a co-supervisor - not only for his constant scientific guidance and critical advice, but also for handling most of the bureaucratic and organizational matters, the last of which has been acting as chairman in the final defense. I would also like to express gratitude to all members of the examination committee, including Prof. Gaquière, Prof. Nauwelaers, and Dr. Avolio, for their valuable comments and feedbacks.

Being part of two research groups at a time involved many opportunities and just as many difficulties. The best aspect was undoubtedly the chance to meet

many talented people, whom I owe much of my professional growth. Therefore, I wish to mention Daniel, Rafael, Tommaso, Corrado, Rudi and Pier Andrea from University of Bologna, and Gustavo, Pawel, Mamad, Marco, Saeed, Song, Alessandra, Raul, Tomislav, and Tom from KU Leuven. Thank you for endless (yet, never worthless) discussions, and for sharing both sad and happy moments with me.

I would also like to thank all students met during this period, from the ones attending the laboratory sessions, to the ones I had the pleasure to supervise during their thesis project. While I hopefully taught them some basics, they indirectly helped me out by suggesting innovative perspectives and original thinking.

Such an open research network allowed me to collaborate with other institutions and companies. In this sense, I would like to thank Dr. Vanden Bossche and Dr. Pailloncy from National Instruments, and Dr. Nielsen and Dr. Tafuri from Keysight Technologies, for sharing hints, providing samples, and lending hardware.

Last but not least, I am very grateful to my family and friends. Two people deserve a special mention. My father, for having instilled into me the culture of hard working to set the bar always a bit higher, and my girlfriend, Aleksandra, for withstanding and mitigating the human consequences resulting from this.

Gian Piero Gibiino  
Bologna, April 2016

# Abstract

The fast development of telecommunications systems experienced during the last two decades has strongly influenced the way we communicate and exchange information. Yet, much progress is still expected in the coming years with the introduction of new infrastructures capable of delivering fast data-rates and ubiquitous connectivity. Such a development, however, can only happen through the evolution of RF technology and systems, which should be capable of working at high-power, at high-frequency and over a large operating bandwidth. At the same time, the power dissipation, already a burden for the telecommunication network infrastructure, should be minimized. In order to reach these demanding specifications, radio-frequency (RF) power amplifier (PA) design is evolving from the classic linear or quasi-linear topology into complex architectures. In such conditions, various mechanisms of distortion arise, which are dependent both on the PA topology as well as on the semiconductor technology upon which the PA is designed. These should be suitably compensated for, otherwise the system will not meet the emission constraints and the information it transmits will be corrupted. This work makes use of tailored large-signal measurement techniques in order to characterize and model such distortions in modern applications. In particular, two distinct fields of application are investigated. The first one deals with the characterization and modeling of the non-idealities shown by Gallium Nitride (GaN) HEMTs, a promising semiconductor technology yet suffering from process defects. In particular, the effect of charge trapping is characterized with the exploitation of a double-pulse technique, capable of preconditioning the charge trapping state and allowing improved understanding of the dispersive effects. Such an investigation has culminated with the introduction of new lag-functions for the description of the nonlinear dynamics triggered by traps, as well as the presentation of a new approach for GaN HEMT modeling. The second part deals with RF PAs in which the supply voltage is modulated to obtain higher efficiency, in architectures such as envelope-tracking (ET). In this work, innovative measurement techniques aimed at the characterization of the interface between the PA and the supply modulator at the drain-supply terminal,

has been introduced. Moreover, a three-port behavioral model, taking into account the presence of a modulated supply voltage and the mutual dynamic interaction with the modulated RF input, is proposed. Such a model, based on a modified Volterra series truncation, is also extended to predict the dynamically drained current and the dynamic power added efficiency (PAE). Finally, a real-time predistortion algorithm for supply modulated PAs, based on the proposed modeling approach, is presented.

# Sommario

Il rapido sviluppo dei sistemi di telecomunicazione avvenuto durante gli ultimi vent'anni ha fortemente influenzato il modo in cui comunichiamo e scambiamo informazioni. Ciò nonostante, nuovi sviluppi sono attesi per i prossimi anni, con l'introduzione di nuove infrastrutture capaci di fornire connessione a banda larga e connettività diffusa. Questo sviluppo, d'altra parte, sarà possibile solo attraverso l'evoluzione della tecnologia e dei sistemi a radiofrequenza, che dovranno essere in grado di lavorare ad alte potenze, alte frequenze, e a larga banda. Al tempo stesso, la dissipazione di potenza, già un grosso onere per le infrastrutture di rete, dovrà essere minimizzata. Per poter raggiungere queste complesse specifiche, il progetto di amplificatori di potenza a radiofrequenza sta evolvendo da topologie lineari o quasi lineari a complesse architetture. In queste condizioni nascono vari meccanismi di distorsione che sono dipendenti sia dalla topologia dell'amplificatore, che dalla tecnologia dei dispositivi a semiconduttore utilizzati. Queste distorsioni devono essere adeguatamente compensate, altrimenti il sistema non potrà garantire le specifiche di emissione, e l'informazione trasmessa sarà corrotta. Questo lavoro utilizza tecniche di misura a grande segnale per caratterizzare e modellare queste distorsioni in casi operativi. In particolare, due campi di interesse vengono qui indirizzati. Il primo è relativo alla caratterizzazione e la modellazione delle non idealità mostrate dai dispositivi elettronici di tipo HEMT in Nitruro di Gallio (GaN), una promettente tecnologia elettronica che però presenta ancora difetti provenienti da un processo non ancora del tutto maturo. Gli effetti di intrappolamento di carica vengono qui caratterizzati attraverso l'uso di una tecnica a doppio impulso, in grado di condizionare lo stato delle trappole e permettere una comprensione degli effetti dispersivi ad esse correlati. La ricerca in questo ambito ha prodotto l'introduzione di nuove funzioni dette *lag functions*, atte alla descrizione degli effetti nonlineari dinamici innescati dall'intrappolamento di carica. A partire da questa caratterizzazione, viene derivato un nuovo modello compatto per transistori HEMT in Nitruro di Gallio. La seconda parte della ricerca è invece destinata agli amplificatori di potenza in cui l'alimentazione viene

modulata per ottenere maggiore efficienza, così come avviene in architetture di tipo *envelope-tracking*. In questo ambito, vengono introdotte nuove tecniche di misura, mirate alla caratterizzazione dell'interfaccia tra l'amplificatore di potenza e il modulatore dell'alimentazione al terminale di drain. In aggiunta, viene presentato un modello comportamentale in grado di considerare la presenza di un'alimentazione dinamica, e la mutua interdipendenza dinamica con un segnale a radiofrequenza. Questo modello, basato su un troncamento della serie di Volterra modificata, viene esteso per la predizione della corrente di drain e l'efficienza dinamica. Infine, per mezzo del modello proposto, viene presentato un algoritmo per la predistorsione in tempo reale di amplificatori ad alimentazione dinamica.

# Beknopte samenvatting

De snelle ontwikkeling van telecommunicatiesystemen zoals we tijdens de laatste twee decennia ervaren hebben, heeft een sterke invloed gehad op de manier waarop we communiceren en informatie uitwisselen. Toch is er nog veel vooruitgang te verwachten in de komende jaren met de introductie van nieuwe infrastructuren die snelle data-snelheden toelaten alsook alomtegenwoordige connectiviteit. Een dergelijke ontwikkeling kan evenwel enkel gebeuren via vooruitgang in RF technologie en RF systemen die kunnen werken bij hoog vermogen, bij hoge frequenties, en over een grote werkingsbandbreedte. Tegelijkertijd dient de vermogendissipatie, die reeds een belasting is voor de telecommunicatie netwerkinfrastructuur, te worden geminimaliseerd. Om deze veeleisende specificaties te behalen, is het ontwerp van de radiofrequentie (RF) vermogenversterker (PA) aan het evolueren van de klassieke lineaire of quasi-lineaire topologie naar complexe architecturen. In dergelijke omstandigheden doen zich verschillende mechanismen van vervorming voor, die afhankelijk zijn van zowel de PA topologie als van de halfgeleider technologie waarin de PA gefabriceerd is. Deze vervormingsmechanismen moeten voldoende gecompenseerd worden, vermits anders het telecommunicatiesysteem niet aan de emissie beperkingen zal voldoen, en ook de transmissie van informatie zal gecorrumpereerd worden. Dit doctoraatsonderzoek maakt gebruik van specifiek ontwikkelde groot-sigitaal meettechnieken, om deze vervormingen in moderne toepassingen te kunnen karakteriseren en te modelleren. Hierbij worden twee onderscheiden toepassingsgebieden onder de loep genomen. De eerste betreft de karakterisering en modellering van de niet-idealiteiten aanwezig in galliumnitride (GaN) hoge-elektronen mobiliteit transistoren (HEMT's), hetgeen een veelbelovende halfgeleider technologie is, die echter nog lijdt onder fabricatiedefecten. Met name het effect van ladingstrapping wordt gekarakteriseerd door het gebruik van een dubbele-puls techniek, die preconditionering van de ladingstrapping toelaat, waardoor dispersieve effecten beter kunnen bestudeerd en begrepen worden. Dit onderzoek heeft geresulteerd in het introduceren van nieuwe verdragingsfuncties voor de omschrijving

van de niet-lineaire dynamica veroorzaakt door trapping, alsook in een nieuwe benadering voor GaN HEMT modelleren. Het tweede deel gaat over RF PA's waarbij de voedingsspanning gemoduleerd wordt om alzo hoger rendement te behalen, zoals in architecturen als envelop tracking (ET). In dit doctoraatsonderzoek werden innovatieve meettechnieken gericht op de karakterisering van de interface tussen de PA en de voedingsmodulator, aan de drain-voedingsklem, ontwikkeld. Bovendien wordt een driepoort-gedragsmodel, voorgesteld dat rekening houdt met de aanwezigheid van een gemoduleerde voedingsspanning en met de dynamische interactie onderling met de RF gemoduleerde ingang. Dit model, dat gebaseerd is op een gewijzigde Volterra reeks truncatie, werd uitgebreid om de dynamisch afgenomen stroom alsook het vermogenrendement (PAE) te kunnen voorspellen. Tenslotte wordt een reële-tijd voorvormings-algoritme voorgesteld voor dergelijke PAs met gemoduleerde voeding.

# Abbreviations

<b>2G</b>	Second-generation wireless telephone technology
<b>2DEG</b>	High-density 2D electron gas
<b>3G</b>	Third-generation wireless telephone technology
<b>4G</b>	Fourth-generation wireless telephone technology
<b>5G</b>	Fifth-generation wireless telephone technology
<b>ACPR</b>	Adjacent channel power ratio
<b>ADC</b>	Analog-to-digital converter
<b>AlGaN</b>	Aluminium gallium nitride
<b>AM/AM</b>	Amplitude/amplitude characteristic
<b>AM/PM</b>	Amplitude/phase characteristic
<b>APT</b>	Average power tracking
<b>AWG</b>	Arbitrary waveform generator
<b>BW</b>	Bandwidth
<b>CMOS</b>	Complementary metal-oxide semiconductor
<b>CW</b>	Continuous wave
<b>DDR</b>	Dynamic-deviation reduction
<b>DE</b>	Drain efficiency
<b>DLT</b>	Dynamically linear trapping effects
<b>DNLT</b>	Dynamically nonlinear trapping effects
<b>DPIV</b>	Double-pulsed drain current-voltage characteristic
<b>DPD</b>	Digital predistortion
<b>DSP</b>	Digital signal processing
<b>DUT</b>	Device-under-test
<b>ESG</b>	Electronic signal generator
<b>ET</b>	Envelope-tracking
<b>EER</b>	Envelope elimination and restoration
<b>FPGA</b>	Field Programmable Gate Array
<b>FET</b>	Field-effect transistor
<b>GaN</b>	Gallium nitride

<b>GMP</b>	Generalized memory polynomial
<b>GSM</b>	Global System for Mobile Communications
<b>HBT</b>	Heterojunction bipolar transistor
<b>HDSPA</b>	High speed downlink Packet Access
<b>HEMT</b>	High-electron-mobility transistor
<b>HPR</b>	Harmonic phase reference
<b>IV</b>	Current-voltage characteristic
<b>IM</b>	Intermodulation products
<b>IMD</b>	Intermodulation distortion products
<b>LDMOS</b>	Laterally-diffused metal-oxide-semiconductor
<b>LF</b>	Low-frequency
<b>LF-LSNA</b>	Low-frequency-extended large-signal network analyzer
<b>LINC</b>	Linear amplification with nonlinear components
<b>LO</b>	Local oscillator
<b>LSNA</b>	Large-signal network analyzer
<b>LTE</b>	Long Term Evolution
<b>LTE-A</b>	Long Term Evolution Advanced
<b>LUT</b>	Look-up table
<b>MIM</b>	Metal-insulator-metal
<b>MIMO</b>	Multiple-input multiple-output
<b>MMIC</b>	Microwave monolithic integrated circuit
<b>MP</b>	Memory polynomial
<b>MP-TDNA</b>	Multiple-pulse time domain network analyzer
<b>NMSE</b>	Normalized mean square error
<b>NVNA</b>	Nonlinear Vector Network Analyzer
<b>OFDM</b>	Orthogonal Frequency Division Multiplexing
<b>PA</b>	Power amplifiers
<b>PAE</b>	Power-added efficiency
<b>PAPR</b>	Peak-to-average power ratio
<b>PIV</b>	Pulsed current-voltage characteristic
<b>RF</b>	Radio-frequency
<b>RFIC</b>	Radio-frequency integrated circuit
<b>SCS</b>	Signal component separation
<b>Si</b>	Silicon
<b>SiC</b>	Silicon carbide
<b>SM</b>	Supply modulator
<b>SMS</b>	Short message service
<b>SOLT</b>	Short-open-load-thru
<b>TOI</b>	Third-order intercept point
<b>VNA</b>	Vector network analyzer
<b>VSA</b>	Vector signal analyzer

---

<b>VSG</b>	Vector signal generator
<b>VST</b>	Vector signal transceiver
<b>WCDMA</b>	Wideband code division multiple access



# Contents

<b>Abstract</b>	<b>iii</b>
<b>Abbreviations</b>	<b>ix</b>
<b>Contents</b>	<b>xiii</b>
<b>List of Figures</b>	<b>xvii</b>
<b>List of Tables</b>	<b>xxv</b>
<b>1 Introduction</b>	<b>1</b>
1.1 Telecommunication industry trends . . . . .	1
1.2 Semiconductor technology for RF PAs . . . . .	4
1.2.1 Overview . . . . .	4
1.2.2 Dispersive effects in GaN HEMTs . . . . .	6
1.2.3 GaN HEMTs large-signal modeling trends . . . . .	8
1.3 RF Power Amplifier architectures . . . . .	10
1.3.1 Linearity-efficiency trade-off . . . . .	10
1.3.2 Load modulation . . . . .	11
1.3.3 Supply modulation . . . . .	13
1.4 RF Power Amplifier modeling . . . . .	17

1.4.1	Approaches for PA modeling . . . . .	17
1.4.2	Overview of PA behavioral models . . . . .	18
1.4.3	Volterra-based models . . . . .	20
1.4.4	Recent trends . . . . .	24
1.5	This work . . . . .	26
1.5.1	Objectives . . . . .	26
1.5.2	Organization of the text . . . . .	26
<b>2</b>	<b>Characterization and modeling of GaN HEMTs</b>	<b>29</b>
2.1	Introduction . . . . .	29
2.2	Multiple-Pulse Time Domain Network Analyzer . . . . .	30
2.2.1	Operation . . . . .	30
2.2.2	Calibration . . . . .	32
2.3	Pulsed IV measurements . . . . .	32
2.4	Double-pulse technique . . . . .	34
2.4.1	Theory . . . . .	34
2.4.2	Implementation . . . . .	36
2.4.3	Validation . . . . .	37
2.5	Double-pulse Characterization . . . . .	38
2.5.1	PIV and DPIV characteristics . . . . .	38
2.5.2	Thermal dependency . . . . .	42
2.5.3	Technology assessment . . . . .	44
2.6	Nonlinear and Linear Lag Functions . . . . .	47
2.6.1	Nonlinear Lag Function . . . . .	47
2.6.2	Linear Lag Function . . . . .	49
2.7	GaN HEMT modeling based on the double-pulse technique . .	52
2.7.1	Formulation . . . . .	53

2.7.2	Identification . . . . .	56
2.7.3	Experimental extraction and validation . . . . .	59
2.8	Conclusion . . . . .	61
<b>3</b>	<b>Nonlinear dynamic characterization of RF PAs</b>	<b>63</b>
3.1	Introduction . . . . .	63
3.2	Sampler-based and mixer-based large-signal measurements . . .	65
3.2.1	Sampler-based large-signal measurements . . . . .	65
3.2.2	Low-frequency-extended large-signal network analyzer . .	68
3.2.3	Mixer-based large-signal measurements . . . . .	72
3.3	Custom set-ups for supply-modulated PAs . . . . .	73
3.3.1	Combined LF-RF pulsed set-up based on the PNA-X . .	73
3.3.2	Pulsed-RF PA characterization . . . . .	76
3.3.3	Combined pulsed-RF and pulsed supply measurements . .	78
3.3.4	ET set-up based on the VST . . . . .	81
3.4	Characterization methods at the drain-supply terminal . . . . .	84
3.4.1	Set-up requirements for supply-modulated PAs . . . . .	84
3.4.2	PA drain port nonlinear impedance-like function ( $Z_{PA}$ ) . .	86
3.4.3	Characterization with multi-sine modulation . . . . .	89
3.4.4	Supply Modulator nonlinear output impedance ( $Z_{SM}$ ) . .	91
3.5	Supply terminal active load-pull . . . . .	94
3.6	Characterization and modeling of self-heating in RF PAs . . . .	97
3.6.1	Introduction to thermal effects in RF PAs . . . . .	97
3.6.2	Model formulation and identification . . . . .	99
3.6.3	Measurement set-up . . . . .	101
3.6.4	Experimental results . . . . .	103
3.7	Conclusion . . . . .	105

<b>4</b>	<b>Three-port modeling for supply-modulated PAs</b>	<b>107</b>
4.1	Introduction . . . . .	107
4.2	Modified Volterra series . . . . .	108
4.3	Behavioral model formulation . . . . .	111
4.3.1	Three-port quasi-static representation . . . . .	111
4.3.2	RF excitation . . . . .	113
4.3.3	Supply port excitation . . . . .	115
4.4	Model identification procedure . . . . .	118
4.4.1	Frequency-domain model re-formulation . . . . .	118
4.4.2	Frequency-domain kernels identification . . . . .	121
4.5	Experimental results . . . . .	124
4.5.1	Characterization of the kernels . . . . .	124
4.5.2	Model validation . . . . .	128
4.6	Linearization technique . . . . .	137
4.6.1	Model inversion algorithm . . . . .	137
4.6.2	Real-time processing technique . . . . .	141
4.6.3	Results . . . . .	142
4.7	Conclusion . . . . .	144
<b>5</b>	<b>Conclusion</b>	<b>147</b>
5.1	Main achievements . . . . .	147
5.2	Future challenges . . . . .	149
5.2.1	Compact modeling of GaN HEMTs . . . . .	149
5.2.2	PA behavioral modeling and predistortion . . . . .	149
	<b>Bibliography</b>	<b>151</b>
	<b>Curriculum Vitae</b>	<b>173</b>

# List of Figures

1.1	(a) Breakdown of the power consumption in a cellular network (from [11]); (b) Power consumption in a radio base station (from [15]). . . . .	2
1.2	PAPR of the signals from GSM to 4G, from [15]. . . . .	3
1.3	Semiconductor materials in use versus power and frequency, from [17]. . . . .	5
1.4	(a) GaN HEMT structure; (b) Energy band diagram. The various location of trapping centers are indicated in both pictures. . . .	7
1.5	Classic representation of an RF PA with power flows explicitly indicated. . . . .	11
1.6	(a) Functional blocks of an outphasing PA. (b) Functional blocks of a Doherty PA. SCS stands for signal component separation and it is usually implemented in a digital way. . . . .	12
1.7	(a) Functional blocks of EER. (b) Functional blocks of ET. . .	14
1.8	Hammerstein-Wiener behavioral model structures. . . . .	19
2.1	Block diagram of the MP-TDNA. . . . .	30
2.2	(a) Voltage (top) and current (bottom) waveforms sampled at the drain port of a 1-mm GaN HEMT, when double-pulsed excitations are applied both at the gate and drain sides. The time interval between dotted lines suggests the time-position for IV sampling. (b) Dynamic locus under double-pulse excitation, while numbers indicate rise and fall edges of the waveforms in (a).	37

- 2.3 The double-pulse technique depicted with input and output pulsed characteristics; pre-pulses peaks (in red) precondition the charge-trapping state. Measure-pulse peaks (blue) are swept to obtain the full characteristic. The cross indicates the quiescence point. . . . . 38
- 2.4 Consistency test of the double-pulse technique performed on a 1-mm GaN HEMT. (a) Standard PIV from two quiescent points chosen on the isothermal locus at about  $95^{\circ}\text{C}$  ( $P_D=4\text{ W}$ ,  $\theta_B=40^{\circ}\text{C}$ ); (b) DPIV obtained through the double-pulse technique with:  $\hat{v}_G \simeq -4.3\text{ V}$  and  $\hat{v}_D \simeq 50\text{ V}$ . Gate voltage  $v_G$  sweep:  $-4\text{ V} \div -1\text{ V}$ , step:  $0.5\text{ V}$ . . . . . 39
- 2.5 PIV (red with circles) vs. DPIV (blue with stars) characteristics for 1-mm GaN HEMTs from two different foundries. (a) Foundry A. (b) Foundry B. . . . . 40
- 2.6 1-mm GaN HEMT standard PIV (red lines with circles) and DPIVs with  $\hat{v}_D = 25\text{ V}$  (up triangles),  $30\text{ V}$  (stars),  $35\text{ V}$  (down triangles),  $40\text{ V}$  (squares) and negative peak gate voltages  $\hat{v}_G$  near pinch-off, all at  $v_g = -2.5\text{ V}$ , pulsed from  $V_{GQ} = -2.5\text{ V}$ ,  $V_{DQ} = 20\text{ V}$ . . . . . 40
- 2.7 DC drain currents corresponding to the PIV (red lines with circles) and various DPIVs for  $10 \times 100\ \mu\text{m}$  ( $L = 0.5\ \mu\text{m}$ ) GaN HEMTs from two foundries. (a) Foundry A. DPIVs  $\hat{v}_D$ :  $35\text{ V}$  (up triangles),  $40\text{ V}$  (down triangles), and  $50\text{ V}$  (stars) and  $\hat{v}_G \simeq V_T$ . Bias:  $V_{GQ} = -2.5\text{ V}$ ,  $V_{DQ} = 20\text{ V}$ . (b) Foundry B. DPIVs  $\hat{v}_D$ :  $30\text{ V}$  (up triangles),  $40\text{ V}$  (down triangles), and  $50\text{ V}$  (stars) and  $\hat{v}_G \simeq V_T$ . Bias:  $V_{GQ} = -0.6\text{ V}$ ,  $V_{DQ} = 20\text{ V}$ . . . . . 42
- 2.8 (a) 1-mm GaN HEMT dc drain current component ( $I_{D0}$ ) corresponding to a standard PIV characteristic from  $V_{GQ}=-2.5\text{ V}$ ,  $V_{DQ}=30\text{ V}$  ( $I_{DQ} \simeq 180\text{ mA}$ )  $v_G$ :  $-4.25\text{ V} \div -1.75\text{ V}$ , step:  $0.5\text{ V}$ ;  $v_D$ :  $0\text{ V} \div 75\text{ V}$ , step:  $2.5\text{ V}$  (b)  $I_{D0}$  corresponding to PIV (standard) and DPIV at  $40^{\circ}\text{C}$  (blue stars),  $55^{\circ}\text{C}$  (green circles),  $70^{\circ}\text{C}$  (red squares) for  $v_G = -4.25\text{ V}$ . The DPIV are obtained with  $\hat{v}_G \simeq -4.5\text{ V}$ , near pinch-off, and  $\hat{v}_D \simeq 75\text{ V}$ . . . . . 43
- 2.9 (a) Activation threshold voltage ( $\Delta V_D^{AT}$ ) graphical estimation for  $v_G=-4.25\text{ V}$  under PIV from  $V_{GQ}=-2.5\text{ V}$ ,  $V_{DQ}=30\text{ V}$ . Dotted black lines represent the different slopes reported in Table 4.3. (b)  $\Delta V_D^{AT}$  vs.  $v_G$  and  $\theta_B$ . . . . . 44

2.10	8x125 $\mu\text{m}$ GaN HEMT, type A. Comparison of different pulsed IV at $v_G = 0$ V with the aim of evaluating the charge trapping phenomena. . . . .	45
2.11	DPIVs of 8x125 $\mu\text{m}$ GaN HEMTs from $(V_{GQ}^{nom}, V_{DQ}^{nom})=(-3.1$ V, 25 V), $I_{DQ} = 100$ mA with $\hat{v}_G \simeq V_T$ , $\hat{v}_D \simeq 60$ V. Device type A: dotted lines; type B: continuous lines. . . . .	47
2.12	Nonlinear Lag Function ( $\lambda_{NLF}$ ) (a) vs. pulsed gate voltages and (b) vs. pulsed drain voltages. . . . .	49
2.13	DPIVs from different on-state quiescent conditions $(V_{GQ}, V_{DQ})$ lying on the same isothermal locus corresponding to a 2.4 W dissipated power, namely: (-2.7 V, 10 V), $I_{DQ} = 240$ mA: red continuous lines; (-3.2 V, 20 V), $I_{DQ} = 120$ mA: black dashed lines; (-3.4 V, 30 V), $I_{DQ} = 80$ mA, blue dotted lines. For all DPIVs: $\hat{v}_G = -4$ V, $\hat{v}_D = 60$ V. . . . .	50
2.14	DPIVs from different off-state quiescent conditions, with $\hat{v}_G = -4$ V, $\hat{v}_D = 60$ V. (a) $(V_{GQ}, V_{DQ})=(-4.5$ V, 30 V), continuous lines; $(V_{GQ}, V_{DQ})=(-8$ V, 30 V), dashed lines. (b) $(V_{GQ}, V_{DQ})=(-8$ V, 10 V), continuous lines; $(V_{GQ}, V_{DQ})=(-8$ V, 30 V), dashed lines. . . . .	51
2.15	$\lambda_{LLF}(V_{GQ}, V_{DQ})$ in the chosen sensing point. Dots: experimental results. Dashed lines represent a piecewise linear interpolation. . . . .	52
2.16	GaN HEMT nonlinear model. (a) Extrinsic parasitic network. (b) Intrinsic device schematic. . . . .	53
2.17	(a) Nonlinear function associated with state equation (2.20) in the GaN transistor case. (b) Qualitative waveforms corresponding to a periodic low-duty-cycle pulsed regime, showing activation of the nonlinear dynamics associated with charge trapping phenomena in GaN transistors. . . . .	56
2.18	Simulated (line) and measured (dot) IV characteristics. (a) DPIV from $V_{GQ} = -3$ V, $V_{DQ} = 30$ V, $\theta_B = 40^\circ\text{C}$ and pre-pulses toward $\hat{v}_G = -4$ V, $\hat{v}_D = 60$ V. (b) Standard PIV with from the same bias point and at the same $\theta_B$ . . . . .	60
2.19	LF model validation at $f_0 = 4$ MHz under sinusoidal excitation. Device loaded with $Z_L$ as described in the text. Model based on the DPIV: red continuous line. Model based on the PIV: dashed green line; measurements: blue circles. (a) RF output power and PAE. (b) Drain current and dissipated power. . . . .	60

2.20	Waveforms prediction at $f_0= 4$ MHz under sinusoidal excitation. Device loaded with $Z_L$ as in Fig. 2.19. Model based on the DPIV: red continuous line. Model based on the PIV: dashed green line; measurements: blue circles. . . . .	61
2.21	RF model validation at $f_0= 5$ GHz under sinusoidal excitation. Device loaded with $Z_L^{opt}$ . Model based on the DPIV: red continuous line. Model based on the PIV: dashed green line. Measurements: blue circles. (a) RF output power and PAE. (b) Drain current and dissipated power. . . . .	62
2.22	Intermodulation test for the model extracted from DPIVs. Fundamental output power and third-order IMD product (dot – measure, line – prediction). $Z_L = 50 \Omega$ , $f_0= 1.5$ GHz, $\Delta f= 1$ MHz. . . . .	62
3.1	Representation of the harmonic sampling technique and the de-scrambling of the down-converted tones in case of wideband acquisition; $f_s$ is the sampling frequency, $f_M$ the frequency step of the modulation grid around each harmonic. . . . .	66
3.2	Block diagram of a sampler-based large-signal network analyzer (LSNA). . . . .	67
3.3	Low-frequency-extended LSNA (LF-LSNA). . . . .	69
3.4	Block diagram of a mixer-based large-signal network analyzer, also known as nonlinear vector network analyzer (NVNA). . . . .	72
3.5	Set-up based on the PNA-X for the pulsed RF and pulsed supply characterization of PAs. (a) Block diagram. (b) Photo of the set-up. . . . .	75
3.6	Pulsed CW characterization of a handset PA by means of the point-in-pulse PNA-X measurement capability. The acquisition delay is reported on the plots. (a) first harmonic, (b) second harmonic and (c) third harmonic. . . . .	77
3.7	$X$ -parameters acquired under pulsed CW conditions (the acquisition delays are reported in the Figures). As from (1.15), for a generic parameter $X_{ynxm}^{(S)} = S_{ynxm}$ , $x$ and $y$ stand, respectively, for the input and the output port; $m$ and $n$ stand for the harmonic frequency of, respectively, the incident and the scattered waves. . . . .	79

3.8	Comparison of the transients due to pulsed supply and pulsed RF excitations ( $T=100 \mu s$ , duty cycle=25%). (a) RF output power. (b) Drain current. . . . .	80
3.9	Supply-drain terminal $I/V$ waveforms acquisition under pulsed conditions ( $T=100 \mu s$ , duty cycle=20%). (a) Constant dc supply and pulsed RF excitation. (b) Both supply and RF pulsed. . .	80
3.10	VST-based envelope-tracking set-up with IV baseband sensing. (a) Block diagram. (b) Picture of the set-up. . . . .	82
3.11	Shaping table extraction performed with the set-up in Fig. 3.10. (a) Constant gain (20 dB) shaping table. (b) Optimum PAE shaping table. . . . .	83
3.12	Comparison between the 20 dB constant gain (red) and the optimum PAE (blue) shaping tables under ET operation and with 20 MHz LTE signal RF excitation. (a) Voltages and currents measured at the PA supply node. (b) Measured instantaneous PAE. . . . .	84
3.13	Diagram for the definition of impedance-like quantities $Z_{PA}$ and $Z_{SM}$ . . . . .	87
3.14	Characterization of $Z_{PA}$ for a GaAs-based handset-PA, with $f_0 = 0.95$ GHz. (a) $Z_{PA}$ at $f_{LF}=1$ MHz. $V_{D0}=4.5$ V (crosses), 4 V (triangles), 3.5 V (squares) 3 V (circles). (b) $Z_{PA}$ at $V_{D0}= 4.5$ V, RF $P_{out} = 9 \div 24$ dBm. . . . .	88
3.15	X-band GaN MMIC PA characterization. (a) $Z_{PA}$ vs. $V_{D0}=8 \div 20$ V and $f_{LF}=0.1 \div 8$ MHz (b) $Z_{PA}$ vs. RF $P_{in}=15 \div 30$ dBm and $V_{D0}=8 \div 20$ V. $V_{GQ}=-2.8$ V. . . . .	89
3.16	(a) $Z_{PA}$ characterization for an hand-set PA with Schroeder multi-tone excitation, RF $P_{in} \in [-6, 10]$ dBm (from dark to light) at $f_0 = 0.85$ GHz. $V_{D0} = 2$ V (b) Same as (a) with $V_{D0} = 4$ V. . . . .	90
3.17	$Z_{SM}$ for a supply-modulator type A under operation with hand-set PA with RF $P_{in} \in [-6, 10]$ dBm (from dark to light). (a) $V_{D0} = 1$ V. (b) $V_{D0} = 4$ V. . . . .	92
3.18	$Z_{SM}$ of a supply modulator type B in APT mode under operation with hand-set PA with RF $P_{in} \in [-6, 10]$ dBm (from dark to light). $V_{D0} = 2.8$ V. . . . .	93

- 3.19 (a)  $Z_{SM}$  of a supply-modulator type B with linear block enabled, under operation with hand-set PA with RF  $P_{in} \in [-6, 10]$  dBm (from dark to light).  $V_{D0} = 1.5$  V (b) Same as (a) with  $V_{D0} = 3.8$  V. . . . . 94
- 3.20  $IM3$ ,  $P_{RF}^{OUT}$  and PAE versus  $\Gamma_{SM}$  synthesized at  $f_{LF}=2\Delta f=2$  MHz, for RF two-tone signal with  $P_{RF}^{IN}=24$  dBm. Similar patterns are obtained if performing the LF load-pull at other frequencies.  $V_{G0}=-2.8$  V,  $V_{D0}=18$  V. . . . . 95
- 3.21  $IM3$  versus  $P_{RF}^{IN}$ : average distortion (a) and asymmetry (b).  $Z_{SM}$ :  $-0.36+0.1j \Omega$  (circles),  $0.23-0.53j \Omega$  (crosses),  $0.45-0.03j \Omega$  (squares),  $0.01+0.37j \Omega$  (triangles), at  $f_{LF}=2\Delta f=4$  MHz.  $V_{G0}=-2.8$  V,  $V_{D0}=20$  V. . . . . 96
- 3.22  $IM3$  versus  $V_{D0}$  under LF loadpull. (a) average distortion. (b) asymmetry.  $Z_{SM}$ :  $-0.51+j0.28 \Omega$  (circles),  $0.33-j0.42 \Omega$  (crosses),  $0.46+j0.16 \Omega$  (squares),  $0.07+j0.52 \Omega$  (triangles), at  $f_{LF}=2\Delta f=6$  MHz.  $P_{IN}^{RF}=22$  dBm.  $V_{G0}=-2.8$  V. . . . . 97
- 3.23 Diagram of the measurement set-up for PA self-heating characterization . . . . . 102
- 3.24 (a) Foto of the measurement set-up depicted in Fig. (b) Zoom of the PA with the DUT and the temperature sensing board. . . . 102
- 3.25 Measured isothermal curves of the gain characteristic ( $H$ ) at three fixed temperatures. . . . . 103
- 3.26 Measured gain sensitivity to temperature ( $h_{\theta}$ ) . . . . . 104
- 3.27 (a) Measured isothermal curves of the supply current ( $F$ ) at three equivalent junction temperatures  $\theta^*$ . (b) Measured current sensitivity to temperature ( $f_{\theta}$ ). . . . . 105
- 3.28 (a) Validation of the extracted model (lines) vs gain measurements (crosses). CW characteristic (black) is obtained at constant  $\theta_C=30^{\circ}\text{C}$ . (b) Validation of the model vs current measurements. 105
- 4.1 Representative diagram for region of validity of the truncated Volterra and the truncated modified Volterra series.  $\tilde{f}$  and  $\tilde{x}$  are the input signal frequency and amplitude, respectively (from [115]). 109
- 4.2 Representation of the PA as a three-port device. The supply port represents the third port and is excited by a modulated supply. 112

- 4.3 Schematic diagram of the experiments to identify the kernels from RF and LF excitations. . . . . 122
- 4.4 (a) Quasi-static modeling. (b) 25-tone excitation at RF and supply ports. . . . . 125
- 4.5 Dynamic deviation functions due to the RF input excitation at port 1, measured in frequency domain.  $H_{21}$  [(a) and (b)] and  $\tilde{H}_{21}$  [(c) and (d)] are measured around at port 2.  $K_{31}$  [(e) and (f)] is measured around dc at port 3. Plots correspond to a  $V_3^{(0)} = 5$  V. The input  $P_{in}$  is indicated in the legend,  $\Delta\nu = 100$  kHz. . 126
- 4.6 Dynamic deviation functions due to the dynamic supply excitation at port 3, measured in frequency domain.  $H_{23}$  [(a) and (b)] is measured around  $f_0$  at port 2.  $K_{33}$  [(c) and (d)] is measured around dc at port 3. Plots correspond to a  $V_3^{(0)} = 5$  V. The input  $P_{in}$  is indicated in the legend,  $\Delta\nu = 100$  kHz. . . . . 127
- 4.7 Absolute values of the dynamic deviation functions  $H_{21}$ ,  $\tilde{H}_{21}$ ,  $H_{23}$ , and  $K_{33}$  plotted versus RF  $P_{in}$  and dc supply voltage. Plots correspond to  $\nu = 8$  MHz. . . . . 127
- 4.8 Two-tone test for three average RF  $P_{in}$ : (top) 0 dBm, (central) 4 dBm, and (bottom) 8 dBm;  $\Delta f \in [20$  kHz, 5.5 MHz]. Step: 500 kHz. . . . . 130
- 4.9 (a) RF two-tone input, output and model predictions for RF  $P_{in}=4$  dBm and  $\Delta f \in [20$  kHz,5.5 MHz]. Step: 500 kHz. (b)  $\Delta PAE$  prediction error (%) calculated as in (4.52) under two-tone RF excitation and single-tone modulation of the supply voltage ( $P_{in}$  as in Fig. 4.8). . . . . 131
- 4.10 (a)  $i_3(t)$  modeling under 5 MHz, 25-tone with a frequency spacing of 250 kHz ( $T=4$   $\mu$ s) modulated supply voltage with  $V_3^{(0)} = 3$  V and CW RF  $P_{in} = 8$  dBm. (b)  $i_3(t)$  under concurrent 25-tone (same type as in (a)) modulation at supply ( $V_3^{(0)} = 4$  V,  $V_{3pp}=1.8$  V) and RF  $P_{in}=4$  dBm, PAPR=10 dB. . . . . 133
- 4.11 Measured and modeled  $b_2(t)$  under concurrent modulated supply ( $V_3^{(0)} = 5$  V,  $V_{3pp} = 2$  V) and RF input (5-tone, 5 MHz, PAPR = 8 dB,  $\Delta f = 1.25$  MHz ( $T = 1.6$   $\mu$  s),  $P_{in} = 4$  dBm) versus time (a) and frequency (b). (c) Time-domain and (d) frequency-domain of  $\Re\{\delta(t)\}$ . (e) Time-domain and (d) frequency-domain of  $\Im\{\delta(t)\}$ . 134

4.12	Measured and modeled $b_2(t)$ under concurrent modulated supply ( $V_3^{(0)} = 5$ V, $V_{3pp} = 2$ V) and RF input (25-tone, 5 MHz, PAPR=10.2 dB, $\Delta f = 250$ kHz ( $T = 4$ $\mu$ s), $P_{in} = 4$ dBm) versus time (a) and frequency (b). (c) Time-domain and (d) frequency-domain of $\Re\{\delta(t)\}$ . (e) Time-domain and (d) frequency-domain of $\Im\{\delta(t)\}$ . . . . .	135
4.13	Functional scheme for the implementation of the iterative procedure, where the first iteration ( $n = 0$ ) is a simple quasi-static inversion (A and B blocks in Fig. 4.14. . . . .	141
4.14	Processing at each iteration stage. A: Calculation of $\Delta(k)$ . B: Quasi-static model inversion. . . . .	141
4.15	Architecture for the digital implementation of a nonlinear convolution, necessary to calculate the terms in (4.58) and (4.59) (within block A in Fig. 4.13). . . . .	142
4.16	Applied supply voltage time-domain modulation waveforms (SM) corresponding to different average PAE. No SM: 12.4% PAE, SM 1: 18.2% PAE, SM 2: 21.8% PAE, SM 3: 23.4% PAE. . . . .	143
4.17	Spectrum of the RF output for a random-phase 25-tone RF input test signal with peak-to-average power ratio (PAPR) = 8 dB under the supply modulation (SM) 1 reported in Fig. 4.16. Linearized gain: 15 dB. . . . .	143
4.18	Left (top) and right (bottom) ACPR vs. iteration number $n$ for the supply voltages in Fig. 4.16. RF input test signal as in Fig. 4.17. . . . .	144
4.19	Output NMSE vs. iteration number $n$ with the supply voltages of Fig. 4.16. RF input test signal as in Fig. 4.17. . . . .	144
4.20	Number of iterations needed to guarantee $\max\{\text{ACPR}\} < -45$ dBc. RF test signal as in Fig. 4.17. . . . .	145

# List of Tables

2.1	Analysis of the dc current component versus $\theta_B$ . . . . .	44
2.2	Trap-related technology performance indicators. . . . .	47
4.1	Model test with a multi-tone modulation at the supply . . . . .	132
4.2	Experimental results for the PA under concurrent RF and supply random multi-tone modulation . . . . .	136



# Chapter 1

## Introduction

### 1.1 Telecommunication industry trends

During the last thirty years, the world has assisted to an incredible progress in the way people communicate and connect, causing a huge impact to the modern economy and society. The continuous progress of semiconductor technology, together with increasingly better performing analogue and digital electronics, have been the engines behind this revolution. The introduction of smart methods of digital signal processing (DSP), communication algorithms, as well as the development of complex telecommunication infrastructure, allowed for a large-scale deployment of wireless communication. Industry has been exploiting the new opportunities in a fast and productive way, and has contributed to a virtuous circle between new products, new services, and further research investments. First mobile phones, designed uniquely for voice communication, were introduced back in the 1980s [1]. The second generation (2G) systems, released in 1992, implemented the first digital communications allowing data services such as text messaging (SMS). The 3G (2001) introduced digital standards such as WCDMA (Wideband Code Division Multiple Access) and HSDPA (High-Speed Downlink Packet Access), featuring high-speed internet access for audio and video streaming. The fourth-generation (4G), which is still being introduced, is based on an OFDM (Orthogonal Frequency Division Multiplexing) modulation, denominated LTE/LTE-A (Long Term Evolution / Advanced) [2],[3]; once the 4G technology will be fully implemented, the threshold of 1 Gbps of data rate will be reached. Yet, both the demand for higher data rates and the number of connected devices are dramatically increasing. Analysts predict tens of billions of wireless devices in a decade, and suggest a 1000x fold increase in the network

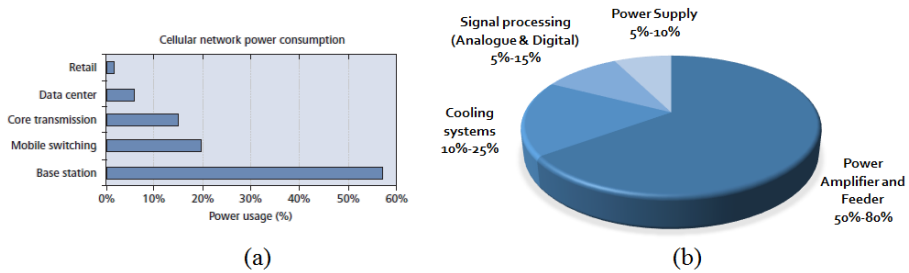


Figure 1.1: (a) Breakdown of the power consumption in a cellular network (from [11]); (b) Power consumption in a radio base station (from [15]).

capacity by 2020 to avoid congestion [4],[5]. Roughly, a new wireless standard has been introduced every ten years and the objectives of a fifth generation (5G) of wireless communications are already towards a formal definition. The primary of these is undoubtedly a further increase (1000x) in data rate. Besides the already mentioned expansion in the network capacity, a latency of about 1 ms (relative to the 15 ms of 4G) is also foreseen to allow new services such as the ones indicated under the keyword *Internet of Things* [5]. At the same time, energy and cost per transmitted bit should decrease a 100-factor, and such metric would account for the whole network including base stations and backhaul.

Three mutually-dependent technologies are investigated to reach such demanding objectives: massive multiple-input multiple-output (MIMO), use of the millimetre-wave spectrum, and ultra-densification of networks [5],[6]. The shift towards the millimetre-waves is driven by the overcrowding of the used spectrum. Today, the telecommunication systems transmit in a bandwidth from 700 MHz to 2.6 GHz in 200 MHz frequency slots and channels with 20 MHz of bandwidth. Considering that the data rate is directly proportional to the bandwidth, the idea is to use larger bandwidth allocations in the mostly unexploited spectrum from 3 to 300 GHz [6]. At the same time, the 5G foresees very dense heterogeneous networks which will include not only standard base stations, but also nested small cells such as pico-cells (range under 100 meters) and femto-cells (WiFi-like range) [7]. This poses challenges not only in terms of a more complex network coordination and mobility support but, most importantly, in creating lower-power and cheaper cells, as well as in affording the rising costs of installation, maintenance and backhaul. Of the total amount of operational expenditures of a telecom infrastructure, a large stake is the cost necessary for powering radio sites. Also, of the total mobile network power consumption, the majority is used to run base stations, in a percentage between 50% and 90%

depending on technology advancements and operators (Fig. 1.1(a) from [8]). Indeed, a reduction in base stations' power consumption not only allows higher economic sustainability, but it is also the main driver, in combination with the introduction of renewable energy sources, towards greener telecommunication networks [9]. Strategies to increase the energy efficiency includes network management approaches such as minimization of cell coverage for a given target, the design of adaptive algorithms to dynamically turn off radio sites when no active user should be served, and the choice between many micro-cells or fewer macro-cells [10]. However, the leading way to reduce the total base stations' power consumption is to reduce the power consumed by each radio site. A base station consists of a series of transceivers (e.g., 12 in LTE base stations [8]), each of which drives an antenna. Each transceiver is composed by an ac/dc unit for the connection to the electrical power grid, a dc/dc power supply, a baseband signal processor, a transmitter (downlink) module, a receiver (uplink) module, a radio-frequency (RF) power amplifier (PA), and an interface towards the antenna. Such interface consists of the feeder, filter diplexers and matching networks. The power amplifier is responsible for the power conversion of the power absorbed from the supply to RF. By evaluating the breakdown of the power consumption of a base station (Fig. 1.1(b) from [11]), one clearly sees that over 60% of the total power consumption is due to power amplifier and feeder, while another substantial part is absorbed for cooling [8],[11].

Although the importance of the PA is mitigated for small power stations [12], there is no doubt that the greatest potential for increasing the overall base station efficiency stems from improving the efficiency of the PA and antenna, and from optimizing the power transfer between them [8]. Moreover, less PA dissipation automatically means reduced power consumption for operating cooling systems, and slower degradation. Power consumption is a key parameter also for handsets, as it directly impacts battery life. Even though handset power consumption analysis is highly influenced by the habits of the user (e.g., voice, video streaming, etc.) and is sensible to the presence of specific hardware,

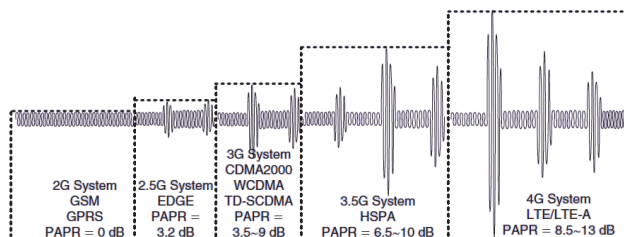


Figure 1.2: PAPR of the signals from GSM to 4G, from [15].

parts dedicated to wireless communications are indicated as a major source of energy dissipation [13]. Not surprisingly, the RF PA is one of the largest power consumers of a handset [14]. Both for base stations and handsets, increasing the efficiency of the PA is not a trivial task, considering that it should fulfil the increasingly demanding linearity specifications. Modern modulation techniques, such as OFDM, maximize the amount of information stored in a given bandwidth. Unfortunately, a drawback of this kind of techniques is that the resulting signal features a high peak-to-average power ratio (PAPR). In Fig. 1.2 [15], the trend towards increasing PAPR throughout the telecommunication standards is reported. As will be addressed in section 1.3, due to the characteristics of modulated signals, the challenges related to the PA indirectly limit the achievable data rates. In fact, such type of signals has a critical impact on the design and efficiency of RF PAs, while stringent specifications must be targeted by addressing both the semiconductor technology, which will be discussed in section 1.2, and the PA topologies, which are the subject of section 1.3.

## 1.2 Semiconductor technology for RF PAs

### 1.2.1 Overview

Transistor technology capable of delivering high gain at RF has been one of the enablers of wireless communications. The introduction of semiconductors based on heterostructures has given birth to devices such as the heterojunction bipolar transistor (HBT) and the high-electron-mobility transistor (HEMT) which boosted PA developments until now and, although evolving with new materials and techniques, are still fundamental for future PA performance enhancements. A heterojunction consists of two layers of III-V compound semiconductors with different band-gaps. One of the two layers is highly doped, while the other is undoped. Due to the band-gap mismatch, high-density two-dimensional electron gas (2DEG) is formed at the interface of the two materials, creating a very low resistivity channel that allows current conduction at very high frequencies, up to hundreds of GHz [16]. HBTs are bipolar transistors in which the emitter-base form an heterojunction. In HEMTs, the conductivity of the layer is controlled through a field effect mechanism such as in other types of field effect transistors (FETs). The compound materials in use along with their capability with respect to power and frequency of operation are summarized in Fig. 1.3 [17]. In the low power region (up to tens of Watt), HBTs and HEMTs based on Gallium Arsenide (GaAs) are still the most used for cellular handsets, low-noise receivers, Wi-Fi and GPS transmitters. Their diffusion is also enabled by the maturity of integration processes with passive elements for microwave monolithic integrated

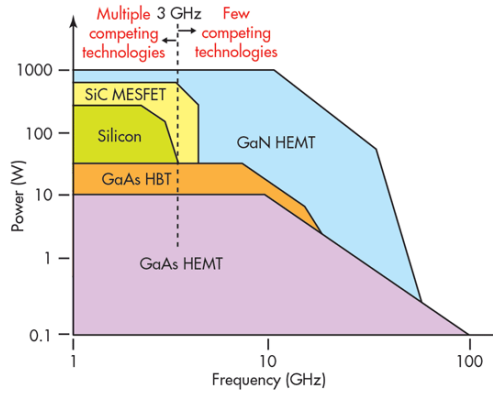


Figure 1.3: Semiconductor materials in use versus power and frequency, from [17].

circuits (MMICs). At the same time, Watt-level RF CMOS technology (not reported in Fig. 1.3) has been demonstrated at several tens of GHz and it is very promising in terms of costs and integration with other chipsets for high data-rate mobile communications [18]. Much less options are available at high-power, especially for high-frequency applications. Up to LTE/4G, the highest frequency of operation in telecommunication base stations is 2.6 GHz. At this frequency, silicon laterally-diffused MOSFET (LDMOS), in which large parallel gate fingers are combined with an extended drain region to achieve high breakdown voltage, still represents the best compromise between performance and cost [19]. However, LDMOS performance is too limited for a shift towards higher frequencies as well as for the developments of wireless backhaul [20].

Instead, the most promising technology for high-power and high-frequency is represented by Gallium Nitride (GaN) HEMTs, which are based on a heterojunction formed by a stack of AlGaN alloy and undoped GaN [21]. In fact, contrarily to GaAs HEMTs, in GaN HEMTs the 2DEG is not formed due to tailored doping profiles, but by both piezoelectric and spontaneous polarization induced effects. Due to the wide energy band-gap of GaN (3.44 eV) relative to GaAs (1.42 eV), AlGaN/GaN HEMTs combine the high-mobility channel mechanism with high breakdown voltages. High saturated drift velocity ( $2.5 \cdot 10^7$  cm/s) implies high current density, which in turn means that the total transistor area can be reduced, obtaining more Watt per mm of gate periphery. This also entails low output capacitance per Watt. High-breakdown allows high drain operating voltages, implying higher output impedance per Watt, enabling easier and more efficient matching. However, RF continuous-

wave (CW) power densities of more than a few W/mm create the necessity for efficient thermal dissipation to avoid unbearable operating temperatures. Along with the transistor technology, which fastly has evolved from 0.5  $\mu\text{m}$  and 0.25  $\mu\text{m}$  towards 0.15  $\mu\text{m}$  of gate length to allow PA design at increasingly higher frequencies [22]-[24], integrated passive components such as thin film resistors and metal-insulator-metal (MIM) capacitors has allowed MMIC design [25]. With these characteristics, GaN is the most promising candidate for next generation wireless infrastructure applications, whose operating frequency will be too high for LDMOS. Moreover, due to the low values of on-state resistance and of parasitic capacitances, GaN-on-SiC and GaN-on-Si transistors find applications as controlled switching devices for power converters [26],[27]. These two aspects make GaN a major enabling technology for the implementation of the transmitter architectures that will be addressed in section 1.3. However, despite this encouraging premise, GaN devices have unique characteristics that cause unwanted effects in their electrical behavior, which inevitably still prevent them from mainstream diffusion. The remainder of this section is dedicated to the description of these aspects. Furthermore, the state-of-the-art in GaN modeling techniques is addressed.

## 1.2.2 Dispersive effects in GaN HEMTs

Dispersive effects refer to low-frequency phenomena that affect the RF behavior of the transistor. These mainly include thermal effects and charge trapping effects. Charge trapping, in particular, has strong impact especially in compound semiconductors. Traps can originate from defects in the bulk, lattice mismatching of stacked semiconductor layers, and termination of the device surface [28]. While epitaxy of doped semiconductor layers of the same material is a fully developed process and yields high purity crystals, the growth of film layers of different materials with different lattice constants and different temperature coefficients implies material stress at the interface region and, at worse, causes modification of the crystal structure. Both thermal and charge trapping effects are critical in GaN-based transistors. As already discussed in section 1.2.1, the high power density reachable in GaN implies the necessity to dissipate power efficiently. High operating junction temperature causes a lower carrier mobility and saturation velocity, with the consequence of lower output current and RF output power. Although materials with very high thermal conductivity such as silicon carbide (3.5 W/cmK) or diamond (10-20 W/cmK) enable good power dissipation, the long heating and cooling transients, much slower than the RF signal variations, induce long-term memory effects on the RF behavior. As GaN is not yet a fully mature process, it suffers from a relatively high concentration of crystal defects, which in turn cause the presence of charge trapping centres

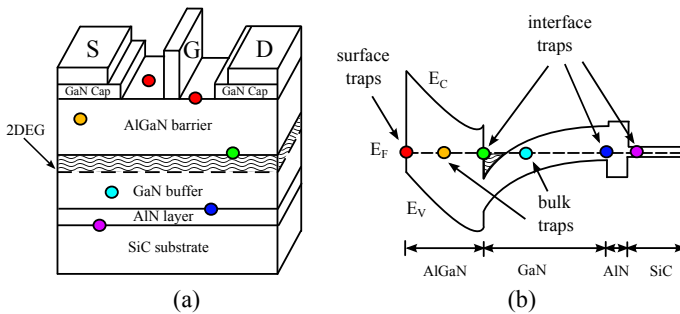


Figure 1.4: (a) GaN HEMT structure; (b) Energy band diagram. The various location of trapping centers are indicated in both pictures.

in various locations of the device, as shown in Fig. 1.4. Surface traps close to the gate act as a negatively charged *virtual* gate, causing a limitation to the maximum RF current [29]. To mitigate such effect, proper surface passivation can be implemented [30]. The presence of traps at the interface between the AlGaN and the GaN layers has influence in determining the 2DEG density. GaN buffer charge trapping, caused by lattice mismatch with the substrate, is activated in presence of high drain-source voltage. In fact, electrons moving in the 2DEG channel are rapidly accelerated, gaining enough kinetic energy to be injected into the buffer layer, where they are trapped [28]. These and other similar mechanisms can also be triggered by specific input configurations or thermal conditions, and may induce reversible or non-reversible degradation [31].

A detailed characterization and explanation of the charge trapping mechanisms has been target of much research work in the past years [32], and it is out of the scope of this Introduction. These are typically studied through various methods such as physical simulations [33], transient spectroscopy [34], or by measurement techniques [35]. Yet, it is worth describing the typical effects directly observable in the RF behavior [36]. In fact, the combination of filled and un-filled traps form a quasi-static charge layer in the device that modulates the electrical field distribution, whose concentration, in turn, can trigger additional trapping mechanisms. This results in a complex dependency on both the applied gate and drain voltages. Moreover, trap dynamics associated to charge capture and release show time scales ranging from  $\mu\text{s}$  to several seconds, much longer than the time-period of RF signals used in wireless applications. In particular, capture times in the ns- $\mu\text{s}$  range and emission times in the ms-s range have been reported for charges trapped in deep levels such as the ones localized in the GaN buffer [37]. Although the trap configuration can be assumed to remain in a steady state

under RF CW excitation, it still depends on the signal amplitude, on the thermal state and on the bias conditions. Moreover, in presence of modulated signals with envelope frequency in the MHz range, such as in case of telecommunication modulations, the traps configuration cannot be considered constant, originating long-term nonlinear memory effects. As a consequence, they are a major source of distortion and are critical in those wireless applications where high-linearity is a fundamental specification [38]. More in detail, dispersive phenomena affect transistor behavior both under small- and large-signal operation [39]. These involve, for example, abrupt variations, referred to as *kink effect*, in the static IV characteristics, and frequency variations in the small-signal transconductance and output conductance. These impairments are determined by deep trap levels located in the epitaxial layer [40], in the GaN buffer layer below the gate, or in the upper band gap region of the AlGaN barrier [41],[42]. Under large signal, trap-related effects lead to specific types of performance reduction known as *knee walkout* and *current collapse*. *Knee walkout* is a shift of the knee voltage ( $V_D^K$ ) of the IV characteristic towards higher values of the drain voltage  $V_D$  when in presence of large-signal RF excitation. Such a shift causes a dramatic limitation of the transistor saturation region, with a consequent reduction of the available RF output power and an increase in output distortion. *Current collapse* is a consistent drop in the drain current which takes place at increasing RF input powers, and it is caused by the presence of traps either in the surface layer or in the GaN buffer [39]. To conclude, output power and drain efficiency expected from nominal maximum current and breakdown voltage are not easily obtainable in actual microwave circuit implementations. In practice, PA performances do not improve by adopting higher quiescent voltages and higher driving signal amplitudes, as theoretically expected. In order to allow PA design, the dispersive phenomena described in this section should be suitably understood, characterized and included in reliable device models. The next section is a brief overview of the modeling approaches adopted towards this objective.

### 1.2.3 GaN HEMTs large-signal modeling trends

As GaN technology has shown great potential for high-frequency and high-power applications, the demand for reliable yet practical large-signal models to be used for PA design has steadily increased [43]. Considering the many phenomena affecting the GaN HEMT's operation, such a task has resulted to be not straightforward. One of the great difficulties is that the model formulation should work in the various transistor operating modes - including the sub-threshold region - in which dispersive effects can assume very different behaviours. Also, electro-thermal modeling gains higher importance due to the

high-power operating mode: tailored analysis and measurements of the thermal resistance have been reported [44],[45]. In other words, models should be able to scale in terms of bias, temperature, and geometry [46]. At the same time, the formulation should be engineered to work with standard simulation engines such as transient and harmonic balance (HB) analyses. Two general modeling approaches can be followed [21].

The first one is table-based, and consists of the acquisition of data measured on the device. For this type of techniques to be successful, a significant amount of data points are needed. Measurements adopted can be multi-bias static IV characteristics, multi-bias  $S$ -parameters, pulsed  $S$ -parameters and pulsed IV (PIV), load-pull and large-signal sinusoidal measurements. Then, large amounts of data must be suitably managed with interpolation or approximation techniques. Although black-box, behavioral-level methods such as  $X$ -parameters [47] have also been used to such an aim [48], a partial knowledge on the mechanisms occurring in the device is key to tailor measurements and give a better conditioning to data. In this sense, the pioneering work in [49] takes into account the asymmetrical capture and release times of GaN charge traps, and their dependency on the peak values of gate and drain voltages through an equivalent electrical network. Such description, for example, enhances the feasibility of the latest *DynaFET* model for GaN devices [50], in which a massive amount of large signal measurements, both low- and high-frequency, is used to train a neural network. One concern related to measurement-intensive modeling approaches is that the device-under-test (DUT) may change its behavior during the characterization process. As mentioned in section 1.2.2, some dispersive effects are dependent on high-voltage or high-temperature stress, which may trigger long spurious transients or soft degradation.

The second approach involves the description of the active device by closed-form equations, whose parameters can be extracted from measured data. The preliminary tentative approach consisted in applying, with success, formulations developed for GaAs HEMTs to GaN HEMTs [51]. In this way, the proven simulation capabilities and the designers' confidence in these models are leveraged. Although some good results have been reported [52] major changes became necessary, in particular to include traps-related effects and to allow better fitting of the drain current curve for increasing compression. Updates include improved thermal modeling [53], handling of the  $g_m$  and  $g_{ds}$  frequency dispersion [54], and optimization of the intermodulation distortion (IMD) at large signal [55]. Finally, hybrids of the approaches described above have proven to be good compromises for applications. In this sense, pulsed measurements [56],[57], which will be more extensively addressed in section 2.3, technically allow obtaining *isothermal* and *isodynamic* characteristics, allowing the characterization of dispersive effects and enhancing model fitting [58]. Another successful technique

consists in model parameter extraction based on combined low-and high-frequency large-signal sinusoidal measurements, allowing the direct identification of nonlinear dynamic dependencies under practical operating conditions [59],[60]. In both cases, tailored hardware for the large-signal characterization, later described in Chapters 2,3, should be available. Yet, the introduction of GaN-based PA in base station applications is still problematic [61]. In fact, until now, LDMOS has dominated the base station market and has been the technology of choice for proposing new high-power PA architectures, as the ones discussed in section 1.3.

## 1.3 RF Power Amplifier architectures

### 1.3.1 Linearity-efficiency trade-off

As mentioned in section 1.1, power amplifiers play a major role in the efficiency of base stations and handsets in modern telecommunication systems. As from literature [62],[63], a power amplifier can be designed to operate in different classes of operation, depending on the trade-off between linearity and efficiency. Let us consider a classic representation of an RF PA, as depicted in Fig. 1.5, where the power flows are explicitly indicated. The power  $P_S$ , drained from power supply at dc or low-frequency (LF), is modulated and delivered to the output load at RF. Such a conversion is not 100% efficient, and part of the drained power is dissipated in various unuseful forms, such as heat and spurious harmonics. We can define the drain efficiency ( $DE$ ) and the power-added efficiency ( $PAE$ ) of the PA as follows:

$$DE = \frac{P_{OUT}}{P_S} \quad (1.1)$$

$$PAE = \frac{P_{OUT} - P_{IN}}{P_S} = (G - 1) \frac{P_{IN}}{P_S} \quad (1.2)$$

where the PA gain is indicated by  $G = \frac{P_{OUT}}{P_{IN}}$ . If the PA must behave linearly,  $G$  should be kept constant. As a consequence,  $PAE$  depends on the proportionality between the drained power  $P_S$  and the input power  $P_{IN}$ . Linear RF PAs can only operate in A or B classes, in which the proportionality between input and output fundamentals is maintained. Indeed, for both classes, the conduction angle  $\theta$  of the current is invariable with respect to the input amplitude, although  $\theta = 2\pi$  for class A, while  $\theta = \pi$  for class B. Therefore, class A and B  $DE$  are, respectively, quadratic ( $DE_A^{MAX} = 50\%$ ) and linear ( $DE_B^{MAX} = 78.5\%$ ) with respect to the input power. If considering the high PAPR signals of modern telecommunication standards previously mentioned in section 1.1, PAs

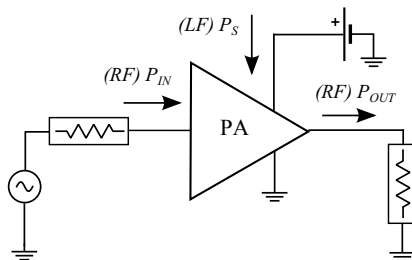


Figure 1.5: Classic representation of an RF PA with power flows explicitly indicated.

must be operated at large output power back-off to avoid distortions, and therefore very low average efficiencies are reached (e.g., 22% average vs 65% peak in class B, 4% average vs 42% peak in class A for a WCDMA signal [64]). Other classes of operation are extensively documented in the literature and report impressive efficiency for narrowband applications [62]. They implement switching operation (class D), further reduction of the current conduction angle (class C), or voltage and current overdrive (class S, F), together with harmonic tuning. Unfortunately, tough linearity constraints together with high PAPR and wideband requirements of modern standards makes such operating classes not directly suitable for wireless communications. Instead, the tendency is towards more complex transmitter architectures, as will be seen in next sections.

### 1.3.2 Load modulation

Modern transmitter architectures implement various single-stage PAs, supplies, power combiners, or other tailored designs in order to deal and optimize the linearity-efficiency compromise presented in section 1.3.1. Such architectures can be classified in broad terms as implementing load modulation or supply modulation of a main RF PA. Load modulation consists of dynamically modifying the instantaneous drain load impedance presented to the PA. This approach allows reproducing an impedance locus as close as possible to the one at maximum efficiency, which can be identified beforehand through load-pull measurements [65]. Load modulation can be typically implemented through varactor-based tunable matching networks [66],[67], or adding additional PAs. The most notable examples of the latter are the outphasing PA and the Doherty PA, respectively introduced by H. Chireix in 1935 [68] and W. Doherty in 1936 [69].

The outphasing amplifier, also referred to as linear amplification with nonlinear components (LINC), is based on the separation of the input signal in two constant envelope signals driving two parallel branches (Fig. 1.6(a)). Since none of the two signals features amplitude modulation, the PAs in each branch can be designed with high-efficiency operating modes, such as saturated or switching. In order to reconstruct the amplitude modulation, the two amplified signals are combined at the output. Although this configuration allows, in theory, to reach extremely high efficiency [70], many implementation drawbacks prevent the diffusion of outphasing PAs in wireless systems [71]. Firstly, the two phase-modulated signals have very wide bandwidths: this aspect may degrade the performance of the PAs, which are typically highly tuned. Moreover, digital trigonometric functions that generate the phase modulations also require high-speed hardware. Other issues concern the output recombination. It is clear that the output is highly sensitive to mismatches between the two branches. Furthermore, it should be noted that the two PAs are excited by a constant RF input power and a constant amount of power from the supply. This means that the output combiner must either dissipate or reflect the excess of power injected by the PA in order to produce an amplitude modulation at the output. If the combiner is dissipative, the only chance to maintain the efficiency is to reuse power by re-injecting it into the power supply [72]. Most commonly, however, the combiner is not or just minimally dissipative. Thus, part of the power is reflected, behaving as a variable load for the PAs, and introducing nonlinear distortion.

The Doherty PA, whose functional block schematic is depicted in Fig. 1.6(b), is a very popular design technique. It consists of a main amplifier and an auxiliary amplifier, designed such that the output current is linearly proportional to the input signal, and that the maximum of the fundamental component of the

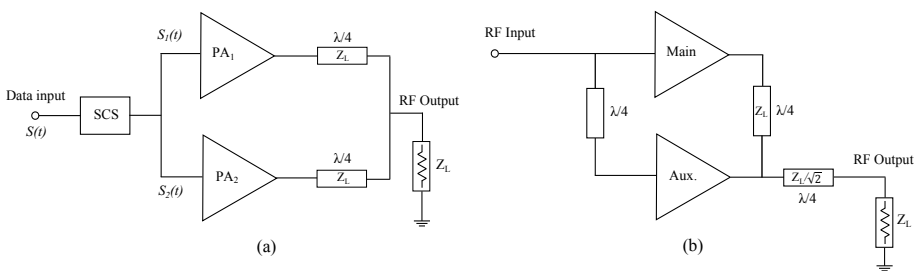


Figure 1.6: (a) Functional blocks of an outphasing PA. (b) Functional blocks of a Doherty PA. SCS stands for signal component separation and it is usually implemented in a digital way.

current, for each PA, is  $\frac{I_{MAX}}{2}$ , being  $I_{MAX}$  the maximum output current of the combination of the PAs [62], [73]. The PA loads are connected through a quarter-wavelength transmission line, which acts as an impedance inverter, with characteristic impedance  $Z_L$ , with  $Z_L = Z_{OPT}$ , being  $Z_{OPT}$  the optimal load impedance of the main PA. For low powers, the auxiliary amplifier is off and the load impedance of the carrier amplifier is  $2Z_{OPT}$ . As a consequence, the main amplifier reaches saturation at typically 6 dB less than the maximum combined power of the two PAs. For higher powers, the auxiliary amplifier turns on, and the load impedance seen by both the main and the auxiliary PAs decreases towards  $Z_{OPT}$  due to the load-pulling effect of the auxiliary PA. In actual implementations, class B and C PAs are used for the main and the auxiliary PAs, respectively. In Doherty PAs, the average efficiency can be increased to levels well above 30% for high PAPR signals, making it one of the most used architectures in modern base stations [74],[75]. In terms of linearity, the Doherty PA architecture allows room for optimization by designing the auxiliary PA gate biasing such that part of the IMD products of the main PA are canceled [69]. Nevertheless, major drawbacks remain, such as the AM/PM distortion induced by the load modulation [76] and the inherent limitation of operative bandwidth due to the impedance transformer. Although major advancements in this sense have been demonstrated [77],[78], digital predistortion techniques are usually necessary in order to meet the linearity requirements.

### 1.3.3 Supply modulation

In standard PA, the fixed supply voltage is set to accommodate the linearity constraints for the maximum RF power level foreseen by the application: this means that, in presence of high PAPR signals, the average efficiency of the PA is very low. A way of improving the efficiency of a transmitter is making use of a dynamic voltage supply [79]. The two most common PA architectures implementing supply modulation are envelope elimination and restoration (EER), originally proposed in [80], and envelope-tracking (ET) [81]. The architecture of an EER PA (Fig. 1.7(a)) is composed by a supply modulator (SM) and a saturated switching PA. The RF signal at the input of the switching PA features a constant-envelope modulation, carrying information only in its phase. The power of the RF input is limited to a level that saturates the switching PA so that, in this way, the maximum output current is set by the supply voltage. Therefore, the amplitude modulation at the RF output is uniquely applied through a modulation of the supply voltage. In this way, RF  $P_{OUT}$  is proportional to power drained from the supply ( $P_S$ ), and the linearity-efficiency compromise depicted for class A and B PAs does not apply anymore. However, some other issues should be considered. First of all, in case

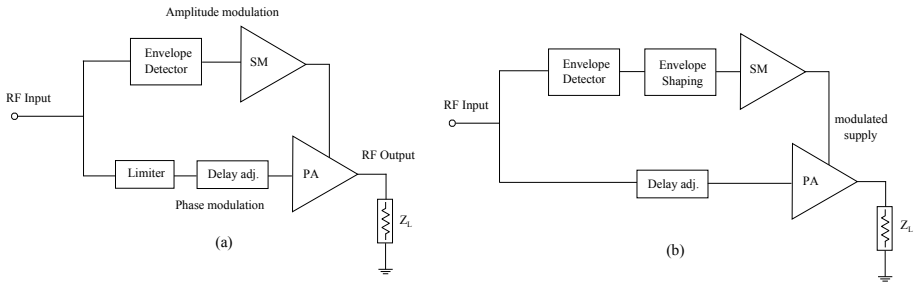


Figure 1.7: (a) Functional blocks of EER. (b) Functional blocks of ET.

of small RF output power, the PA stays driven by the constant-envelope RF input power, while its supply is diminished to small values. Such a configuration not only may cause instability, but also implies a very low gain and efficiency, as the PA should dissipate the unnecessary RF input drive. In second place, it is clear that the efficiency problem is moved to the supply modulator. The total efficiency of the transmitter would be the product of the efficiencies of the SM and of the PA, thus also the SM should be designed to work in an efficient class of operation. At the same time, the linearity of the RF output signal directly depends on the linearity of the SM. Finally, a number of distortion mechanisms take place in EER transmitters, as reported in [82],[83]. The constant-envelope phase-modulated RF signal has a very wide bandwidth which should be handled by both the digital hardware and the switching PA. In addition, the synchronization between the RF and the supply signals should be very accurate to avoid misalignments and a consequent dramatic performance reduction. Moreover, the unwanted effects of the supply voltage on the output have to be taken into account. These include the nonlinear transition between switching and linear transistor operations, as well as the AM/PM distortion caused by the output capacitance which varies with the dynamic supply and does not allow a straightforward output matching [82].

The ET technique [81] consists of dynamically adapting the supply voltage of the PA so that the power dissipation is minimized (Fig. 1.7(b)). With respect to EER, no conditioning is made on the RF input signal. On the other hand, linear classes of operation such as AB or B are normally chosen for the main PA. The supply is modulated to dynamically track the RF input envelope and keep the main PA close to saturation, with the aim of minimizing the power drained by the supply. However, the RF input-output characteristic cannot be compressed as much as in EER in order to maintain linearity for amplitude modulation. Although the PA peak efficiency is not modified relative to the case with fixed supply, the average efficiency can largely increase, as the PA always

works close to its peak efficiency [84]. The improvement is clear if considering a class A PA (for example 16% vs. 9% of average efficiency for WCDMA signal), but it is more evident if biasing the PA in class B (59 % vs. 35%) [71]. The instantaneous RF input envelope maps into an instantaneous supply voltage through a relationship called *shaping function*. This function allows adapting the dynamic voltage drive and introduces a degree of freedom to obtain, for example, constant gain or constant *PAE* characteristics. Unlike EER, PA gain never becomes too small, making it less critical for low powers. Furthermore, ET has lower sensitivity with respect to the dynamic supply voltage, which means less critical synchronization between the PA and the supply modulator, and smaller variations of the output capacitance. At the same time, the main PA has no particular bandwidth requirements. Moreover, the supply modulator may be implemented with milder bandwidth requirements without necessarily causing distortions.

Notwithstanding the many positive features of ET, many critical aspects should be considered when designing and operating an ET PA. First of all, it should be noted that, as in EER, various operating modes can be activated due to the variation of the supply voltage [85]: theoretically, in ET, the RF output power should depend linearly on the RF input power and be independent from the supply voltage. However, for small supply voltages, the transistor is operated near the knee voltage, and the dependency on the output voltage may become non-negligible. Moreover, the mutual interaction between a modulated RF input and the modulated supply stimulates nonlinear-dynamic effects, depending on the device dispersive phenomena and on the implemented matching and bias networks. In particular, the bias-tee at the drain node is the most critical one, as no decoupling capacitor should be placed in order to allow voltage modulation. As a consequence, quarter-wavelength stub is often used [15]. However, due to the fact that the drain port of the transistor sees a variable load at low-frequency, stability issues may arise [86]. Last but not least, the efficiency of the supply modulator should be maximized. The linearity constraints of the supply modulator are not as tough as for EER, but its operation has a critical impact on the output distortion and noise. Much research has been invested in the design of highly efficient supply modulators and they can be roughly divided into three categories. Linear modulators, as for example class A/AB amplifiers, maintain high linearity and high bandwidth, delivering excellent out-of-band spectral components and a smooth voltage waveform at the expense of poor efficiency. Another category is represented by switched-mode power supplies. Such converters make use of pulse modulation schemes, such as pulse width modulation (PWM), and can reach very high efficiency. However, an important limitation is represented by bandwidth, which is inversely proportional to the converter efficiency and directly depends on the switching frequency of the transistors. In addition, the presence of switching circuitry increases, in general,

the out-of-band spectral noise and the ripples on the voltage waveform. As a consequence, the output of a switching converter is usually low-pass-filtered in order to reduce the high-frequency noise, although this influences the RF PA dynamic behaviour. In order to increase the bandwidth of the converter, multilevel approaches can be adopted, with better results also in terms of output ripples [87]-[89]. The last category, known as hybrid-switching amplifiers, implement both switching and linear circuitry. A classic configuration consists of a high-bandwidth linear modulator operating in parallel with a high-efficiency buck converter [90]. The buck provides most of the power in an efficient way, while the linear modulator handles the higher frequency components of the dynamic voltage, while carrying a smaller portion of power.

Although its inherent complexity and the many challenges in terms of design and system optimization, ET remains the most promising PA architecture for future efficient RF transmitters, both for base station and handset applications. ET has also been used in conjunction with load modulation techniques, such as Doherty, with the aim of combining the high-efficiency obtained at high power with load modulation, while optimizing the ET operation in the low-power region [91]. Another promising aspect of ET is the possibility to tailor the PA operation with respect to the modulation type, which is a key advantage in multi-mode multi-band PAs [79]. With respect to handset PAs, most of solutions feature ET-operated HBT PAs. For handsets, the supply modulator is often designed in CMOS technology and recent research has shown that it can be directly integrated with the PA in an RFIC [92]. Private companies have heavily invested in such solutions, and commercial products are hitting the market [93],[94]. On the other hand, although high-power ET PAs have been demonstrated in the literature [95],[96], their diffusion in base stations is undoubtedly under the full potential. A reason of their limited diffusion is that ET requires composite architectures both for the presence of complex supply modules, but also for the digital signal processing framework necessary to control both RF input and dynamic voltage. In this sense, any supply-modulated PA requires new linearization techniques that mitigate the composite distortion mechanisms previously described. To do so, tailored PA models are needed. In conclusion, the costs and efforts related to transmitter infrastructure evolving towards ET must be justified by a consistent improvement relative to the simpler but high-performance solutions in use, such as fixed-supply Doherty.

## 1.4 RF Power Amplifier modeling

### 1.4.1 Approaches for PA modeling

As seen in section 1.3, the linearity of the PAs determines the quality of the transmitted signal. PA linearity assessment can be done experimentally, by measuring RF input and output for the extraction of well-known metrics such as compression points and intermodulation distortions [97]. Out of such characterizations, one might already build a simple PA model based on an RF input-output characteristic, and predict whether a specific PA would be sufficiently linear for a specific signal or application. However, due the inherent complexity of the phenomena described in section 1.2.2 and the various sources of distortion reported in section 1.3, giving a good description of the linearity of a modern transmitter is not as easy as one can imagine. As a consequence, various PA modeling techniques have been developed in the past years. They can be roughly divided into two groups: circuit models and behavioral models [98]. Circuit models are based on a network of equivalent electrical elements. Such models can be highly precise and are often used to better understand mechanisms or control variables that are not easy to handle in an experimental way. However, they usually require large computational resources making it impossible to describe complex transmitters such as the ones in section 1.3. On the other hand, behavioral models attempt to model the system with little or no a priori knowledge of the circuits. They are obtained uniquely from measurements on the PA, and can be usually implemented for fast simulation and data processing. In order to efficiently describe the complex effects due to semiconductor properties as well as PA topology if no a priori knowledge is assumed, nonlinear system identification theory is exploited. In this sense, the PA is described as an operator that maps a function of time (the input signal  $\tilde{x}(t)$ ) in another function of time (the output signal  $\tilde{y}(t)$ ) through the following state equation:

$$f\left[\tilde{y}(t), \frac{d\tilde{y}(t)}{dt}, \dots, \frac{d^P\tilde{y}(t)}{dt^P}, \tilde{x}(t), \frac{d\tilde{x}(t)}{dt}, \dots, \frac{d^P\tilde{x}(t)}{dt^P}\right] = 0 \quad (1.3)$$

where  $P$  is the maximum derivative order to be considered. Under the hypothesis of operator causality, stability, continuity and fading memory [98], the general equation of (1.3) can be represented by a non-recursive form where the relevant input past is restricted to a limited memory span  $T$ :

$$\tilde{y}(t) = f[\tilde{x}(t), \tilde{x}(t - \tau_1), \tilde{x}(t - \tau_2), \dots, \tilde{x}(t - T)], \quad (1.4)$$

with  $\tau_1 < \tau_2 < \dots < T$ . The multidimensional function in (1.4) can be structured in various ways. In literature, direct look-up tables (LUTs),

polynomial filters and artificial neural networks (ANNs) received particular attention due to their formal mathematical support and straightforward translation into implementation [99],[100]. An important aspect to mention is that since the information is carried by the modulation signal, it is not strictly necessary to model a PA with respect to its RF input and output. Although passband behavioral models have been proposed, the vast majority of behavioral models is constructed through a baseband-equivalent representation, in which the input and output of the model are the complex envelopes  $x(t)$  and  $y(t)$  of the input-output RF signals  $\tilde{x}(t)$  and  $\tilde{y}(t)$ :

$$\tilde{x}(t) = \Re\{x(t)e^{j2\pi f_0 t}\}; \quad \tilde{y}(t) = \Re\{y(t)e^{j2\pi f_0 t}\}; \quad (1.5)$$

where  $f_0$  is the carrier frequency. Various behavioral modeling approaches have been proposed in literature and they can differ depending on their mathematical structure, the use of fitting parameters, upon their definition in continuous or discrete time domain, and many other properties, as comprehensively reported in [98].

## 1.4.2 Overview of PA behavioral models

PA models can be categorized with respect to the type of distortion they are able to reproduce. Three main categories are quasi-memoryless (quasi-static) models, models with linear memory, and models with nonlinear memory [99]. Nonlinear quasi-memoryless models are applicable to PAs in which the output depends on the instantaneous value of the input signal. Thus, they can be represented as two algebraic functions of the instantaneous envelope amplitude. One function, describing the output amplitude, is widely known as the AM/AM characteristic. The other function, describing the output phase, is known as the AM/PM characteristic. Such characteristics can be implemented as look-up tables (LUTs) directly obtained from measurements and properly interpolated, or as parametric characteristics. As an example, a power series with complex coefficients  $h$  results in

$$y(t) = F[|x(t)|] = \sum_{p=1}^P h_{2p-1} |x(t)|^{2p-1} \quad (1.6)$$

where a pure nonlinear odd symmetry is considered, and no dynamic distortion from even-terms is assumed [99]. A more general representation including both odd and even terms is represented instead as:

$$y(t) = \sum_{p=1}^P h_p x(t) |x(t)|^{p-1} \quad (1.7)$$

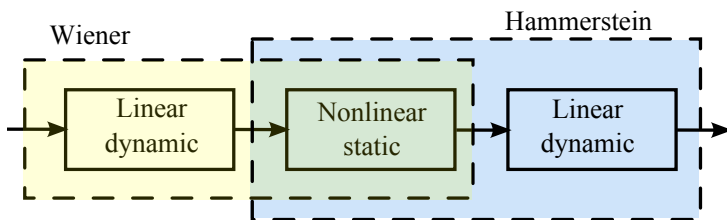


Figure 1.8: Hammerstein-Wiener behavioral model structures.

Some examples of this category are the Saleh models [101], the Rapp model [102], the Fourier series model [98], the Bessel Fourier model [98], and Hetrakul and Taylor models [98]. However, with the progressive increase of signal bandwidth together with the technology-related phenomena such as the ones described in section 1.2.2, memory effects have become a major issue to address.

A preliminary approach consists of assuming that the memory effects and the nonlinearity can be separated, implying that the memory is linear with respect to the input. Such a simplification is at the basis of the so called "two-box" models. Two major examples of this kind are the Hammerstein model, which consists of a nonlinearity followed by a filter, and the Wiener model, which consists of a filter followed by a nonlinearity (Fig. 1.8). It should be noted that the Hammerstein approach is natively linear in the parameters, while Wiener is not. If applying both methods together, one obtains a "three-box" model structure which includes a pre-filtering and a post-filter: examples of this kind are reported in [101]-[103]. As last category, nonlinear memory modeling has been widely addressed in the literature [99]. Nonlinear memory effects are the cause of frequency-dependent two-tone intermodulation response, nonlinear impulse response, and dynamic response of modulated signals even in case of narrowband excitation. In fact, such effects are also observed with relative modulation bandwidths  $< 1\%$  at carriers around  $\simeq 2$  GHz, so that RF carrier effects, such as the ones introduced by matching networks, may be ruled out [99]. A preliminary way to include these effects is to introduce additional parametric dependencies to extend standard AM/AM and AM/PM quasi-static characteristics [104]. Other approaches consists in a large but finite number of parallel branches of nonlinear memoryless blocks and filters, arranged following the Wiener [105] or Hammerstein [106] topologies. It should be noted that they do not contain all cross memory terms between the various delayed input values, because they are 1-D approximations. However, unlike the one-branch cases described above for linear memory, such structures can reproduce a nonlinear memory mechanism by using different filters for different nonlinear orders.

It is worth mentioning that the coefficients of such nonlinear memory models

are often obtained by the acquisition of modulated input-output data of sample RF signals. As a consequence, no independent experiments for the extraction of the coefficients are performed. Instead, these are selected to minimize an error function between determined measured and predicted PA responses. Such an identification strategy is followed either if the model structure does not allow to isolate the various linear and nonlinear contributions at the various orders, or if the measurements needed for the identification of the single kernels are too demanding in terms of complexity and hardware. Although this identification approach is proposed in many nonlinear dynamic models and offers a practical way to deal with complexity, it creates issues in defining the real applicability range of the extracted model. In fact, such an optimization does not guarantee a unique solution, nor that the model will keep its accuracy when predicting the response to excitations different from the ones used for model extraction [99]. As a consequence, the higher is the sensitivity of a model structure to coefficients variations, the more precise, and possibly direct, should be the identification of the coefficients. To deal with such limitation, it is of critical importance to properly select the extraction signals in order to excite all possible modes and orders accounted for in the model formulation. If done properly, the over-dimensional identification matrix upon which error minimization is performed should not be ill-conditioned.

Alternative approaches have been proposed to implement the general formulation in (1.4). A number of behavioral modeling and implementation techniques, such as the ones based on neural networks or on nonlinear feedbacks, are out of the scope of this Introduction. Instead, the section 1.4.3 is dedicated to widely used behavioral models derived from the general Volterra formulation. The general Volterra formulation [107] represents a formal framework to model nonlinear systems with nonlinear memory. Together with the use of polynomial filters, it is particularly spread as it results in modeling structures that are linear in the parameters, enabling the use of systematic linear extraction procedures.

### 1.4.3 Volterra-based models

The Volterra series approximates the function in (1.4) as a Taylor series in which the nonlinear coefficients are expressed as a multifold convolution integral of a multidimensional impulse response:

$$\tilde{y}(t) = \sum_{p=1}^{+\infty} \int_{-\infty}^{+\infty} \cdots \int_{-\infty}^{+\infty} \tilde{h}_p(\tau_1, \dots, \tau_p) \prod_{m=1}^p \tilde{x}(t - \tau_m) d\tau_m \quad (1.8)$$

where  $h_p$  is the  $p$ -th impulse response. The continuous-time formulation in (1.8) can be described in discrete-time by sampling the signals at a uniform sampling

rate  $T_s$ , obtaining

$$\tilde{y}[n] = \sum_{p=1}^P \sum_{m_1=0}^M \sum_{m_2=0}^M \cdots \sum_{m_p=0}^M \tilde{h}_p[m_1, m_2, \dots, m_p] \prod_{j=1}^p \tilde{x}[n - m_j] \quad (1.9)$$

where the index  $n$  corresponds to the samples at  $t_0 + nT_s$ ,  $t_0$  is an arbitrary time instant,  $P$  is the maximum nonlinear order, and  $M$  is the maximum memory length. In most cases, however, such formulation is applied to the baseband-equivalent signals  $x(t)$ ,  $y(t)$ . In this case, one can reduce the number of coefficients by considering only the terms that fall at the envelope frequencies [108]:

$$y[n] = \sum_{p=1}^P \sum_{m_1=0}^M \sum_{m_2=0}^M \cdots \sum_{m_p=m_{p-1}}^M \sum_{m_{p+1}=0}^M \sum_{m_{p+2}=m_{p-1}}^M \cdots \quad (1.10)$$

$$\sum_{m_{2p-1}=m_{2p-2}}^M h_{2p-1}[m_1, m_2, \dots, m_{2p-1}] \prod_{i=1}^p x[n - m_i] \prod_{j=p+1}^{2p-1} x^*[n - m_j]$$

As mentioned, the Volterra series is capable of modeling nonlinear characteristics and nonlinear memory effects. Nevertheless, its range of applicability is valid only in case of weakly nonlinear memory. In fact, it produces an optimal approximation around the point in which it is expanded, providing good modeling properties in the small-signal regime. At the same time, it shows fast degradation under large signal conditions. This is due to the non-convergence of the series in case of strong nonlinearities, the increase in computational complexity with series order and the difficulties in measuring the higher-order Volterra kernels [98]. Considering that the formulation is linear in the parameters, it easily allows to estimate the kernels from input-output data. However, the choice of input signals and parameter optimisation criteria are critical elements of the identification procedure, especially considering the bad convergency properties in case of hard nonlinearities. Alternatively, publications such as [109] present enhanced measurement techniques for Volterra kernels but, despite the possibility of measuring higher-order kernels, there is a practical limit to the nonlinear order. Much research has been carried out in order to overcome the limitation of the standard Volterra series, resulting in modifications of the formulation in (1.8). These, for example, include enhancements of the multidimensional kernels structure for the discrete formulation [110], as well as pruning of cross-correlated terms to minimize the number of coefficients [111]. In the next subsections, the attention is drawn to two widely adopted Volterra-based modeling approaches.

## Polynomial models

The memory polynomial (MP) model is designed in the discrete-time domain and can be interpreted as an extension of the Taylor series to include memory, or as a reduction of the standard Volterra formulation where only the diagonal memory terms are included. Such a formulation, equivalent to a parallel Hammerstein model [112], shows a good compromise between generality and ease of parameter estimation. The formulation is as follows:

$$y[n] = \sum_{p=1}^P \sum_{m=0}^M h_{p,m} x[n-m] |x[n-m]|^{p-1} \quad (1.11)$$

with the same notation as in (1.10). Since the absence of cross-terms may be a limitation for some applications, a generalized memory polynomial (GMP) model including further cross-terms has also been proposed [113]:

$$y[n] = \sum_{p=1}^P \sum_{m=0}^M \sum_{q=0}^M h_{p,m,q} x[n-m] |x[n-m-q]|^p \quad (1.12)$$

It should be noted that the applicability of polynomial models derived by the Volterra formulation is, not surprisingly, limited to weakly nonlinear PAs. Moreover, as no direct experiments for the identification of the parameters is usually done, the critical aspects mentioned in section 1.4.2 concerning the coefficients estimation represent a possible limitation in the applicability of such models.

## Modified Volterra

In order to overcome the limitation of only weak nonlinearities, an alternative formulation of the series in (1.8) has been proposed and denominated *modified Volterra* series [114],[115]. Such a new formulation has originated by considering that while the nonlinear characteristic is somehow inherent to the behavior of electronic components, the presence of memory (and especially nonlinear memory) is an unwanted feature of RF systems, which must be minimized by all possible means. Under this idea, it makes little sense to apply the standard Volterra series, which is unsuitable to model strong nonlinearities. The *modified Volterra* approach consists of reformulating (1.8) in terms of dynamic deviations of the input signal:

$$\tilde{y}(t) = f[\tilde{x}(t)] + \sum_{p=1}^{\infty} \int_{-\infty}^{+\infty} \cdots \int_{-\infty}^{+\infty} \tilde{g}_p[\tilde{x}(t), \tau_1 \cdots \tau_p] \prod_{m=1}^p [\tilde{x}(t - \tau_m) - \tilde{x}(t)] d\tau_m \quad (1.13)$$

where  $f$  is a quasi-static function of the input signal and  $g_p$  are kernels of the modified Volterra series, which are nonlinearly dependent on the input  $x(t)$ . The notable feature of the formulation in (1.13) is that memory effects are separated from the quasi-static nonlinearity. Nevertheless, it can be shown [115] that (1.8) is a particular case of (1.13) for  $x(t) = 0$  and that the coefficient  $g_p$  can be written in terms of the coefficients of the classical Volterra series. As a consequence, (1.8) and (1.13) are equivalent representations with the same convergence properties. However, considering that only a small number of kernels is practically measured, their practical range of application is very different. If, for example, both are truncated to a one-fold integral, the standard Volterra model describes a linear system, while the modified one includes a first-order approximation of nonlinear memory effects. The modified Volterra, in fact, is effective for all systems in which the dynamic deviations determined by nonlinear memory effects are small, either because the amplitude variations are small or because the nonlinear memory is short. While the approach in (1.13) represents a general theory for nonlinear-dynamic systems and has been preliminarily applied to transistors [114], it has also largely been used for baseband-equivalent modeling of PAs [116]-[118].

Depending on the extraction methodology, two approaches can be followed. The first, proposed in [116],[118], consists of mapping (1.13) in the envelope domain, and analytically deriving the dependencies of the terms for the input and output envelopes. Given the better properties of the truncation error as well as the complexity in addressing higher orders, a first order direct extraction from measurements is usually proposed. The second approach, derived in [119] and known as *Dynamic-deviation reduction* (DDR), rewrites the modified Volterra in terms of the classic Volterra coefficients and formulates it in discrete-time domain:

$$y[n] = \sum_{p=1}^P h_p x^p(n) + \sum_{p=1}^P \left\{ \sum_{r=1}^p \left[ x^{p-r}[n] + \sum_{i_1=1}^M \cdots \sum_{i_r=i_r-1}^M h_{p,r}(i_1, \dots, i_r) \prod_{j=1}^r x(n - i_j) \right] \right\} \quad (1.14)$$

where  $r$  is the order of the dynamic kernels progressively accounted for in the model. This mathematical manipulation allows obtaining a model that is linear in the parameters, enabling the identification of higher orders by using minimization error techniques to extract the model coefficients from input-output data. Although this formulation has been a breakthrough due to its inherent flexibility in accounting for higher dynamic orders, also in this case the

critical aspects related to the optimization of the coefficients, already mentioned for MP and GMP, should be addressed with tailored extraction excitations.

#### 1.4.4 Recent trends

One of the main reasons behind the extraction of a behavioral model for RF PAs is to use it for linearization. As a consequence, an important aspect to address is the availability of model inversion procedures. While for quasi-static models one may assume a bi-univocal relationship between the input and output signals, which allows a direct analytical inversion, models with memory cannot leverage on immediate inversion procedures. As a consequence, digital predistortion techniques are often based on the identification of predistorter coefficients [120]. Usually, an observation path allows capturing the distorted PA output, and an error with respect to the desired modulated signal is obtained. Then, a processor extracts the optimal predistorter for linearization. This can be done either through a direct or indirect learning architecture, as summarized in [120]. The predistorter is often based on a nonlinear-dynamic modeling function such as the ones reported in section 1.4.3. However, in the vast majority of cases, the linearization performance only partially relies on the capability of the model in reproducing the nonlinear memory effects of the PA, while it is strongly dependent on the feedback capability and on a continuous update of the coefficients [121]. By all means, it works as a control system. Indeed, MP or eventually DDR are often reported as sufficient predistortion capabilities for the linearization of PAs, at least until a few MHz bandwidths are considered for carriers up to a few GHz. Yet, two major aspects may disrupt this way of operating: firstly, the increase of modulation bandwidth to hundreds of MHz as well as the necessity of multi-carrier operation create problems in designing an ideal wideband feedback path. Furthermore, the combination of fast and slow phenomena such as charge trapping and thermal effects, or specific distortion effects due to a complex PA topology, may be incompatible with the idea of continuously adjusting the predistorter.

Moreover, the higher complexity in the architectures of PAs has also triggered the interest in reliable models for RF system simulation. Indeed, in case of simple PA architectures, circuit models are still manageable in terms of complexity and simulation time. Instead, when considering the advanced architectures described in section 1.3, the PA becomes too complex, and feasible simulations require behavioral-level representations. Such behavioral models should not only reproduce the output distorted signal, but also the electrical interaction (e.g., termination at all ports and mismatch at the frequency of interest) for considering antenna mismatch, load modulation, and supply modulation [122]. Moreover, the major sources of nonlinear memory effects determined by the

semiconductor properties or circuit interactions should be modeled [123]. A well-known behavioral approach is the *Polyharmonic Distortion* (PHD) modeling framework [47], also known as *X*-parameters [124]. Although such a model has been already mentioned in section 1.2.3 for applications to devices, its principal application is RF power amplifier modeling for system level simulations [125]. It is formulated in frequency domain and it is based on the linearization around a large-signal operating point (LSOP). It is capable of predicting scattered waves at both input and output ports at the harmonic frequencies of interest through the following formulation:

$$B_{e,f} = X_{e,f}^{(F)}(|A_{11}|)P^f + \sum_{g,h} X_{e,f,gh}^{(S)}(|A_{11}|)P^{f-h}A_{gh} + \sum_{g,h} X_{e,f,gh}^{(T)}(|A_{11}|)P^{f+h}A_{gh}^* \quad (1.15)$$

where  $A$  and  $B$  represent the incident and scattered waves,  $e$  and  $f$  ( $g$  and  $h$ ) are the indexes of the output (input) ports and harmonics, respectively, and  $P = e^{j\phi(A_{11})}$ . In the classical formulation of (1.15), the LSOP is set by a large tone  $A_{11}$ ; however, the LSOP can be eventually forced by a multi-tone input or depend on the output mismatch [124]. Yet, the model in (1.15) only gives quasi-static predictions. Further developments have led to the formulation of the dynamic *X*-parameters, which are formulated as an additional dynamic deviation around the quasi-static formulation [126]:

$$B(t) = \left( X^{(F)}(|A(t)|) + \int_0^{+\infty} G(|A(t)|, |A(t-\tau)|, \tau) d\tau \right) e^{j\phi(A(t))} \quad (1.16)$$

where  $G(x, y, t) = \sum_{i=1}^N D_i(x)(P_i(y) - P_i(x))k_i(t)$  is a general nonlinear-dynamic function, and the  $i^{th}$  hidden variable represents an underlying dynamical process. The impulse response functions  $k_i$  represent the system dynamics with respect to each hidden state variable. In this formulation, the dynamic effects are accounted for around the fundamental frequency (not at harmonics). Moreover, similarly to [118], the formulation proposes a linearization of the dynamics around a large-signal operating point. Yet, the behavioral-level function  $G$  linking the source of distortion with the effects on the outputs should be accurately identified through proper identification procedures, which in this case consist of a set of RF amplitude steps [126]. Indeed, a powerful aspect of the *X*-parameter framework is the availability of a tailored measurement framework - the Nonlinear Vector Network Analyzer (NVNA) software application running on the Keysight PNA-X hardware - capable of automating the measurements and providing a synthesized model ready to be simulated with HB and RF envelope engines.

## 1.5 This work

### 1.5.1 Objectives

The Ph.D. work focuses on two major research lines. The first one concerns the characterization and compact modeling of GaN-on-SiC power transistors for RF applications. In order to study the nonlinear charge trapping and its effects on the output electrical behavior, a recently introduced pulsed set-up has been used and customized in order to acquire iso-dynamic pulsed IV characteristics. This has led to a formal reformulation and experimental characterization of the lag effects measurable on GaN devices. Finally, a compact modeling approach based on the proposed experimental techniques is proposed. The second research topic concerns the behavioral modeling of supply-modulated power amplifiers. As described in section 1.3.3, envelope-tracking is the most promising PA architecture both for handset and base station applications. Although a supply-modulated PA should be considered as a three-port device, none of the available approaches in the literature was giving a formal framework for the nonlinear dynamic characterization and modeling accounting for the supply excitation. As a consequence, large-signal PA characterization techniques have been investigated to formulate, extract, and validate a new behavioral modeling approach for supply-modulated PAs. Furthermore, a linearization technique based on the model is proposed. It is worth mentioning that both research activities have requested advanced large-signal measurements and, in some cases, a customized use of the instrumentation as well as the introduction of additional components in an innovative set-up has been necessary. As a consequence, research in such topics has resulted as key aspects of the work.

### 1.5.2 Organization of the text

The present manuscript is organized as follows:

- Chapter 2 is devoted to the characterization and modeling of GaN devices. In particular, GaN pulsed measurements are investigated, and a novel *double-pulse* technique for the empirical characterization and assessment of dispersive effects such as gate- and drain-lag as well as current collapse is presented. Finally, a compact GaN device modeling approach based on the double-pulse technique is proposed.
- Chapter 3 is dedicated to the application of large-signal measurement techniques to supply-modulated PAs. First, a description of instrumentation and custom set-ups, developed during the activity, is detailed. Then,

two sections are dedicated to the characterization of the drain-supply terminal in supply-modulated PAs. Finally, a section is dedicated to the characterization of thermal effects.

- In Chapter 4, a behavioral model for RF power amplifiers with supply modulation is described. A three-port, nonlinear-dynamic modeling approach based on the *modified Volterra* series is formulated, along with the description of extraction procedure as well as experimental validation. Finally, a linearization algorithm based on such model formulation is also proposed.
- In Chapter 5, conclusions are drawn: the main results achieved during the Ph.D. are reported and some future research proposals are discussed.



## Chapter 2

# Characterization and modeling of GaN HEMTs

### 2.1 Introduction

As already discussed in section 1.2.3, although PA solutions are becoming available, GaN technology is still far from being a mature process. Thus, advanced characterization procedures are needed for the device performance assessment, technology evaluation as well as compact empirical modeling. This Chapter is dedicated to the efforts made in characterizing and modeling GaN HEMT devices provided by various foundries, among which United Monolithic Semiconductor (UMS) [22] and Selex ES [24]. Much of the measurements are obtained with a custom set-up (described in section 2.2) denominated *Multiple-Pulse Time Domain Network Analyzer* (MP-TDNA), already present at the University of Bologna before the start of the Ph.D. and progressively updated to double-pulse excitation during the research activity. The capabilities of such a set-up have been progressively upgraded from standard pulsed IV (PIV) to excitations specifically tailored for the dispersive phenomena present in GaN. In particular, a method implementing a *double-pulse* waveform has been found useful for dealing with the nonlinear dynamics induced by charge trapping. Section 2.3 discusses the use of PIV measurements for device characterization, and the issues arising with GaN. The double-pulse technique is detailed in section 2.4, with a focus on the effects measured on pulsed and dc current characteristics. The results achieved in this phase have been published in [127]-[131]. New lag characterization functions, denominated nonlinear and linear

lag functions ( $\lambda_{NLF}$  and  $\lambda_{LLF}$ , respectively) are introduced in section 2.6, in order to give a new description of the nonlinear dispersion due to traps. Finally, a modeling approach based on double-pulsed IV (DPIV) characteristics and published in [132], is depicted in section 2.7, along with large-signal validation. It should be mentioned that the work detailed in this Chapter is the result of the collaboration with the group at University of Bologna.

## 2.2 Multiple-Pulse Time Domain Network Analyzer

### 2.2.1 Operation

Many works have shown the usefulness of low-frequency measurements for the identification of device models [133]. This is especially important for GaN devices due to the presence of dispersive phenomena, which should be suitably characterized and included in the compact model formulation. Among the various empirical identification approaches, pulsed drain current versus voltage (PIV) characterization has emerged as a powerful method for transistor modeling [134]. PIV characteristics are obtained by applying low-duty-cycle narrow-width pulsed periodic gate and drain excitations, in order to acquire IV measured samples without changing the thermal state and the charge-trapping state of the device. An analysis regarding the use of pulsed IV characteristics for transistor characterization and modeling will be carried out in section 2.3. In order to obtain an isodynamic IV characteristic it is necessary to apply pulses that are shorter than the time constants associated with dispersive phenomena. Unfortunately, conventional set-ups such as the ones in [135]-[137] are based on

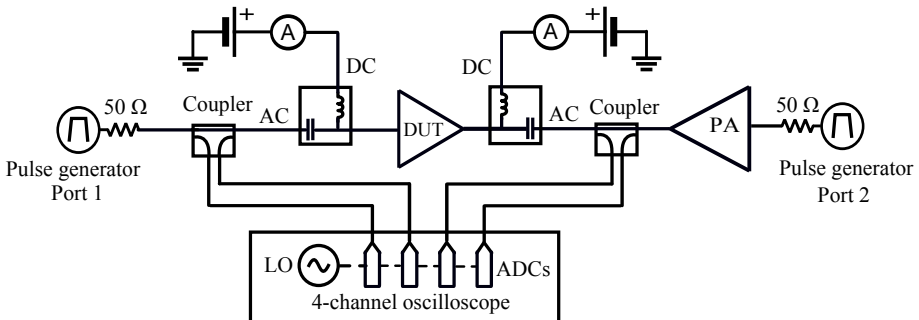


Figure 2.1: Block diagram of the MP-TDNA.

pulsed voltage generators with an ideally zero output impedance and are usually limited to a pulse length of about 200 ns. Instead, the MP-TDNA, whose block schematic is represented in Fig. 2.1, is conceived in a  $50\ \Omega$  environment. The port excitations are generated with a two-channel arbitrary function generator (AFG) whose internal impedance is  $50\ \Omega$ . Such an instrument is capable of synthesizing pulsed waveforms with 20 V peak to peak maximum amplitudes on  $50\ \Omega$  loads and programmable rise/fall times from 2.5 ns upwards. The generator outputs are connected through  $50\ \Omega$  cables to wideband matched dual directional couplers (10 kHz to 1 GHz), while two bias-tees (max. current: 400 mA, bandwidth: 200 kHz to 12 GHz) provide dc and ac current path separation [138]. If needed, a wideband power amplifier can be added at port 2 in order to reach higher voltage pulse amplitudes: a 10 kHz to 250 MHz, 25 W power amplifier has been used for the measurements on GaN HEMTs. The coupled signals are sampled with a four-channel equivalent-time oscilloscope: throughout the Ph.D. research, two oscilloscopes, one featuring 1.5 GHz, 2 GS/s, and the other 2.5 GHz, 5 GS/s per channel have been used. On-wafer measurements are carried out by means of a thermally-controlled probe station. A full list of commercial names of the components used in such a set-up can be found in [138]. A MATLAB remote control software guides the user through the calibration and measurement procedures, allowing for the design of excitations, acquisition of the measured data and post-processing. The advantages of such a PIV set-up with respect to the conventional ones can be briefly resumed in the following key points [139]:

- the  $50\ \Omega$  resistive termination enhances stability, while most other set-ups may force the user to introduce resistive components;
- as the mismatches are practically eliminated, reflections are minimized and pulse widths down to 50 ns can be obtained. Moreover, the set-up allows for simplified on-wafer calibration procedures and more freedom in the choice of cables;
- such as in VNAs, the dc path is separated by the ac path. As a consequence, the biasing does not depend on the generated pulse width and it allows for independent monitoring of the dc current.

In fact, since the MP-TDNA allows for the acquisition of the absolute incident and scattered waves at the two ports, it can be seen by all means as a low-frequency implementation of a sampler-based large signal network analyzer. As a consequence, it requires an absolute calibration including magnitude and phase corrections, as described in the following section. Indeed, pulsed voltage and currents waveforms are retrieved through a straightforward transformation

of the incident and scattered waves, and a recombination of the dc and ac components.

## 2.2.2 Calibration

The calibration of the MP-TDNA corrects the quantities acquired at the scope receivers in order to obtain the incident and scattered waves at the reference calibration plane, which is defined at the probe tips for on-wafer measurements. Moreover, as all waves are synchronously acquired by a triggered acquisition of the oscilloscope, the configuration is the same as for LSNA, as will be seen in Chapter 3. The main difference with respect to a classic two-port LSNA configuration is that the calibration path does not include an independent mixing stage, meaning that the waves, whose frequency components typically range from 10 kHz up to hundreds of MHz, are directly injected in the oscilloscope channels. The scope, internally, manages sampling and digitalization of the waves. The scope receivers, calibrated by the manufacturer, are considered as an absolute reference. However, receiver correction can eventually be applied, and it may be especially useful to compensate the internal adaptation of the attenuator-buffer channel interface modified by the amplitude range settings. The internal impedance of the input ports of the scope is assumed to be  $50 \Omega$ , thus any reflection is neglected. Despite these details, the typical procedure consisting of a relative calibration and absolute magnitude and phase calibrations is deployed. The relative one is an on-wafer Short-Open-Load-Thru (SOLT) calibration making use of standards on a calibration substrate. The magnitude and phase calibrations should be, in theory, performed with an additional calibration step, needed to move the calibration plane from the probe tips to an auxiliary coaxial calibration plane. Instead, given the low-frequency operation of the set-up, it has been verified [138] that the effects of the probes can be neglected. Moreover, the absolute calibration steps do not make use of a power sensor nor of an absolute phase reference, as will be seen in section 3.2.1. Instead, they are substituted by an additional step in which a sinusoidal excitation at port 1 is injected while the direct path (at the DUT) and the coupled path are measured at the same time. Thus, both the amplitude attenuation as well as the relative phase between the direct and the coupled paths can be directly obtained through a frequency sweep in the bandwidth of interest.

## 2.3 Pulsed IV measurements

It is well known that narrow-pulsed characterization techniques are extremely important for assessing the actual performances of compound semiconductor

HEMTs [56], [57]. Ideally, all the data points in a PIV characteristic correspond to the same channel temperature, as the pulsed excitation is shorter than the thermal transient. Moreover, if the amount of charges trapped at the layer interfaces is set to a given state corresponding to the quiescent condition, all points of the pulsed characteristic would also share the same charge trapping state. In such a case, if acquiring PIV from different bias points, one would characterize the drain current with the following formulation:

$$i_D(t) = F[v_G(t), v_D(t), \underline{\chi}(t), \theta(t)] \quad (2.1)$$

where  $\theta$  is the junction temperature and  $\underline{\chi}[\chi_1, \dots, \chi_N]^T$  is a vector of state variables describing the internal charge trapping state of the transistor. In this case,  $\underline{\chi}$  can be considered as a function of the quiescent point  $\underline{\chi}[V_{GQ}, V_{DQ}]$ . However, according to published results and as already commented in section 1.2.2, time constants associated with captures and releases of charges in GaN HEMTs are strongly different [140],[141]. In particular, very slow (in the *ms* to *s* range) charge release transients have been measured. At the same time, charge trapping takes place very fastly (a few ns), so that standard pulse widths of hundreds of ns are not short enough to avoid captures of traps during the pulses [49],[139],[141]. Thus, in general, standard PIV can still be considered *isothermal*, but not *isodynamic*, as the charge trapping state  $\underline{\chi}$  not only depends on the biasing conditions, but also on voltage peaks reached by  $v_G(t)$  and  $v_D(t)$ . As from [49], fast charge trapping is activated either when positive voltage pulses are applied at the drain terminal of the transistor or negative pulses are applied to the gate terminal. In other words, positive drain pulses and negative gate pulses force the trap state to change with respect to the quiescent state. On the contrary, when negative drain pulses and positive gate pulses are applied, no variations in the trap state are expected. Thus, the state can be referred to as  $\underline{\chi}[V_{GQ}, V_{DQ}, v_G(t), v_D(t)]$ . Despite this consideration, pulsed techniques might still be used for gaining insights on the gate- and drain-lag effects, although one should consider specific pulses configurations in order to control if charge trapping mechanisms are triggered during the measurements. Indicating  $V_T$  as the threshold voltage of the transistor and  $V_{DQ}^{max}$  as the maximum drain quiescent voltage, a possible method consists in obtaining pulsed characteristics from the three following bias points: 1)  $(V_{GQ}, V_{DQ})_1 = (0 \text{ V}, 0 \text{ V})$ , 2)  $(V_{GQ}, V_{DQ})_2 = (V_T, 0 \text{ V})$ , 3)  $(V_{GQ}, V_{DQ})_3 = (V_T, V_{DQ}^{max})$ . To obtain the characteristic in 1), only negative gate pulses and positive drain pulses are applied: the device is biased in the configuration where minimum amount of traps are active, but both mechanisms of fast charge capture are dynamically activated when applying the pulses. For the characteristic in 2), all gate-related traps are statically activated. Gate and drain positive pulses are applied, meaning that fast charge traps only related to the drain voltage are dynamically activated. Finally, for the characteristic in 3), the maximum amount of static

charge trapping is active. The positive gate pulses and the negative drain pulses used to obtain the characteristic do not change the trap state. By comparing 1) and 2), gate-lag effects can be quantified. Likewise, by comparing 2) and 3), drain-lag effects are characterized.

It should be noted, however, that the effects on the output characteristic due to the gate and drain lag are characterized separately, and no mutual dynamic mechanism is considered. Such an approximation may be too simplistic, as will be shown in the following. Moreover, the approach does not easily lead to the practical modeling of dispersive effects. The bias points at which the pulsed characterization is performed are not the usual ones for a power amplifier design (e.g., class A,B). Using those measurements to reproduce a suitable IV characteristic for design is not straightforward. On the other hand, as already discussed, the points of a classic PIV characteristic measured from an operative bias point do not share the same charge-trapping state, and thus the PIV characteristics cannot be considered *isodynamic*. The peculiar architecture of the MP-TDNA is helpful in addressing this specific point: the separate acquisition of the dc component of the drain current allows, in fact, to gain an independent knowledge concerning the charge trapping taking place while the pulsed excitation is applied. Specifically, it has been shown in [139] that a dc current drop is measured when a pulsed excitation triggers charge trapping in GaN HEMTs. As a matter of fact, the dc drain current can be assumed as an indicator of the conversion effects due to the nonlinear relationship between trapped charges and applied voltages. Through the observation of this parameter, it is shown that the trap state for the different data points in a standard PIV characteristic of GaN FETs is not always the same. Such a phenomenon does not happen in case of GaAs devices [139]. Poor prediction of power supply consumption and energetic efficiency, sometimes shown by GaN foundry models based on pulsed characteristics, is likely to be connected with this aspect. In the next section, a new technique to deal with such limitations is proposed.

## 2.4 Double-pulse technique

### 2.4.1 Theory

Given the issues related to the standard pulsed characterization of GaN devices, a new pulsing procedure, named *double-pulse* technique, is engineered in order to pre-condition the charge trapping state before the actual acquisition of each data point of a pulsed characteristic [127]. The objective is obtaining PIV characteristics whose data points all share the same charge trapping state  $\underline{\chi}$ ,

and thus can be considered isodynamic. The proposed technique makes use of a specific pulsed excitation which consists, both at the gate and drain side, in the time-repetition of a customized basic pattern formed by two elementary non-overlapping pulses. These are designed to be contiguous or separated by a very short time interval. The preliminary pulse, also referred as *pre-pulse* is aimed at conditioning the state of charges trapped at the layer interfaces. The resulting pre-pulsed peak gate voltage will be named  $\hat{v}_G$ , while the pre-pulsed drain voltage is  $\hat{v}_D$ . The second pulse voltages  $v_G$  (gate) and  $v_D$  (drain) act as in standard techniques and reach the point where the dynamic drain current is actually sampled. As already mentioned, positive drain voltage pre-pulses ( $\hat{v}_D > V_{DQ}$ ) and negative gate voltage pre-pulses ( $\hat{v}_G < V_{GQ}$ ) trigger the fast capture of traps [49]. Provided that the gate and drain instantaneous voltage values after the application of the pre-pulses do not exceed the pre-pulse values (i.e.,  $v_G(t) > \hat{v}_G$  and  $v_D(t) < \hat{v}_D$ ), the trap-state reached will be maintained (due to slow trapped charge release) in a time long enough to apply a second couple of simultaneous gate and drain measure-pulses for dynamic drain current sampling at constant trap state (indeed, determined by  $\hat{v}_G$ ,  $\hat{v}_D$ ). Thus, the generic port excitation  $v(t)$  can be described analytically as the superposition of a bias and the periodic repetition with period  $T$  of a nearly zero-mean double-pulse pattern), i.e.:

$$v(t) = V_0 + \sum_{n=-\infty}^{+\infty} v_p(t - nT) \quad (2.2)$$

being

$$v_p(t) = v_{p1} \prod \left( \frac{t - t_{C1}}{\tau_1} \right) + v_{p2} \prod \left( \frac{t - t_{C2}}{\tau_2} \right) \quad (2.3)$$

where  $\tau_1, t_{C1}$  and  $v_{p1}$ , are the width, center time position and amplitude of the pre-pulse, while  $\tau_2, t_{C2}$  and  $v_{p2}$ , are the corresponding quantities of the actual measure-pulse. In (2.3), the rectangle function  $\prod(x)$  is 0 outside the interval  $[-\frac{1}{2}, \frac{1}{2}]$  and 1 inside it. Thus, the duty cycle  $\rho$  of the pulsed excitation results in [127]:

$$\rho = \frac{t_{C2} + \frac{\tau_2}{2} - t_{C1} + \frac{\tau_1}{2}}{T} \quad (2.4)$$

It is worth noting that, if very short duty-cycles are assumed (e.g., below 1%), the mean value of the pattern (2.3) is practically zero. However, a zero-mean value of  $v_p(t)$  can be forced in practice by means of ac-coupling within the bias-tee. The double-pulsed IV (DPIV) characteristic obtained with the described method can be written as

$$i_D(t) = \tilde{F}[v_G(t), v_D(t), \tilde{\chi}, \theta] \quad (2.5)$$

where  $\tilde{\chi}[\hat{v}_G, \hat{v}_D, v_G(t), v_D(t)]$  is a set of state variables non-linearly dependent on voltages. In particular,  $\tilde{\chi}$  keeps constant for  $v_G(t) > \hat{v}_G$  and  $v_D(t) < \hat{v}_D$  while it changes elsewhere. By choosing  $\hat{v}_G$  and  $\hat{v}_D$  such that  $v_G(t) \gg \hat{v}_G$  and  $v_D(t) \ll \hat{v}_D$ , the trap state can be kept constant across the necessary characterization region. It is worth noting that  $\hat{v}_G$  and  $\hat{v}_D$  can be made coincident with the far right edge of the dynamic load-line related to an actual operation regime within a particular transistor nonlinear application. As far as the channel temperature is concerned under pulsed excitations, this is known to be dependent on the baseplate temperature  $\theta_B$  and on the self-heating due to the power dissipation at the actual bias point  $(V_{GQ}, V_{DQ})$ .

## 2.4.2 Implementation

A demonstration of the proposed technique is provided through the on-wafer characterization of a 1-mm GaN-on-SiC HEMT ( $L = 0.25 \mu\text{m}$ ) by means of the MP-TDNA described in section 2.2. More in detail, the double-pulse pattern can be generated by suitable programming of arbitrary waveform generators used in the set-up. Indeed, one must consider that the frequency spectrum of the double-pulse signal properly passes through the ac path of the bias-tees (100 kHz  $\div$  6 GHz): in this work, gate and drain pulse widths (both pre-pulse and measure-pulse) are about 110 ns and 70 ns, respectively. The drain pulses are synchronized in order to result almost centered with respect to the corresponding gate pulses when applied simultaneously. A value  $T=10 \mu\text{s}$  is chosen so that the duty cycle is less than 2%. As the gate input port of the DUT behaves almost like an open load for the pulse-wave source all over the frequency bandwidth of the applied excitation, the voltage waveform applied on the gate voltage corresponds to the one measured through the couplers by the scope channels. Indeed, loading conditions are not the same at the drain side. In fact, by loading the DUT with  $50 \Omega$ , peculiar to the MP-TDNA, the gate voltage pre-pulse affects the drain voltage, as it can be observed in Fig. 2.2, where pulse waveforms (a) and a diagram to depict the load-line are shown. Due to the combined effects of the gate and drain pre-pulses, fast trap captures are forced leading the device into a particular state  $\tilde{\chi}$  set, in Fig. 2.2, by  $\hat{v}_G = -4 \text{ V}$  and  $\hat{v}_D = 60 \text{ V}$ . The immediately following gate and drain measure-pulses allow a current sampling at  $v_G \simeq 0 \text{ V}$  and  $v_D \simeq 17 \text{ V}$  (the interval where the current can be measured is shown between dotted lines in Fig. 2.2). Since the complete double-pulse shape can be kept shorter than 250 ns, the current sampling can be considered occurring at the same thermal state of the quiescent condition  $V_{G0} \simeq -2.7 \text{ V}$  ( $I_{D0} \simeq 160 \text{ mA}$ ),  $V_{D0} = 30 \text{ V}$  with baseplate temperature  $\theta_B=40^\circ\text{C}$ . By programming nested sweeps of double-pulse excitations with different gate and drain measure-pulse targets, IV pulsed

characteristics that are not only isothermal, but isodynamic can be measured. In Fig. 2.3, the double-pulse excitations with marked trap pre-condition and measurement points are shown for a GaN-on-SiC, 10x100 HEMT ( $L=0.25 \mu\text{m}$ ) from another foundry.

### 2.4.3 Validation

A further experimental validation of the assumptions previously made on charge capture and release dynamics and, above all, of the whole characterization technique is provided through the following test. Two quiescent voltage pairs  $V_{GQ}^I = -2.4 \text{ V}$ ,  $V_{DQ}^I = 20 \text{ V}$  and  $V_{GQ}^{II} = -2.2 \text{ V}$ ,  $V_{DQ}^{II} = 15 \text{ V}$  are selected on the isothermal locus at constant dissipated power of 4 W, corresponding to a channel temperature of about  $95^\circ\text{C}$ . Such a value could be estimated by means of the thermal resistance provided by the foundry. Standard PIV characteristics (pulse width: 150 ns,  $T = 10 \mu\text{s}$ ) measured from these quiescent conditions are plotted in Fig. 2.4 (a). Remarkable differences between the two sets of curves as well as anomalous current slope changes at the quiescent drain voltages are observed. The two IV characteristics are measured again by using the proposed double-pulse technique, by realizing  $\hat{v}_G \simeq -4.3 \text{ V}$  and  $\hat{v}_D \simeq 50 \text{ V}$  through

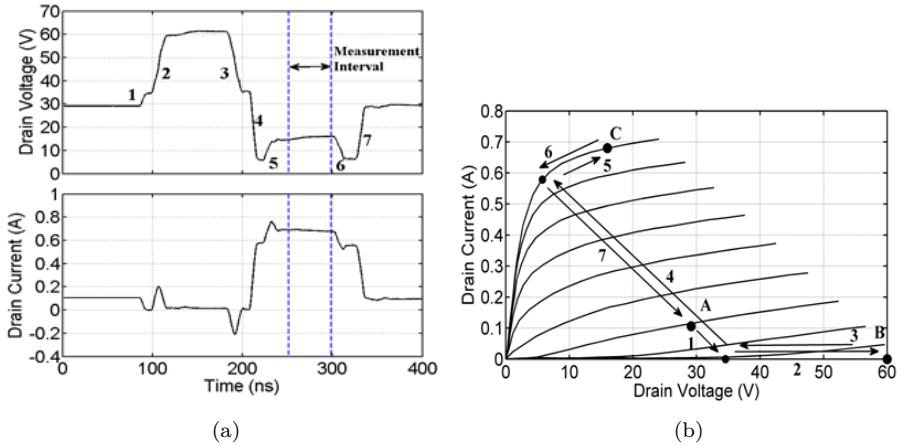


Figure 2.2: (a) Voltage (top) and current (bottom) waveforms sampled at the drain port of a 1-mm GaN HEMT, when double-pulsed excitations are applied both at the gate and drain sides. The time interval between dotted lines suggests the time-position for IV sampling. (b) Dynamic locus under double-pulse excitation, while numbers indicate rise and fall edges of the waveforms in (a).

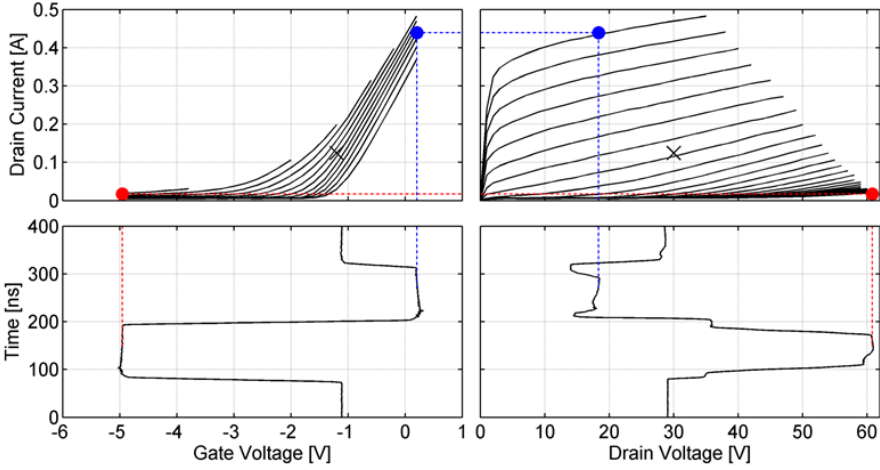


Figure 2.3: The double-pulse technique depicted with input and output pulsed characteristics; pre-pulses peaks (in red) precondition the charge-trapping state. Measure-pulse peaks (blue) are swept to obtain the full characteristic. The cross indicates the quiescence point.

the pre-pulses. Almost coincident DPIV sets are obtained (Fig. 2.4 (b)), as expected. The more severe knee walkout in Fig. 2.4 (b) is due to the effect of the trapping state set by the pre-pulses: this behavior is expected to describe more accurately the actual device performance when operating in an amplifier whose load-line dynamically reaches  $v_D \simeq 50$  V.

## 2.5 Double-pulse Characterization

### 2.5.1 PIV and DPIV characteristics

In this section, an analysis of the DPIV characteristics obtained with the double-pulse technique is carried out. As already mentioned, while DPIVs can be thought to be acquired at a fixed charge trapping state  $\tilde{\chi}$ , not all the data points of the characteristics acquired with a standard PIV share the same charge trapping conditions. A comparison between PIV and DPIV characteristics is shown in Fig. 2.5 for a 1-mm GaN-on-SiC HEMT ( $L = 0.25 \mu\text{m}$ ) from two different providers [129]. Both single and double-pulsed characteristics are

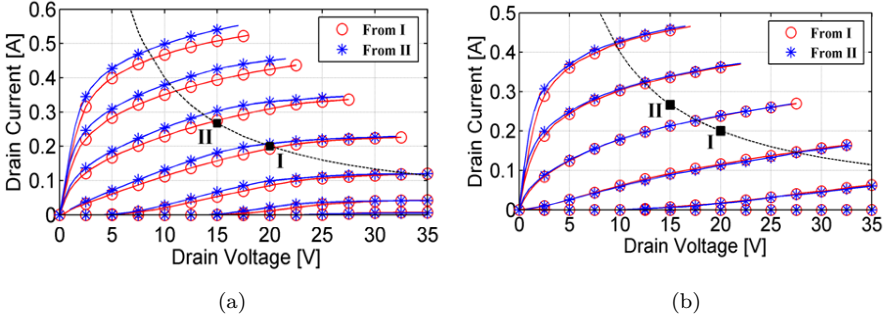


Figure 2.4: Consistency test of the double-pulse technique performed on a 1-mm GaN HEMT. (a) Standard PIV from two quiescent points chosen on the isothermal locus at about  $95^{\circ}\text{C}$  ( $P_D=4\text{ W}$ ,  $\theta_B=40^{\circ}\text{C}$ ); (b) DPIV obtained through the double-pulse technique with:  $\hat{v}_G \simeq -4.3\text{ V}$  and  $\hat{v}_D \simeq 50\text{ V}$ . Gate voltage  $v_G$  sweep:  $-4\text{ V} \div -1\text{ V}$ , step:  $0.5\text{ V}$ .

measured with the MP-TDNA and pulsed from  $V_{GQ} = -2.5\text{ V}$   $V_{DQ} = 20\text{ V}$  in 2.5(a) and from  $V_{GQ} = -0.6\text{ V}$   $V_{DQ} = 20\text{ V}$  in 2.5(b). For both devices, the DPIV characteristic has been obtained with  $\hat{v}_D \simeq 50\text{ V}$  and  $\hat{v}_G$  at pinch-off. It is worth noticing, especially from Fig. 2.5(a), that all single-pulsed characteristics show a slope change when positive drain pulses are applied. At the same time, the double-pulsed characteristics show evident knee walkout and current collapse, although the change in the characteristic slope seems eliminated. The DPIV characteristic is actually the one that should be taken into account for the evaluation of the limit performances of a power amplifier under large-signal operation, for instance in terms of maximum output power. The measured performance drop is likely one of the motivations why, in GaN power amplifier applications, increasing the drain bias voltage beyond a certain value does not give any improvement of power density causing a drop of efficiency, since the lag trap phenomena associated to high drain voltage operation become dominant for the device performance. Other DPIV characteristics were measured by adopting the same quiescent condition and different choices (namely intermediate values of  $5\text{ V}$ ,  $30\text{ V}$ ,  $35\text{ V}$ ,  $40\text{ V}$ ,  $50\text{ V}$ ) of the drain pre-pulse  $\hat{v}_D$  and the same value of the gate-prepulse  $\hat{v}_G$  at pinch-off. In Fig. 2.6, only the curves at  $v_G = V_{GQ}$  are shown for a clearer comparison: all curves share the same biasing conditions, while each of them corresponds to different pre-pulsing conditions. Thus, the actual drop of the pulsed drain current characteristics due to increasing effects of charge trappings can be evaluated for each value of  $\hat{v}_D$ : every curve in the range  $v_D \leq \hat{v}_D$  can be interpreted as an ideal PIV where the traps state is determined by the corresponding voltage couple  $(\hat{v}_G, \hat{v}_D)$ . Instead, by considering the PIV

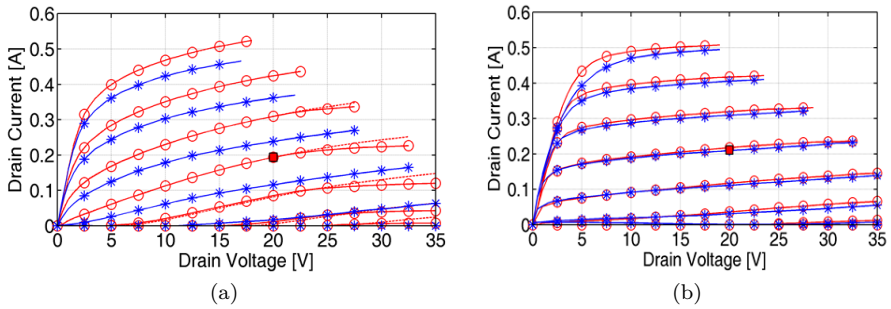


Figure 2.5: PIV (red with circles) vs. DPIV (blue with stars) characteristics for 1-mm GaN HEMTs from two different foundries. (a) Foundry A. (b) Foundry B.

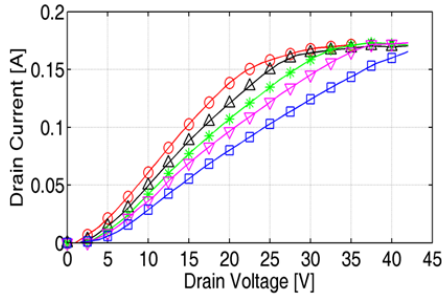


Figure 2.6: 1-mm GaN HEMT standard PIV (red lines with circles) and DPIVs with  $\hat{v}_D = 25$  V (up triangles), 30 V (stars), 35 V (down triangles), 40 V (squares) and negative peak gate voltages  $\hat{v}_G$  near pinch-off, all at  $v_g = -2.5$  V, pulsed from  $V_{GQ} = -2.5$  V,  $V_{DQ} = 20$  V.

set (the red line with circles) each sample measured in the region  $v_D > V_{DQ}$  can be thought of as belonging to a differently state-modified characteristics set by the voltage peak reached by  $v_D$ , thus not at the same charge trapping state. The same comment can be made for those samples of each characteristics out of the charge-trapping preconditioning region, i.e., for  $v_D > \hat{v}_D$ . Indeed, when the preconditioning is not taking place, the data points are coincident.

As the MP-TDNA allows the separate measurement of the dc current component, it is interesting to acquire it while the pulsed excitations such as in Fig. 2.6 are applied. In Fig. 2.7, the dc current components acquired under single-pulsed and double-pulsed excitations with various preconditioning are shown. In the

case of an unperturbed trap state for a particular pulsed excitation, the dc current should not change with respect to the quiescent value in the presence of sufficiently low duty cycles. Instead, this is only observed for negative drain pulses. In the case of positive drain pulses a drop in the dc value of the drain current, which is dependent on the pulse peak, is well evident. More precisely, it is worth to note that the change in the dc current slope does not appear starting exactly at  $v_D = V_{DQ}$ , but at  $v_D = V_{DQ} + \Delta V_D^{AT}$ , where  $\Delta V_D^{AT} \simeq 5 \div 10$  V is here considered as a threshold voltage for the activation of the trapping effects induced by the drain voltage peak (a more detailed analysis will be discussed in section 2.5.2). We associate the dc current drop with a change of the trap state, as the the ac/dc conversion observed is an effect of its nonlinear behavior. Actually, the impact on the dc current component seems to be the main effect of the trap-assisted state change. In fact, if every PIV curve were obtained by summing the actual ac component to the nominal dc drain current  $I_{DQ}$ , instead of the actually trap-modified dc drain current  $I_{D0}$  measured with the source measurement unit (SMU) and correspondent to the pulsed ( $v_G$ ,  $v_D$ ), the slope change would almost completely disappear, as shown by the red slashed line curves in Fig. 2.5(a). In fact, the slope of these characteristics in the quiescent point is coherent with low-frequency drain conductance measurements, as proved in [139].

The so obtained IV characteristics could theoretically approximate the ideal behavior, being purely isothermal and with the trap state frozen into the quiescent condition. It is worth noting that these characteristics are not directly measurable: first, because of lack of pulsed instrumentation capable of generating high-voltage pulsed waveforms with pulse widths shorter than the trap capture time constants (few ns), and second because, even if such an instrumentation were available, the pulsed waveform spectra would likely extend up to microwave frequencies where other reactive effects related to displacement charges take place. The curves in Fig. 2.7 confirm that the dc current for each DPIV set is reduced with respect to the quiescent condition value due to the charge trapping. The amount of reduction coherently depends on the actual peak drain voltage  $\hat{v}_D$ . The dc current keeps constant for  $v_D < \hat{v}_D$  as expected. For  $v_D > \hat{v}_D$ , the dc current of each modified set coincides with the dc current of the standard PIV characteristic. A final comment can be made with respect to the observed dc current variation: indeed, one may wonder if such a current variation, together with the fact that charge trap release time constants are long, influence the thermal state of the device under pulsed characterization, making the characteristics not anymore isothermal. Indeed, current transients influence the thermal regime undergone by the DUT when repetitive pulsed waveforms are applied. Taking into account such a phenomenon means calculating a thermal compensation for each excitation regime with a thermal model. In the case of double-pulse characteristic, the whole characterization undergoes the same

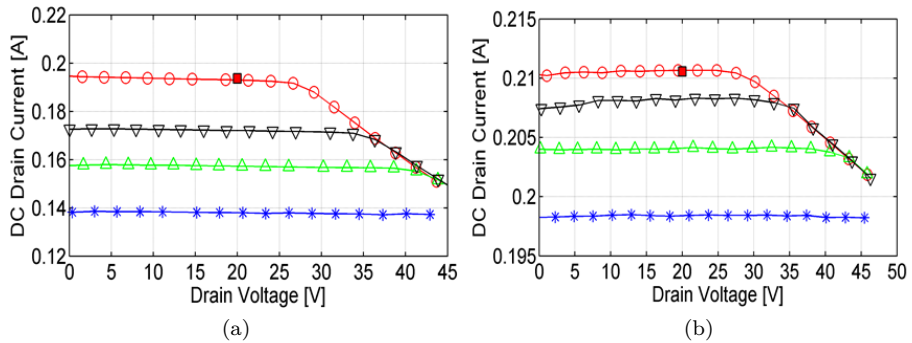


Figure 2.7: DC drain currents corresponding to the PIV (red lines with circles) and various DPIVs for  $10 \times 100 \mu\text{m}$  ( $L = 0.5 \mu\text{m}$ ) GaN HEMTs from two foundries. (a) Foundry A. DPIVs  $\hat{v}_D$ : 35 V (up triangles), 40 V (down triangles), and 50 V (stars) and  $\hat{v}_G \simeq V_T$ . Bias:  $V_{GQ} = -2.5$  V,  $V_{DQ} = 20$  V. (b) Foundry B. DPIVs  $\hat{v}_D$ : 30 V (up triangles), 40 V (down triangles), and 50 V (stars) and  $\hat{v}_G \simeq V_T$ . Bias:  $V_{GQ} = -0.6$  V,  $V_{DQ} = 20$  V.

regime as the dc component of the current is constant for all points. Despite this analysis, the self-heating impact of a few mA may be considered negligible in first instance.

## 2.5.2 Thermal dependency

It is well known that charge trapping mechanisms are inherently enhanced by the temperature at which the transistor is operating. This section is dedicated to a set of measurements done in order to assess the temperature dependency of the mechanisms observed in section 2.5.1. To this aim, the device is stressed by applying baseplate temperature variations through a thermally-controlled chuck. In this analysis we consider channel temperature variations  $\Delta\theta$  coincident with baseplate temperature variations  $\Delta\theta_B$ , thus neglecting possible (small) relative thermal differences triggered by the charge trapping due to self-heating effects in the quiescent condition  $V_{GQ}, V_{DQ}$ . In other words, both single and double-pulsed characteristics are indeed still considered isothermal. Identical pulsed measurement tests from  $V_{GQ} = -2.5$  V,  $V_{DQ} = 30$  V are repeated by only changing the baseplate temperature, and the corresponding variations on the measured dc component of the drain current  $I_{D0}$  are evaluated. In Fig. 2.8(a), the one correspondent to single-pulse characterization is shown versus  $v_G$  and  $v_D$ . The measurements of  $I_{D0}$  under both standard (single) and double-pulsed regime

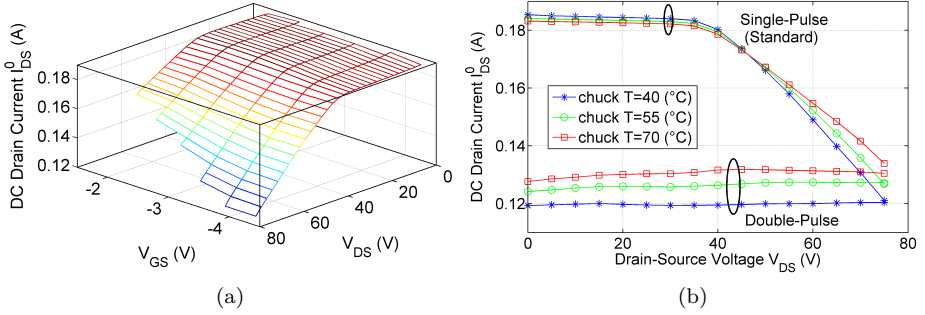


Figure 2.8: (a) 1-mm GaN HEMT dc drain current component ( $I_{D0}$ ) corresponding to a standard PIV characteristic from  $V_{GQ}=-2.5$  V,  $V_{DQ}=30$  V ( $I_{DQ} \simeq 180$  mA)  $v_G$ :  $-4.25$  V  $\div$   $-1.75$  V, step:  $0.5$  V;  $v_D$ :  $0$  V  $\div$   $75$  V, step:  $2.5$  V (b)  $I_{D0}$  corresponding to PIV (standard) and DPIV at  $40^\circ\text{C}$  (blue stars),  $55^\circ\text{C}$  (green circles),  $70^\circ\text{C}$  (red squares) for  $v_G = -4.25$  V. The DPIV are obtained with  $\hat{v}_G \simeq -4.5$  V, near pinch-off, and  $\hat{v}_D \simeq 75$  V.

for  $v_G=-4.25$  V at three baseplate temperatures ( $\theta_B = 40^\circ\text{C}$ ,  $55^\circ\text{C}$ ,  $70^\circ\text{C}$ ) are presented in Fig. 2.8(b). It is observed how  $I_{D0}$  tends to assume lower values at increasing baseplate temperature for  $v_D < (V_{D0} + \Delta V_D^{AT})$ , as expected due to the decrease of the electron mobility. However, such a difference (1 mA as from Table 4.3) does not cause relevant differences due to self-heating among the DPIVs. On the other hand, the  $I_{D0}$  behavior observed for  $v_D > (V_{D0} + \Delta V_D^{AT})$ , shows an opposite dependency on the operating temperature. In particular, the drop rate appears smaller at lower temperatures (Table 4.3). An additional thermal characterization has been performed by using the DPIV technique to measure  $I_{D0}$  in presence of a pre-conditioned charge trapping state obtained by means of pre-pulses towards  $\hat{v}_G \simeq -4.5$  V (pinch-off) and  $\hat{v}_D \simeq 75$  V. The  $I_{D0}$  measured under double-pulse periodic regime is also shown in 2.8(b). It can be noted how the  $I_{D0}$  takes larger values at higher temperatures, coherently with the single pulse curves at  $v_D = \hat{v}_D \simeq 75$  V. This behavior can be explained in terms of the thermal impact on the trapped charges. As an additional test, the temperature dependency of the trap activation threshold voltage (introduced in 2.5.1) is also investigated. To this aim, a graphical procedure is defined in order to estimate the slope changes in the  $I_{D0}$  versus  $v_D$  plot. In practice, the  $I_{D0}$  drop rate versus  $v_D$  is evaluated for  $v_D \ll V_{DQ}$  and for  $v_D \gg V_{DQ}$ : in this way, two lines can be extrapolated for the respective sections of the plot. The intersection point is assumed here for the definition of the voltage activation threshold  $\Delta V_D^{AT}$ . The concept is graphically explained in Fig. 2.9(a), corresponding to the case  $v_G = -4.25$  V and to three baseplate temperatures.

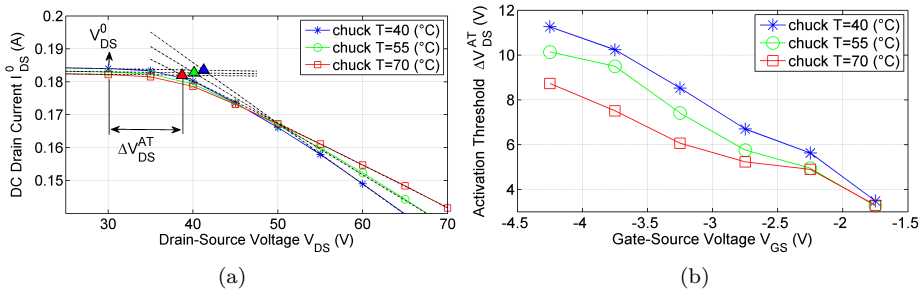


Figure 2.9: (a) Activation threshold voltage ( $\Delta V_D^{AT}$ ) graphical estimation for  $v_G = -4.25$  V under PIV from  $V_{GQ} = -2.5$  V,  $V_{DQ} = 30$  V. Dotted black lines represent the different slopes reported in Table 4.3. (b)  $\Delta V_D^{AT}$  vs.  $v_G$  and  $\theta_B$ .

Table 2.1: Analysis of the dc current component versus  $\theta_B$

Chuck temperature $\theta_B$ ( $^{\circ}\text{C}$ )	40	50	70
DC drain current (mA)			
$v_D < (V_{DQ} + \Delta_D^{AT})$	185	184	183
DC drain current drop slope (mA/V)			
$v_D > (V_{DQ} + \Delta_D^{AT})$	-1.65	-1.50	-1.28
DC drain current (mA)			
double-pulse, any $v_D$	120	125	130

The same characterization has been performed for a set of  $v_G$  values. The results are plotted in Fig. 2.9(b). It is interesting to note that the estimated trap activation threshold voltage is decreasing for increasing temperature [128].

### 2.5.3 Technology assessment

In this section, the use of the double-pulse technique in order to define trap-related performance parameters of GaN HEMTs is investigated. A meaningful technology evaluation method should be directly related to the expected transistor behavior under dynamic large signal regime in actual applications, such as PAs. One can assume that the presence of traps is one of the main causes responsible for performance reduction in GaN HEMTs. So, the charge trapping state corresponding to typical operation regimes is here investigated.

The trapping state in GaN strongly and nonlinearly depends on the applied voltage excursions. Semiconductor foundry engineers, on the basis of breakdown evaluations and reliability constraints, usually suggest the nominal drain voltage bias in typical power amplifier applications. The value  $V_{DQ}^{nom} = 25 \text{ V}$  is assumed for the performed tests. On the other hand, the class of operation, A or B or AB, sets the minimum limit of the gate voltage  $v_G^{min}$ , which is  $V_T \simeq -4 \text{ V}$  for the class-A and about  $2V_T$  for the class-B, while the maximum instantaneous drain voltage  $v_D^{max}$  between  $40 \text{ V}$  and  $60 \text{ V}$  due to breakdown. As from the discussion in section 2.5.1, a maximum of trapped charges seems to be present in the region of gate voltage around the threshold voltage  $V_T$ . Moreover, as will be shown in section 2.6, the application of waveforms with incrementally negative gate voltage peaks extending beyond the threshold voltage (e.g., class B PA operation) does not seem to correspond to a larger amount of trapped charges. Thus, one can assume the threshold voltage  $V_T$  and the maximum of the drain voltage  $v_D^{max}$  as the worse case for performance reduction due to the nonlinear charge trapping phenomena.

First, a standard PIV of a  $8 \times 125 \mu\text{m}$  AlGaIn/GaN HEMT (type A) was measured from the nominal bias point  $(V_{GQ}^{nom}, V_{DQ}^{nom}) = (-3.1 \text{ V}, 25 \text{ V})$ ,  $I_{DQ} = 100 \text{ mA}$ . The nominal bias represents an appropriate condition for this test, since it would correspond to almost class-B operation with sinusoidal gate excitation, while it preserves a minimum drain current for eventually observing the dc current drop due to the charge trapping state variations. In order to obtain an IV curve representative of the transistor behavior in presence of the worse case charge trapping state, a DPIV has been measured from  $(V_{GQ}^{nom}, V_{DQ}^{nom})$  by applying pre-pulses to reach the critical condition  $v_G \simeq V_T$ ,  $v_D \simeq 60 \text{ V}$ , which is the expected

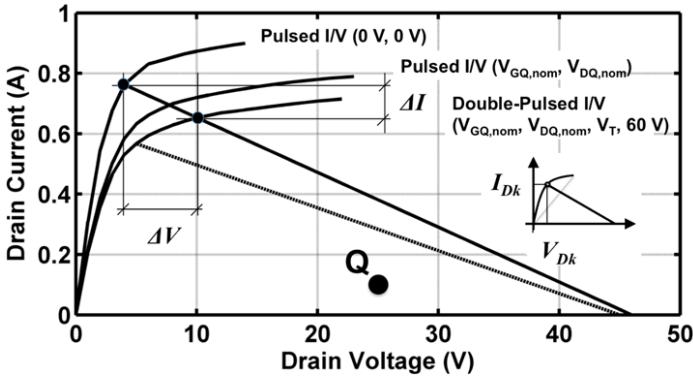


Figure 2.10:  $8 \times 125 \mu\text{m}$  GaN HEMT, type A. Comparison of different pulsed IV at  $v_G = 0 \text{ V}$  with the aim of evaluating the charge trapping phenomena.

maximum instantaneous voltage value in large-signal RF operation. Finally, an IV curve pulsed from  $V_{GQ} = 0$  V,  $V_{DQ} = 0$  V has also been obtained. As from the discussion in section 2.3, such a set of characteristic is not isodynamic, as negative gate pulses and positive drain pulses trigger fast charge trapping; however, the curve at  $v_G = 0$  V, in the knee region (at small  $V_D$ ), where negligible charge trapping occurs, can be assumed as representative of the ideal device behavior with minimum amount of charge trapped. The PIV, DPIV and the characteristic from  $(V_{GQ}, V_{DQ}) = (0, 0)$  V, all at  $v_G = 0$  V, are shown in Fig. 2.10 for comparison. Such a plot gives an idea about of the drain current drop and the knee walkout due to trap state variations. These curves are nearly isothermal (40°C) since the nominal bias point (nearly class B) corresponds to negligible amount of self-heating. In any case, these small differences are easily compensated by baseplate heating/cooling. In order to evaluate the impact of the nonlinear charge trapping lagging effects, the following trap-related power reduction ratio  $\Delta_{TR}$  is introduced [130]:

$$\Delta_{TR} = \frac{P_{NTR}^{lin} - P_{TR}^{lin}}{P_{NTR}^{lin}} \quad (2.6)$$

where the actual power device capabilities are conventionally evaluated by considering the maximum output power achievable under the constraints of linear, ideal class-A or class-B operation, as:

$$P^{lin} = \frac{1}{2}(V_{D0} - v_D^k) \frac{i_D^k}{2} \quad (2.7)$$

where  $v_D^k$  and  $i_D^k$  are, respectively, the knee voltage and current coordinates of the intercept point between the  $v_G=0$  V curve of an IV characteristic and a loadline, as graphically depicted in Fig. 2.10. The generic definition in (2.7) is used twice in (2.6) for defining the power capabilities of the device in the nearly-ideal case of absence of traps ( $P_{NTR}^{lin}$ ) or in presence of traps ( $P_{TR}^{lin}$ ). The value of  $P_{NTR}^{lin}$  is obtained by using the characteristic pulsed from  $V_{GQ} = 0$  V,  $V_{DQ} = 0$  V. The value of  $P_{TR}^{lin}$ , instead, is determined by using the DPIV characteristic. The knee walkout  $\Delta V$  and the current drop  $\Delta I$ , graphically defined in Fig. 2.10, and their values for the two process technologies A, B are reported in Table 2.2. In order to provide a full comparison between the technologies A and B, two additional power ratio indicators are defined as:

$$\Delta_{AB,TR} = \frac{P_{TR,A}^{lin} - P_{TR,B}^{lin}}{P_{TR,A}^{lin}} \quad (2.8)$$

$$\Delta_{AB,NTR} = \frac{P_{NTR,A}^{lin} - P_{NTR,B}^{lin}}{P_{NTR,A}^{lin}}$$

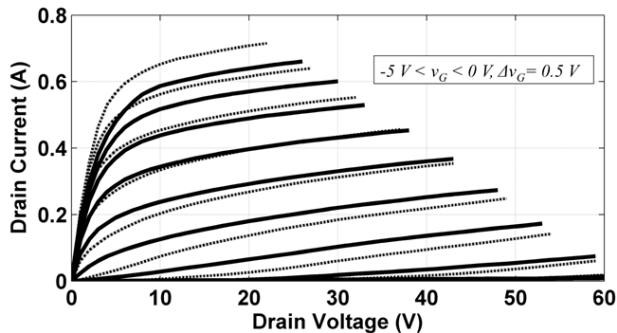


Figure 2.11: DPIVs of  $8 \times 125 \mu\text{m}$  GaN HEMTs from  $(V_{GQ}^{nom}, V_{DQ}^{nom}) = (-3.1 \text{ V}, 25 \text{ V})$ ,  $I_{DQ} = 100 \text{ mA}$  with  $\hat{v}_G \simeq V_T$ ,  $\hat{v}_D \simeq 60 \text{ V}$ . Device type A: dotted lines; type B: continuous lines.

Parameter	Technology A	Technology B
$\Delta V$ (V)	6	9
$\Delta I$ (mA)	-110	-192
$\Delta_{TR}$	29%	36%

Table 2.2: Trap-related technology performance indicators.

which represent the relative differences of maximum linear output power capabilities between the two technologies A and B, estimated in presence ( $\Delta_{AB,TR}$ ) or in absence ( $\Delta_{AB,NTR}$ ) of traps. Thus, the DPIV curves set, previously described for type A, has also been measured for type B; a comparison between the two DPIV sets is reported in Fig. 2.11. Type B technology provides slightly less maximum current density than type A: this is also confirmed by the indicator in (2.8), which results in  $\Delta_{AB,TR} = 14\%$  and  $\Delta_{AB,NTR} = 4\%$  [130]. These values and the ones reported in Table 2.2 suggest that a relevant role in power reduction is due to nonlinear charge trapping.

## 2.6 Nonlinear and Linear Lag Functions

### 2.6.1 Nonlinear Lag Function

It has been mentioned in 2.5.1 that the main measurable effect of charge trapping under pulsed excitation is a drop in the dc component of the drain

current. The interesting aspect is that such kind of measurements allow to relate a measurable quantity to the charge trapping behavior: this permits to empirically quantify the dependency on charge trapping phenomena not only in terms of performance evaluation, but also in terms of its nonlinear dependencies, which is not considered in many previous works, such as in [49]. More in detail, one can make use of the dc component of the drain current measured during single-pulsed characterization to define the following normalized quantity [132]:

$$\lambda_{NLF}(V_{GQ}, V_{DQ}, v_G(t), v_D(t)) = \frac{I_{DQ} - I_{D0}}{I_{DQ}} \quad (2.9)$$

where  $I_{DQ}$  is the quiescent value in absence of pulsed excitation, and  $I_{D0}$  is the dc drain current component measured under single-pulsed excitation. The term  $\lambda_{NLF}$  will be referred to as *nonlinear lag function*. Such a quantity, which is obtained as a normalized variation of the dc current with respect to its quiescent value, also represents a normalized variation of the charge trapping state  $\chi$ . In other words, the measured variation of  $I_{D0}$  is used here as a sensor of the charge trapping state in which the device is operating. A characterization of the  $\lambda_{NLF}$  for a 1-mm GaN HEMT is reported in Fig. 2.12. Such a function resumes many important details about the behavior of traps: first of all, it gives a direct quantification of the presence and the impact of charge-trapping phenomena. In fact, it confirms the fast charge trapping activation due to the specific configuration of pulses described in section 2.5.1: it is zero for  $v_G > V_{GQ}$  and  $v_D < V_{DQ}$ , as no trapping is activated. Moreover, it provides the dependency with respect to the voltage excitations: it can be seen, for example, that for a fixed value of  $v_D$ ,  $\lambda_{NLF}$  increases as  $v_G$  diminishes, reaching a maximum in correspondence with the threshold voltage  $V_T$ . However, such an increase may not be considered linear for each value of  $v_D$ , and even so, the slope is not the same in all curves. When the signals go through the threshold, the dc current is sampled while pulsed excitation deeply pinches-off the transistor and  $\lambda_{NLF}$  shows a different slope, suggesting that less charges are trapped. Indeed, once the threshold is reached, the channel disappears and the transistor experiences an abrupt change of the electrical field, fundamentally influencing the trapping mechanisms. Further research should be spent in order to understand the mechanisms activated once the threshold is crossed. A few more comments on the sub-threshold behavior are provided in the next paragraph. By evaluating the dependency on  $v_D$ , it can be seen that a linear approximation may hold, although some variations versus  $v_G$  are observed. Thus, the dependency on  $v_G$  and  $v_D$ , not only may be nonlinear, but also not separable, i.e.,  $\lambda_{NLF}$  is inherently a two-dimensional function of the applied voltages. Indeed, such a conclusion makes sense if considering that both gate and drain voltage act in setting the electrical field within the transistor, which is responsible of charge trapping activation. As the information on charge trapping (dc current drop) is only available for  $v_G < V_{GQ}$  and  $v_D > V_{DQ}$ , one should choose a minimum

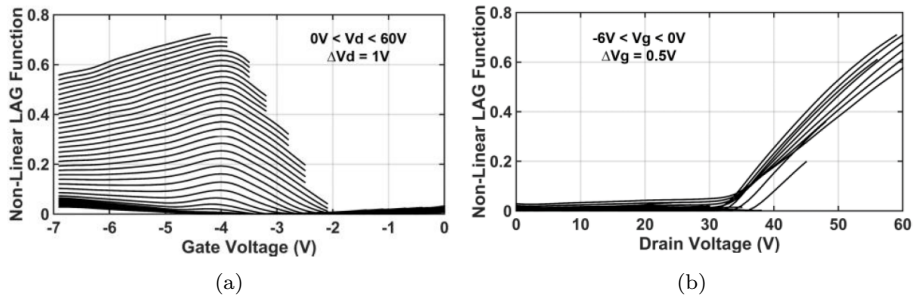


Figure 2.12: Nonlinear Lag Function ( $\lambda_{NLF}$ ) (a) vs. pulsed gate voltages and (b) vs. pulsed drain voltages.

drain quiescent point  $V_{DQ}^{min}$  and a maximum gate quiescent point  $V_{GQ}^{max}$  (e.g.,  $V_{GQ}^{max} = 0$  V,  $V_{DQ}^{min} = 0 + \epsilon$  V, where  $\epsilon$  is introduced to have  $I_{DQ} \neq 0$ ) in order to trigger charge trapping over the full region of interest and obtain the most complete  $\lambda_{NLF}$ . Although  $\lambda_{NLF}$  is normalized with respect to the biasing condition from which it is measured, it is not straightforward to generalize the dependencies it describes in a coherent way for more than one bias point, and further research must be carried out on the topic. By investigating towards a multi-bias characterization, one may leverage on the double-pulse technique to acquire pulsed characteristics for which any dynamically nonlinear trapping (*DNLT*) [131] mechanism (i.e., fast captures and slow releases) is activated. Any residual effect on the drain current characteristics pulsed by various bias points should be accounted as additional lag phenomena.

## 2.6.2 Linear Lag Function

Owing to the possibility of pre-setting a fixed maximum amount of captured *DNLTs* by means of the double-pulse technique, an investigation has been carried out for checking the possible simultaneous presence of dynamically linear trapping effects *DLTs*, i.e., charges related to dynamics with equally slow capture and release times. Similarly to what was mostly observed in GaAs devices, the presence of *DLTs* can be detected by means of deviations of the dynamic drain current which depend on the average gate and drain voltage values. To this aim, a set of DPIVs measurements was carried out from different on- and off-state quiescent voltages by always adopting the same pre-pulsing condition  $\hat{v}_G = -4$  V,  $\hat{v}_D = 60$  V, which forces the capture of the same amount of *DNLTs* in all cases. On-state quiescent point variations are first considered. Three DPIVs from quiescent conditions lying on the same locus at constant (2.4

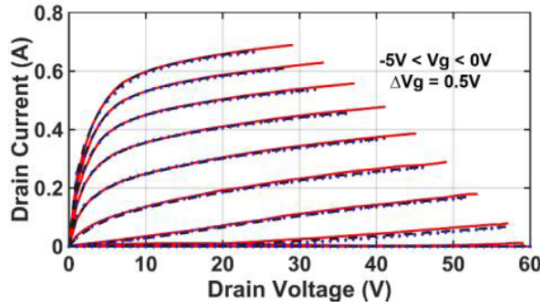


Figure 2.13: DPIVs from different on-state quiescent conditions ( $V_{GQ}$ ,  $V_{DQ}$ ) lying on the same isothermal locus corresponding to a 2.4 W dissipated power, namely: (-2.7 V, 10 V),  $I_{DQ} = 240$  mA: red continuous lines; (-3.2 V, 20 V),  $I_{DQ} = 120$  mA: black dashed lines; (-3.4 V, 30 V),  $I_{DQ} = 80$  mA, blue dotted lines. For all DPIVs:  $\hat{v}_G = -4$  V,  $\hat{v}_D = 60$  V.

W) dissipated power, namely, (10 V, -240 mA), (20 V, -120 mA), (30 V, -80 mA), are compared in Fig. 2.13. The comparison between the three DPIVs is thermally coherent since the internal equivalent temperature is affected in all cases by the same amount of self-heating, while the baseplate temperature was feedback-controlled at 40°C. Such a test resembles the one carried out in section 2.4.3, and again shows that the three DPIVs practically coincide, indicating no variation in the amount of captured  $DLTs$  and confirming that dispersive phenomena affecting the drain current can be completely characterized by means of the  $\lambda_{NLF}$ .

Next, DPIVs from off-state quiescent conditions were also considered. In these cases, the internal equivalent device temperature  $\theta$  coincides with the baseplate temperature  $\theta_B$ , since no self-heating occurs. A thermally coherent comparison between IV curves is thus still straightforward (although at slightly lower temperature with respect to the on-state experiments). Different quiescent conditions were chosen in order to quantify possible  $DLT$ -related drain current deviations by separately changing the quiescent gate voltage  $\Delta V_{GQ}$  and the drain voltage  $\Delta V_{DQ}$ . A first test is shown in Fig. 2.14(a), where two DPIVs from ( $V_{GQ}$ ,  $V_{DQ}$ ) pairs: (-4.5 V, 30 V) and (-8 V, 30 V) are shown. Considerable drain current deviations are observed in this case, corresponding to a considerable amount of charge trapping in  $DLTs$ , when adopting the well-below-threshold quiescent condition  $V_{GQ} = -8$  V. A second result is shown in 2.14(a), where two DPIVs from ( $V_{GQ}$ ,  $V_{DQ}$ ) pairs (-8 V, 10 V) and (-8 V, 30 V) are compared. Again, drain current deviations due to  $DLT$  are present, although slightly lower current deviations are observed versus  $\Delta V_{DQ}$  than  $\Delta V_{GQ}$ . Again, as already

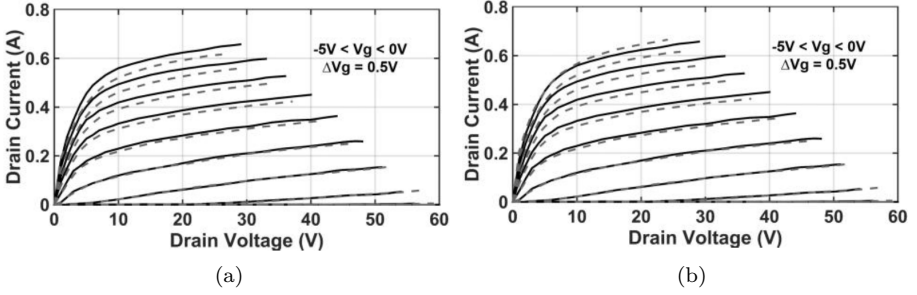


Figure 2.14: DPIVs from different off-state quiescent conditions, with  $\hat{v}_G = -4$  V,  $\hat{v}_D = 60$  V. (a)  $(V_{GQ}, V_{DQ}) = (-4.5$  V, 30 V), continuous lines;  $(V_{GQ}, V_{DQ}) = (-8$  V, 30 V), dashed lines. (b)  $(V_{GQ}, V_{DQ}) = (-8$  V, 10 V), continuous lines;  $(V_{GQ}, V_{DQ}) = (-8$  V, 30 V), dashed lines.

mentioned, the sub-threshold region seems behaving fundamentally differently from the on-state. Moreover, when biasing the transistor at pinch-off, one cannot rely anymore on the dc current component as a suitable indicator of charge trapping. Instead, the pulsed drain current deviations observed in Figs. 2.13 and 2.14 can be adopted as a trap status sensing parameter, in order to define a quantitative measure of the captured  $DLT$ . To this aim, since different  $\Delta i_D^{DP}$  values can be recorded depending on the particular voltage pair  $(v_G, v_D)$  considered, a particular sensing point  $S(\tilde{v}_G, \tilde{v}_D)$  must then be somehow defined for a point on the pulsed IV characteristic. Thus, it has been chosen to record the drain current deviations  $\Delta i_D$  in a point  $S$  at  $v_G = 0$  V,  $v_D = 20$  V. Following this assumption, we can define the function as the double-pulsed drain current observed in the sensing point  $\tilde{v}_G, \tilde{v}_D$ , by applying pre-pulses towards the point of max-captured  $DNLTs$  ( $\hat{v}_G = V_T, \hat{v}_D = v_D^{max}$ ) from the quiescent condition  $(V_{GQ}, V_{DQ})$ . Then, a *linear lag function* can be defined as:

$$\lambda_{LLF}(V_{GQ}, V_{DQ}) = \frac{\tilde{i}_D^{DP}(V_{GQ}^{nom}, V_{DQ}^{nom}) - \tilde{i}_D^{DP}(V_{GQ}, V_{DQ})}{\tilde{i}_D^{DP}(V_{GQ}^{nom}, V_{DQ}^{nom})} \quad (2.10)$$

where  $(V_{GQ}^{nom}, V_{DQ}^{nom})$  represents the nominal quiescent point. A preliminary example of the behavior of function (2.10) is sketched in Fig. 2.15. The above-defined  $\lambda_{LLF}$  can be conveniently used, analogously to  $\lambda_{NLF}$  in the  $DNLT$ -case, for the accurate characterization of the charge-trapping in the multi-bias case: detailed technology-related information on the power performance degradation due to traps is obtained, when considering both Linear and Nonlinear Lag functions. In the next section, technology assessment experiments by means of the double-pulse technique are reported.

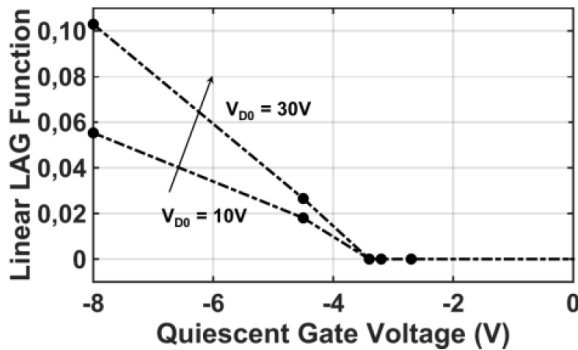


Figure 2.15:  $\lambda_{LLF}(V_{GQ}, V_{DQ})$  in the chosen sensing point. Dots: experimental results. Dashed lines represent a piecewise linear interpolation.

## 2.7 GaN HEMT modeling based on the double-pulse technique

As introduced in section 1.2.2, various approaches based on conventional small- and large-signal bias dependent VNA measurements and standard pulsed IV characteristics have been proposed for GaN HEMT modeling. In some cases, the transistor is directly characterized under high-frequency periodic steady-state nonlinear operation (e.g., [50],[123]). In others, the nonlinear FET behavior is modeled by separating the description into the low-frequency resistive drain current component and the high-frequency gate and drain displacement contributions. With this respect, two main approaches are followed in terms of the type of stimuli used for the characterization at low frequencies. Sinusoidal excitation is a potentially interesting choice [142] since the stimulus is quite similar to the actual operating condition in typical power amplifier applications. This approach can be used for the modeling of GaAs and GaN devices. However, in the case of GaN transistors, the strongly nonlinear dynamics of trap-related dispersive effects makes model extraction from sinusoidal-based characterization more difficult, because trap state mainly depends on peak values of electric fields in the region where the charge trapping effects take place. As already discussed, a time domain pulsed characterization approach can be a valid alternative, leading to a more efficient extraction of the nonlinear dynamic model for the trapping effect. This section focuses on the formulation and validation of an empirical modeling approach which takes advantage of the double pulse technique for an accurate charge trapping characterization.

### 2.7.1 Formulation

The adopted model circuit topology is presented in Fig. 2.16, showing the extrinsic parasitic network (a) and the circuit schematic of the intrinsic device (b). The main focus of the work has been the description of the electro-thermal channel current model, while a simple multi-bias quasi-static approach is instead followed for the gate and drain displacement current components [143]. By using the same notation as in section 2.3, let  $\underline{\chi}$  be a vector of state variables describing the internal charge trapping state of the transistor and  $\theta$  an equivalent internal channel temperature. The instantaneous resistive component of the drain current (channel current) can be described by a formulation such as the one already reported in (2.1). With respect to the thermal model, it is well known that the main effects of the temperature variations on the electrical transistor performance are observed on electron mobility (decreasing for increasing temperatures) and on threshold voltage (decreasing for increasing temperatures). Thus, the following model is here assumed for the current:

$$i_D(t) = (1 + \alpha_{\theta_m}(\theta(t) - \theta^*))F[v_{G_\theta}(t), v_D(t), \underline{\chi}(t), \theta^*] \quad (2.11)$$

$$v_{G_\theta}(t) = v_G(t) + \alpha_{\theta_t}(\theta(t) - \theta^*) \quad (2.12)$$

where  $\alpha_{\theta_m}$  and  $\alpha_{\theta_t}$  are parameters to be determined. The temperature  $\theta^*$  is an equivalent channel temperature evaluated at a reference condition given by:

$$\theta^* = \theta_B + R_\theta P_D^* \quad (2.13)$$

with  $\theta_B$  representing a predetermined baseplate temperature,  $R_\theta$  the thermal resistance and  $P_{DQ}^*$  the power dissipated in a reference quiescent bias  $V_{GQ}^*$ ,  $V_{DQ}^*$  corresponding to the static current  $I_{DQ}^*$ . Under the mild approximation

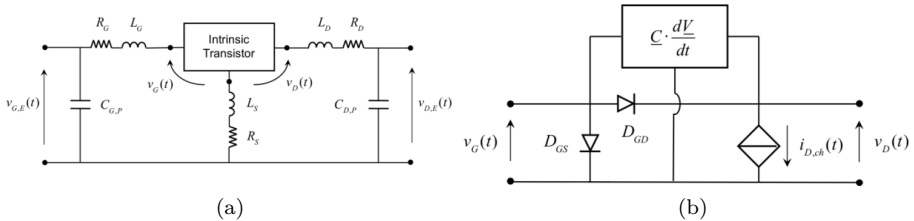


Figure 2.16: GaN HEMT nonlinear model. (a) Extrinsic parasitic network. (b) Intrinsic device schematic.

of a quasi-linear thermal behavior and period steady-state excitation, the temperature  $\theta(t)$  can be expressed as

$$\theta(t) \simeq \theta_B + \int_0^{+\infty} z_\theta(\tau) p_D(t - \tau) d\tau \simeq \theta_B + R_\theta P_{D0} \quad (2.14)$$

where  $z_\theta(\tau)$  represents the thermal impulse response of the device,  $\theta_0$  is the average temperature and  $P_{D0}$  is the mean value of the dissipated power. Let us assume that the dynamics of the charge trapping state is determined by the following state equation:

$$\frac{d\underline{\chi}}{dt} = \tilde{h}[\underline{\chi}(t), v_G(t), v_D(t)]. \quad (2.15)$$

For a given quiescent point, the (steady) state of the transistor related to traps can be described, without any loss of generality, through a non-linear function of the quiescent values:

$$\underline{\chi} = \underline{\chi}_{QS}[V_{GQ}, V_{DQ}] \quad (2.16)$$

which satisfies the following equation:

$$\tilde{h}[\underline{\chi}_{QS}(t), v_G(t), v_D(t)] = 0 \quad (2.17)$$

defining the steady-state regime. In large-signal operation, the same function  $\underline{\chi}_{QS}$  can be exploited to provide the equivalent steady state  $\underline{\chi}_{QS}[v_G(t), v_D(t)]$  corresponding to the instantaneous working point  $v_G(t), v_D(t)$ . The dynamic deviations  $\underline{\chi}(t) - \underline{\chi}_{QS}[v_G(t), v_D(t)]$  are due to non-negligible time constants (i.e., the presence of memory effects) that relate the trap occupation state to the time evolution of the transistor internal electric fields, and can be considered as the main controlling quantities on the trap state variation rate of  $\underline{\chi}(t)$ . More precisely, through an algebraic manipulation, the state equation in (2.15) can be written as:

$$\begin{aligned} \frac{d\underline{\chi}}{dt} &= \tilde{h}'[\underline{\chi}(t) - \underline{\chi}_{QS}[v_G(t), v_D(t)], \underline{\chi}_{QS}(t), v_G(t), v_D(t)] \\ &= \tilde{h}''[\underline{\chi}(t) - \underline{\chi}_{QS}[v_G(t), v_D(t)], v_G(t), v_D(t)] \end{aligned} \quad (2.18)$$

Since the instantaneous values  $v_G(t), v_D(t)$  already strongly affect the deviations (thus, the state derivative) through  $\underline{\chi}_{QS}$ , independently from the past evolution of the voltages (which instead determine, together with the initial conditions,

the value  $\underline{\chi}(t)$ ), it is reasonable to neglect the explicit dependence of  $\underline{h}$  from  $v_G(t), v_D(t)$ . This justifies the following simplified equation:

$$\frac{d\underline{\chi}}{dt} \simeq \underline{h}[\underline{\chi}(t) - \underline{\chi}_{QS}[v_G(t), v_D(t)]] \quad (2.19)$$

where  $h = 0$  when  $\underline{\chi} = \underline{\chi}_{QS}[v_G, v_D]$  since  $\underline{\chi}_{QS}$  represents the steady-state trap state corresponding to the present values of  $v_G, v_D$ . Analogously to the thermal case, a single equivalent state variable will be considered in the following for the sake of simplicity, thus obtaining:

$$\frac{d\chi}{dt} \simeq h[\chi(t) - \chi_{QS}[v_G(t), v_D(t)]] \quad (2.20)$$

The scalar function  $h$  defines the trap state rate of change as a function of the actual distance of  $\chi$  from the corresponding steady state  $\chi_{QS}$ . In the case of GaAs-based transistors  $h$  is normally assumed to be a linear function, since the same time constant applies for capture and release in charge trapping phenomena. Instead, in GaN-based devices a strongly nonlinear dynamic behavior is encountered, since trap capture time constant  $\tau_F$  is much faster than the time constant  $\tau_S$  associated with release phenomena. The nonlinear function  $h$  can be described in the case of GaN-based transistors by a piecewise linear approximation, which takes the form outlined in Fig. 2.17(a) in the simplest case of a two-slope approximation. The slope  $-\frac{1}{\tau_F}$  of the fast charge capture phenomena, which occur when  $\chi(t) < \chi_{QS}[v_G(t), v_D(t)] - \chi_{TH}$ , is much greater than the slope  $-\frac{1}{\tau_S}$  associated with release phenomena. The value  $\chi_{TH}$  defines a threshold for fast ( $\tau_F$ ) charge trapping phenomena ( $\tau_F \ll \tau_S$ ), and corresponds to a voltage activation threshold, as seen in section 2.5.1. By considering that only moderate changes in the trap state can be expected in a reasonably good-quality device, the isothermal current-voltage IV function  $F[v_G, v_D, \chi, \theta^*]$  can be linearized with respect to the state variable  $\chi$  around a value  $\chi_M$ , which can be conveniently chosen as the expected maximum value of  $\chi$  in typical large signal operating conditions. Thus, by linearizing the isothermal resistive drain current function  $F$  in (2.1), we obtain

$$F[v_G, v_D, \chi, \theta^*] \simeq F[v_G, v_D, \chi_M, \theta^*] + f_\chi[v_G, v_D, \chi_M, \theta^*](\chi - \chi_M) \quad (2.21)$$

where  $f_\chi[v_G, v_D, \chi_M, \theta^*] = \left. \frac{\partial F}{\partial \chi} \right|_{\chi=\chi_M}$  is the drain current sensitivity to trap state changes. In the following, periodic steady-state operation above release-cutoff (i.e., with respect to the slow charge trap release dynamics, when  $\tau_S \gg \frac{1}{f_0}$ ) will be considered also for the trap state, so that we will assume  $\chi(t) \simeq \chi_0$ , where  $\chi_0$  can be evaluated by harmonic balance circuit analysis.

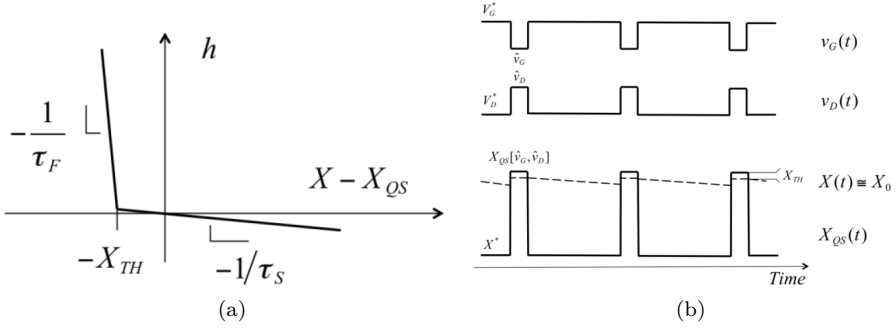


Figure 2.17: (a) Nonlinear function associated with state equation (2.20) in the GaN transistor case. (b) Qualitative waveforms corresponding to a periodic low-duty-cycle pulsed regime, showing activation of the nonlinear dynamics associated with charge trapping phenomena in GaN transistors.

## 2.7.2 Identification

The  $\chi_{QS}[v_G, v_D]$  function and the  $\chi_{TH}$  parameter, which appear in the state equation (2.20) through  $h$  (Fig. 2.17(a)), can be experimentally determined by measuring the variation of the drain current dc component  $I_{D0}$  with respect to a reference quiescent value  $I_{DQ}^*$  under low duty-cycle pulsed regime with pulse repetition frequency  $f_p$  which satisfies above-cutoff conditions (i.e.,  $f_p \gg \frac{1}{\tau_S}$ ). The latter assumption guarantees that the trap state is practically time invariant during any periodic pulse repetition (see Fig. 2.17(b)). The low duty-cycle condition, instead, guarantees that, for a fixed reference bias voltage and baseplate temperature, the variation of the drain current dc component can derive only from trap state variations strictly related to the peak values of voltage pulses. Under such conditions, by applying the mean value operator to (2.11) and (2.21), under the hypothesis of a sufficiently low duty-cycle of the pulse sequence, we obtain the following expression for the normalized variation of the dc drain current with respect to the quiescent value:

$$\frac{I_{D0} - I_{DQ}^*}{I_{DQ}^*} \approx \frac{f_\chi[V_{GQ}^*, V_{DQ}^*]}{I_{DQ}^*} (\chi_0[\hat{v}_G, \hat{v}_D] - \chi^*[V_{GQ}^*, V_{DQ}^*]) \quad (2.22)$$

where  $\chi_0 - \chi^*$  is the trap status variation caused by the voltage pulse peaks  $\hat{v}_G, \hat{v}_D$  (dependency on  $\chi_M$  and  $\theta^*$  has been dropped in (2.22) for the sake of notation simplicity). This variation is non-zero only when pulses capable of activating fast charge capture phenomena are applied, e.g., positive drain or negative gate pulses starting from the reference voltages  $V_{GQ}^*, V_{DQ}^*$  or, more

generally, when the pulse amplitude and signs are such as to activate the dynamic nonlinearity described by the  $h$  function defined in (2.20) and piecewise linearly approximated according to the graph in Fig. 2.17(a). More precisely, this happens when the instantaneous differences between the time-varying  $\chi_{QS}[v_G(t), v_D(t)]$  and the trap state  $\chi$  reach the fast capture threshold level  $\chi_{TH}$ , so that fast charge capture is activated and, consequently, the trap status quickly becomes the time-invariant value  $\chi_0$ , almost coincident with the steady-state  $\chi_{QS}[\hat{v}_G, \hat{v}_D]$ . This situation is qualitatively described in Fig. 2.17(b). In such conditions, we have:

$$\chi_0[\hat{v}_G, \hat{v}_D] - \chi_{QS}[\hat{v}_G, \hat{v}_D] = -\chi_{TH}. \quad (2.23)$$

By recalling the definition of  $\lambda_{NLF}$  in (2.9), one can rewrite (2.22) as:

$$\begin{aligned} \lambda_{NLF}[V_{GQ}^*, V_{DQ}^*, \hat{v}_G, \hat{v}_D] &\simeq -\frac{f_\chi[V_{GQ}^*, V_{DQ}^*]}{I_{DQ}^*} (\chi_0[\hat{v}_G, \hat{v}_D] - \chi^*[V_{GQ}^*, V_{DQ}^*]) \\ &= s^* \Delta\chi \end{aligned} \quad (2.24)$$

where  $s^* = -\frac{f_\chi[V_{GQ}^*, V_{DQ}^*]}{I_{DQ}^*}$  can be defined as the drain current sensitivity to the trap status. In other words,  $\lambda_{NLF}$  is used here as an indirect sensor of the trap status variations. It should be noted that the value of  $s^*$  cannot be easily determined as the trap state variable  $\chi$  is not directly measurable. However, as will be shown in the following, its actual value is not relevant for the drain current prediction. By considering (2.23), one obtains:

$$\chi_{QS}[\hat{v}_G, \hat{v}_D] - \chi^*[V_{GQ}^*, V_{DQ}^*] = -\frac{\lambda_{NLF}[V_{GQ}^*, V_{DQ}^*, \hat{v}_G, \hat{v}_D]}{s^*} + \chi_{TH}. \quad (2.25)$$

which holds for  $\lambda_{NLF} \neq 0$ , otherwise  $\chi_{QS}$  cannot be determined using (2.25). It is interesting to note that all the features of  $\lambda_{NLF}$  pointed out in section 2.6 regarding its dependency on  $(v_G, v_D)$  can now be interpreted in terms of charge trapping state variation  $\chi_{QS}[\hat{v}_G, \hat{v}_D] - \chi^*[V_{GQ}^*, V_{DQ}^*]$ . By applying the  $\lambda_{NLF}$  measurement technique already depicted, one can think of implementing the charge-trapping model by directly using the values of  $\lambda_{NLF}$  in a look-up table (LUT) with a suitable interpolation. Otherwise, one can fairly assume a linear dependency on  $\hat{v}_D$ , the same approximation cannot be made for the dependency on  $\hat{v}_G$ ; thus, the following formulation can be adopted:

$$\begin{aligned} \chi_{QS}[\hat{v}_G, \hat{v}_D] - \chi^*[V_{GQ}^*, V_{DQ}^*] &= -\frac{\lambda_{NLF}[V_{GQ}^*, V_{DQ}^*, \hat{v}_G, \hat{v}_D]}{s^*} + \chi_{TH} \\ &\simeq w^*[\hat{v}_G] + \gamma^*[\hat{v}_G]\hat{v}_D. \end{aligned} \quad (2.26)$$

This shows that the one-dimensional functions  $w^*[\hat{v}_G]$  and  $\gamma^*[\hat{v}_G]$ , which characterize the trap state equation (2.20) together with the parameter  $\chi_{TH}$ , can be directly identified by mean square fitting of the measured function  $\lambda_{NLF}$ . The identification of the drain current model (2.21) is based on two different sets of DPIVs  $i_{D,M}$  and  $i_{D,M}^+$  measured from the same quiescent point ( $V_{GQ}^*, V_{DQ}^*$ ) and reaching the two different pre-pulse peak values ( $V_{GM}, V_{DM}$ ) and ( $V_{GM}, V_{DM} + \Delta V_D$ ), which respectively lead to the values of the state variable:

$$\begin{aligned}\chi_M &= \chi_{QS}[V_{GM}, V_{DM}] - \chi_{TH} \\ \chi_M^+ &= \chi_{QS}[V_{GM}, V_{DM} + \Delta V_D] - \chi_{TH}\end{aligned}\quad (2.27)$$

The DPIV characteristic  $i_{D,M}$  directly defines the model function

$$F[v_G, v_D, \chi_M, \theta^*] = i_{D,M}. \quad (2.28)$$

Moreover, the drain current sensitivity function can be computed as:

$$f_\chi[v_G, v_D, \chi_M, \theta^*] = \frac{i_{D,M}^+ - i_{D,M}}{\chi_M^+ - \chi_M} = s^* \frac{i_{D,M}^+ - i_{D,M}}{\lambda_M^+ - \lambda_M} \quad (2.29)$$

where:

$$\begin{aligned}\lambda_M &= \lambda_{NLF}[V_{GQ}^*, V_{DQ}^*, V_{GM}, V_{DM}] \\ \lambda_M^+ &= \lambda_{NLF}[V_{GQ}^*, V_{DQ}^*, V_{GM}, V_{DM} + \Delta V_D].\end{aligned}\quad (2.30)$$

It is important to note that according to (2.21), (2.25) and (2.29) the actual value of the normalized sensitivity  $s^*$  does not affect at all the relationship between measured data (i.e., the  $\lambda_{NLF}$  function) and the predicted drain current  $i_D(t)$ , since it appears both at the numerator and denominator in the same product term in (2.21). Thus, one can arbitrarily assume, without loss of generality,  $s^* = 1$  and also  $\chi^*[V_{GQ}^*, V_{DQ}^*] = 0$ , since only variations with respect to the reference trap state variable  $\chi_M$  are important in (2.21).

As far as the thermal model parameters  $\alpha_{\theta_M}$ ,  $\alpha_{\theta_t}$ ,  $R_\theta$  are concerned, these can be evaluated from pulsed drain current measurements carried out at different baseplate temperatures. In particular, the thermal resistance  $R_\theta$  can be evaluated through the pulsed drain current measurement technique in [45]. The parameters  $\alpha_{\theta_M}$ ,  $\alpha_{\theta_t}$  can be instead obtained by numerical fitting of the differences between two DPIVs starting from the same quiescent point ( $V_{GQ}^*, V_{DQ}^*$ ) and reaching the same trap status  $\chi_M$  defined in (2.27) at two different baseplate temperatures. As already mentioned, parasitic components

of the extrinsic network shown in Fig. 2.16(a) have been extracted on the basis of cold-FET procedures based on [143], and their values can be found in [132]. All the DPIVs and  $S$ -parameters have been accurately de-embedded from parasitic elements in order to obtain the characterization of the intrinsic device. Gate and drain displacement current components have been modeled through standard quasi-static equations implemented on the basis of a LUT-based multi-bias capacitance-function matrix. The gate-source and gate-drain diodes  $D_{GS}$  and  $D_{GD}$  in 2.16(b) have been characterized through cold-FET dc measurements at forward gate voltages and implemented into CAD environment by using standard analytical models.

### 2.7.3 Experimental extraction and validation

The model depicted in the previous sections can be straightforwardly implemented in CAD tools, as largely described in [132]. The method has been applied to a 1-mm GaN HEMT ( $L=0.25 \mu\text{m}$ ) and  $\lambda_{NLF}$  has been extracted as described in section 2.6, from a reference condition  $V_{GQ}^* = -3\text{V}$ ,  $V_{DQ}^* = 30\text{V}$ ,  $I_{DQ}^* = 80 \text{ mA}$  at the baseplate temperature  $\theta_B = 40^\circ\text{C}$ . To the aim of characterizing the function  $F[v_G, v_D, \chi_M, \theta^*]$  in (2.21), the corresponding DPIV starting from the quiescent point  $V_{GQ}^* = -3\text{V}$ ,  $V_{DQ}^* = 30\text{V}$  and pre-pulses reaching  $\hat{v}_G = -4 \text{ V}$  ( $V_{GM}$ ),  $\hat{v}_D = 60 \text{ V}$  ( $V_{DM}$ ) has been measured. In such conditions, a constant trap state  $\chi_M$  defined by (2.27), is guaranteed over the voltage plane region for which  $\chi_{QS}[v_G, v_D] \leq \chi_M + \chi_{TH}$ , which should include the whole region of possible dynamic operating conditions, defined as  $v_G \geq v_G^{min} \simeq -8 \text{ V}$  and  $v_D \leq v_D^{max} \simeq 60 \text{ V}$ . According to the shape of  $\lambda_{NLF}$ , the condition for a constant trap state in the operating region is satisfied using  $V_{DM} = v_D^{max}$  and  $V_{GM} = V_T \simeq -4 \text{ V} > v_G^{min}$ , as  $\lambda_{NLF}$  is here assumed constant for  $v_G \leq V_T$ . In order to characterize the drain current sensitivity function  $f_\chi$  in accordance with (2.29), another DPIV characteristic was measured with the same  $V_{GM} \simeq V_T$  and  $V'_{DM} = V_{DM} + \delta V_D$  with  $\delta V_D = -10 \text{ V}$ . Finally, in order to determine also the thermal parameters  $\alpha_{\theta_m}$ ,  $\alpha_{\theta_t}$  according to the outlined procedure, a DPIV characteristic starting from the same quiescent point and reaching the same trap status  $\chi_M$  was measured at the incremented baseplate temperature  $\theta_B^* = 90^\circ\text{C}$ . In particular,  $\alpha_{\theta_m} = -20 \cdot 10^{-4}$  and  $\alpha_{\theta_t} = 1.5 \cdot 10^{-3}$  have been extracted [132]. A preliminary model validation was carried out by verifying the model capability of correctly predicting different IV characteristics measured under single- and double-pulsed excitations. Figure 2.18 shows a very good agreement between simulation and measurements for these two different operating conditions. Then, an extensive large-signal model validation has been carried under sinusoidal excitation, starting with a single tone with fundamental frequency  $f_0 = 4 \text{ MHz}$ . This was intentionally chosen low

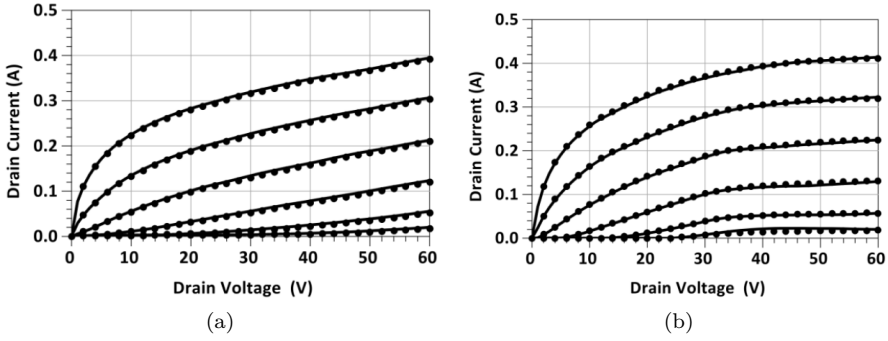


Figure 2.18: Simulated (line) and measured (dot) IV characteristics. (a) DPIV from  $V_{GQ} = -3$  V,  $V_{DQ} = 30$  V,  $\theta_B = 40^\circ\text{C}$  and pre-pulses toward  $\hat{v}_G = -4$  V,  $\hat{v}_D = 60$  V. (b) Standard PIV with from the same bias point and at the same  $\theta_B$ .

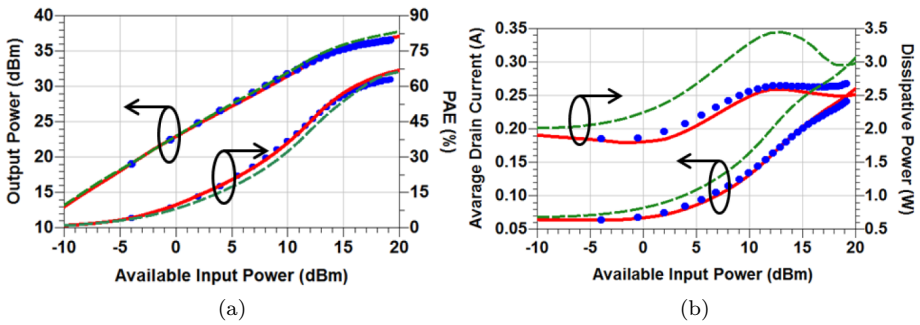


Figure 2.19: LF model validation at  $f_0 = 4$  MHz under sinusoidal excitation. Device loaded with  $Z_L$  as described in the text. Model based on the DPIV: red continuous line. Model based on the PIV: dashed green line; measurements: blue circles. (a) RF output power and PAE. (b) Drain current and dissipated power.

enough in order to observe the effects of the resistive drain current model only, and avoid other effects due to the displacement current components. The 1-mm GaN transistor has been biased at  $V_{GQ} = -3$  V and  $V_{DQ} = 30$  V for class-AB dynamic operation. Measurements of output power at the fundamental tone, PAE, average drain current and dissipated power are reported in Fig. 2.19 for a  $Z_L$  with the following first three harmonics: 1)  $74-j7 \Omega$ , 2)  $70-j15 \Omega$ , 3)  $61-j19 \Omega$ . In the Figures, also the predictions obtained by using a model based

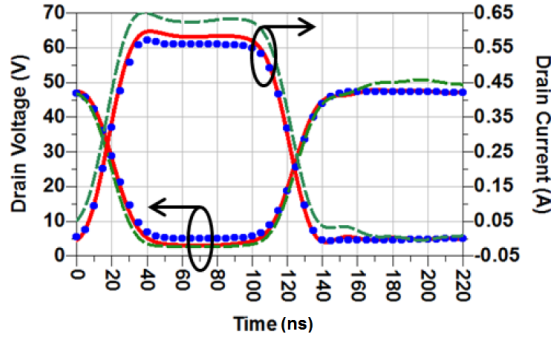


Figure 2.20: Waveforms prediction at  $f_0 = 4$  MHz under sinusoidal excitation. Device loaded with  $Z_L$  as in Fig. 2.19. Model based on the DPIV: red continuous line. Model based on the PIV: dashed green line; measurements: blue circles.

on the standard PIV instead of the DPIV are reported, showing higher accuracy for the DPIV approach. In Fig. 2.20, the current and voltage waveforms are reported. Analogous results have been obtained at 5 GHz based on the same transistor loaded for maximum power added efficiency  $Z_L^{opt}$  (Fig. 2.21). Finally, an intermodulation distortion test has been carried out at 1.5 GHz by adopting a tone spacing of 1 MHz and load impedance equal to  $50 \Omega$ . The good agreement reported in Fig. 2.22 between measured and predicted IMD values confirms the validity of the proposed model for signal distortion analysis and suggests that it could also be used for optimizing digital predistortion algorithms for microwave power amplifiers in communication systems.

## 2.8 Conclusion

In this Chapter, a pulsed measurement technique specifically tailored for GaN HEMT characterization and modeling has been presented. Such a method, referred to as double-pulse technique, enables a direct way to identify lag functions related to nonlinear charge-trapping effects. These have revealed the nonlinear dependencies between the activation of charge trapping effects and the combination of applied gate and drain pulsed peak voltages. As a consequence, it allows for direct characterization of the electrical performance of a transistor under operative conditions. Moreover, it has been shown that it is also a key characterization technique for the state-space formulation of a compact modeling approach. While this approach addresses the problem of nonlinear memory effects at the device level, in the next Chapter the focus will

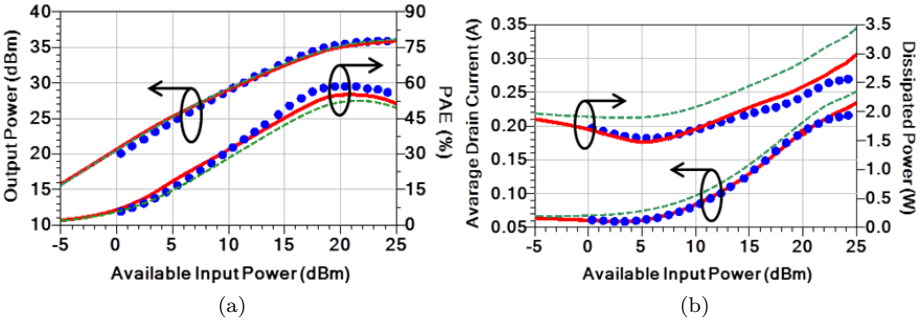


Figure 2.21: RF model validation at  $f_0 = 5$  GHz under sinusoidal excitation. Device loaded with  $Z_L^{opt}$ . Model based on the DPIV: red continuous line. Model based on the PIV: dashed green line. Measurements: blue circles. (a) RF output power and PAE. (b) Drain current and dissipated power.

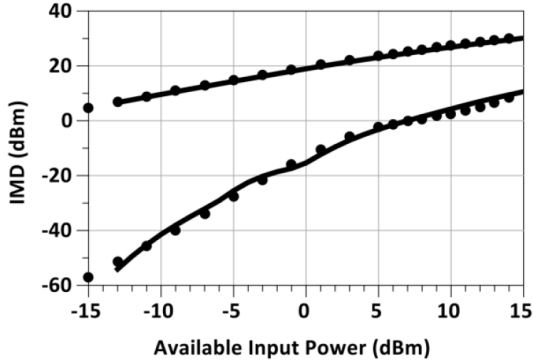


Figure 2.22: Intermodulation test for the model extracted from DPIVs. Fundamental output power and third-order IMD product (dot – measure, line – prediction).  $Z_L = 50 \Omega$ ,  $f_0 = 1.5$  GHz,  $\Delta f = 1$  MHz.

be on characterization and modeling at PA level. Large-signal analysis and nonlinear measurements will provide the necessary tools for predicting nonlinear and dynamic behavior.

## Chapter 3

# Nonlinear dynamic characterization of RF PAs

### 3.1 Introduction

Linear time-invariant (LTI) system theory is a very well established mathematical tool which has always been a workhorse for engineering: RF and microwaves make no exception. Linear systems obey to the superposition principle, meaning that a combination of input signals results in the same linear combination of output signals. Since the Fourier transform is a linear operator, the frequency spectrum at the output of a linear device will only contain the frequency components excited at its input. In other words, no frequency conversion or spectrum regrowth takes place. As a consequence, single tone measurements fully describe the response of an LTI device:  $S$ -parameters [144] are independent of input power, thus can be obtained from relative measurements of incident and scattered power waves swept over the frequency of interest. Unfortunately, as seen in section 1.3.1, increasing the efficiency of a PA imposes the necessity to deal with nonlinear systems. Although transistors are inherently nonlinear devices, the usual approach has often been to impose a *small-signal* operation regime in which the device-under-test (DUT) characteristics are linearized, allowing the application of classical techniques for LTI systems,  $S$ -parameters included. The presence of Vector Network Analyzers (VNAs), capable of accurately measuring  $S$ -parameters, has driven RF PA design for many years. Notwithstanding the success of this approach, PA architectures are lately pushing the operation beyond the small-signal limits, in conditions where  $S$ -

parameters quantitatively fail to describe the system [145]. Moreover, it should be underlined that the rich nonlinear behavior is absolutely not captured by the few commonly indicated parameters, such as the 1-dB compression point or the third-order intercept (TOI) point. They are instead useful to quantify up to which limit a linearization is reasonably feasible. In general, all systems that do not behave linearly can be indicated as nonlinear. Yet, nonlinear systems normally considered in this field are the ones that convert a periodic input into a periodic output of the same period, and can be suitably described by a Volterra series. Other types of systems featuring discontinuities, hard nonlinearities, chaotic behavior, etc. fall out of this category [107]. The presence of harmonic distortion and spectral regrowth tarnishes the linear relationship between input and output also at the fundamental frequency component, with the consequence that both the frequency and power dimensions should be independently varied to cover the region of interest. This means that incident and scattered waves should be separately measured both in terms of amplitude and phase, while the phase coherence of the various spectral components of a signal should be maintained to allow a time-domain reconstruction.

In addition to a direct scope acquisition of the waves (as seen in section 2.2 for the MP-TDNA), two approaches have been historically followed to implement large-signal microwave measurements [146]: the so called *sampler-based* approach [147], and the *mixer-based* approach [148]. They are the subject of the next section, where set-ups introduced before the start of the Ph.D., but heavily used during the activity, are described. Section 3.3 is instead dedicated to set-ups composed during the Ph.D., which are both thought for the characterization of supply-modulated PAs. More in detail, they have been conceived as alternative approaches to the LF-LSNA described in 3.2.2. The first, which makes use of a mixer-based large signal network analyzer, allows for the characterization of a PA under concurrent pulsed supply and pulsed RF input excitations. The second, based on a vector signal transceiver architecture, features wider modulation bandwidth and eliminates the need of defining a measurement frequency grid, while it does not perform a full two-port network analysis. Both set-ups have been developed in the framework of master thesis projects. Sections 3.4 and 3.5 are dedicated to the characterization of power amplifiers under supply modulation. The presented experiments have been mainly developed at KU Leuven. This activity started in coincidence with the Ph.D., as no previous approaches or framework was available in the research group with respect to supply-modulated architectures. Section 3.4, whose contents has been published in [149], [150], and [151], deals with the characterization of the interactions between the drain terminal of the supply-modulated PA and the supply modulator. In particular, nonlinear impedance-like functions are characterized for the PA and the supply modulator. Most of the measurements have been performed with the LF-LSNA of section 3.2.2, already available in the

lab, although some tests, yet to be published, were also carried out on the newly implemented set-up described in section 3.3.4, which enables measurements over a larger bandwidth. Section 3.5 is based on the publication in [152] and presents active load-pull characterization performed at the drain terminal of the PA, at LF. Section 3.6 presents, instead, a characterization experiment performed at the University of Bologna. It is based on a set-up similar to the one shown in section 3.3.4, although differences in both the supply node sensing as well as in the available PA excitation regimes are present. This work, published in [153], shows a technique for empirically modeling self-heating effects in RF PAs.

## 3.2 Sampler-based and mixer-based large-signal measurements

### 3.2.1 Sampler-based large-signal measurements

As mentioned in section 3.1, for large-signal network analysis it is necessary not only to acquire absolute powers, but also coherent phases over the spectrum of interest: in time-domain, this means capturing the full waveform. In fact, the idea behind large-signal sampler-based instrumentation is to synchronously sample the waveforms at all ports with the maximum available bandwidth. A straightforward approach one may imagine consists in the synchronous acquisition by means of digitizers or scopes. Although this is a feasible and flexible approach, it is mainly limited by the data throughput of the digitizers. More precisely, this not only concerns the sample rate at which analog-to-digital converters (ADCs) can operate, but the inherent compromise with the resolution of the acquisition: in synthesis, this often means that measurements at high frequencies must be traded-off for poor dynamic range. To overcome this limitation, suitable frequency down-conversion techniques should be applied. One of these is the *equivalent-time* sampling, as featured in off-the-shelf oscilloscopes, which nowadays reach sampling rates up to a few GS/s. Yet, if the objective is to measure at tens of GHz of frequency, more effective down-conversion techniques should be used. A successful down-conversion approach which extends the equivalent-time principle towards microwaves is used in the so called *large-signal network analyzer* (LSNA) [147], and it is referred to as *harmonic sampling*. Such a technique, whose mathematical aspects are detailed in [154], makes use of frequency aliasing to obtain a time-stretching of the waveforms to be measured. It operates as follows: a *FracN* [145] frequency synthesizer generates an oscillation with a very high resolution, better than 1 Hz. A step recovery diode (SRD) transform the output of the *FracN* into a train of narrow pulses, which drives the sampling heads

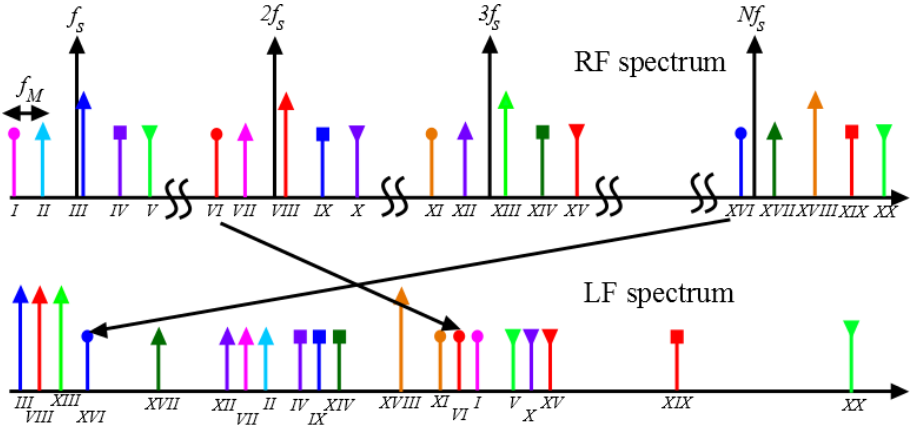


Figure 3.1: Representation of the harmonic sampling technique and the de-scrambling of the down-converted tones in case of wideband acquisition;  $f_s$  is the sampling frequency,  $f_M$  the frequency step of the modulation grid around each harmonic.

of the system. As the sampling frequency can be chosen very precisely and non-commensurable with the frequency components of interest, the sampling results in a down-converted spectrum from which all spectral lines can be suitably retrieved, as shown in Fig. 3.1. Indeed, as the Shannon-Nyquist sampling theorem is not respected, the technique leverages on the fact that a measurement frequency grid should be defined upfront. As a consequence, LSNA measurements are limited to periodic excitations. However, a rather ingenious *de-scrambling* [154] of the down-converted frequency tones allows to place a large number of frequency bins (defined by the ADCs in use) on the RF spectrum, wherever it is allowed by the hardware limitations of the various blocks. Such complex functionalities must be eventually engineered through a relevant software layer. The set-up commercialized by NMDG [155], used in this work, allows performing measurements from 600 MHz to 50 GHz with a modulation bandwidth of up to around 20 MHz around each harmonic by means of  $2 \times 10^6$  frequency bins. Since the whole spectrum is acquired in a single take, the mutual phase relationships between the harmonics are maintained. A typical LSNA architecture for coaxial measurements is shown in Fig. 3.2. The incident and scattered waves are measured at the two ports through bidirectional couplers, whose coupled arms are directly connected to the under-sampling set. Then, attenuators regulate the input power such that the sampling hardware is not driven into nonlinear operation, while a variable gain block sets the proper power at the input of the digitizers. Under the hypothesis

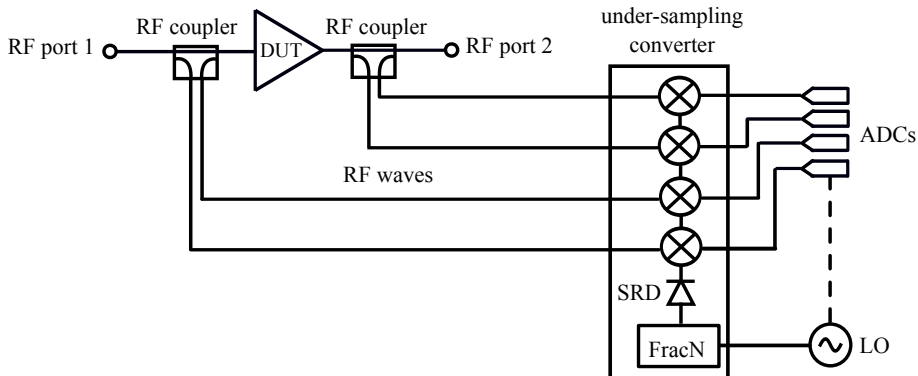


Figure 3.2: Block diagram of a sampler-based large-signal network analyzer (LSNA).

of linearity of the paths and of negligible electrical coupling between input and output, the calibration consists of identifying the following matrix:

$$\begin{bmatrix} a_{1D}^i \\ b_{1D}^i \\ a_{2D}^i \\ b_{2D}^i \end{bmatrix} = K^i \begin{bmatrix} 1 & \beta_1^i & 0 & 0 \\ \gamma_1^i & \delta_1^i & 0 & 0 \\ 0 & 0 & \alpha_2^i & \beta_2^i \\ 0 & 0 & \gamma_2^i & \delta_2^i \end{bmatrix} \begin{bmatrix} a_{1M}^i \\ b_{1M}^i \\ a_{2M}^i \\ b_{2M}^i \end{bmatrix} \quad (3.1)$$

where  $a$  and  $b$  are the incident and scattered waves, respectively, and  $K^i = |K^i|e^{j\phi_K^i}$  is complex. The subscript  $D$  indicates the device plane, the subscript  $M$  refers to the measurement plane, and  $i$  is the harmonic index of the selected measurement frequency grid. First of all, the seven coefficients  $\alpha_2$ ,  $\beta_{1,2}$ ,  $\gamma_{1,2}$  and  $\delta_{1,2}$  are determined through a standard relative calibration, e.g., SOLT. The complex coefficient  $K$  is identified through absolute power and phase calibrations. The power calibration allows characterizing the exact value of power flowing into the DUT and consists, in case of a coaxial set-up, of a power meter measurement at port 1 (Fig. 3.2) of the LSNA calibration plane. To perform the phase calibration, an additional calibration element, namely an harmonic phase reference (HPR), allows determining the frequency-dependent phase distortion of the set-up. Such a reference can be generated by a comb generator, a device which features a strong nonlinear characteristic capable to generate a very sharp pulse waveform with a high number of harmonics from a single-tone input excitation. It should be mentioned that the available frequency of excitation and its capability for harmonic generation are the major limitations to the definition of the measurement frequency grid. The LSNA phase calibration step consists of applying the comb generator output at port 1 (Fig. 3.2) of the calibration plane, while the RF source path is terminated

with  $50 \Omega$ . Such an excitation is measured at the receivers and compared with known phase relationships, so that a characterization of the frequency-dependent phase distortion introduced by the LSNA is obtained. In case of on-wafer measurements, it is not possible to apply the power sensor or the HPR, which both present coaxial connectors. Thus, the calibration plane is shifted to an auxiliary port through a SOL (Short-Open-Load) calibration. Due to the need of the HPR, the coefficients in (3.1) are only measured over an harmonic frequency grid. Although properly adapted over frequency, the coefficients are assumed to be constant over the measured modulation bandwidth (BW), as long as this is narrow with respect to the fundamental frequency. If this hypothesis is not applicable, further calibration should be applied over the modulation BW [156].

Considering that the measurements are performed through a wideband acquisition technique, the main limitation of the LSNA architecture is the dynamic range: this is typically  $\simeq 60$  dB, relative to the typical  $\simeq 100$  dB of a VNA, such as the HP8510. In fact, the dynamic range of the instrument is the lowest between the one of the sampling down-converter block and the one guaranteed by the digitizers: while the first depends on the conversion characteristics of the mixing, the second is mitigated as faster and larger-memory ADCs are introduced in the market. Moreover, the modulation bandwidth and the use of discrete frequency grids can also represent major limitations for some applications, such as in case of wideband telecommunication standards. However, the LSNA architecture still provides a basis for state-of-the-art measurement techniques and many works have demonstrated its specific capabilities also for pulsed, pulsed RF [157],[158], and optimal active load-pull [159] characterizations.

### 3.2.2 Low-frequency-extended large-signal network analyzer

Intermodulation products (IMs) generated by nonlinear devices excited by modulated signals spread out not only in the carrier frequency range, but at higher harmonics and at low frequencies, possibly close to dc [97]. These IMs should be suitably measured in order to reconstruct the distorted output waveforms. While harmonics are typically taken into account in commercial set-ups, low-frequency products fall often out of the measurable frequency band, while they are of primary importance to model transistors' nonlinear behavior and PA mismatches empirically. Moreover, as seen in Chapter 2, low-frequency measurements are necessary for characterizing the slow dynamics of the dispersive phenomena. Also at PA level, there is an increasing demand of calibrated large-signal measurements both at RF, to evaluate antenna mismatch and load modulation, as well as at LF, for supply-modulated

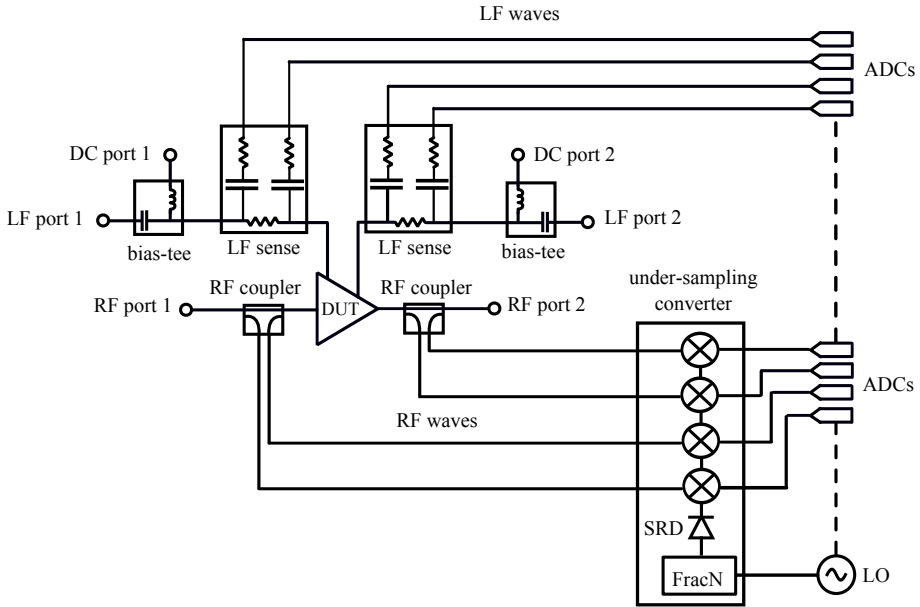


Figure 3.3: Low-frequency-extended LSNA (LF-LSNA).

PAs. Apart from a few tailored solutions [160],[161], all of them oriented to transistor characterization, no complete set-up was available for combined LF-RF measurements until the introduction, by NMDG, of a low-frequency-extended version of the RF LSNA. Such a system, also referred to as *dynamic bias* [162] consists of an LF part and an RF part combined in a unique measurement set-up, which is depicted in Fig. 3.3. The RF path is the same as in the RF LSNA architecture already depicted. The LF path consists of an LF implementation of the RF architecture. Coupler-like sensing boards are deployed to capture voltage and currents at LF. Such a sensing can be done either with transmission-line couplers or in a resistive way. LF couplers typically present low insertion loss, but their frequency range is often limited to tens of kHz. On the other hand, resistive sensing allows measuring down to dc, but choosing the resistor value may pose a compromise between the measurement accuracy and the introduction of impairments in the DUT performance. In the LF-LSNA set-up available at the KU Leuven laboratory and used for this work, resistive sensing is implemented. For a better measurement accuracy, the dc component is filtered out and separately measured by standard source/measurement units (SMUs). Otherwise, the presence of a large dc component would have limited the available dynamic range. The LF IV sampling can be done either with a dedicated oscilloscope or with ADCs. Suitable LF bias-tees enable the separation

between LF and dc terminations, allowing passive (or active, see section 3.5) impedance control at LF. The bandwidth of the LF test-set used in this work ranges from 10 kHz to 24 MHz, although the lower frequency limit can be easily diminished. The LF path can detect spectral components up to  $\pm 30$  V peak-peak and  $\pm 2$  A peak-peak, and can sense voltages and current down to  $20 \mu\text{V}$  and  $3 \mu\text{A}$ , respectively. DC voltages and current limits are  $\pm 60$  V and  $\pm 2$  A, respectively. The lower and upper frequency limits are set by the cut-off frequency of the LF bias-tees and the sampling frequency of the ADCs, respectively. It is worth mentioning that a straightforward extension of the frequency range could be done by employing faster ADCs and customized bias-tees. Depending on the DUT, the LF and RF paths to be measured may be physically separated or not. In the first case, which applies to PA or device fixture that typically include their own matching and bias networks, separate RF and LF receivers can be directly used. In other cases, such as for on-wafer transistors, only one electrical path provides both the LF and RF signals. Then, dc, LF and RF should be combined at the same reference plane, while they should be properly routed to different receivers. To this aim, standard RF bias-tees cannot be used, as their dc path normally filter out the low-frequency spectrum. Instead, one may use either customized bias-tees with a broadband dc path or diplexers with a sufficiently wide LF bandwidth also including the dc path, and with a large enough RF bandwidth. Commercial diplexers featuring an LF bandwidth from DC to 25 MHz and an RF bandwidth from 90 MHz up to 45 GHz have been used.

The calibration of the LF-LSNA in Fig. 3.3 consists of three steps: an RF calibration, an LF calibration, and an alignment procedure between the two [163]. The RF calibration, which includes a standard relative calibration, plus absolute power and phase calibrations, follows the steps described in section 3.2.1. The LF calibration is performed by following the same conceptual steps of the RF one. Instead of performing measurements through frequency sweeps, the availability of an arbitrary waveform generator (AWG) allows for the generation of a modulated excitation covering the whole calibration spectrum. This is useful especially if one wants to perform measurements on a uniform grid with narrow frequency step: the LF-LSNA implements a 10 kHz step, which means 2400 frequency points if reaching the receiver nominal maximum bandwidth of 24 MHz. A Schroeder multi-tone signal defined in frequency domain as:

$$X(f) = \sum_{n=1}^N X_N e^{j2\pi \frac{n(n-1)}{N}} \delta(f - n f_0) \quad (3.2)$$

can be applied to characterize the channel in one take, provided that the tone spacing is narrow enough to possibly allow interpolation. In fact, the signal in (3.2) is defined such that its PAPR is low, so that a linear operation can

be enforced despite the large number of injected tones. For the set-up in use this number is  $N = 2400$  with a fundamental frequency  $f_0 = 9.956$  kHz. Such a signal is used not only during the relative calibration (for which SOLT is implemented in this work), but also as amplitude and phase reference. In fact, this excitation should be characterized in advance and stored in a file as reference. In case of on-wafer measurements, also the LF calibration exploits a SOL procedure making use of an auxiliary port. Once both LF and RF calibration are performed, all coefficients are known besides an unknown delay  $\tau_{LF} - \tau_{RF}$ :

$$\begin{bmatrix} a_{1D,LF}^i \\ b_{1D,LF}^i \\ a_{2D,LF}^i \\ b_{2D,LF}^i \end{bmatrix} = |K_{LF}^i| e^{j\phi_{K,LF}^i} \begin{bmatrix} 1 & \beta_{1,LF}^i & 0 & 0 \\ \gamma_{1,LF}^i & \delta_{1,LF}^i & 0 & 0 \\ 0 & 0 & \alpha_{2,LF}^i & \beta_{2,LF}^i \\ 0 & 0 & \gamma_{2,LF}^i & \delta_{2,LF}^i \end{bmatrix} \begin{bmatrix} a_{1M,LF}^i \\ b_{1M,LF}^i \\ a_{2M,LF}^i \\ b_{2M,LF}^i \end{bmatrix} \quad (3.3)$$

$$\begin{bmatrix} a_{1D,RF}^i \\ b_{1D,RF}^i \\ a_{2D,RF}^i \\ b_{2D,RF}^i \end{bmatrix} = |K_{RF}^i| e^{j\phi_{K,RF}^i} \begin{bmatrix} 1 & \beta_{1,RF}^i & 0 & 0 \\ \gamma_{1,RF}^i & \delta_{1,RF}^i & 0 & 0 \\ 0 & 0 & \alpha_{2,RF}^i & \beta_{2,RF}^i \\ 0 & 0 & \gamma_{2,RF}^i & \delta_{2,RF}^i \end{bmatrix} \begin{bmatrix} a_{1M,RF}^i \\ b_{1M,RF}^i \\ a_{2M,RF}^i \\ b_{2M,RF}^i \end{bmatrix} \quad (3.4)$$

where  $\phi_{K,LF}^i = 2\pi i f_{0,LF} \tau_{LF} + \phi_{LF}^i$  and  $\phi_{K,RF}^i = 2\pi i f_{0,RF} \tau_{RF} + \phi_{RF}^i$ ;  $f_{0,LF}$  and  $f_{0,RF}$  are the fundamental frequencies of the LF and RF frequency grids, respectively. Indeed, the presence of such delays impairs the correct reconstruction of the waveform. The RF and LF calibrations can be aligned by exploiting the in-phase (I) baseband output and the modulated RF output of an electronic signal generator (ESG). The standard procedure for the LF-LSNA consists in setting the carrier frequency of the ESG to the fundamental of the RF frequency grid, while the modulation frequency is fixed to 100 kHz. First of all, the two outputs of the ESG are measured by triggering synchronously two LSNA receivers, so that the delay due to the ESG internal hardware and cables can be estimated. Indeed, it is assumed that such a delay is independent on the frequency. Consequently, the I output and the RF output are applied to LF port 1 and RF port 1, respectively, and captured synchronously by the receivers. The acquired waveforms are firstly corrected by applying the RF and LF calibration coefficients. Then, they are aligned to the ESG reference waveforms. Finally, their mutual delay is eliminated by also accounting for the delay of the ESG reference waveforms previously characterized. For the on-wafer set-up, the same procedure is implemented, although the RF and I excitation must be applied to port 2, while a thru is placed between port 1 and port 2 [163].

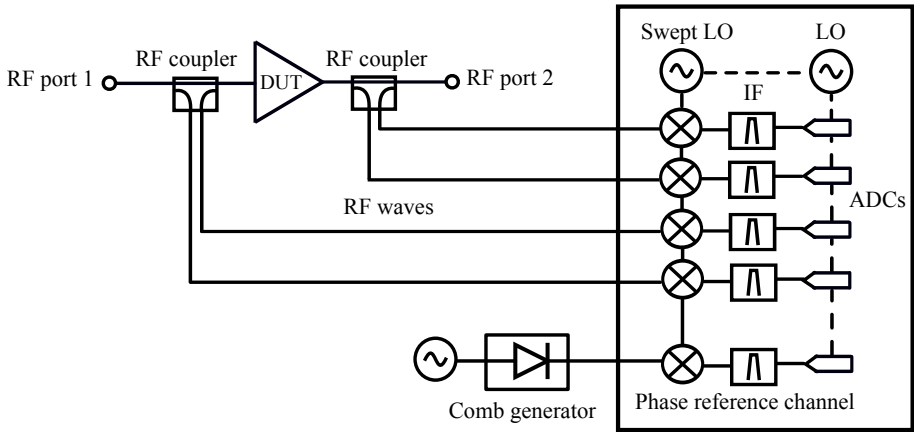


Figure 3.4: Block diagram of a mixer-based large-signal network analyzer, also known as nonlinear vector network analyzer (NVNA).

### 3.2.3 Mixer-based large-signal measurements

Another approach to large-signal measurement acquisition makes use of the heterodyne principle to down-convert the RF signals to an intermediate frequency (IF) spectrum, such as in classical VNAs. Indeed, the instruments implementing this method, such as the Keysight PNA-X [164], are denominated nonlinear network vector analyzers (NVNAs) [148]. Unlike in sampler-based instruments such as LSNAs, NVNAs down-convert and acquire one frequency component at a time. As a consequence, they must be correctly stitched together in order to obtain the spectrum, with particular care to the mutual phase relationships among the spectral lines. The functional blocks of an NVNA are reported in Fig. 3.4. The DUT can be excited at both ports and a classical RF test-set composed by source and directional couplers is included. The down-conversion process is performed by mixers (one per channel), all driven by the same local oscillator (LO). When sweeping the frequency to span the spectrum of interest, the LO phase will change by an unknown quantity. As long as the LO phase is not known, the phase relationships among the spectral lines of the signal to be measured are unknown, and the waveforms cannot be retrieved. Indeed, the phases acquired depend on the unknown phase of the LO. To obtain the correct phase values, an HPR is used. Considering that the mutual phase relationships of the harmonics are static, the HPR response, acquired by means of a separate channel (Fig. 3.4), can be used to retrieve the correct measured phases. It should be noted that the HPR is fundamental for the operation of NVNAs, while it is not for the operation of LSNAs (even though, it is still

needed for the calibration). Despite this difference, the calibration procedure of NVNAs is very similar to the one described in section 3.2.1 for LSNAs. Indeed, the measurable frequency grid depends on the reference signal generated by the HPR: in general, such a grid is regular (as it must refer to an harmonic reference), and the frequency step is set by the HPR CW excitation. In [164], for example, the HPR can be excited with a frequency down to 625 kHz to measure up to 67 GHz. Clearly, the smaller is the frequency of excitation, the lower will be the power of the spectral lines at high frequencies, which increases the uncertainty of the phase calibration. Such type of grid can be limiting for measuring modulated signals, as narrow frequency spacings at high frequencies cannot be calibrated on frequency spacings narrower than the HPR fundamental excitation. On the other hand, narrow path acquisitions allow a dynamic range of  $\sim 100$ -120 dB, much higher than the one of LSNA. However, it should be mentioned that NVNA measurements are not limited to narrow acquisition: for example, the presence of wideband receiver path also allows for pulsed-RF measurements [165], as will be described in section 3.3.2.

### 3.3 Custom set-ups for supply-modulated PAs

#### 3.3.1 Combined LF-RF pulsed set-up based on the PNA-X

As seen in section 3.2.3, the PNA-X [164] is a modular commercial instrument from Keysight Technologies based on a classical VNA architecture, but it can be equipped with an active comb generator as HPR which, together with tailored software applications, allows performing nonlinear vector network analysis with a mixer-based approach. One of its commercial versions (N5247A), available at KU Leuven, provides two-port large-signal network analysis up to 67 GHz and performs measurements on the frequency grid set by the HPR fundamental excitation, which is typically the LO at 10 MHz. Indeed, performing modulated signal measurements on such a grid is rather limiting, especially if the objective is to characterize the PA for telecommunication applications. Thus, other measurement modes are provided by the manufacturer as optional features to be independently activated; in addition to the blocks depicted in section 3.2.3, the system additional options may enable internal hardware and alternative acquisition capabilities. In the instrument used during this work, a set of four internal pulse generators, the pulse measurements capabilities, two modulators (options 008, 021, 022) and the option (514) for the automatic measurement of  $X$ -parameters (introduced in 1.4.4) are enabled. Such features make the PNA-X a viable instrument for characterization of PA memory effects. In effect, pulsed

RF excitation can be used as a suitable identification signal for nonlinear and dynamic behavioral models [117],[126].

To acquire pulsed RF signals, the PNA-X measures either through a narrowband or a wideband acquisition path, depending on the waveform to be acquired. While the narrowband mode is the typical one used for VNA-like measurements, the wideband acquisition mode allows for removing the hardware IF filters so that the bandwidth capabilities of the digitizers, which feature 100 MS/s of sampling rate [166], can be exploited. As in standard CW measurements, the mixers downconvert the waves from RF to IF. Then, with narrowband acquisition mode, the IF spectra are bandpass-filtered (both in hardware and software) and acquired by precisely selecting the frequency. In case of pulsed excitations, this means that only the first lobe of the pulse spectrum can be acquired, while the other lobes must be rejected to avoid an incomplete acquisition. To do this properly, spectral nulling techniques, in which the zeros of the filter transfer function are aligned with the spectral lobes, are implemented. Instead, in the case of wideband detection mode, the full pulse spectrum falls within the bandwidth of the digitizers. Receiver gating allows performing the acquisition only when the pulse excitation is on. Three pulse measurement modes are allowed: *average pulse measurement*, *point-in-pulse*, and *pulse profiling* [167]. Average pulse measurements make no attempt to position the trace point at a specific point within the pulse, and the displayed wave represents the average value of the pulse. Such a measurement is obtained through narrowband detection without any receiver gating. Point-in-pulse, instead, results from taking data only during a user-defined acquisition window within the pulse and it must be triggered by receiver gating. In wideband detection mode, such a window can be selected by setting the data sampling period, while in narrowband detection mode, the gating should be set with a hardware switch. An arbitrary delay can be set so that the acquisition window can be positioned within the pulse to be measured. Pulse profiling measurements allow to reconstruct the pulse amplitude and phase in time domain. The data is acquired at uniformly spaced time positions across the pulse. This is achieved by capturing a set of point-in-pulse measurements obtained by varying the delay of the measurement with respect to the pulse. While average pulse or point-in-pulse are useful for isothermal characterizations, pulse profiling enables the evaluation of time-domain responses.

The choice between either using narrow or wideband detection modes is dictated by the bandwidth of the pulse signal to be measured: if it is too wide with respect to the digitizer capabilities, then narrowband with spectral nulling techniques is used. The advantage of narrowband detection is that there is no lower pulse-width limit. The disadvantage, however, is that the measurement dynamic range is a function of duty cycle: as the duty cycle of the pulses

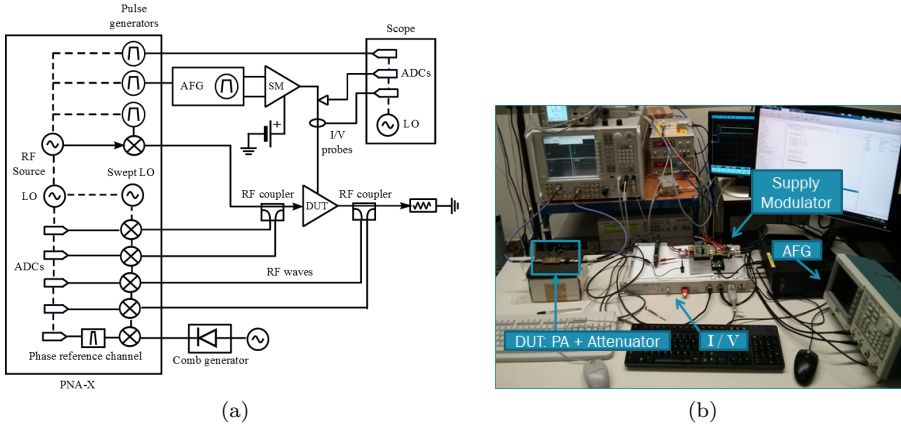


Figure 3.5: Set-up based on the PNA-X for the pulsed RF and pulsed supply characterization of PAs. (a) Block diagram. (b) Photo of the set-up.

becomes smaller, the power of the central spectral component becomes smaller, resulting in less signal-to-noise ratio. For the available PNA-X, equipped with the latest DSP version 5, the minimum acquisition window is 200 ns, while the minimum pulse widths measurable in wideband detection mode depend on the IF bandwidth and can be found in [166]. For pulse widths in the  $\mu\text{s}$  range, wideband acquisition mode with custom digital filters for noise reduction is automatically set by the PNA-X firmware, as the user cannot directly choose the detection mode from the software application. The RF calibration of the PNA-X is performed by following the typical steps depicted in section 3.2.3; if performing pulse acquisition, the pulse excitation should be activated upfront, so that internal switches in the calibration path are properly set.

The described configuration of the PNA-X has been used as the main instrument of a more complete set-up for the characterization of supply-modulated PAs. In particular, instruments and hardware have been added so that supply modulation and IV acquisition at the supply terminal of a PA could be performed. The block diagram of such a set-up is shown in Fig. 3.5. The RF path makes use of the already described PNA-X features in terms of large-signal acquisition and pulse excitation and measurement. To accommodate the necessary DUT power levels, two external bidirectional couplers may be employed. The signals of the four internal pulse generators, can be either brought externally at 3.3 V from the PNA-X rear-panel with a specific interface (Keysight N1966A Pulse I/O Adapter), or redirected internally to modulate the internal sources and generate the pulsed RF excitation. To acquire the dynamic voltage and current at the supply node of the PA, commercial high-impedance and current probes have

been used, respectively. The current probe (Keysight N2893A [168]) features up to 50 MHz bandwidth for up to 15 A of current, and it is based on a transformer sensor (for the ac components) combined with an Hall effect sensor (down to dc). Both voltage and current signals are acquired with a commercial equivalent-time oscilloscope [169]. No low-frequency calibration such as in section 3.2.2 has been implemented at the moment of writing. The attenuation due to the LF cables has been considered negligible at the baseband frequencies, while the time alignment of the waveforms has been done manually, by referring the pulse excitations at LF and RF to a third pulsed waveform, generated by one of the four pulsed sources internal to the PNA-X. Pulsed RF, defined as a pulse modulating a CW RF, is a key type of excitation for RF PAs: first of all, it allows iso-thermal PA measurements, which is sometime necessary for some PAs which cannot thermally handle a CW operation up to the maximum of RF output power. Moreover, a pulsed RF input stimulates the time response of the RF output power, which carries the signature of the presence of dynamic effects: indeed, the electrical transient response depends on the rise and fall times of the pulses, while the thermal state and dynamics also depend on the duty cycle of the pulsed waveform. Two types of preliminary pulsed characterization have been performed with the presented set-up, and they are subjects of the following sections. The first consists of pulsed RF measurements and an  $X$ -parameters extraction under pulsed RF conditions; the second is a PA characterization under pulsed excitations at both the RF input and at the supply terminal.

### 3.3.2 Pulsed-RF PA characterization

By means of the pulse capabilities of the PNA-X, a pulsed RF characterization of an hand-set PA in GaAs HBT technology from RFMD (RFPA3809), operating at the fundamental frequency of 2.15 GHz with a saturated output power of 30 dBm and 12 dB gain, has been performed. The response of the DUT at various acquisition delays has been measured by means of the point-in-pulse mode. Then, slope differences between the measurements have been compared. Such differences, if present, are indicators of non-instantaneous step response, and thus, the presence of memory effects. As already mentioned in section 1.4.4, by evaluating the time-responses in relation to the pulsed input power, one may create a set of identification measurements to obtain a behavioral model capable of describing nonlinear memory effects at the harmonics. However, such an objective has not been pursued in this case. The measurements of the first three output harmonics acquired under pulsed RF excitation with various acquisition delays are reported in Fig. 3.6 [170], showing measurable discrepancies due to memory effects. The fundamental harmonic shows a first order-like system behavior, as it reaches the steady state with negligible ripples, especially in

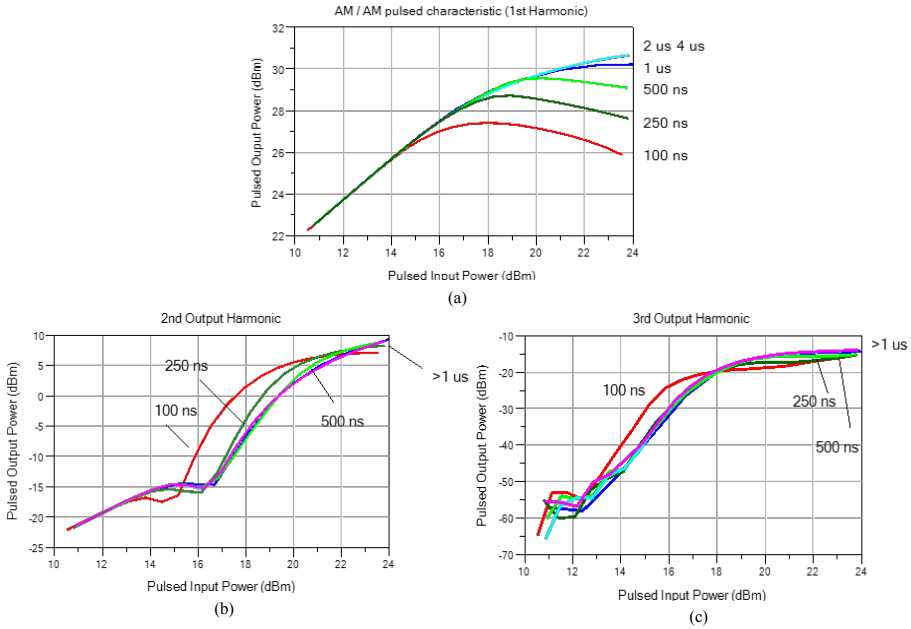


Figure 3.6: Pulsed CW characterization of a handset PA by means of the point-in-pulse PNA-X measurement capability. The acquisition delay is reported on the plots. (a) first harmonic, (b) second harmonic and (c) third harmonic.

full saturation. For this device, the steady-state at maximum output power is reached with a few  $\mu\text{s}$  delay. Another behavior can be noted for the second and third harmonics: in particular, the slope obtained at 100 ns delay shows meaningful differences also at lower output powers (for example, the “sweet spot” measured at the second harmonic shifts as the delay increases). In second place, an  $X$ -parameters characterization has been performed.  $X$ -parameters, whose formulation has already been introduced in section 1.4.4, provide a straightforward framework to characterize devices under nonlinear operation and represent a formal superset of  $S$ -parameters. The availability of a tailored PNA-X option allows automatic acquisition of  $X$ -parameters, given that the RF input power level and the number of harmonics to be accounted for are inserted by the user. However, as from their formulation,  $X$ -parameters are measured under CW excitations around multiple large-signal operating points (see [124] for the identification procedure) and represent a quasi-static model. For this work, instead, the  $X$ -parameters characterization framework has been applied under pulsed CW with different acquisition delays. Then the results have been compared with  $X$ -parameters measured using CW excitations [170] in order to

assess the limitation of the  $X$ -parameters description of this PA. In Fig. 3.7, examples of  $X$ -parameters measured under CW and pulsed CW conditions are reported for a pulse width of  $5 \mu\text{s}$  and a pulse period of  $50 \mu\text{s}$ . Since the pulse profiling mode is not compatible with the  $X$ -parameters measurements mode, this characterization has been performed by manually changing the acquisition delay. As expected, when the acquisition delay increases, the slopes of the  $X^{(S)}$  and  $X^{(T)}$  terms of (1.15) resemble the same quasi-static  $X^{(S)}$  and  $X^{(T)}$  terms. However, the parameters at different delays do not show a uniform convergence to the static behavior, presenting ripples versus time and power; e.g., parameter  $S_{11,11}$  (Fig. 3.7(a)), when measured with  $100 \text{ ns}$  delay, shows higher values with respect to the static measurement. At the same time, when it is measured with  $2 \mu\text{s}$  delay,  $S_{11,11}$  shows values smaller than the static case. For other parameters, the presence of local minima and their position versus input power can only be noticed under pulsed excitation, while static curves do not reveal such behavior. In conclusion, it is clear that a characterization limited to the quasi-static case might lead to errors in predictions of the fundamental output power and its harmonics under dynamic conditions.

### 3.3.3 Combined pulsed-RF and pulsed supply measurements

While the RF pulsed excitation is directly provided by means of the PNA-X internal hardware, the low-frequency excitation at the supply terminal port of the PA must be provided by external blocks, as shown in Fig. 3.5. A first preliminary attempt to provide a pulsed supply was made by using the pulsing functionalities of the E5270 dc SMU from Keysight Technologies. This dc supply can be easily triggered with one of the internal pulse generators of the PNA-X. However, such kind of instrument provides rather slow rise and fall times ( $\sim 30 \mu\text{s}$ ), thus they are not suitable for transient characterizations. Instead, a supply modulator (SM) capable of providing the needed slew rate as well as showing rather small output impedance has been used. Such a device, a preliminary product from Texas Instruments [171], is based on a hybrid topology consisting of a linear amplifier and a dc/dc switching converter, such as introduced in section 1.3.3. This SM can operate either in average power tracking (APT) or ET mode. In ET mode, when driven by a differential signal at the input, the SM provides a dynamic output voltage as modulated supply for the RF PA, up to several MHz of bandwidth (the linear amplifier features  $\sim 75 \text{ MHz}$  of small-signal bandwidth). In order to provide the differential input, a commercial AWG [172] is used. Although any waveform can be generated, in this work the objective was to provide pulsed excitation with various periods and duty cycles, so that a pulsed supply excitation with fast rise/fall times could be delivered to the PA supply terminal. The AWG can be configured so that it is triggered by

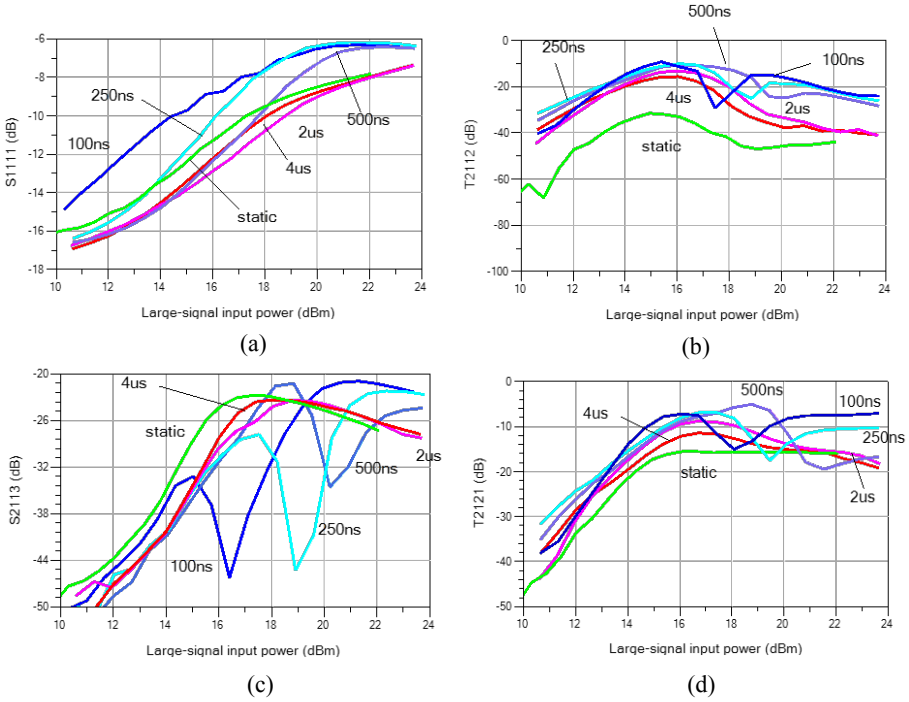


Figure 3.7:  $X$ -parameters acquired under pulsed CW conditions (the acquisition delays are reported in the Figures). As from (1.15), for a generic parameter  $X_{ynxm}^{(S)}$ ,  $x$  and  $y$  stand, respectively, for the input and the output port;  $m$  and  $n$  stand for the harmonic frequency of, respectively, the incident and the scattered waves.

one of the internal pulse generators of the PNA-X, which feature  $\sim 30$  ns of rise/fall times. With such configuration, both the RF and the supply pulsed waveforms can be defined by programming the pulse application on the PNA-X. To do this in an automatic way, suitable remote control software in MATLAB has been developed.

Such an automated measurement set-up has been tested on a handset PA based on an HBT in GaAs technology from Eudyna Devices, which, biased at  $I_{D0} \sim 20$  mA,  $V_{D0} \sim 3.8$  V, features  $\sim 15$  dB of gain at  $f_0 = 0.95$  GHz. The objective of the characterization was to capture the output power and drain current transient responses due to pulsed RF and pulsed supply excitations. In order to detect the RF output transient, the pulse profiling acquisition mode of the PNA-X has been used. First, a characterization under constant dc supply and

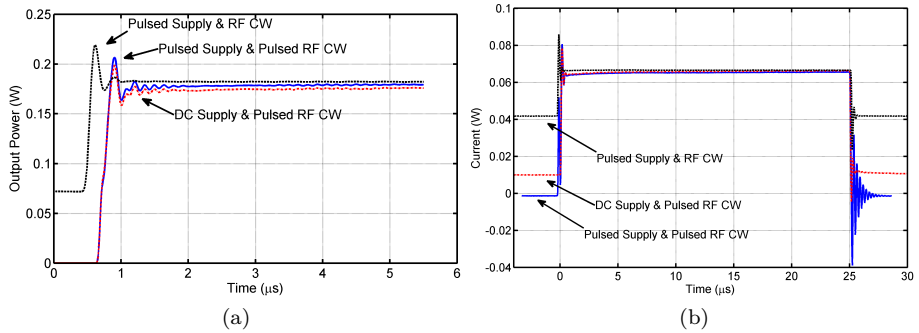


Figure 3.8: Comparison of the transients due to pulsed supply and pulsed RF excitations ( $T=100 \mu\text{s}$ , duty cycle=25%). (a) RF output power. (b) Drain current.

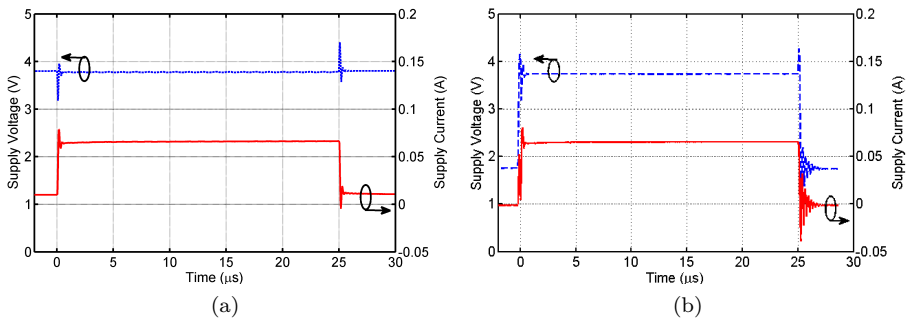


Figure 3.9: Supply-drain terminal  $I/V$  waveforms acquisition under pulsed conditions ( $T=100 \mu\text{s}$ , duty cycle=20%). (a) Constant dc supply and pulsed RF excitation. (b) Both supply and RF pulsed.

pulsed RF excitation with various RF input amplitudes, pulse periods and duty cycles has been performed. Then, the same pulsed RF input excitations have been applied in presence of a synchronized pulsed dc supply. Finally, pulsed dc supply waveforms have been applied while the RF input was excited by an RF CW. The idea behind these tests was to identify the dependency of the output transients with respect to the two ports. An example of such comparison is shown in Fig. 3.8, while the IV pulsed waveforms at the drain-supply terminal are shown in Fig. 3.9. In order to make comparable acquisition, the dc supply has been pulsed from  $\sim 2.2$  V to the biasing condition  $V_{D0} \sim 3.8$  V. The period of the pulsed excitation has been swept from  $20 \mu\text{s}$  to  $100 \mu\text{s}$  and the duty

cycle from 10% to 25%. As can be seen from the Figures, no major differences are measured among the transient responses for this PA. In order to have an increased time resolution, the pulse profiling acquisition delay has been set to 10 ns, with an acquisition window of 200 ns. Such parameters determine a rather long measurement time (several dozens of minutes per RF power point, depending on the waveform period) which makes such detection technique rather not practical for the high-resolution acquisition of longer transient responses.

### 3.3.4 ET set-up based on the VST

Another measurement set-up for supply-modulated PAs has been developed around the Vector Signal Transceiver (VST) from National Instruments [173]. Such an instrument consists of RF generation and acquisition channels with 80 MHz of modulation bandwidth and a field-programmable gate array (FPGA): it is configured such that it combines the functionalities of a vector signal generator (VSG) and a vector signal analyzer (VSA) with real-time signal processing, which allows the user to define, via software, the instrument capability. Moreover, the version in [173] features two baseband 16-bit digitizers with 40 MHz of bandwidth. These two channels, in the commercialized solution, can only be used to inject or output the in-phase and quadrature modulation of the RF signal. Instead, for the set-up presented in this section, the baseband channels hardware control has been customized in order to generate dynamic signals and acquire the voltage and current waveforms. In particular, the baseband output channel, capable to generate ac voltage up to 0.5 V peak-peak on a 50  $\Omega$  load in single-ended configuration and a dc voltage between -1 V and +1 V, is used to feed a supply modulator of an envelope-tracking system. The baseband acquisition channels, which are dc-coupled and can acquire up to 2 V peak-peak signals, are used to measure the dynamic supply voltage applied to the PA and the dynamic drain current flowing from the supply modulator. Both baseband generation and acquisition sample rates are fixed to the internal VST sample clock (120 MS/s). The block diagram of the developed set-up is represented in Fig. 3.10. The VST is installed in an NI PXIe-1082 chassis, which supplies an internally generated 10 MHz clock with an independent buffer on the backplane, used to synchronize any other external modules. An NI standard dc supply was also installed on the same chassis.

In order to acquire dynamic voltage and current at the drain-supply terminal, a resistive sensing board has been designed, following the approach used for the LF-LSNA in section 3.2.2. With respect to that solution, however, here both dc and ac components are not separated, but sampled together. To limit the swing at the channels, a voltage divider which applies a 1/21 ratio on the measured voltages, is obtained by placing a 1 k $\Omega$  resistor on each node. Indeed,

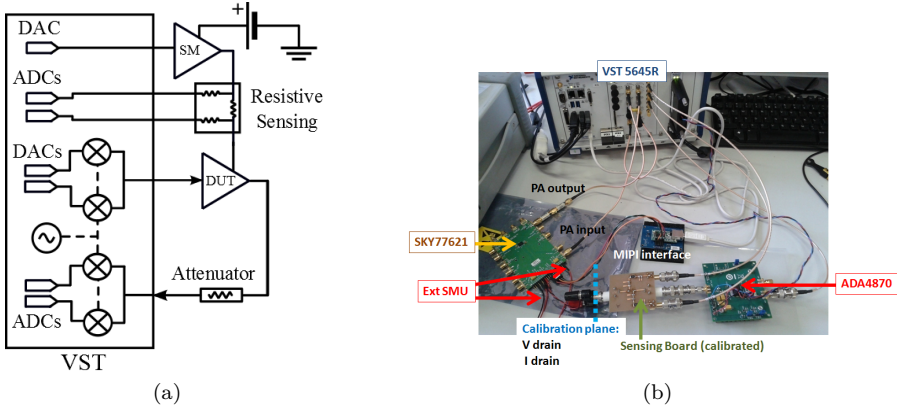


Figure 3.10: VST-based envelope-tracking set-up with IV baseband sensing. (a) Block diagram. (b) Picture of the set-up.

the presence of both dc and ac components possibly leads to reduced dynamic range in the measurement, especially in case of small variations around a large dc component, as mentioned in section 3.2.2. However, 36 different amplitude acquisition ranges from 32 mV to 2 V peak-peak can be configured to optimize the dynamic range: if, for example, setting the 0.4 V peak-peak input range, the maximum measurable voltage at the drain-supply terminal, accounting for the sensing ratio, is 10 V peak-peak with a resolution of 3.4 mV. Thus, such values can be considered acceptable to characterize handset PAs for mobile applications [174]. As they were not thought for such a purpose, the baseband acquisition channels of the VST are not calibrated by the manufacturer. Moreover, due to the fact that the sensing board is home-made, while it must work up to 40 MHz, a calibration of the baseband path was found necessary. Such a calibration follows the LF approach in 3.2.2, thus will not be described again. However, it should be mentioned that the VST baseband input channels show an intrinsic dc offset, which is not compensated by the calibration [174]. Such an offset has been characterized for various voltages and for each input range; then, it is compensated by referring to voltmeter measurements. The voltage drop on the sensing resistor is taken into account by acquiring two additional dc measurements and suitably compensated. With respect to the RF path, the VST channels are supposed terminated with an ideal  $50 \Omega$ . As only one acquisition channel is available, it is not possible to perform a two-port network analysis. Instead the cable attenuation and distortion should be accounted for separately, and RF input and output signals should be suitably aligned by, for example, a correlation analysis.

Unfortunately, such a set-up could not be yet used for the retrieval of meaningful

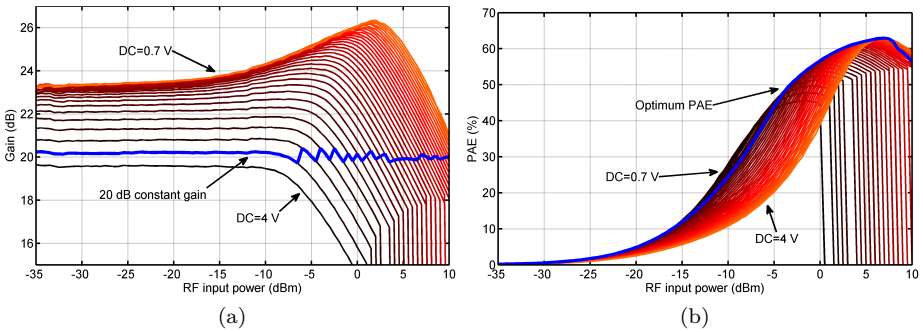


Figure 3.11: Shaping table extraction performed with the set-up in Fig. 3.10. (a) Constant gain (20 dB) shaping table. (b) Optimum PAE shaping table.

characterization and modeling work at the time of writing. However, much effort has been invested in the design of software applications aimed to exploit the hardware capabilities. Specifically, a shaping table extraction software and a characterization bench for the PA-SM system have been developed. More in detail, such software performs nested sweeps of coherent RF and LF measurements for which a CW on the RF input and constant voltage on the PA supply terminal are applied. Then, the user can automatically extract and save constant gain or optimum PAE shaping tables. The characterization bench application allows driving the PA and the SM with CW modulated, or other, user-defined, identification signals, as well as voltage, power, and modulation frequency sweeps. Furthermore, a reference application for envelope-tracking and DPD operation, native from National Instruments, has been updated and tailored to the custom hardware configuration. This software [174] allows the user to operate the PA under ET and visualize RF input/output waveforms, supply voltage/current waveforms, as well as the instantaneous PAE. The AM-AM/AM-PM characteristics, the normalized mean square error (NMSE), and the adjacent channel power ratio (ACPR) can be evaluated. The RF and baseband paths reciprocal delay is estimated and compensated by minimizing the standard deviation of the AM-PM characteristics.

A preliminary characterization has been carried out on a multi-mode and multi-band handset PA from Skyworks and a SM evaluation board from Analog Devices, under ET operation. This specific PA design was not tailored for ET operation, but the drain capacitors have been removed in order to support supply modulation. The SM features high slew rate and bandwidth, making it a good choice to deliver a dynamic voltage and test the PA under ET operation, although its efficiency is rather low. Two shaping tables have been extracted

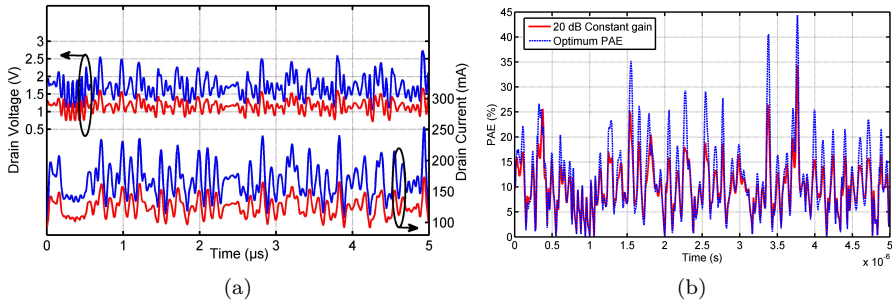


Figure 3.12: Comparison between the 20 dB constant gain (red) and the optimum PAE (blue) shaping tables under ET operation and with 20 MHz LTE signal RF excitation. (a) Voltages and currents measured at the PA supply node. (b) Measured instantaneous PAE.

with the software described above: a 20 dB constant gain shaping table (Fig. 3.11 (a)) and shaping table for optimal PAE (Fig.3.11(b)). A characterization under a 20 MHz LTE as RF input signal has been performed: in Fig. 3.12(a) the waveform measured at the supply node by applying the two different shaping tables is reported. In Fig. 3.12(b), the instantaneous PAE is shown. With the 20 dB gain shaping table, the measured average PAE was 10%, while it was 11.4% if applying the optimum PAE shaping table. Indeed, the PAE characteristics in Fig. 3.11(b) show a very limited dependency with respect to the supply voltage, resulting in less than a 10 % instantaneous PAE variation. In other words, this specific PA does not seem to deliver a consistent improvement if driven under envelope-tracking operation.

## 3.4 Characterization methods at the drain-supply terminal

### 3.4.1 Set-up requirements for supply-modulated PAs

In order to characterize supply-modulated PAs, the measurement set-up should feature a number of functionalities, which will be briefly described in this section. First of all, the principal functionality is the possibility to acquire in a coherent way the incident and scattered waves at the RF input and output. In particular, absolute amplitude and phase are necessary in order to properly reproduce the model distortions. Moreover, such kind of measurements has

to be carried out not only at the RF ports, but also at the supply port in a synchronous way. As third aspect, measurements have to be done over a modulation bandwidth around both the RF carrier and dc. As already discussed in section 3.3, the LF acquisition involves the use of either a low-frequency coupler or other means of voltage and current sensing. While high-impedance voltage probing does not involve critical issues, it is often problematic to obtain a continuous current acquisition bandwidth ranging from dc to several tens of MHz. If using a low-frequency coupler, the minimum measurable frequency is often limited to several tens of kHz. This implies a recombination between dc and ac current components must be achieved in post-processing. In addition, if part of the kHz-range bandwidth is not acquired, such a configuration does not allow to sense the current generated under application-like operation such as envelope-tracking, in which most of the spectral components of the supply signals are concentrated in a few hundreds of Hz near dc. This inconvenience could be avoided by using a resistive sensing, as done in section 3.3.4. However, this inevitably causes a voltage drop on the supply path. On the other hand, if using a small sensing resistor to minimize the voltage drop, the resolution of the acquisition channel must be proportionally higher. Moreover, if performing a differential measurement, it may be problematic to obtain a high rejection of the common mode at the MHz frequencies.

Nevertheless, whatever the chosen approach, a calibration of the RF and baseband paths should be applied. While RF calibration is often a built-in procedure, the LF calibration is a critical step not only to handle the various non-idealities of the sensing as well as of the acquisition channels in the MHz range, but also to ensure time-alignment between the two paths. Finally, proper excitations should be available at both ports. At RF, one may consider a vector signal generator (ESG) capable of synthesizing modulated signals in the RF bandwidth of interest. As alternative, a baseband arbitrary waveform generator combined with an up-converting mixer is also an option. At the supply node, the set-up should include the possibility of a dynamic voltage generation in the amplitude range requested by the PA, and up to several MHz. Different approaches can be followed, also depending on how the current sensing is done. The most general one consists in using a dc-coupled arbitrary waveform generator (usually terminated in  $50\ \Omega$ ) together with a voltage buffer featuring a low output impedance. This typically ensures maximal flexibility in the voltage waveform synthesis, as well as the possibility to generate continuously down to dc. Alternatively, one may use a wideband power amplifier in the MHz range. However, such a PA would usually be terminated in  $50\ \Omega$ , possibly necessitating more power to impose a voltage in case of a low-resistive load. Moreover, PAs typically do not work down to dc, thus a bias-tee for combining the dc component of the voltage and the output of the amplifier is required. Although a few approaches are published in literature [174]-[176], it is worth

mentioning that no commercial set-up is available for performing full three-port supply-modulated PA measurements for telecommunications applications. The characterization shown in the following either makes use of the LF-LSNA of section 3.2.2 (despite its frequency limitations) or the custom set-up presented in section 3.3.4.

### 3.4.2 PA drain port nonlinear impedance-like function ( $Z_{PA}$ )

In linear PA configurations, the power supply usually must deliver power at dc only. Thus, at the node between the PA drain terminal and the supply, the dc voltage is ideally imposed by the supply, while the PA acts as an ideal current source. Indeed, this configuration only happens if the output impedance of the supply is zero, so that no voltage ripple is generated whatever is the amount of drained current. A very low supply output impedance at dc is typically reached within the supply through active circuits and multiple electrical feedbacks. Such an architecture, however may generate higher output impedance at higher frequencies. Thus, frequency chocking at higher frequencies is provided by bias networks (e.g., by means of large capacitances) to be included in the PA design. Conversely, the PA typically shows very high impedance (such as an ideal current generator) as long as the transistor (e.g., a FET) is driven into the saturation region (i.e., the current characteristic does not depend on the drain voltage).

This configuration dramatically changes in case of supply modulation. Indeed, one cannot rely on classical drain bias networks, as they would prevent any dynamic voltage. As a consequence, the frequency chocking must be determined by the supply modulator, which, in other words, ideally should show a very low output impedance ( $Z_{SM}$ ) in the whole range of operation, up to tens of MHz. As already mentioned in section 1.3.3, this is a tough requirement if SM efficiency is a constraint. On the other hand, if large voltage modulation is applied, the PA may be driven such as the transistor operates in its linear region, meaning that the output signal becomes a function of the supply voltage [85]. This also implies that the impedance of the PA at the drain terminal ( $Z_{PA}$ , as depicted in the diagram in Fig. 3.13) may sensibly become smaller under PA large-signal operation, determining a load modulation effect for the SM. It is clear that the value of  $Z_{PA}$  determines the current drained by the PA: as a consequence, its characterization is necessary to estimate the dynamic power consumption and the PAE of a supply-modulated PA. However, it should be noted that  $Z_{SM}$  and  $Z_{PA}$  quantities are dependent not only on frequency, but also on the dynamic drain voltage  $v(t)$  and current  $i(t)$ , and on the large-signal excitation of the PA at RF. More precisely, these quantities should be referred to as impedance-like functions which are nonlinearly and dynamically dependent on the large-signal

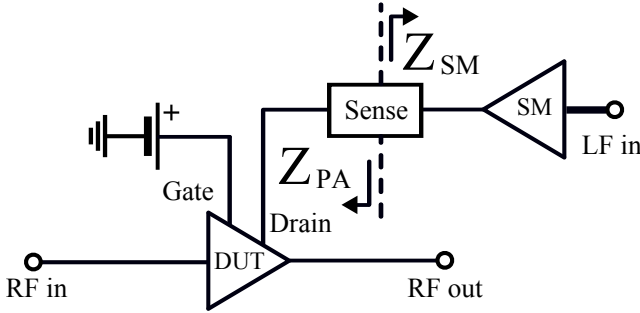


Figure 3.13: Diagram for the definition of impedance-like quantities  $Z_{PA}$  and  $Z_{SM}$ .

operating point [151]. A formal derivation for such functions will be presented in Chapter 4. For the characterization shown in this section, instead, they could be considered as simple frequency-defined quantities dependent on the large-signal operating point (LSOP).

Let us consider the RF input and output power waves  $\mathcal{A}_1$  and  $\mathcal{B}_2$  of the PA. They can be formulated through a classic baseband envelope-equivalent notation as follows:

$$\begin{aligned} \mathcal{A}_1(t) &= \Re\{a_1(t)e^{j2\pi f_0 t}\}; \\ \mathcal{B}_2(t) &= \Re\{b_2(t)e^{j2\pi f_0 t}\}; \end{aligned} \tag{3.5}$$

where  $a_1(t)$  and  $b_2(t)$  are complex envelopes. Throughout this work, the RF input and output ports will be assumed as ideally matched to the source and load impedances, respectively, so that  $\mathcal{A}_2(t) = 0$  and  $\mathcal{B}_1(t) = 0$ . In case the LSOP is set by just the bias and by a CW RF excitation at port 1, the input envelope reduces to a constant  $a_1(t) = A_1$ , and the PA and SM impedance-like functions can be written as  $Z_{PA}[V_{D0}, A_1, f]$  and  $Z_{SM}[V_0^S, I_{D0}, f]$ , where  $V_{D0}$  and  $I_{D0}$  are the PA quiescent (dc) voltage and current, respectively, and  $V_0^S$  is a constant voltage applied at the input of the SM. At the beginning of this research, no supply modulator was available. Instead of using a SM, the supply modulation is generated by means of an LF source [172] coupled with a standard dc supply and combined with a bias-tee. Thus, the attention has been focused on the characterization of the  $Z_{PA}$ . The extraction of  $Z_{SM}$  is, instead the subject of section 3.4.4. Once the PA is driven into a LSOP set by  $V_{D0}$  and  $A_1$ , a straightforward way to measure  $Z_{PA}$  over frequency is to apply, through the LF source, a small signal sinusoidal excitation to the drain terminal. The LF-LSNA allows to measure incident and reflected waves at

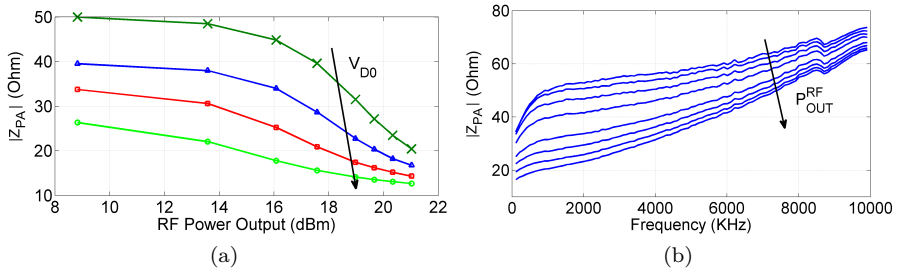


Figure 3.14: Characterization of  $Z_{PA}$  for a GaAs-based handset-PA, with  $f_0 = 0.95$  GHz. (a)  $Z_{PA}$  at  $f_{LF}=1$  MHz.  $V_{D0}=4.5$  V (crosses), 4 V (triangles), 3.5 V (squares) 3 V (circles). (b)  $Z_{PA}$  at  $V_{D0}=4.5$  V, RF  $P_{out}=9 \div 24$  dBm.

both RF and LF outputs. In other words, it permits to acquire LF waves (or currents and voltages) under operating large-signal conditions. By sweeping the frequency as well as the LSOP (i.e., sweeping  $V_{D0}$  and  $a_1(t)$ ), one samples  $Z_{PA}$  over the conditions of interest, and a simple LUT model can be built. In Fig. 3.14, the experimental evaluation (up to 10 MHz) of  $Z_{PA}$  for a handset-PA [177] based on HBT technology is provided. The  $Z_{PA}$  dramatically reduces as the RF input power increases, since the waveforms hit the nonlinearities of the output characteristic of the transistor (Fig. 3.14(a)). Indeed,  $Z_{PA}$  is proportional to the dc bias  $V_{D0}$ , as stronger nonlinearity will appear at lower supply voltage. With respect to the frequency dependence, instead, it is not straightforward to interpret the trend shown in Fig. 3.14(b). On one hand, one may surely expect to characterize the output capacitance of the transistor. However, in this particular case, a full PA not tailored for ET (thus, including bias and matching networks) has been measured: the obtained characterization is thus the combination of its reactive effects at low-frequency. A preliminary validation of the characterization presented here is shown in [150], where it allowed to predict the modulated current generated in presence of a simple four-tone excitation injected by the LF source. Moreover, as the LF-LSNA coherently provides measurements at LF and RF, this characterization technique has been found useful to evaluate the up-converted products generated at RF at port 2. Indeed, when exciting the LF drain terminal, one drives the PA in a "mixer-like" operation. In some preliminary published results [150], it has been shown that the frequency-dependency of the up-conversion mechanism can be suitably predicted with this measurement technique, eventually as an alternative to the classic swept  $IM3$  measurement if the characterized nonlinear memory is introduced by the bias-tee [149].

In Fig. 3.15, the same characterization as in Fig. 3.14 has been performed on a

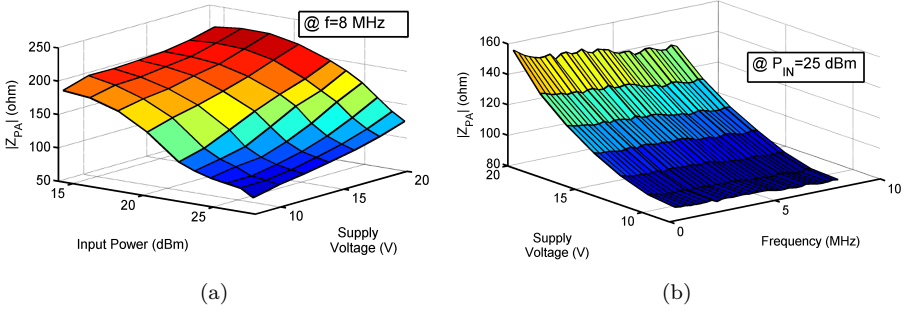


Figure 3.15: X-band GaN MMIC PA characterization. (a)  $Z_{PA}$  vs.  $V_{D0}=8 \div 20$  V and  $f_{LF}=0.1 \div 8$  MHz (b)  $Z_{PA}$  vs. RF  $P_{in}=15 \div 30$  dBm and  $V_{D0}=8 \div 20$  V.  $V_{GQ} = -2.8$  V.

GaN MMIC operating at  $f_0 = 10$  GHz [178]. In this case, the PA features a drain bias network consisting of a  $\lambda/4$  transmission line terminated by a capacitor on the supply side, which shorts the RF frequency. Thus, on the transistor side of the  $\lambda/4$ , a high-impedance is presented at the carrier frequency. Such a bias network does not affect the LF characterization in the MHz range, allowing to reach the transistor plane. Again, the  $Z_{PA}$  is proportional to the  $V_{D0}$  and inversely proportional to the  $P_{IN}^{RF}$ . In the next section, it is shown how the same characterization results can be obtained by using modulated multi-tone signals.

### 3.4.3 Characterization with multi-sine modulation

As shown in the previous section, the nonlinear, impedance-like function  $Z_{PA}$  has been characterized through a frequency sweep of a small signal tone. Such a sweep has been performed for each large-signal operating point, which is, in turn, changed by sweeping the dc supply voltage and the RF  $P_{in}$  level injected as a CW excitation. Such a way of characterization straightforwardly enables a direct sampling of all dimensions of  $Z_{PA}$ . On the other hand, it involves long measurement times. In case this characterization technique is used for model extraction (see Chapter 4), such long identification times may be incompatible with the application. Thus, in this section an equivalent, yet faster way to identify  $Z_{PA}$  is presented. To this aim, let us report the following multi-tone

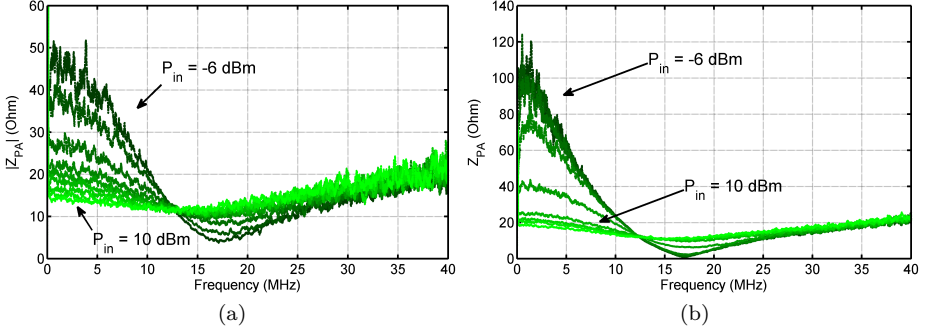


Figure 3.16: (a)  $Z_{PA}$  characterization for an hand-set PA with Schroeder multi-tone excitation, RF  $P_{in} \in [-6, 10]$  dBm (from dark to light) at  $f_0 = 0.85$  GHz.  $V_{D0} = 2$  V (b) Same as (a) with  $V_{D0} = 4$  V.

modulation for the supply voltage  $v(t)$ :

$$v(t) = V_{D0} + \sum_{k=1}^K \Re\{V_k e^{j2\pi\phi_k f_k}\} \quad (3.6)$$

with

$$\phi_k = \frac{-k(k-1)\pi}{K} \quad (3.7)$$

where  $V_{D0}$  is the dc value of the voltage waveform and  $V_k$  is the amplitude of the  $k$ -th tone. The modulated signal in (3.6) is known in the literature as the *Schroeder multi-sine* [179]. In general, the time-domain waveform of a multi-tone signal features a peak-to-average power ratio (PAPR) which is dependent on the mutual tone phases. For example, the PAPR is maximum when all tones are in phase. The signal in (3.6) features a specific relationship between the phases such that the time-domain waveform presents a low crest factor. This key features permits the use of (3.6) to acquire the frequency response of a DUT without modifying its large-signal operating point. In other words, one can independently fix the LSOP by setting the  $RFP_{in}$  and the  $V_{D0}$ . At the same time, by applying  $V_k = \tilde{V} \ll V_{D0}$ , the behavior of  $Z_{PA}$  over frequency is excited and acquired for the specific LSOP. Then, the same experiment is repeated for the necessary number of LSOPs. This is a useful technique when performing a characterization over a wide frequency band. The approach has been tested by using the VST based set-up of section 3.3.4, which allows the baseband acquisition up to 40 MHz to characterize commercial an handset (from Skyworks) RF PA. A Schroeder multi-sine modulated  $v(t)$  with

4000 tones (with  $\Delta f = 10$  kHz) has been programmed in LabVIEW, generated by the low-frequency channel and fed into the supply modulator. Calibrated IV waveforms have then been acquired by the low-frequency channel of the VST. The results are shown in Fig. 3.16 for two values of  $V_{D0}$ . A similar behavior as in Figs. and 3.15 can be evaluated versus RF  $P_{in}$ , although here it can be more clearly assess how and up to which frequency the frequency response is affected by the LSOP. In the next section, the same technique is applied to measure the output impedance-like nonlinear function of the supply modulator.

### 3.4.4 Supply Modulator nonlinear output impedance ( $Z_{SM}$ )

As already mentioned, no frequency chocking should be used for supply-modulated PAs in the frequency range of the dynamic supply voltage. In case of ET PAs, the modulated supply should follow the amplitude of the envelope  $a_1(t)$  applied at the RF input. The voltage control signal is usually directly extracted from the absolute value of the complex input ( $|a_1(t)|$ ), and then adapted by means of a shaping table (section 1.3.3). Due to the nonlinearity of the modulus operation, the bandwidth of  $v(t)$  may be consistently larger than the bandwidth of  $a_1(t)$ . If considering a typical LTE signal bandwidth of 20 MHz, this means that the bandwidth of  $v(t)$  may span several tens of MHz (a  $\times 5$  is usually considered sufficient). As discussed in section 3.4.1, an ideal supply modulator should present a very low output impedance over the frequency of operation extending to several tens of MHz. While such a characteristic may be optimized for a test-bench voltage buffer, this is not straightforward to obtain when high-efficiency is a constraint. It should be noted, however, that this is often the case in supply-modulated PAs, as it would make little sense to reduce the power consumption of the PA at the expense of increasing the one of the supply. As a consequence, the availability of a characterization technique capable to assess the capability of the SM in imposing a supply voltage over frequency can constitute a key indication for successful system design.

The impedance-like quantity describing the electrical output of the supply modulator ( $Z_{SM}$ ) depends, in general on the nonlinear operating point and frequency, such as it has been shown for  $Z_{PA}$ . It is likely, in fact, that the  $Z_{SM}$  increases as the current to be supplied increases, i.e., for increasing RF powers. Moreover, the higher the frequency of operation, the more critical is the linear operation of the SM, especially if it involves the use of feedback. As a consequence, the output function can be written as  $Z_{SM}[V_{S0}, I_{D0}, f]$ , where  $V_S$  is the dc component of the SM input voltage and  $I_{D0}$  is the current drained by the PA under CW. These two quantities, equivalently to  $V_{D0}$  and the RF  $P_{in}$ , determine the LSOP. In fact,  $V_S$  and  $P_{in}$  are the only controllable inputs of an operating supply-modulated PA, while the supply-drain node is not directly

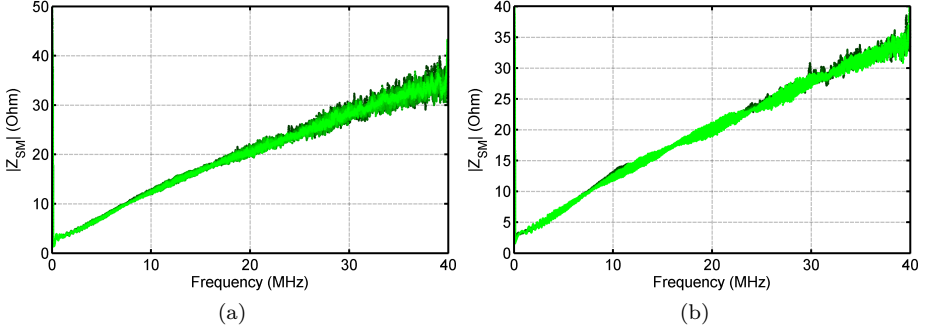


Figure 3.17:  $Z_{SM}$  for a supply-modulator type A under operation with hand-set PA with RF  $P_{in} \in [-6, 10]$  dBm (from dark to light). (a)  $V_{D0} = 1$  V. (b)  $V_{D0} = 4$  V.

accessible if the SM is not considered ideal. However, under CW excitation and with constant  $V_S$  ( $V_{S0}$ ), the constant quantities ( $V_{D0}$ ,  $I_{D0}$ ) are set on the supply-drain terminal. To sample  $Z_{SM}$  over frequency, once established the LSOP, one should generate a modulated current, while measuring the relative voltage modulation at the supply node. Such a modulation can be indirectly generated through the PA with an RF input excitation. One may, in fact, generate a small tone modulation at the RF input, and sweep it over the frequency of interest. Coherently, a small current modulation will appear at the supply, working as an excitation signal to determine  $Z_{SM}$ . By following the same approach of section 3.4.3, one may also generate a suitable modulation to obtain the frequency response in a single take. In this case, one should generate a suitable Schroeder multi-sine modulated envelope at the RF input:

$$a(t) = A_0 + \sum_{\substack{k=-K \\ k \neq 0}}^K A_k e^{j2\pi\phi_k f_k} \quad (3.8)$$

where  $A_0$  is the CW amplitude of the RF input setting the large-signal operating point, and  $\phi_k$  is the same as in (3.7). Also in this case, the tone amplitudes should satisfy the condition that  $A_K = \tilde{A} \ll A_0$  to ensure that the LSOP is not perturbed by the modulation. More in detail, the modulation amplitude  $\tilde{A}$  must be set so that, ideally, a Schroeder modulation of the current is generated. This will however depend on the nonlinear transfer function which maps the RF input in the drained current, as will be discussed in Chapter 4. However, the RF input excitation can be tuned accordingly with the measured modulated current. This technique is implemented with the same VST set-up used for  $Z_{PA}$  in section 3.4.3, and applied to two types of commercial supply modulators. The

first, referred to as type A, is a bipolar high speed current feedback amplifier. As such, it does not enhance any specific strategy for energy efficiency. The second supply modulator, referred to as type B, is an hybrid architecture featuring a switching converter for the dc voltage and a linear feedback amplifier to enhance higher frequency. As such, it features two operating options: the average power tracking (APT) mode, which disables the linear amplifier, and the envelope-tracking (ET) mode, which also enables the linear part. The same  $Z_{SM}$  characterization has been applied to both by means of the Skyworks PA measured in section 3.4.3. The results are reported in Figs 3.17, 3.18 and 3.19. The  $Z_{SM}$  of the type A SM (Fig. 3.17) does not show any particular dependency on the LSOP. The magnitude of  $Z_{SM}$  is very small close to dc, while it dramatically increases over frequency reaching up to  $40 \Omega$ . Such a trend should be taken into account when generating the modulated SM control  $v_s(t)$ , and such characterization can possibly enable a compensation of this effect. Type B SM shows a critically different behavior. The first test is made by setting the APT mode. Indeed, not a great performance is expected over frequency for such operation mode. In fact, as reported in Fig. 3.18, the SM shows a very small impedance around dc, but it sharply increases up to hundreds of  $\Omega$  in the MHz range, with a resonance at around 23 MHz. Different slopes are obtained when the SM is switched to ET mode (Fig. 3.19). In particular, both the dependency over frequency as well as the maximum value reached dramatically change. However, up to  $200 \Omega$  are measured at  $\sim 15$  MHz, while no significant dependency on the drained current was evaluated when  $V_{D0} = 1.5$  V. Despite this, a change in the dc voltage causes evident changes in the  $Z_{SM}$  frequency dependency. One may wonder how the supply-modulated PA linearity and efficiency may be affected by the variety of behaviors shown by the supply modulators. In the next section, an experiment implementing low-frequency

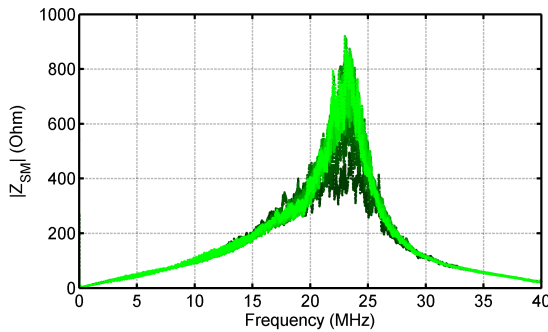


Figure 3.18:  $Z_{SM}$  of a supply modulator type B in APT mode under operation with hand-set PA with RF  $P_{in} \in [-6, 10]$  dBm (from dark to light).  $V_{D0} = 2.8$  V.

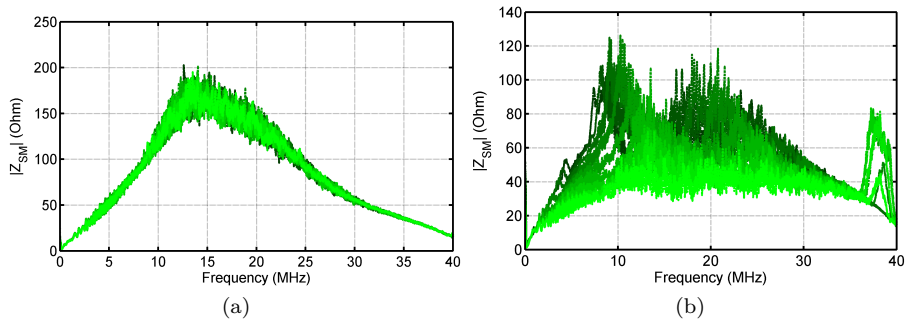


Figure 3.19: (a)  $Z_{SM}$  of a supply-modulator type B with linear block enabled, under operation with hand-set PA with RF  $P_{in} \in [-6, 10]$  dBm (from dark to light).  $V_{D0} = 1.5$  V (b) Same as (a) with  $V_{D0} = 3.8$  V.

load-pull at the drain terminal of the PA is presented.

### 3.5 Supply terminal active load-pull

As shown in the previous section,  $Z_{SM}$  may be far from ideal, typically showing higher level of output impedance at higher frequencies. As a consequence, one may wonder how the behavior of the PA changes with respect to the LF termination, in the same way one is interested to its RF load termination. Indeed, a few works have proposed set-ups to measure the drain-supply terminal up to several tens of MHz [174],[176]. In this section, despite its frequency limitation, we make use of the LF-LSNA to perform an LF active load-pull at the drain terminal of the PA. This experiments is meant to conceptually demonstrate how such measurement technique could be of use to assess PA sensitivity to LF load variations and eventually assist ET PA designs. To this aim, the GaN MMIC PA whose characterization is shown in Fig. 3.15 has been used. The active load-pull at baseband is obtained by feeding the drain path with a  $50\text{-}\Omega$  source [172]: the impedance synthesized in this way will be still referred to as  $Z_{SM}$  (Fig. 3.13), while the correspondent reflection coefficient is  $\Gamma_{SM}$ . The RF signal is provided by means of a vector signal generator (Agilent E4438C) feeding a passive mixer and an additional broadband amplifier. When a RF signal with two tones at  $f_0 \pm \Delta f$  is applied at the input port of the PA, it generates intermodulation mixing products, one of which is at  $\Delta f$ . Subsequently, a small tone at LF is applied in order to perform active load-pull at the same frequency  $2\Delta f$  and change the equivalent  $Z_{SM}$  impedance. The RF signals

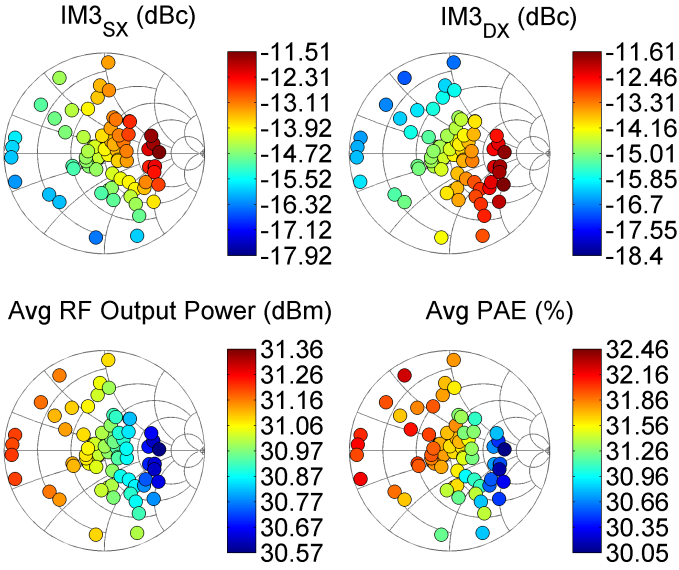


Figure 3.20:  $IM3$ ,  $P_{RF}^{OUT}$  and PAE versus  $\Gamma_{SM}$  synthesized at  $f_{LF}=2\Delta f=2$  MHz, for RF two-tone signal with  $P_{RF}^{IN}=24$  dBm. Similar patterns are obtained if performing the LF load-pull at other frequencies.  $V_{G0}=-2.8$  V,  $V_{D0}=18$  V.

are applied on-wafer, and a printed circuit board (PCB) is designed to access the bias nodes via coaxial cable [152]. The PA is biased at a gate bias voltage  $V_{G0}=-2.8$  V (class AB), and excited with a central RF frequency  $f_0=10$  GHz. For the range of RF input power levels ( $10 \div 16$  dBm) and DC supply voltages ( $8 \div 20$  V), the two-tone RF signal is applied with a frequency spacing around  $f_0$ , while randomly sweeping amplitudes and phases of the small signal generated at the drain supply port at  $2 \Delta f$ . The experiment is repeated for  $\Delta f = 0.1$  MHz, 1 MHz, 2 MHz and 3 MHz. For each synthesized load  $Z_{SM}$ , all waves, including the ones at LF, are captured. Thus, the RF output power,  $IM3$  and PAE are characterized versus the reflection coefficient  $\Gamma_{SM}$  and reported in Fig. 3.20.

By analyzing the distribution of the captured values on the Smith chart one can assess how  $Z_{SM}$  influences the linearity of the PA. In particular, Fig. 3.20 shows that the lower and upper  $IM3$  ( $IM3_{SX}$  and  $IM3_{DX}$ , respectively) are strongly dependent on the synthesized  $\Gamma_{SM}$ . Minimum  $IM3_{SX}$  are found in the capacitive area, for low resistance and  $\Im\{\Gamma_{SM}\} < -0.5$ ; maximum  $IM3_{SX}$  are

for more resistive LF conditions, and inductive behavior such as  $\Im\{\Gamma_{SM}\} > 0.5$ . On the contrary,  $IM3_{DX}$  is minimum for an inductive load ( $\Re\{\Gamma_{SM}\} < 0.1$  and  $\Im\{\Gamma_{SM}\} > 0.5$ ), and maximum for a capacitive load ( $\Re\{\Gamma_{SM}\} > 0.5$  and  $\Im\{\Gamma_{SM}\} < -0.5$ ). Such results depend on the phase shift induced not only by the low-frequency impedance, but also by the transcharacteristic of the transistor and on the second harmonic termination (assumed  $50 \Omega$  in these experiments), as detailed in [180]. Under the measurement conditions tested in the lab, one can conclude that, for this PA, the asymmetry between the intermodulation  $\Delta IM3 = |IM3_{DX} - IM3_{SX}|$  is maximum for a purely capacitive load and for a purely inductive load, in agreement with [180]. Clearly, the PA shows maximum memory effects when a purely reactive load is placed at the LF port. On the other hand, the total distortion increases proportionally to the LF resistance, given that the spurious current components at LF will be transformed at higher LF voltage components. Thus, an LF short termination guarantees minimum distortion without introducing memory effects. These results are in agreement with those reported in the literature for transistors alone [160], [181], [182],[183].

In Fig. 3.21, the  $IM3$  characterization versus RF input power with  $\Delta f=2$  MHz is reported. Since no deterministic control is implemented to synthesize the  $Z_{SM}$ , those results are reported at four loads for which each of the points of the RF input sweep share the same  $\Gamma_{SM}$ . Figure 3.22 shows the dependence of  $IM3$  on the dc supply voltage. Also in this case, the loads are chosen to guarantee that each point of the supply voltage sweep shares the same  $\Gamma_{SM}$ . Besides the

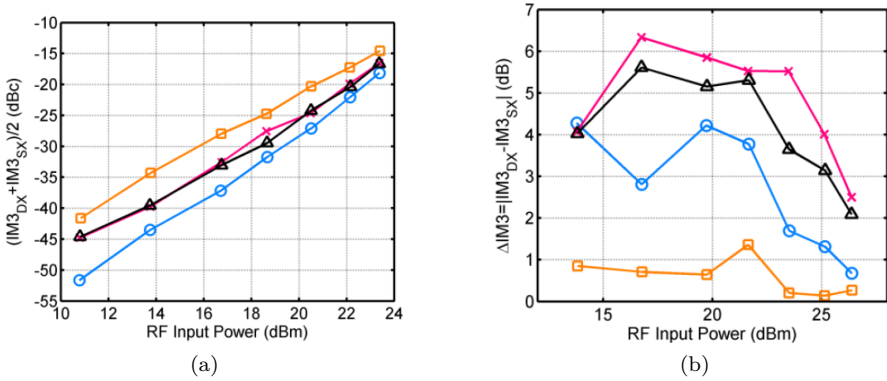


Figure 3.21:  $IM3$  versus  $P_{RF}^{IN}$ : average distortion (a) and asymmetry (b).  $Z_{SM}$ :  $-0.36+0.1j \Omega$  (circles),  $0.23-0.53j \Omega$  (crosses),  $0.45-0.03j \Omega$  (squares),  $0.01+0.37j \Omega$  (triangles), at  $f_{LF}=2\Delta f=4$  MHz.  $V_{G0}=-2.8$  V,  $V_{D0}=20$  V.

$IM3$  asymmetry already discussed, a rate of  $IM3$  reduction of  $-1.5$  dB/V (where the volt refers to the dc supply voltage value) has been measured for this PA. In [152], RF output power, dynamic PAE, and LF time-domain IV waveforms are also shown for various  $Z_{SM}$ . Moreover, an analysis is provided to understand the mechanism behind the dynamically dissipated power and PAE. For the measurements performed in this investigation, the average PAE calculated under two-tone excitation does not vary more than a few percentage points versus the  $Z_{SM}$ , as reported in Fig. 3.20. It should be mentioned, however, that further characterizations are needed to model the PA under realistic supply modulation. In fact, only passive  $Z_{SM}$  have been synthesized in this experiment, while power is typically injected into the PA (i.e.,  $\Re\{Z_{SM}\} < 0$ ).

### 3.6 Characterization and modeling of self-heating in RF PAs

#### 3.6.1 Introduction to thermal effects in RF PAs

This section, with respect to the previous ones, concerns a separate issue in PA behavioral modeling. While before the focus has been on empirical characterizations for envelope-tracking systems, here a technique to characterize and model self-heating effects in PAs is presented. Although the two activities

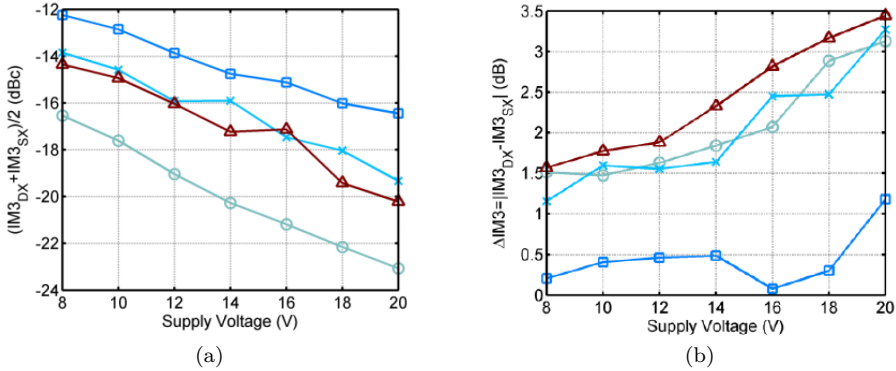


Figure 3.22:  $IM3$  versus  $V_{D0}$  under LF loadpull. (a) average distortion. (b) asymmetry.  $Z_{SM}$ :  $-0.51+j0.28 \Omega$  (circles),  $0.33-j0.42 \Omega$  (crosses),  $0.46+j0.16 \Omega$  (squares),  $0.07+j0.52 \Omega$  (triangles), at  $f_{LF}=2\Delta f=6$  MHz.  $P_{IN}^{RF}=22$  dBm.  $V_{G0}=-2.8$  V.

have been developed separately (this, in particular, has been promoted by the University of Bologna), they share the use of a similar measurement set-up, although properly modified for the objective as will be reported in section 3.6.3. In fact, if one wants to empirically characterize the (dynamic) thermal behavior of a PA, should, inevitably, be able to assess the power balance at its ports. This involves acquiring the input and output signals at both the RF ports and at the supply port. Moreover, investigating thermal effects is an effort towards the interpretation of the frequency dependencies characterized in the previous sections. Indeed, such dependencies are the result of a number of mixing contributions: having a method to partially de-embed some of them (e.g., the ones due to self-heating) enables the interpretation of the other phenomena taking place in supply-modulated PAs. In fact, memory effects are commonly divided into two categories, depending on the time constants involved [184]: fast memory effects, which present small ( $< \sim \text{ns}$ ) dynamics time constants, are due to charge storage phenomena and parasitics in the active device, as well as RF dynamics in the matching networks. Slow memory effects, which present large ( $> \sim \mu\text{s}$ ) time-constants, are due to slow phenomena such as self-heating, supply voltage modulation (due, for example, to bias networks), charge trapping, and, finally, device degradation. Due to the wide range of these phenomena, it is tricky to combine both slow and fast effects in a unique model formulation, and they should be considered separately [185]. A possible approach is to rely on physics-based simulations to identify thermal effects, and to couple thermal with electrical models. While physics-based simulations can provide flexibility in the evaluation of thermal diffusion on the physical geometry of the device, as well as good accuracy, they are too computationally demanding if combined with the wide bandwidth modulations of modern telecommunication systems [186]. However, considering the fast development of complex sub-systems, high-level models are needed for system simulations. Indeed, these should provide reliable results also in case of nonlinear and dynamic behavior and long transients. The idea presented here is to capture the essential impact of thermal effects on the input-output performance by relatively simple equations and straightforward identification techniques to be used with standard laboratory instrumentation [45],[126]. The experiment presented here is a step towards the integration of temperature dependency in behavioral models, such as it is done for devices (section 2.7.2). The presented approach is tested on a PA in LDMOS technology. Such a choice was specifically aimed to avoid the impairment of the typical charge trapping phenomena present in GaN, which have time constants in the same range as the thermal ones. However, the technique developed here should be preparatory to a behavioral modeling approach for GaN-based PAs.

### 3.6.2 Model formulation and identification

The approach presented here is based on a complex RF input-output transfer function  $H$ , as most commonly done in the literature. The generic input-output relationship for a matched RF PA can be written as follows:

$$b(t) = H[|a(t)|, \theta(t)]a(t), \quad (3.9)$$

where  $a(t)$  and  $b(t)$  are, respectively, the complex baseband-equivalent input and output power waves as from (3.5),  $\theta(t)$  is an equivalent junction temperature and  $H$  is a complex function of real variables. First of all, it is worth noting that the quantity  $\theta(t)$ , although featuring the physical dimensions of temperature, may not correspond to a measurable temperature. It would be impractical, in fact, to define a dynamic temperature to be empirically measured, where instead a temperature is physically distributed over a volume, and depends on the heat flows that pass through it. This kind of difficulties is the main reason why physical thermal models are often preferred to the empirical ones. The variable  $\theta(t)$  can be instead thought as a state variable, which specifically gives information on the thermal state. Indeed, one may think of it as (but not limited to) an average temperature of the PA, however, the aim of such state variable is not providing the characterization of a temperature, but to functionally synthesize the thermal state of the PA, so that improved prediction of output signals can be obtained. Let us suppose that the mentioned impact of thermal effects on the behavior of the PA is small enough to allow a linearization with respect to the equivalent temperature  $\theta(t)$ . Such an hypothesis comes from the idea that any thermal phenomena on the PA transfer characteristic are unwanted, and that the designer makes any possible effort to reduce them either by providing a device with a large enough active area, by applying efficient thermal sinking to the PA. In that case, one obtains

$$H(|a(t)|, \theta(t)) = H^*[|a(t)|, \theta^*] + h_\theta[|a(t)|, \theta^*](\theta(t) - \theta^*), \quad (3.10)$$

where  $H^*$  is the isothermal characteristic at a specific (yet arbitrary) equivalent junction temperature  $\theta^*$  and  $h_\theta$  is the sensitivity function of the PA characteristic versus equivalent temperature changes. Such a quantity is naturally defined through the partial derivative of  $H$  versus the temperature variation:

$$h_\theta[|a(t)|, \theta^*] = \left. \frac{\partial H[|a(t)|, \theta(t)]}{\partial \theta(t)} \right|_{\theta^*}. \quad (3.11)$$

If the model should allow a straightforward calculation of self-heating, then it should account for the input and output power flows, and therefore this must be included in the formulation. Although the PA is assumed perfectly matched at the RF input and output ports, the power flow at the supply port may

not be ignored. Despite the experimental tests proposed here do not feature a modulated supply voltage (thus, the power flow modulation at the supply is only due to the dynamically drained current) the approach is applicable to supply-modulated PAs. Let us consider the following formulation for the current drained from the supply:

$$i(t) = F[|a(t)|, \theta(t)] \quad (3.12)$$

where  $F$  is a real-valued nonlinear function of the RF input envelope and of the equivalent temperature  $\theta(t)$ . Again, if assuming the same hypothesis done for (3.10), one can consider an analogous linearization by means of another sensitivity function  $f_\theta$ , which is now defined as the sensitivity of current variations versus equivalent temperature variation

$$F[|a(t)|, \theta(t)] \simeq F^*[|a(t)|, \theta^*] + f_\theta[|a(t)|, \theta^*](\theta(t) - \theta^*), \quad (3.13)$$

Such a sensitivity is defined similarly to (3.11) as follows:

$$f_\theta[|a(t)|, \theta^*] = \left. \frac{\partial F[|a(t)|, \theta(t)]}{\partial \theta(t)} \right|_{\theta=\theta^*}. \quad (3.14)$$

Equations (3.10) and (3.13) account for the impact of the state  $\theta(t)$  on the RF output and drain current, respectively. The way such a dependency behaves is instead contained in the sensitivities (3.11) and (3.14). The model depicted in the previous equations should be suitably coupled with a state equation, i.e., an equation that determines what is the evolution of  $\theta(t)$  with respect to the excitations. In this work, a simple thermo-electrical model has been considered:

$$\theta(t) \simeq \theta_C(t) + R_\theta(v(t)i(t) + |a(t)|^2 - |b(t)|^2) \quad (3.15)$$

where  $R_\theta$  is an equivalent thermal resistance,  $\theta_C(t)$  is the temperature of the case upon which the PA is positioned, and  $v(t)$  is the supply voltage applied to the PA, which may be considered constant  $v(t) = V_0$  to the extent of the work reported here. The definition of  $\theta_C(t)$  is critical from the modeling point of view, as it defines the boundary of the modeled thermal effects. In fact, as  $\theta_C$  is a temperature to be physically measured, it must be chosen in a practical way. For example, this can correspond to the ambient temperature. In such a case, the model would handle any temperature variation with respect to the ambient temperature, most probably featuring extremely long time constants. On the contrary, if placed as close as possible to the active device, then the modeling span will be minimized and the model functions would be simplified. As a general principle,  $\theta_C$  should be defined as the temperature of a point as close as possible to the active device, but still a temperature that can be accurately measured. With respect to this aspect, it should be mentioned that

it is extremely challenging to accurately measure a fast-varying temperature. This is due to the trivial fact that the temperature sensor cannot be indefinitely small, and, as a consequence, carries a non-negligible thermal capacitance. Thus, the measurement point where fetching  $\theta_C$  should also be chosen accordingly. For example, it can be chosen on the heat sink, as close as possible to the device. In this way, the critical heat flow (i.e., the one from the active device to the sink) is accounted for in the model, and the temperature on the sink does not vary too fast for a commercial resistive sensor. The identification of the proposed model consists in the characterization of the following quantities: the isothermal functions  $H^*$  and  $F^*$ , the sensitivity functions  $h_\theta$  and  $f_\theta$ , and the thermal resistance  $R_\theta$ . In particular, isothermal functions  $H^*$  and  $F^*$  must be measured at the specific temperature  $\theta^*$  and in absence of self-heating effects. Such a configuration can be obtained by imposing (externally, as will be depicted in section 3.6.3) a specific  $\theta_C$  and setting the nominal bias ( $V_0, I_0$ ) at which the model should be extracted. After a steady-state condition is reached, an equivalent temperature  $\theta^* \simeq \theta_C + R_\theta V_0 I_0$  is obtained. In such conditions, a pulsed RF input with a modulation rate shorter than the thermal constants (but slow enough to avoid the influence of high-bandwidth effects such as the ones of matching networks and parasitics) is applied, and RF output envelope and current can be synchronously captured. Such a measurement technique resembles, to some extent, the pulsed IV measurements discussed in section 2.3 for the isothermal characterization of active devices. The sensitivity functions  $h_\theta$  and  $f_\theta$  are obtained by isothermal measures at two different equivalent junction temperatures  $\theta^*$  and  $\theta^* + \Delta\theta$ . In other words, they are obtained by considering the quotient differential of arbitrarily small  $\Delta\theta$ :

$$h_\theta[|a(t)|, \theta^*] = \frac{H[|a(t)|, \theta^* + \Delta\theta] - H[|a(t)|, \theta^*]}{\Delta\theta} \quad (3.16)$$

$$f_\theta[|a(t)|, \theta^*] = \frac{F[|a(t)|, \theta^* + \Delta\theta] - F[|a(t)|, \theta^*]}{\Delta\theta} \quad (3.17)$$

Finally, the equivalent thermal resistance  $R_\theta$  can be obtained by acquiring two or more steady state conditions at different excitations. This may be obtained by either evaluating the initial and the final values of a step response transient or forcing different CW excitations. Also in this case, a parallel with device thermal model can be found in [45]. In the following, the measurement set-up used for the identification will be presented.

### 3.6.3 Measurement set-up

The measurement set-up used for the identification and validation of the proposed model is based on the VST and resembles, to some extent, the set-up

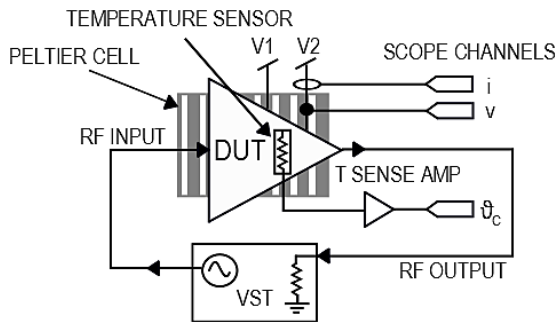


Figure 3.23: Diagram of the measurement set-up for PA self-heating characterization

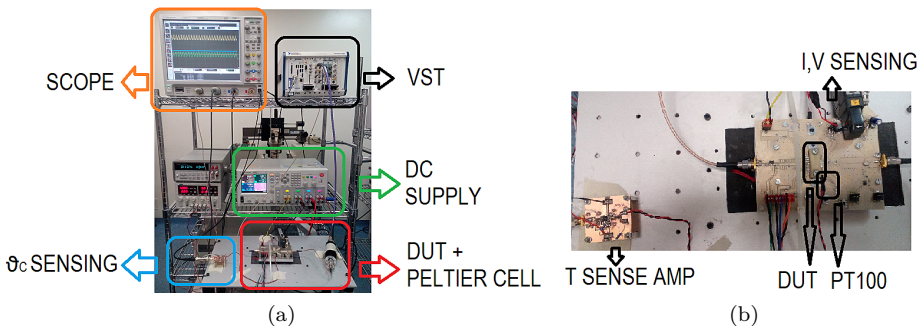


Figure 3.24: (a) Foto of the measurement set-up depicted in Fig. (b) Zoom of the PA with the DUT and the temperature sensing board.

proposed in section 3.3.4. However, this one was implemented at University of Bologna, while the one of section 3.3.4 was engineered at KU Leuven. It makes use of the NI VST [173] for the generation and the acquisition of RF input and output signals. The diagram of the set-up is reported in Fig. 3.23. The version of the VST available at UNIBO, however, does not feature the baseband channel for acquisition and generation. Thus, in order to sense the dynamic current and the voltage at the supply node, a commercial current sensor (based on the combination of a wideband Hall sensor and a transformer [168]) and a high-impedance sensor have been used. Both signals are acquired with a commercial oscilloscope. As in section 3.3.1, the LF quantities are considered calibrated at the scope acquisition plane, thus no additional calibration was implemented this time. At RF, the input and output ports are matched, so no reflection is accounted for. The case temperature  $\theta_C$  can be imposed by a Peltier cell positioned under the DUT and can be sensed by means of a resistive

sensor (PT100), whose signal is properly amplified and conditioned in order to be captured by the oscilloscope. The photo of the set-up can be found in Fig. 3.24(a), while the detail of the DUT and of the temperature sensing circuitry is in 3.24(b). The measured PA is a three-stage RF PA operating at 1.84 GHz, composed by a pre-driver and a two-stage LDMOS PA. It is biased in class AB providing a maximum output power of  $\sim 48$  dBm and a maximum drain current of  $\sim 2$  A.

### 3.6.4 Experimental results

Although the proposed behavioral model has been applied to a three-stage DUT, the drain current measurements as well as the thermal network take into account only the final stage, as the pre-driver and the driver mainly work linearly and minimally contribute to overall self-heating. Isothermal PA characteristics and sensitivity functions obtained through the methodology previously described are reported in Figs. 3.25 and 3.26, respectively. In particular, the temperature  $\theta_* = 59.1^\circ\text{C}$  has been chosen as the reference one for the linearization. Then, two additional isothermal characteristics, at the maximum ( $77.8^\circ\text{C}$ , limited by the Peltier Cell) and minimum ( $32.5^\circ\text{C}$  as no cooling was applied to avoid condensation) temperature achievable with the set-up have been measured. In such a range, a maximum gain variability of  $\sim 2$  dB has been measured. By using these data, the complex sensitivity function  $h_\theta$  has been measured by calculating various differential quotients among the available temperatures. All possible calculations have result in the same function, which is the one

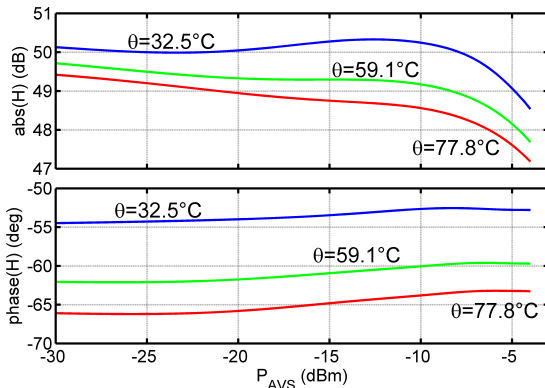


Figure 3.25: Measured isothermal curves of the gain characteristic ( $H$ ) at three fixed temperatures.

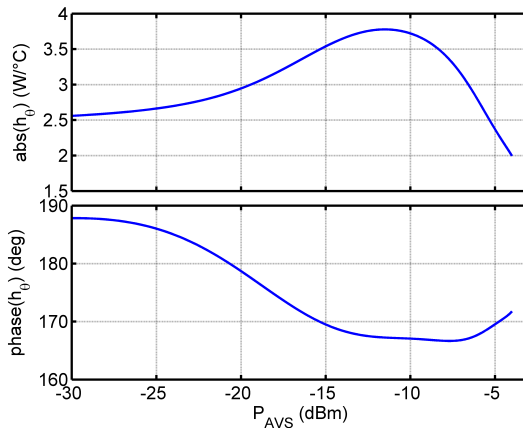


Figure 3.26: Measured gain sensitivity to temperature ( $h_\theta$ )

displayed in Fig. 3.26. This reveals how the thermal effects impact the input-output transfer characteristic. By also accounting for the phase of  $h_\theta$ , one may interpret such data as follows: at small input power, the sensitivity is positive due to the effects on the threshold of the transistor. When the RF power increases, the sensitivity becomes negative, as the increasing temperature impacts the mobility of the carriers. Similar comments can be made on the current characteristics reported in Fig. 3.27, where a coherent behavior can be noticed, and a drain current drop of  $\sim 300$  mA is observed over the temperature range. Also in this case, the same behavior of the sensitivity can be noticed. As expected, the empirical model extracted at  $\theta^*=59.1^\circ\text{C}$  suitably predicts isothermal characteristics measured at  $\theta_{MIN}$  and  $\theta_{MAX}$  (Fig. 3.28). In fact, it has been already commented that the sensitivity function could have been calculated by any two characteristics of the three measured. Moreover, a CW validation has been performed. Such measurements have been obtained by imposing a constant case temperature with the Peltier Cell ( $\theta_C=30^\circ\text{C}$ ) and waiting the settling of long-term self-heating effects before the acquisition for each input power. The model reliably reproduces both the gain and the supply current quasi-static characteristics affected by self-heating with a relative error  $< 4\%$ . An equivalent thermal resistance  $R_\theta \simeq 1^\circ\text{C}/\text{W}$  was measured for this DUT. Unfortunately, thermal dynamic effects could not be modeled, as no thermal impedance was extracted. In theory, however, by simply changing the state equation one may involve thermal and other kinds of dynamics. Such aspects are yet to be addressed within the research.

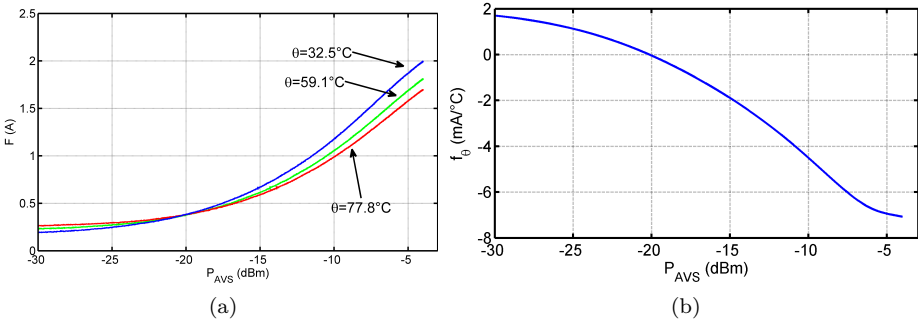


Figure 3.27: (a) Measured isothermal curves of the supply current ( $F$ ) at three equivalent junction temperatures  $\theta^*$ . (b) Measured current sensitivity to temperature ( $f_\theta$ ).

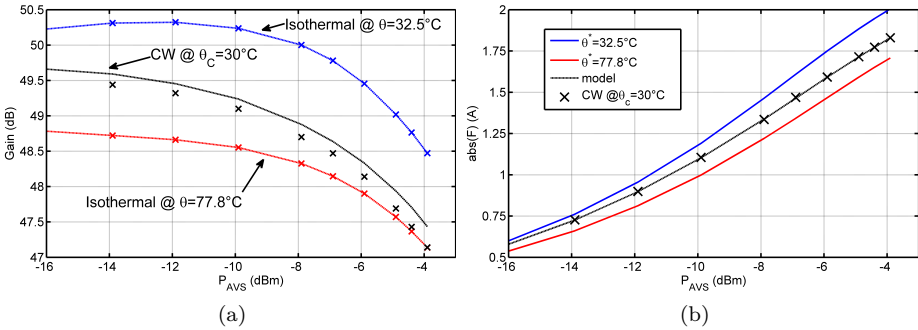


Figure 3.28: (a) Validation of the extracted model (lines) vs gain measurements (crosses). CW characteristic (black) is obtained at constant  $\theta_C = 30^\circ\text{C}$ . (b) Validation of the model vs current measurements.

### 3.7 Conclusion

In this Chapter, large-signal measurement techniques and their use in various types of RF PA characterization have been described. The working principle of sampler-based and mixer-based large signal network analyzers have been reported from literature, along with their calibration approaches. Two new setups for supply-modulated PAs, conceived during the Ph.D., have been presented, along with some preliminary experimental tests. Then, characterization issues related to supply-modulated PAs have been discussed in detail. A technique was presented to measure impedance-like nonlinear functions for the input port of the

PA at the drain terminal ( $Z_{PA}$ ) and for the output port of the supply modulator ( $Z_{SM}$ ). These characterizations have been thought to enable describing the mutual interaction of the PA and of the SM under supply-modulated operation, and to assist system engineers to interface the components. Results have shown that these quantities are indeed dependent on the large-signal operating point. Moreover, strong frequency-dependency may appear on both the PA and the SM, so that they can impair the wanted supply-modulated operation. To further investigate the issue, a low-frequency load-pull experiment has been performed at the drain-terminal of the PA, characterizing the distortion with respect to the synthesized impedance. No critical dependency was however measured on the PAE for this specific DUT. The remainder of this Chapter, instead, was dedicated to the characterization of thermal effects. A custom set-up was used to leverage on pulsed RF excitations as well as the control of the case temperature to extract a simple self-heating model. Such a work can be considered useful to handle and separate thermal effects from other dispersive phenomena. The next Chapter makes use of some of the notions developed for the characterization of the supply-modulated PAs in order to provide a formal derivation for the quantity  $Z_{PA}$  and obtain a three-port PA model.

## Chapter 4

# Three-port modeling for supply-modulated PAs

### 4.1 Introduction

This Chapter is dedicated to the formulation, identification, and validation of a three-port, nonlinear dynamic behavioral model applicable to supply-modulated RF PAs. The presented modeling results have been published in [187], while the linearization approach depicted in section 4.6 is under review [188]. As discussed in section 1.3, the use of power supply modulation, e.g., ET and EER, has been demonstrated in the literature as suitable solution for obtaining increased efficiency in power amplifiers [79],[189]-[193]. Such architectures usually rely on additional signal processing in order to compensate the nonlinear dynamic behavior under supply modulation conditions. Behavioral modeling techniques [99],[104],[190],[194],[195] are needed to properly reproduce the PA behavior in system-level simulations. Predistortion approaches [196]-[198] based on such models are necessary to guarantee the linearity requested by the application. More in detail, techniques to minimize the undesired impact of dynamic supply voltage are of key importance. A possible approach consists of reducing the bandwidth [189] or the slew rate [198] of the supply modulator. However, depending on the envelope shaping strategy, or in case of polar modulators, the supply voltage must be considered as a variable of the PA model [85],[199]-[201]. A quantity of works report 2-D look-up tables (LUTs) or memory polynomial models which include the supply voltage as a static variable in order to take into account the different operating modes in which the PA is driven [190]-[194],

[196]. Much fewer works account for its dynamic influence [198],[202].

A common procedure to obtain the predistortion coefficients consists of applying a portion of the modulated signal used for the application and run a local optimization such that the minimum number of predistortion coefficients for a chosen method is used, while the linearity constraints are satisfied for the specific output signal. Since, in most cases, the supply excitation is not optimized together with the RF predistortion and the dynamic supply current is not modeled, the trade-off between linearity and efficiency may not be fully exploited. This is also pointed out in [193], where a static characterization of the efficiency is used. Yet, due to memory effects, there is no guarantee that, in presence of consistently different RF waveforms, the PA will still maintain the same optimized performance. Thus, such system-level linearization approaches rely on a high-bandwidth feedback, through which the predistortion model coefficients are adjusted in real-time when the RF input signal is changed [197]. However, especially when considering the increasing number of applications for which a high-speed coefficient update is unreliable, due to the non-idealities of the feedback loop, or unfeasible, due to bandwidth limitation as well as feedback stability reasons, the predistortion performance is critically dependent on the capabilities of the adopted PA description. In the case of supply-modulation, the PA should be, in general, considered as a three-port device. First, the inherent nonlinear characteristic of converting power from low to radio-frequency must be fully accounted for including dc and the carrier frequency. Moreover, a desirable feature is the ability of modeling the dynamic supply current consumption, so that the model could predict the dynamic efficiency of the supply-modulated PA. Such a task is made complex by the fact that a PA driven into large-signal operation shows dynamically varying drain IV characteristics, which interact with the supply output impedance [201]. While fixed supply can be designed to ideally show a very low output impedance, this is not feasible for supply modulation, as seen in section 3.4.4. Thus, the possibility to include the supply port and model the PA behavior with respect to dynamic supply voltage and current provides a key for exploiting PA performance, especially in those cases for which the supply modulation is far from ideal. In the next section, the measurement techniques presented in section 3.4 will be used for modeling.

## 4.2 Modified Volterra series

While in section 3.4 has been shown a possible approach for the characterization of the drain-supply terminal in supply-modulated PAs, here a formal behavioral model formulation is investigated. Since the quantities involved are, in general, nonlinear dynamic functions of the inputs, the idea is to leverage on behavioral

modeling approaches such as the ones introduced in section 1.4.3. In particular, the modified Volterra series approach in (1.13) is here considered to model the PA as a nonlinear dynamic three-port device. To do so, a first order approximation ( $p = 1$ ) has been applied to (1.13), obtaining:

$$\tilde{y}(t) = f[\tilde{x}(t)] + \int_0^{T_M} \tilde{g}_1[\tilde{x}(\tau_1)][\tilde{x}(t - \tau_1) - \tilde{x}(t)]d\tau_1 \quad (4.1)$$

where  $T_M$  describes the maximum memory modeled. The choice of such an approximation is a compromise between the accuracy of the model and a straightforward identification technique. In fact, it is well known [109] that the direct identification of high-order Volterra kernels is extremely problematic from a measurement point of view. As already mentioned in section 1.4.3, the most common, yet likewise problematic solution to obtain high-order formulations, leverages on regression methods such as linear least-squares. Instead, the direct (i.e., *orthogonal*) identification of lower order kernels has been preferred in this work. Although such a truncation may sound as a limitation, it has been proved in literature [115] that a first order truncation of the modified Volterra representation provides much larger range of applicability than the classical Volterra one, and provides sufficient accuracy for many applications. More in detail, the modified Volterra formulation entails a separation between a nonlinear quasi-static characteristic ( $f[\cdot]$  in (4.1)) and a *dynamic-deviation* term. In this way, no approximation is made for the representation of the nonlinear quasi-static behavior. Moreover, the truncation error does not directly

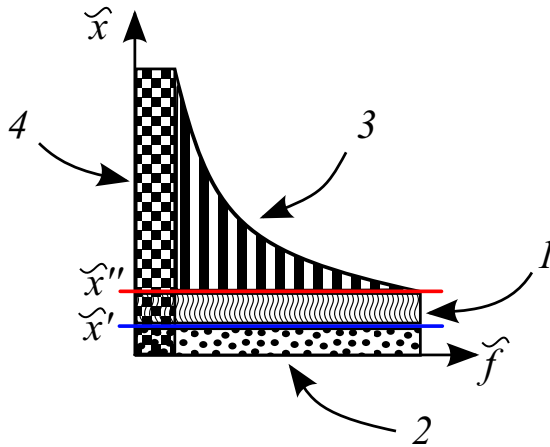


Figure 4.1: Representative diagram for region of validity of the truncated Volterra and the truncated modified Volterra series.  $\tilde{f}$  and  $\tilde{x}$  are the input signal frequency and amplitude, respectively (from [115]).

depend on the amplitude of the input signal involved  $\tilde{x}(t)$  (as in the conventional Volterra series). Instead, it depends on the product between the duration of the nonlinear memory effects  $T_M$  present in the system and the input signal frequency  $\tilde{f}$ . Therefore, the series can be truncated to a one-dimensional kernel even in the presence of strong nonlinear effects, provided that the product  $T_M \cdot \tilde{f}$  is small enough. In other words, it depends on the trade-off between its peak-to-peak value and frequency for a given bandwidth. The upper limit of the truncation error in the classical Volterra series is instead dependent only on the signal amplitude which is not necessarily small. Moreover, it should be noted that no approximation is done on the linear dynamics. In fact, in this case  $p = 0$  and any dynamics is fully accounted for by the memory kernel  $g_0[\cdot]$ , which becomes independent of the amplitudes. In other words, the relationship reduces to linear convolution. Thus, it is worth underlining that the  $T_M$  only refers to the nonlinear memory, while the linear one extends indefinitely, just likewise it happens with the standard impulse response description of linear systems.

In order to allow a qualitative, yet easily understandable, description of the applicability range of (4.1), Fig. 4.1 is provided. In Fig. 4.1, both the truncated Volterra series and the truncated modified one are schematically represented in the space of the signal amplitude  $x$  and its frequency  $\tilde{f}$ . In particular, the area (1+2) symbolically represents the validity region of the truncated conventional Volterra series. In fact, in order to guarantee, for a given system, an upper limit on the truncation error, an upper limit on the signal amplitude ( $\tilde{x} < \tilde{x}''$ ) must be imposed. In particular, for  $p = 1$ , the conventional Volterra series in (1.8) simply becomes a single-fold linear convolution, which can only be used under the so called "small signal" operating conditions (area 2, for which  $\tilde{x} \leq \tilde{x}'$ ). Instead, the validity region for the modified Volterra series also includes the area 3, as mathematically demonstrated in [115]. In particular, for  $p = 0$  the modified Volterra series in (1.13) becomes a purely static nonlinear characteristic, whose validity is clearly limited to low-frequency operations (area 4). However, the modified series is also usable in strongly nonlinear operation provided that memory effects in the system are relatively short with respect to the signal frequency (i.e.,  $T_M \cdot \tilde{f}$  is small enough). To make the modified Volterra approach applicable to supply-modulated PAs, the formulation in (4.1) should be suitably extended for modulated signals in the envelope domain [118]. In addition, it should account for a condition in which not only an RF excitation is injected, but also a modulated baseband voltage is applied. Moreover, it should consider the presence of an additional port, as will be described in the next section.

## 4.3 Behavioral model formulation

### 4.3.1 Three-port quasi-static representation

An RF PA typically features RF input and output ports and two bias (gate and drain) ports. In the following, the gate bias port will not be considered (the developed model will only be valid for a pre-determined gate bias condition), while the drain bias port (i.e., the supply port) is an available input. As a consequence, three ports are considered, two of which will be excited at the RF, and one at LF (around dc). The baseband equivalent formulation of (3.5) is adopted for the description of incident and scattered waves at the RF ports. Therefore, the model only describes the bandpass behavior around a carrier  $f_0$ , while higher harmonics are not included. On the other hand, the baseband quantities at the supply port may be straightforwardly included in the model. In this way, since both RF envelopes and LF supply signals (i.e., voltage and current) share similar timescales (in the range of MHz), a coherency in the model description is obtained. The description of a general three-port device consists of three equations and six quantities (two each port). The two quantities at each port are, equivalently, the incident and scattered waves or the current and voltage (IV). In this work, the waves formalism has been adopted for the RF ports, while the IV formalism has been adopted at the supply port. However, one can transform the quantities from one representation to the other with well-known equations. As depicted in Fig. 4.2, the RF input and output ports will be indicated as port 1 and port 2, respectively. The supply port (operating at LF) is indicated as port 3. For each of the three ports, a controlling variable can be decided. As from typical PA operation, incident powers are assumed as the controlling variables at the RF ports, while the voltage is the controlling variable at port 3. Given such considerations, a three-port description of the PA is provided as follows:

$$\begin{cases} b_1(t) = J[a_1(t), a_2(t), v_3(t)] \\ b_2(t) = H[a_1(t), a_2(t), v_3(t)] \\ i_3(t) = K[a_1(t), a_2(t), v_3(t)] \end{cases} \quad (4.2)$$

where  $a_1(t)$  and  $a_2(t)$  are, respectively, the incident waves at port 1 and 2, while  $b_1(t)$  and  $b_2(t)$  are, respectively, the scattered waves at port 1 and 2. Finally,  $v_3(t)$  and  $i_3(t)$  are the voltage and current at port 3. To the aim of the behavioral modeling approach presented here and as depicted in Fig. 4.2, both port 1 and port 2 have been considered as perfectly matched to the input and output impedances of the PA (i.e.,  $50 \Omega$ ). As a consequence,  $a_1(t) = 0$  and  $b_1(t) = 0$ . Thus, the first equation of (4.2) can be discarded, obtaining the

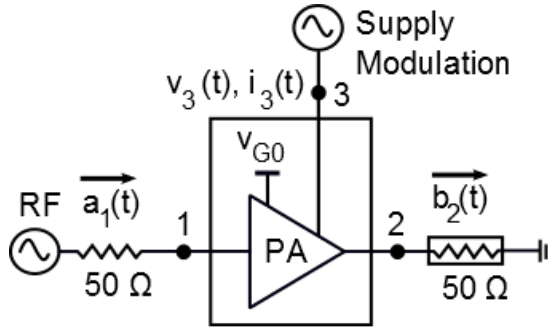


Figure 4.2: Representation of the PA as a three-port device. The supply port represents the third port and is excited by a modulated supply.

following formulation:

$$\begin{cases} b_2(t) = H[v_3(t), a_1(t)] \\ i_3(t) = K[v_3(t), a_1(t)] \end{cases} \quad (4.3)$$

where only the order of dependencies has been changed for a clearer development of the next mathematical steps. Both  $b_2(t)$  and  $i_3(t)$  should be considered, in general, as nonlinear dynamic functions of the controlling quantities  $v_3(t)$  and  $a_1(t)$ . Let us assume, at first, to model the behavior of the PA through quasi-static functions of the inputs. The expression in (4.3) is straightforwardly mapped into:

$$\begin{cases} b_2(t) = H_S[v_3(t), |a_1(t)|]a_1(t) \\ i_3(t) = K_S[v_3(t), |a_1(t)|] \end{cases} \quad (4.4)$$

where  $H_S$  and  $K_S$  are the two quasi-static functions. Despite its simplicity, the approach in (4.4) is widely followed in literature to model supply-modulated PAs. In fact, the first equation in (4.4) consists of complex AM/AM-AM/PM characteristics extended under a set of fixed supply voltages. The second equation, instead, is a simple real function of a real variable. When dealing with large-bandwidth signals, the quasi-static approximation might not be applicable, as memory effects influence the RF input-output nonlinearity. Those phenomena are yet worsened in presence of dynamic supply modulation. As already pointed out in section 4.1, time-variant loading conditions are occurring at the interface between the supply modulator and the RF PA drain port at baseband frequencies, up to tens of MHz. Furthermore, even in PAs specifically designed for supply modulation, RF inductive chocking and decoupling capacitive effects might still be present for stability reasons. Therefore, another independent source

of dynamic effects impacts both the supply current and the RF output power. On the basis of these considerations, the idea is extending the model in (4.4) to include memory effects by means of a first-order truncation of the modified Volterra series. A number of works have shown the approach of separately modeling the dynamic deviations in RF PAs through various formulations [116],[119],[126],[203]. In this work, superposition of dynamic effects due to both  $a_1(t)$  and  $v_3(t)$  is included in a unique nonlinear dynamic model.

### 4.3.2 RF excitation

At first, let us consider the RF input excitation  $a_1(t)$ . Equation (4.4) can be extended to account for a first order approximation around a large-signal operating point set by  $a_1(t)$ ,  $v_3(t)$ , obtaining the following:

$$\begin{cases} b_2(t) = H_S[v_3(t), |a_1(t)|]a_1(t) + \Delta_{21}(t) \\ i_3(t) = K_S[v_3(t), |a_1(t)|] + \Delta_{31}(t). \end{cases} \quad (4.5)$$

The term  $\Delta_{21}(t)$  is a dynamic deviation which accounts for the nonlinear memory with respect to  $a_1(t)$ . By assuming a maximum memory duration of  $T_{M1}$ , it can be made explicit as [118]:

$$\begin{aligned} \Delta_{21}(t) = & \int_0^{T_{M1}} h_{21}[v_3(t), |a_1(t)|, \tau] \{a_1(t - \tau) - a_1(t)\} e^{-j2\pi f_0 t} d\tau \\ & + a_1^2(t) \int_0^{T_{M1}} \tilde{h}_{21}^*[v_3(t), |a_1(t)|, \tau] \{a_1^*(t - \tau) - a_1^*(t)\} e^{j2\pi f_0 t} d\tau. \end{aligned} \quad (4.6)$$

The two additive terms in (4.6) account for the direct and the complex conjugate contribution of the complex RF input envelope  $a_1(t)$  to the RF output envelope  $b_2(t)$ . The two complex kernels  $h_{21}$  and  $\tilde{h}_{21}$  are functions to be suitably identified. It is worth noting that the first term in (4.6) is here taking into account both the linear and nonlinear memory effects, while in the derivation previously published in [118] these were separated into different contributions. Furthermore, unlike the previous formulations adopted in literature [116],[118],[119],  $\Delta_{21}$  is also a function of  $v_3(t)$ , as it represents a deviation around the large-signal quasi-static condition, which is not only set by the RF input wave, but also by the instantaneous supply voltage. In (4.4), the supply current  $i_3(t)$  is expressed as a quasi-static dependency of the same controlling variables  $v_3(t)$  and  $a_1(t)$ . In fact, the dynamic current drained by the PA is also affected by its nonlinear dynamic behavior, and a general expression of the dynamic deviation  $\Delta_{31}(t)$  of

$i_3(t)$  with respect to the RF output signal  $a_1(t)$  can be expressed as:

$$\begin{aligned} \Delta_{31}(t) = & a_1^*(t) \int_0^{T_{M1}} k_{31}[v_3(t), |a_1(t)|, \tau] \{a_1(t - \tau) - a_1(t)\} e^{-j2\pi f_0 t} d\tau \\ & + a_1(t) \int_0^{T_{M1}} k_{31}^*[v_3(t), |a_1(t)|, \tau] \{a_1^*(t - \tau) - a_1^*(t)\} e^{j2\pi f_0 t} d\tau \end{aligned} \quad (4.7)$$

in which the two terms represent the direct and the conjugate contributions to the current due to the complex RF input modulated envelope. In particular, the presence of the conjugates accounts for the down-conversion effect from RF to baseband. It should be noted that in (4.6), the output quantity  $b_2(t)$  is complex, and, as a consequence, two separate kernels  $h$  and  $\tilde{h}$  should be considered to reproduce the nonlinear and dynamic effects of the complex input. In (4.7), instead, the output quantity to be predicted  $i_3(t)$  is real-valued. As a consequence, a single complex kernel  $\tilde{k}$  allows to determine the nonlinear and dynamic effects of  $a_1(t)$  contributions on  $i_3(t)$ . Moreover, the proposed formulation is more general than simply accounting for a dynamic dependency with respect to the amplitude  $|a_1(t)|$ , which would involve a simple real function as a kernel. In (4.7), conversely, different dynamic contributions are separately accounted either if they come from a lower or from an upper side-band modulation of  $a_1(t)$ . The formulation of (4.6) and (4.7) fully account for the first order effects of a modulated RF input. However, a modification which does not involve any approximation from the analytical point of view, but that will be important from the empirical identification perspective, can be applied to (4.7). In general, the drained current  $i_3(t)$  is strictly correlated with the delivered output power. When described with respect to the RF input, in fact, the dynamic drain current would inevitably carry the full nonlinear dynamic response of the PA, whose effects are often quite similar to the ones determined on the RF output power. This would mean that similar modeling is performed two times for the two equations in (4.5). It should make sense, thus, to describe it as dependent on  $b_2(t)$  instead of on  $a_1(t)$ . To do so, one should consider the quasi-static equation of the output power (first in (4.4)). In standard operation, the quasi-static relationship between  $a_1(t)$  and  $b_2(t)$  can be considered monotonic for any  $v_3(t)$ , thus bi-univocal and analytically invertible:

$$a_1(t) = H_s^{-1}[v_3(t), |b_2(t)|] b_2(t) \quad (4.8)$$

where  $a_1(t)$  is obtained as a result of a quasi-static model inversion. With the dependency on  $v_3(t)$  still standing, the quasi-static prediction of the current can be equivalently written as a function of the quasi-static prediction of the RF output wave. The quasi-static formulation of (4.4) can thus acquire the

following form:

$$\begin{cases} b_2(t) = H_S[v_3(t), |a_1(t)|]a_1(t) \\ i_3(t) = K_S^o[v_3(t), |b_2(t)|] \end{cases} \quad (4.9)$$

where  $K_S^o \neq K_S$  accounts for the new dependency. The formulation in (4.9) — equivalent to (4.4) — explicitly relates the output power and the drained current. Moreover, (4.9) is a more suitable formulation for predistortion, in which the algorithms are normally computed starting from the output power as known variable. The second equation in (4.5), including the dynamic deviation, can be accordingly re-written as:

$$i_3(t) = K_S^o[v_3(t), |b_2(t)|] + \Delta_{31}^o(t) \quad (4.10)$$

where  $\Delta_{31}^o$  is obtained by accounting the inversion in (4.8):

$$\Delta_{31}^o(t) = \Delta_{31}(t)|_{a_1(t)=H_s^{-1}[v_3(t), |b_2(t)|]b_2(t)} \quad (4.11)$$

and can be explicitly written as:

$$\begin{aligned} \Delta_{31}^o(t) = & b_2^*(t) \int_0^{T_{M1}} k_{31}[v_3(t), |b_2(t)|, \tau] \{b_2(t - \tau) - b_2(t)\} e^{-j2\pi f_0 t} d\tau \\ & + b_2(t) \int_0^{T_{M1}} k_{31}^*[v_3(t), |b_2(t)|, \tau] \{b_1^*(t - \tau) - b_2^*(t)\} e^{j2\pi f_0 t} d\tau. \end{aligned} \quad (4.12)$$

where the kernel  $k_{31} \neq \tilde{k}_{31}$  accounts for the new dependency. However, the same analysis discussed for  $\Delta_{31}(t)$  in (4.7) equally applies to the  $\Delta_{31}^o(t)$  in (4.12). Finally, the nonlinear dynamic modeling for an RF excitation can be summarized in the following system of equations:

$$\begin{cases} b_2(t) = H_S[v_3(t), |a_1(t)|]a_1(t) + \Delta_{21}(t) \\ i_3(t) = K_S^o[v_3(t), |b_2(t)|] + \Delta_{31}^o(t). \end{cases} \quad (4.13)$$

In the next subsection, the extension of (4.13) to account for a dynamic supply voltage will be discussed.

### 4.3.3 Supply port excitation

The effects of a dynamic supply voltage are suitably introduced in the model by following the modified Volterra approach and leveraging on its superior

approximation of the dynamic effects under nonlinear operation. As already described in the previous section, the dynamic deviations due to the RF input signal are introduced as a linearization around a LSOP set by  $v_3(t)$  and  $a_1(t)$ . In these conditions, one may consider a superposition of dynamic deviations' effects on the outputs, regardless of the inputs that generate them. Indeed, such an hypothesis holds as long as that the dynamic deviations involved are small enough (which is often the case, as described in section 4.2). This approach allows to model the nonlinear dynamic effects produced not only by the RF input, but also by the supply modulation. These are introduced in (4.13) with a further superposition of perturbations on the outputs of the model:

$$\begin{cases} b_2(t) = H_S[v_3(t), |a_1(t)|]a_1(t) + \Delta_{21}(t) + \Delta_{23}(t) \\ i_3(t) = K_S^o[v_3(t), |b_2(t)|] + \Delta_{31}^o(t) + \Delta_{33}^o(t) \end{cases} \quad (4.14)$$

where the added terms  $\Delta_{23}(t)$  and  $\Delta_{33}^o(t)$  account separately for the dynamic dependency of  $b_2(t)$  and,  $i_3(t)$  respectively, due to the dynamic voltage supply. It is noteworthy that  $b_2(t)$  and  $i_3(t)$  are, in general, independently influenced by a dynamic  $v_3(t)$ . For example, the dynamic dependency of the supply current also appears - depending on the circuitry at the PA supply port - at small RF signal. However, the up-converted intermodulation distortion and its dynamic behavior shows up at the RF output only with increasing compression, such as in a mixer-like operation. By assuming a memory duration  $T_{M3}$ , the contribution  $\Delta_{23}(t)$  is made explicit as:

$$\Delta_{23}(t) = a_1(t) \int_0^{T_{M3}} h_{23}[v_3(t), |a_1(t)|, \tau] \{v_3(t - \tau) - v_3(t)\} d\tau \quad (4.15)$$

where  $h_{23}$  is a complex kernel function. The term (4.15) accounts for the up-conversion of the low-frequency excitation at the supply to the RF output. By means of a first order mixing product between  $v_3(t)$  and  $a_1(t)$ , the function  $h_{23}$  maps the variations at the baseband frequency, at which a dynamic supply is applied, into variations around  $f_0$ , represented as baseband-equivalent. Indeed, since the excitation is a real-valued signal, any difference between the low side and the higher side of the RF output power spectrum is due to the nonlinear dynamic behavior of the PA, and is accounted for by the single complex term  $h_{23}$ . The dynamic effects of the supply voltage  $v_3(t)$  on  $i_3(t)$  are modeled through a baseband relationship expressed in terms of the dynamic deviation:

$$\Delta_{33}^o(t) = \int_0^{T_{M3}} k_{33}[v_3(t), |b_2(t)|, \tau] \{v_3(t - \tau) - v_3(t)\} d\tau \quad (4.16)$$

with  $k_{33}$  being a real-valued kernel function dependent on the LSOP. The same transformation (4.8) applied to express the dependency of  $i_3(t)$  on  $b_2(t)$  is here implemented. Notably, the combination of  $K_S^o$  and  $k_{33}$  represents a nonlinear,

admittance-like relationship between the current and the voltage at the supply port, which models the supply port of the PA working in nonlinear operation, under modulated signals. In other words, the convolution involving  $k_{33}$ , provides a formal formulation to the term  $Z_{PA}$ , which was informally introduced in section 3.4 as a frequency-domain characterization technique. More on the interpretation of the results presented in section 3.4 with the modeling approach presented in this section will be discussed in section 4.4. It is noteworthy that the modified Volterra series truncated to a first order term as formulated in (4.14) formally provides a framework for a large-signal extension of  $S$ -parameters. This is a widely addressed topic in the literature, which has culminated with the  $S$ -functions [204] and  $X$ -parameters [47] formulations. With respect to  $X$ -parameters, the presented formulation models the nonlinear dynamic behavior on a bandwidth around a carrier, or around dc. Yet, there is no formal limitation to this, and the formulation can be ultimately extended in order to cover, in theory, an arbitrarily wide frequency spectrum, possibly organized as multiple frequency bands around multiple carriers. In such a case, one should provide all mixing frequency contributions due to the excitations involved. This kind of extension, however, it is out of the scope of this dissertation. By recalling the discussion in section 4.2, a few more words can be spent on the final formulation of the behavioral model in (4.14). The model is symmetrical in accounting for the dynamic deviations due to the RF and supply inputs. Moreover, as it inherits the modified Volterra convergence properties, it can be proven that [118]:

$$|a_1(t - \tau) - a_1(t)|_{max} \leq \min \left\{ T_{M1} \cdot \left| \frac{da_1(t - \tau)}{dt} \right|, A_{1pp} \right\} \quad (4.17)$$

$$|v_3(t - \tau) - v_3(t)|_{max} \leq \min \left\{ T_{M3} \cdot \left| \frac{dv_3(t - \tau)}{dt} \right|, V_{3pp} \right\} \quad (4.18)$$

where  $A_{1pp}$ ,  $V_{3pp}$  are, respectively, the peak-to-peak amplitudes of the RF signal envelope  $a_1(t)$  and of the supply voltage  $v_3(t)$ . Thus, the dynamic deviations (4.17) and (4.18) are small, allowing a first order approximation without involving relevant errors, either when:

1. the amplitudes  $A_{1pp}$ ,  $V_{3pp}$  are small, whatever being the input signal bandwidths;
2. the amplitudes  $A_{1pp}$ ,  $V_{3pp}$  are large, but the input waveforms feature a moderately small-bandwidth in relation with the relatively long duration of the nonlinear memory effects  $T_{M1}$ ,  $T_{M3}$ .

Thus, the dynamic deviations are small not only when the input signal amplitudes are small (e.g., perturbations of a LSOP), but also when the

variations of the signal amplitudes are large, but slow enough in relation to the nonlinear memory effects duration in the PA. From this point of view, whatever identification signals are used, they should not lead to think in terms of a limited range of applicability of the model, which is instead consistently wider. The combination of a simple yet orthogonal extraction (i.e., each measurement sample brings independent yet necessary information for modeling) and a wider range of applicability distinguish this modeling approach with respect to the others found in the literature. Again, it should be noted that no approximation is done on the quasi-static nonlinear functions  $H_S$  and  $K_g^o$  in (4.14). In addition, it is worth recalling that the approach introduces no approximation on the linear dynamics either. This is fully accounted for by the memory kernels, which in this case become independent of the amplitudes, simplifying the model dynamic terms into linear convolutions. A higher order model approximation would be needed only in the case of input signal variations featuring both high-bandwidth and large amplitudes. However, a higher order approximation is obtained at the cost of a sensibly higher complexity in the model formulation, implementation and identification (which often may not be engineered as an orthogonal identification procedure, leading to estimation problems). The first order approximation tested in this research proved to provide a good compromise between complexity and accuracy. In section 4.4, a method to independently identify and directly measure the dynamic kernels of the deviations terms in (4.14) will be described.

## 4.4 Model identification procedure

### 4.4.1 Frequency-domain model re-formulation

The identification of the kernels of the modified Volterra series has already been a topic of research, and results are available in the literature [205]. In particular, two approaches have been presented. One, followed by Mirri *et al.* [118], performs the identification in the frequency domain. The others, followed by Soury *et al.* [203], makes use of pulse-modulated RF signals and evaluates the transient in time-domain. In this work, the frequency-domain approach has been used. This choice is mainly driven by the available measurement set-up. In fact, as will be more precisely documented in section 4.5.1, the LF-LSNA set-up has been used. As described in section 3.2.2, the LF-LSNA works on a discrete frequency grid for a maximum of 20 MHz modulation around the harmonics. Although a number of works have shown pulsed RF measurements performed on LSNA architectures [157], the presence of a discrete frequency grid and limitations in terms of measurable bandwidth do not allow

a straightforward synthesis of pulsed RF identification signals. On the other hand, a frequency-domain approach not only allows characterizing the full available bandwidth with a preferred frequency resolution, but it also permits an orthogonal identification of the kernels, as already anticipated in section 4.3. Indeed, similarly to [206], the main complication derives from accounting for the frequency conversion between the RF and LF excitations. First of all, the quasi-static functions  $H_S$  and  $K_S^o$  in (4.9) can be suitably identified by means of a continuous-wave (CW) characterization at constant supply voltages:

$$\begin{cases} B_2^{(0)} = H_S[V_3^{(0)}, |A_1^{(0)}|]A_1^{(0)} \\ I_3^{(0)} = K_S^o[V_3^{(0)}, |B_2^{(0)}|] \end{cases} \quad (4.19)$$

where the superscript  $\cdot^{(0)}$  indicates the dc term of the Fourier series signals representation. In other words, in (4.19), both the supply voltage  $v_3(t) = V_3^{(0)} = V_{30}$ , the drain current  $i_3(t) = I_3^{(0)} = I_{30}$ , and the RF complex input  $a_1(t) = A_1^0$  and output  $b_2(t) = B_2^0$  envelopes are constant. This means that a CW characterization ( $\mathcal{A}_1(t) = \Re\{A_1^0 e^{j2\pi f_0 t}\}$ ,  $\mathcal{B}_2(t) = \Re\{B_2^0 e^{j2\pi f_0 t}\}$ ) is performed over a swept number of constant supply voltages. As for the dynamic deviations, five kernels —  $h_{21}$ ,  $\tilde{h}_{21}$ ,  $h_{23}$ ,  $k_{31}$ , and  $k_{33}$  — must be identified in an independent way to obtain the model in (4.14). First of all, it is useful to reformulate the kernels in the frequency domain, expressing them with respect to a frequency modulation  $\nu$ . To do so, let us consider the  $\Delta_{21}(t)$  from (4.6). By expressing in frequency the dynamic deviation of the RF input envelope  $a_1(t)$ , we obtain:

$$a_1(t - \tau) - a_1(t) = \int_{BW} A_1(\nu) e^{j2\pi\nu t} (e^{-j2\pi\nu\tau} - 1) d\nu \quad (4.20)$$

$$a_1^*(t - \tau) - a_1^*(t) = \int_{BW} A_1^*(\nu) e^{-j2\pi\nu t} (e^{j2\pi\nu\tau} - 1) d\nu \quad (4.21)$$

where  $BW$  is the bandwidth of interested swept by  $\nu$ . The two additive terms in (4.6) should be considered separately. By using (4.20), the first one results in:

$$\begin{aligned} & \int_0^{T_{M1}} h_{21}[v_3(t), |a_1(t)|, \tau] \int_{BW} A_1(\nu) e^{j2\pi\nu t} (e^{-j2\pi\nu\tau} - 1) e^{-j2\pi f_0 \tau} d\nu d\tau \\ &= \int_{BW} A_1(\nu) e^{j2\pi\nu t} \int_0^{T_{M1}} h_{21}[v_3(t), |a_1(t)|, \tau] (e^{-j2\pi\nu\tau} - 1) e^{-j2\pi f_0 \tau} d\tau d\nu. \end{aligned} \quad (4.22)$$

The integral in  $\tau$  in (4.22) can be considered as the difference between two values of a function  $H_{21}(f)$ , evaluated at the incremental frequencies ( $f_0, f_0 + \nu$ )

[118]:

$$\begin{aligned}
& \int_0^{T_{M1}} h_{21}[v_3(t), |a_1(t)|, \tau](e^{-j2\pi(f_0+\nu)\tau} - e^{-j2\pi f_0\tau})d\tau \\
& \doteq H'_{21}[v_3(t), |a_1(t)|, f_0 + \nu] - H'_{21}[v_3(t), |a_1(t)|, f_0] \\
& \doteq H_{21}[v_3(t), |a_1(t)|, f_0 + \nu].
\end{aligned} \tag{4.23}$$

By using (4.21) in the second term of (4.6), the same procedure can be applied for  $\tilde{h}_{21}$ :

$$\begin{aligned}
& \int_0^{T_{M1}} \tilde{h}_{21}^*[v_3(t), |a_1(t)|, \tau] \int_{BW} A_1^*(\nu) e^{-j2\pi\nu t} (e^{j2\pi\nu\tau} - 1) e^{j2\pi f_0\tau} d\nu d\tau \\
& = \int_{BW} A_1(\nu) e^{-j2\pi\nu t} \int_0^{T_{M1}} \tilde{h}_{21}^*[v_3(t), |a_1(t)|, \tau] (e^{j2\pi\nu\tau} - 1) e^{j2\pi f_0\tau} d\tau d\nu.
\end{aligned} \tag{4.24}$$

Analogously to the previous case

$$\begin{aligned}
& \int_0^{T_{M1}} \tilde{h}_{21}[v_3(t), |a_1(t)|, \tau](e^{-j2\pi(f_0+\nu)\tau} - e^{-j2\pi f_0\tau})d\tau \\
& \doteq \tilde{H}'_{21}[v_3(t), |a_1(t)|, f_0 + \nu] - \tilde{H}'_{21}[v_3(t), |a_1(t)|, f_0] \\
& \doteq \tilde{H}_{21}[v_3(t), |a_1(t)|, f_0 + \nu]
\end{aligned} \tag{4.25}$$

and, by calculating the complex conjugate of (4.25), one obtains:

$$\tilde{H}_{21}[v_3(t), |a_1(t)|, f_0 + \nu] = \int_0^{T_{M1}} \tilde{h}_{21}^*[v_3(t), |a_1(t)|, \tau](e^{j2\pi(f_0+\nu)\tau} - e^{j2\pi f_0\tau})d\tau. \tag{4.26}$$

Now, by considering (4.23) and (4.26), one can write (4.6) in frequency domain:

$$\begin{aligned}
\Delta_{21}(t) & = \int_{BW} H_{21}[v_3(t), |a_1(t)|, f_0 + \nu] A_1(\nu) e^{j2\pi\nu t} d\nu \\
& + a_1^2(t) \int_{BW} \tilde{H}_{21}^*[v_3(t), |a_1(t)|, f_0 + \nu] A_1^*(\nu) e^{-j2\pi\nu t} d\nu
\end{aligned} \tag{4.27}$$

As for the other kernels, equivalent procedures can be followed to obtain:

$$\begin{aligned}
\Delta_{31}^o(t) & = b_2^*(t) \int_{BW} K_{31}[v_3(t), |b_2(t)|, f_0 + \nu] B_2(\nu) e^{j2\pi\nu t} d\nu \\
& + b_2(t) \int_{BW} K_{31}^*[v_3(t), |b_2(t)|, f_0 + \nu] B_2^*(\nu) e^{-j2\pi\nu t} d\nu
\end{aligned} \tag{4.28}$$

$$\Delta_{32}(t) = a_1(t) \int_{BW} H_{23}[v_3(t), |a_1(t)|, \nu] V_3(\nu) e^{j2\pi\nu t} d\nu \quad (4.29)$$

$$\Delta_{33}(t) = \int_{BW} K_{33}[v_3(t), |a_1(t)|, \nu] V_3(\nu) e^{j2\pi\nu t} d\nu. \quad (4.30)$$

It should be noted that  $BW$  is the modulation bandwidth of interest either around  $f_0$  or at baseband, and  $\nu$  is the modulation frequency excited by either a modulated RF input signal or a modulated voltage applied at the supply port, both of which, in general, perturbate the RF output and the drained current. For example, a small tone applied at the modulating frequency  $\nu$  around a LSOP instantaneously set by  $v_3(t)$  and  $a_1(t)$ , generates intermodulation products at both the output variables  $b_2(t)$  and  $i_3(t)$ . By sweeping  $\nu$  in the band of interest, the frequency response of the RF output and the supply current can be measured around each considered LSOP. Such kind of measurement, when applied at the supply node, is the same as the one presented in section 3.4 to characterize  $Z_{PA}$ . As a matter of fact, (4.30) (which corresponds, in time domain, to the convolution in (4.16)) represents the formal derivation of an impedance-like nonlinear function useful to describe the nonlinear dynamic behavior at the PA supply port. More precisely,

$$K_{33}[v_3(t), |a_1(t)|, \nu] = \frac{1}{Z_{PA}[v_3(t), |a_1(t)|, \nu]} = Y_{PA}[v_3(t), |a_1(t)|, \nu] \quad (4.31)$$

is a function, dependent on the LSOP, that describes the dynamic load presented by the PA under nonlinear operation. Such a value can be considered by the designers as the equivalent nonlinear dynamic loading conditions of the supply modulator.

#### 4.4.2 Frequency-domain kernels identification

In order to identify the full model, a small signal excitation should be applied either at the RF input or at the supply port to acquire two sets of independent data, so that the response can be used to separately identify the kernels of the dynamic deviations. A possible approach is depicted in Fig. 4.3. First (switch SWA and SWB in position 1 in Fig. 4.3), a modulated supply is applied to the PA, while the RF input is a CW excitation (constant envelope) at  $f_0$ , and terminated to  $50 \Omega$  at the other frequencies in the bandwidth of interest. In this way,  $A_1(\nu = 0) = A_1^{(0)}$ ,  $A_1(\nu \neq 0) = 0$  and the dynamic contributions measured for  $i_3(t)$  and  $b_2(t)$  are only due to the excitation at port 3. Then (switch SWA and SWB in position 2 in Fig. 4.3), a modulated RF input is applied at port 1; at the same time, only a dc voltage is applied at port 3, while terminating with a short at LF, meaning that  $V_3(\nu \neq 0) = 0$  and  $V_3(\nu = 0) = V_3^{(0)}$ . Let us consider the identification of kernels  $H_{21}$  and  $\tilde{H}_{21}$ . The supply voltage is set to

a constant value  $V_3^{(0)}$ . By applying an RF complex envelope signal excitation like

$$a_1(t) = A_1^{(0)} + \alpha e^{-j2\pi\nu t} \quad (4.32)$$

with  $|\alpha| \ll |A_1^{(0)}|$ , so that  $|a_1(t)| \simeq |A_1^{(0)}|$  a one-tone, small-signal modulation is applied at  $\nu \in [-\frac{BW}{2}, \frac{BW}{2}]$ . As consequence, the output equivalent complex envelope  $b_2(t)$  would include both sides of the spectrum accounting for the direct input amplification and the (third-order) intermodulation distortion at frequency  $-\nu$ . At the same time, a sinusoidal drain current is generated. Thus, we have:

$$b_2(t) = B_2^{(0)} + \delta e^{-j2\pi\nu t} + \chi e^{j2\pi\nu t} \quad (4.33)$$

$$i_3(t) = I_3^{(0)} + \rho \cos(2\pi\nu t) \quad (4.34)$$

At the RF output port, the ratios between complex signals at the two frequencies can thus be measured over the considered band by sweeping  $\nu$

$$W_1(V_3^{(0)}, |A_1^{(0)}|, \nu) = \frac{\delta}{\alpha} \quad (4.35)$$

$$W_2(V_3^{(0)}, |A_1^{(0)}|, \nu) = \frac{\chi}{A_1^{(0)2} \alpha^*}$$

and the two kernels in the frequency domain can be obtained by simply subtracting the value measured at narrowband modulation

$$H_{21}[V_3^{(0)}, |A_1^{(0)}|, f_0 + \nu] = W_1(V_3^{(0)}, |A_1^{(0)}|, \nu) - W_1(V_3^{(0)}, |A_1^{(0)}|, 0) \quad (4.36)$$

$$\tilde{H}_{21}^*[V_3^{(0)}, |A_1^{(0)}|, f_0 + \nu] = W_2(V_3^{(0)}, |A_1^{(0)}|, \nu) - W_2(V_3^{(0)}, |A_1^{(0)}|, 0)$$

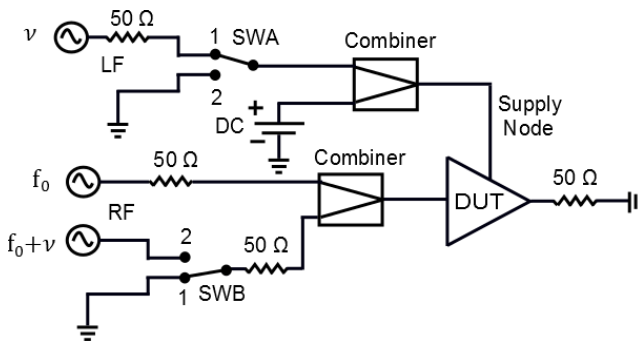


Figure 4.3: Schematic diagram of the experiments to identify the kernels from RF and LF excitations.

As for the current, its dynamics is described by  $K_{31}(\nu)$  in frequency domain with respect to the RF output. Both RF excitations in (4.33) must be accounted for to predict the modulated current. The function  $K_{31}$  can be identified by solving the following complex equation for every  $\nu \in [-\frac{BW}{2}, \frac{BW}{2}]$ , at each LSOP

$$W_3(V_3^{(0)}, |B_2^{(0)}|, \nu) B_2^{(0)*} \delta + W_3^*(V_3^{(0)}, |B_2^{(0)}|, \nu) B_2^{(0)} \chi^* = \rho. \quad (4.37)$$

From this, the representation in frequency domain can be obtained as follows:

$$K_{31}[V_3^{(0)}, |B_2^{(0)}|, f_0 + \nu] = W_3(V_3^{(0)}, |B_2^{(0)}|, \nu) - W_3(V_3^{(0)}, |B_2^{(0)}|, 0) \quad (4.38)$$

The same identification procedure can be performed to measure  $H_{23}$  and  $K_{33}$  if a small, voltage modulating tone is applied at the supply port at  $\nu \in [0, \frac{B}{2}]$ :

$$v_3(t) = V_3^{(0)} + \beta \cos(2\pi\nu t) \quad (4.39)$$

with  $|\beta| \ll |V_3^{(0)}|$ , so that  $|v_3(t)| \simeq |V_3^{(0)}|$ . At the same time, a constant envelope signal  $a_1(t) = A_1^{(0)}$  is applied at the RF input. As a consequence, the RF output envelope and the supply current will be

$$b_2(t) = B_2^{(0)} + \delta' e^{-j2\pi\nu t} + \chi' e^{j2\pi\nu t} \quad (4.40)$$

$$i_3(t) = I_3^{(0)} + \sigma \cos(2\pi\nu t). \quad (4.41)$$

At each sweep point of  $\nu$  in the bandwidth of interest, the modulations of  $b_2(t)$  and  $i_3(t)$  are measured. The kernels are thus straightforwardly identified with the same procedure previously followed:

$$W_4(V_3^{(0)}, |A_1^{(0)}|, \nu) = \frac{\delta'}{A_1^{(0)} \beta} \quad (4.42)$$

$$W_4(V_3^{(0)}, |A_1^{(0)}|, \nu) = \frac{\chi'}{A_1^{(0)} \beta^*}$$

$$W_5(V_3^{(0)}, |B_2^{(0)}|, \nu) = \frac{\sigma}{\beta} \quad (4.43)$$

so that one obtains:

$$H_{23}[V_3^{(0)}, |A_1^{(0)}|, \nu] = W_4(V_3^{(0)}, |A_1^{(0)}|, \nu) - W_4(V_3^{(0)}, |A_1^{(0)}|, 0) \quad (4.44)$$

$$K_{33}(V_3^{(0)}, |B_2^{(0)}|, \nu) = W_5(V_3^{(0)}, |B_2^{(0)}|, \nu) - W_5(V_3^{(0)}, |B_2^{(0)}|, 0)$$

Further details about the measurements performed will be given in section 4.5.1. Indeed, the smaller the frequency sweep step  $\Delta\nu$  around each LSOP,

the longer would be the memory modelled through the kernels. Although the model is identified by small perturbations around LSOPs, it should be clear that the range of applicability of the model exceeds the set of identification signals, and spans wider due to the features of the modified Volterra series, as extensively described in sections 4.2 and 4.3. The kernels are structured as nonlinear filters by implementing the transfer functions which nonlinearly change versus time. It is worth underlining that the model in (4.14) is presented through a baseband formulation (low-pass equivalent for the RF equation). As such, the approach can be directly mapped into the discrete-time domain. The topology of the model is thus similar to the ones in literature [99], and can be easily implemented in either time or frequency domain in modern CAD tools. In the next section, the experimental identification and validation of the model is addressed.

## 4.5 Experimental results

### 4.5.1 Characterization of the kernels

During this research, the identification and validation of the model described in section 4.3 has been performed with the LF-LSNA presented in section 3.2.2. As already described, this instrument allows absolute amplitude and phase measurements on a 20 MHz bandwidth around harmonics at RF and dc. Moreover, it is worth recalling from section 3.2.2 that the dc and ac components of dynamic supply voltage can be separately applied through a bias-tee, by means of a bias supply and a 50  $\Omega$ -terminated AWG. The validation of the model under concurrent excitation at both the RF input and at the supply node was instead done by using both the RF and the IF output of a vector signal generator. Such a configuration allows to generate multi-tone at both ports, obtaining excitations such as the ones in Fig. 4.4(a). Despite the fact that the 20 MHz bandwidth is limited with respect to the nominal bandwidths implemented by the latest telecommunication standards, and although such way of sensing and generating the signals at the supply node does not allow to apply spectral components indefinitely close to dc, the choice of using this set-up was obligated, as no other ready instrumentation with the requested characteristics was available at the beginning of the research. Unfortunately, no time was left to perform the same model identification measurements on the set-ups more recently built and more tailored to the application, such as the ones described in section 3.3. Nevertheless, the LF-LSNA allowed to test the full flow of model identification and validation, as described in sections 4.5.1 and 4.5.2. The DUT used in this work is the GaAs-based handset amplifier already

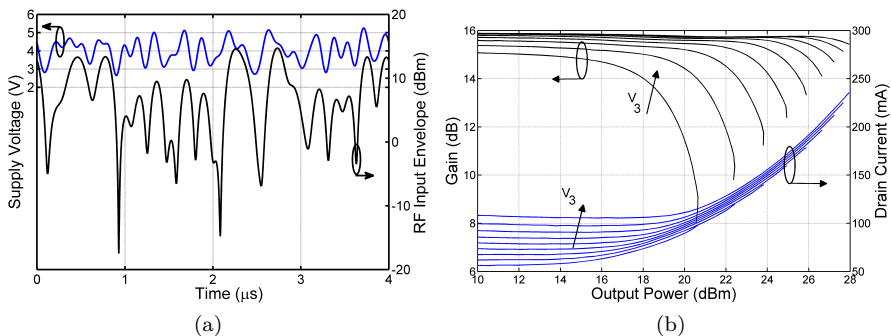


Figure 4.4: (a) Quasi-static modeling. (b) 25-tone excitation at RF and supply ports.

used for the characterization in section 3.4, which features coaxial connectors at both the RF ports and at the supply. The carrier frequency is  $f_0 = 0.95$  GHz. All tests have been performed by biasing the PA at nearly class AB operation ( $I_D^{(0)} = 60$  mA). The PA features an RF output power of 28 dBm and a compression point  $P_{in}^{1dB} = 10$  dBm when supplied with  $V_3^{(0)} = 4$  V. The next section is dedicated to the empirical extraction of the kernels, while the validation of the model is presented in section 4.5.2. The identification of the kernels follows the procedure described in the previous section. The sinusoidal excitation needed at the supply port is applied through the AWG in [172]. At RF, instead, two sinusoidal excitations (one large-signal at the carrier  $f_0 = 0.95$  GHz, the other, small-signal, swept over  $BW$ ) are generated by two separate CW sources and combined by means of a broadband combiner. First, a static characterization of the PA at the various supply voltages is obtained under standard CW operation (Fig. 4.4(b)). Then, multiple measurement sweeps have been programmed to obtain the model kernels, while off-line post-processing in MATLAB allowed to determine the dynamic deviations functions, following the calculations of section 4.4. The model identification is performed over  $V_3^{(0)} \in [2, 6]$  V with step 0.5 V and RF  $P_{in} \in [-20, 12]$  dBm. The chosen frequency step for the frequency identification is  $\Delta\nu = 100$  kHz, which over a 20 MHz bandwidth means 200 frequency points. The RF small signal for the identification applied around the RF carrier is -20 dBc with respect to the large-tone. At the supply port, the amplitude of the small signal dynamic voltage was  $V_3(\nu) = 10$  mV. All experimental data are stored in look-up tables and suitably interpolated through spline functions. Third and fifth order polynomial interpolations of data have also been tested, without critical difference with respect to the spline interpolation. No redundant measurements are taken, nor other processing on the acquired data is performed, apart from the identification

steps outlined in section 4.4. In order to improve the interpolation accuracy, more dense measurement grids or other interpolation techniques may be considered, depending on the application. In case of measurement noise in the obtained results, redundant measurements coupled with optimization techniques (e.g., least-square methods) may be used. The extracted kernels are reported as function of the modulation frequency and of the RF  $P_{in}$  (at fixed  $V_3^{(0)} = 5\text{V}$ ) in Figs. 4.5 and 4.6, and as function of RF  $P_{IN}$  and supply voltage (at fixed modulation frequency  $\nu = 8\text{ MHz}$ ) in Fig. 4.7. Such plots are the direct results of LSNA acquisitions. As expected, all kernels are equal to zero at  $\nu = 0$ .

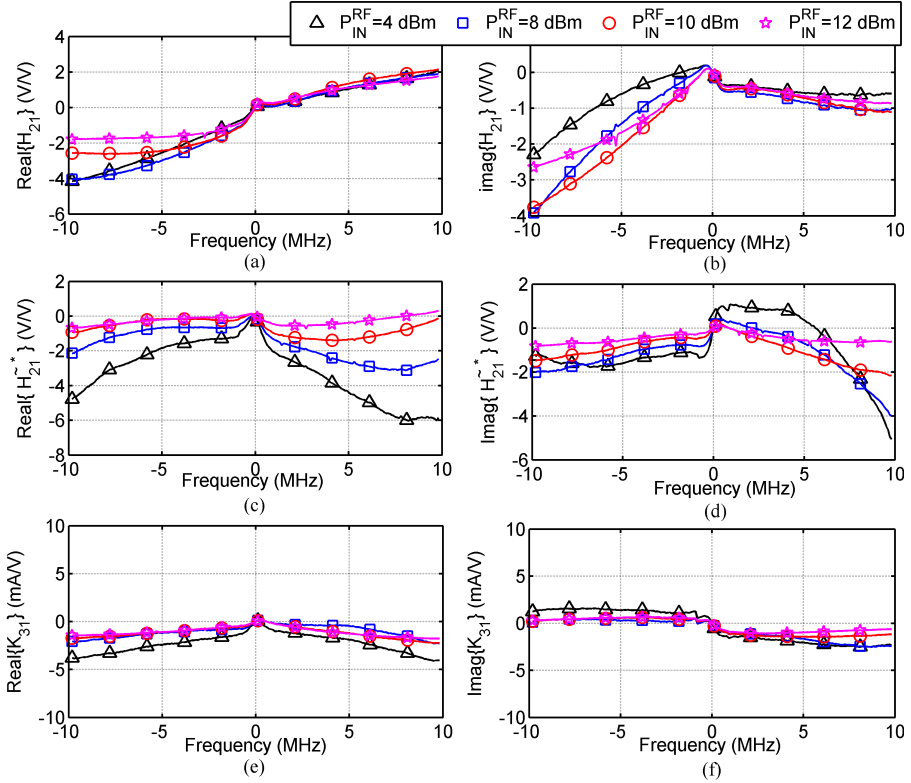


Figure 4.5: Dynamic deviation functions due to the RF input excitation at port 1, measured in frequency domain.  $H_{21}$  [(a) and (b)] and  $\tilde{H}_{21}$  [(c) and (d)] are measured around at port 2.  $K_{31}$  [(e) and (f)] is measured around dc at port 3. Plots correspond to a  $V_3^{(0)} = 5\text{ V}$ . The input  $P_{in}$  is indicated in the legend,  $\Delta\nu = 100\text{ kHz}$ .

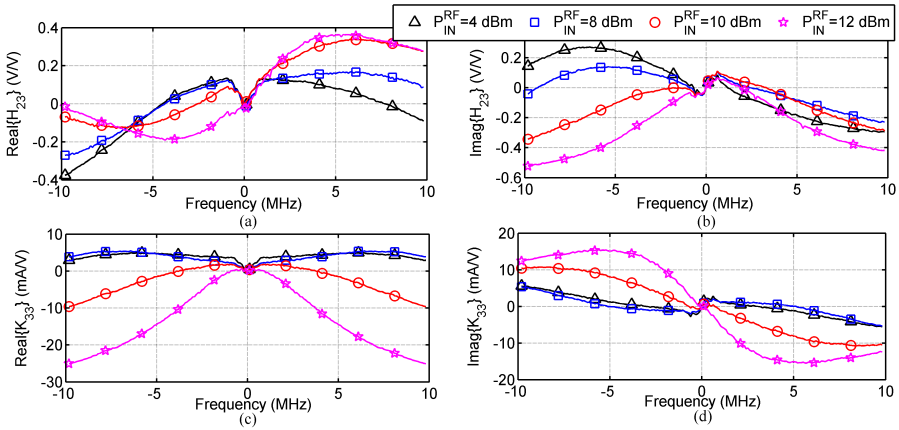


Figure 4.6: Dynamic deviation functions due to the dynamic supply excitation at port 3, measured in frequency domain.  $H_{23}$  [(a) and (b)] is measured around  $f_0$  at port 2.  $K_{33}$  [(c) and (d)] is measured around dc at port 3. Plots correspond to a  $V_3^{(0)} = 5$  V. The input  $P_{in}$  is indicated in the legend,  $\Delta\nu = 100$  kHz.

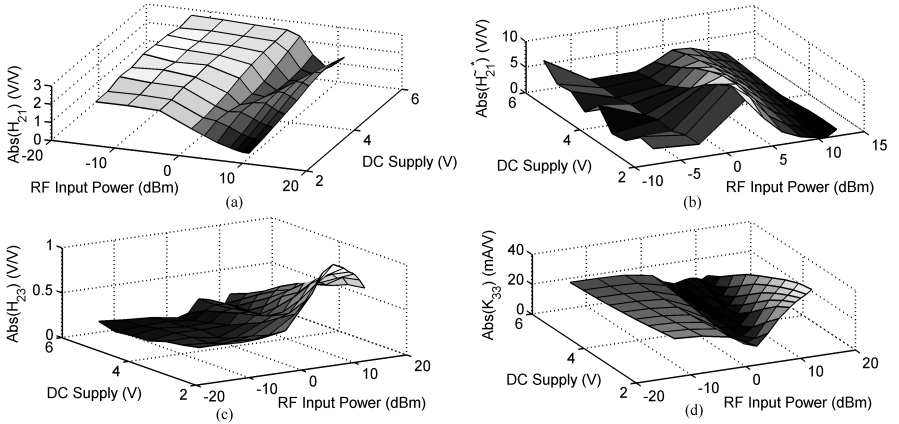


Figure 4.7: Absolute values of the dynamic deviation functions  $H_{21}$ ,  $\tilde{H}_{21}$ ,  $H_{23}$ , and  $K_{33}$  plotted versus RF  $P_{in}$  and dc supply voltage. Plots correspond to  $\nu = 8$  MHz.

In fact, under quasi-static operation the PA is completely described through the purely-algebraic functions  $H_S$  and  $K_S^o$ . As the modulating frequency increases, various sources of memory effects arise and mix together. These are

for instance due to matching and bias networks, as well as thermal or other dispersive effects. A straightforward interpretation of the contribution due to each dynamic phenomenon to the individual kernels is not possible, and should be coupled with techniques such as the one described in section 3.6. However, the kernels allow describing in a separate way the purely-dynamic effects involved in each path between an input and an output port of the PA. The kind of dependency of each kernel on the independent variables gives also critical information. For instance, a mild dependency on RF input power indicates that an almost linear kind of dynamics is involved in the input/output path considered. Kernel  $H_{21}$  represents the direct RF amplification in large-signal conditions; as such, its plot (see Fig. 4.7) resembles a gain curve versus RF  $P_{in}$ . Kernel  $\tilde{H}_{21}$  is the RF-to-RF third-order (also referred as conjugate contribution) side product of a complex modulation under large-signal operation. It sharply increases versus RF input power; eventually, both  $H_{21}$  and  $\tilde{H}_{21}$  compress for larger values of the RF  $P_{in}$  and smaller values of supply voltage. Kernel  $K_{31}$  models the effects of the RF output power on the supply current, which results in a few mA for the PA considered in this work. The baseband-to-RF transfer function  $H_{23}$  is maximum at the maximum level of compression, similarly to what is observed in a mixer-like operation. This kernel is proportional to the RF  $P_{in}$  and inversely proportional to the supply voltage. Finally,  $K_{33}$  is flat as far as transistor threshold and knee-voltage are not touched by the RF load line; then, it decreases as soon as the threshold voltage is reached, and increases again when reaching the knee-voltage, so showing a dependency on the supply voltage.

## 4.5.2 Model validation

An off-line model implementation and validation in MATLAB is performed, and the dynamic deviations formulation in (4.27)-(4.30) was applied in an analytical way for periodic excitations. For a real-time implementation, the time-domain formulation in (4.14) shall be considered, in which the dynamic deviations can be straightforwardly mapped into standard finite impulse response (FIR) nonlinear filters topologies. A real-time processing technique is proposed in section 4.6.2. Considering that the LSNA measures periodic waveforms, random phase multi-tones (e.g., see Fig. 4.4(a)), widely used to stimulate high-order PA nonlinearities [97] are used to validate the performance of the model. Furthermore, given the limitation of 20 MHz as measurable bandwidth, signals with maximum bandwidth of 5 MHz could be tested. This has been a choice of compromise between the need of properly reconstructing the distorted signal, while keeping a signal bandwidth large enough to test the dynamic capability of the model. Once the model kernels are identified, they are saved

and used for all other excitation sets. While the model identification only requires small perturbation around a quasi-static LSOP, the model capabilities are tested under full-bandwidth large-amplitude modulated signals and supply modulation, within the amplitude and frequency limits imposed by the used set-up. Even though tuned models may, in theory, provide very accurate results for specific excitations, the proposed approach targets a sufficient prediction capability without the need to update the model coefficients. This should be kept in mind when evaluating the model accuracy. In order to highlight the nonlinear dynamic behavior of the PA and assess the specific prediction capability of the model, the undistorted behavior of the PA (i.e., small signal behavior) has been isolated by defining  $b_2^{SS}(t) = H^{SS}a_1(t)$ , with  $H^{SS} = |H^{SS}|e^{j\phi(H^{SS})}$  being the complex gain under small-signal behavior, operatively defined as:

$$\begin{cases} |H^{SS}| = |H_S[V_{3n}^{(0)}, 0]| \\ \phi(H^{SS}) = -2\pi ft_0, \end{cases} \quad (4.45)$$

with

$$t_0 = \left. \frac{\partial H_S[V_{3n}^{(0)}, 0]}{\partial f} \right|_{f_0} \quad (4.46)$$

where  $V_{3n}^{(0)}$  is the nominal supply voltage and  $a_1 \rightarrow 0$  to guarantee small-signal operation. Then, the instantaneous output distortion can be defined as

$$\delta(t) = b_2(t) - b_2^{SS}(t) \quad (4.47)$$

being  $\delta(t)$  the deviation from the small-signal operation. Thus, the prediction of the instantaneous output distortion obtained by using only the quasi-static approximation ( $\delta_{QS}(t)$ ) and the one ( $\delta_{DYN}(t)$ ) obtained by also accounting for the dynamic kernels are defined analogously as

$$\delta_{QS}(t) = b_2^{QS}(t) - b_2^{SS}(t) \quad (4.48)$$

$$\delta_{DYN}(t) = b_2^{DYN}(t) - b_2^{SS}(t) \quad (4.49)$$

where  $b_2^{QS}(t)$  is the RF output envelope predicted by the quasi-static model and  $b_2^{DYN}(t)$  is the RF output envelope predicted by the full nonlinear dynamic model. Thus, the static and dynamic models' capability of predicting the RF output are assessed by means of the normalized mean square error (NMSE) between the measured and the modeled instantaneous output distortions

$$NMSE_{QS}(dB) = 10 \log \left( \frac{\int_0^\infty |\delta_{QS}(t) - \delta(t)|^2 dt}{\int_0^\infty |\delta(t)|^2 dt} \right) \quad (4.50)$$

$$NMSE_{DYN}(dB) = 10 \log \left( \frac{\int_0^\infty |\delta_{DYN}(t) - \delta(t)|^2 dt}{\int_0^\infty |\delta(t)|^2 dt} \right). \quad (4.51)$$

In addition, the prediction of the supply current has been measured in terms of relative percentage error, and the power-added efficiency (PAE) prediction as an absolute error from the measured PAE. Three kinds of experiments with different excitation signals have been performed and will be described in the following paragraphs.

## Two-tone validation

The first test consists in applying a two-tone signal with varying frequency spacing around the  $f_0$  carrier. As widely known [97], this is a measurement to characterize the memory effects by checking the asymmetries and frequency-dependency of the third order intermodulation distortion ( $IM3$ ). For this measurement, the supply is modulated with a CW tone corresponding to the frequency spacing  $\Delta f$  between the large-signal RF input tones. Accordingly,  $\Delta f$  has been swept concurrently at both ports (the LF excitation is applied through the IF output of the generator) to measure the  $IM3$  profile over frequency

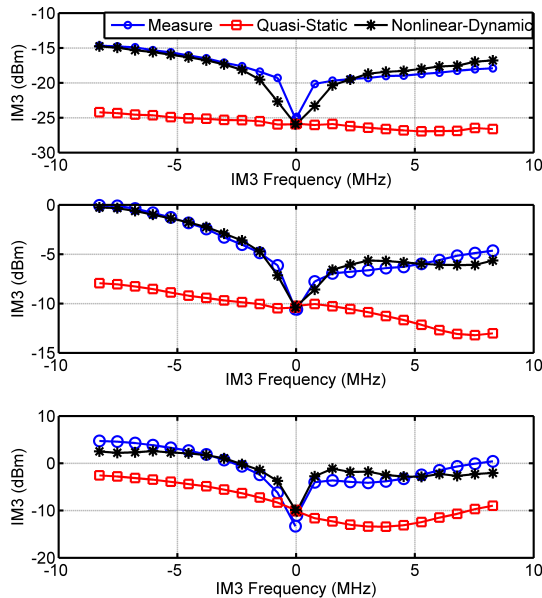


Figure 4.8: Two-tone test for three average RF  $P_{in}$ : (top) 0 dBm, (central) 4 dBm, and (bottom) 8 dBm;  $\Delta f \in [20 \text{ kHz}, 5.5 \text{ MHz}]$ . Step: 500 kHz.

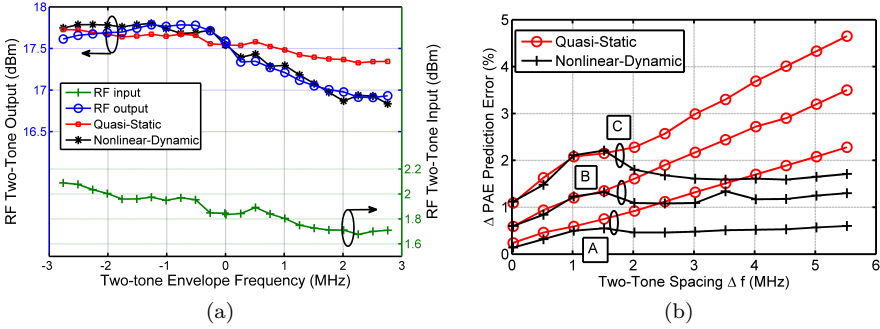


Figure 4.9: (a) RF two-tone input, output and model predictions for RF  $P_{in}=4$  dBm and  $\Delta f \in [20 \text{ kHz}, 5.5 \text{ MHz}]$ . Step: 500 kHz. (b)  $\Delta PAE$  prediction error (%) calculated as in (4.52) under two-tone RF excitation and single-tone modulation of the supply voltage ( $P_{in}$  as in Fig. 4.8).

within the bandwidth of interest. In Fig. 4.8, the  $IM3$  profiles versus frequency are reported, showing good agreement between the measured and the predicted values by means of the implemented three-port model. This experiment is performed at three RF input powers, and  $\Delta f \in [20 \text{ kHz}, 5.5 \text{ MHz}]$ . The model predicts the imbalance between the left and right  $IM3$ . In addition, the static model yields poor prediction as compared to the dynamic model. It is worth noting that slight differences in the amplitudes of the two tones were present at the PA input already, as it can be observed in Fig. 4.9(a). This was due to the absence of feedback control in the vector generator aimed at amplitude leveling. Furthermore, an error in the prediction of the average PAE

$$\Delta PAE(\%) = | \langle PAE_m(t) \rangle (\%) - \langle PAE_{mod}(t) \rangle (\%) |, \quad (4.52)$$

where  $\langle PAE_m(t) \rangle$  is the average measured PAE and  $\langle PAE_{mod}(t) \rangle$  is the average modeled PAE, has been evaluated under these conditions. As can be seen in Fig. 4.9(b), the nonlinear dynamic model shows an improved PAE prediction for three different RF input powers. The average PAE levels are 9% (plot A), 17% (B), and 30% (C) for average RF  $P_{in}$  of 0, 4, and 8 dBm, respectively.

### Modulated supply under RF compression

To evaluate the impact of only  $\Delta_{23}$  and  $\Delta_{33}^o$  (i.e., the impact of a dynamic supply on the outputs, while excluding any RF modulated excitation), a specific

Table 4.1: Model test with a multi-tone modulation at the supply

Excitation signals			NMSE (dB)		$\max\{\Delta i_3/i_3\}$ (%)	
$^1P_{in}$ (dBm)	$V_3^{(0)}$ (V)	$^2V_{3pp}$ (V)	$\delta_{QS}(t)$	$\delta_{DYN}(t)$	$i_{QS}(t)$	$i_{DYN}(t)$
$^{35}$ MHz, 5-tone supply modulation						
10	3	0.6	-27.2	-30.7	3.2	1.4
12	3	0.6	-27.6	-31.5	3.8	1.6
10	4	0.7	-33.5	-35.5	3.0	2.0
12	4	0.7	-31.6	-34.7	2.1	1.4
$^{35}$ MHz, 25-tone supply modulation						
11	3	0.6	-28.1	-29.5	2.8	1.8
12	3	0.6	-29.2	-31.6	3.0	1.2
11	4	0.7	-29.3	-29.5	2.9	1.6
12	4	0.7	-31.8	-32.7	2.3	1.5

<sup>1</sup> CW (constant RF power) applied at  $f_0 = 0.95$  GHz; <sup>2</sup> Voltage swing resulting by the multi-tone modulation applied at the supply port; <sup>3</sup> Multi-tone signal applied at the supply port by the vector signal generator baseband output and through the low-frequency bias tee

test, similarly to [207], is performed. It consists of using the PA as a mixer, where the supply port represents the modulated input, while the RF input is only driven by a single-tone to define the compression point at which the PA is operating. As a result, the envelope of the RF output signal is only due to the supply voltage modulation (as, for example, in EER), while the RF input power boosts the PA into nonlinear operation. The results are obtained for 10 and 12 dBm of RF  $P_{in}$  and for modulations around a set of dc supply voltages. The supply modulation consists of 5- and 25-tone random phase signals (with  $\Delta f = 1.25$  MHz and  $\Delta f = 250$  kHz, respectively). For this test, as well as for the ones that will be shown throughout this work, tones with equal amplitude and equally-spaced in frequency have been used. A maximum relative error for the supply current and the NMSE of  $\delta(t)$  of the RF output have been calculated for both the static and dynamic predictions. The results are presented in Table 4.1. In Fig. 4.10(a), the supply current waveform measured and predicted by static and dynamic models is reported, showing an improved precision for the dynamic extension.

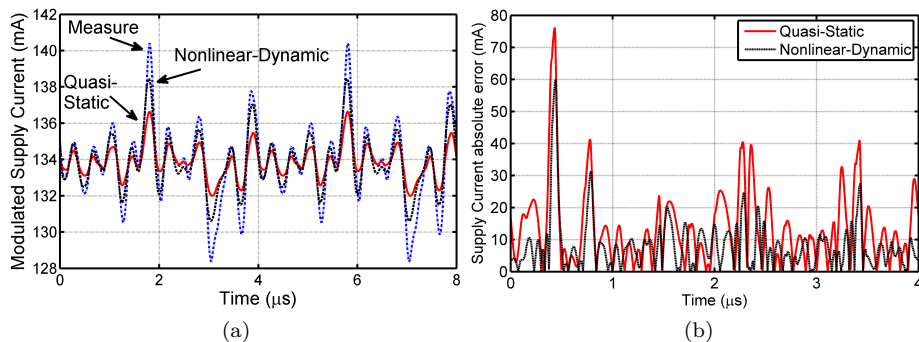


Figure 4.10: (a)  $i_3(t)$  modeling under 5 MHz, 25-tone with a frequency spacing of 250 kHz ( $T=4 \mu\text{s}$ ) modulated supply voltage with  $V_3^{(0)} = 3 \text{ V}$  and CW RF  $P_{in} = 8 \text{ dBm}$ . (b)  $i_3(t)$  under concurrent 25-tone (same type as in (a)) modulation at supply ( $V_3^{(0)} = 4 \text{ V}$ ,  $V_{3pp} = 1.8 \text{ V}$ ) and RF  $P_{in}=4 \text{ dBm}$ , PAPR=10 dB.

### Three-port measurements

An extensive characterization has been performed to test the behavioral model and, in particular, the performance of the nonlinear dynamic extension with simultaneous RF and LF excitations. Concurrent modulated RF input power and modulated supply voltage (such as shown in Fig. 4.4(a)) have been applied by programming various random multi-sines on the vector signal generator. The instantaneous modulated RF output power and supply current have been suitably captured and compared with the model prediction. The results of the characterization, performed for various average input powers, as well as dc voltages and supply voltage swings, are shown in Figs. 4.10(b), 4.11 and 4.12, and reported in Table 4.2. Figure 4.10(b) reports the case of the instantaneous error on the supply current under an RF modulation of a 25-tone random multi-sine. In Fig. 4.11, the performance of the model in the presence of a 5 MHz, 5-tone random multi-sine excitation with 1.25 MHz spacing between the tones and featuring 8 dB of PAPR is shown. Figures 4.11(a) and 4.11(b) report the time-domain, normalized RF output envelope and the RF output spectrum, respectively, along with the model predictions. Figures 4.11(c) to 4.11(f) report the instantaneous distortion  $\delta(t)$ , as defined in (4.47), as well as the quasi-static and nonlinear dynamic predictions in both the time (Figs. 4.11(c) and 4.11(e)), and the frequency (Figs. 4.11(d) and 4.11(f)) domains. The definition (4.47) of the instantaneous distortion  $\delta(t)$  allows for a clearer demonstration of the prediction accuracy at increasing signal powers by taking into account the PA dynamics. An improvement of several dB in the distortion prediction is achieved

at signal peaks (see Table 4.2). Similar comments can be made for a 25-tone random multi-sine with 250 kHz spacing between the tones (Fig. 4.12). The presence of a higher number of tones increases the PAPR from 8 to 10 dB, and the narrower spacing stimulates longer memory effects. Still, the nonlinear dynamic model outperforms the quasi-static model in all conditions, proving that such excitations (not only independent, but also fundamentally different from the perturbations used in the identification phase) is suitably handled by the proposed approach. Table 4.2 also reports the average relative errors on the supply current predictions. The PA dynamics approximation results in several percentage points of improvement in the average current predictions in all cases. In addition, the PAE in all conditions has been calculated. More in detail, the term  $PAE_{QS}(t)$  refers to the instantaneous PAE modeled with

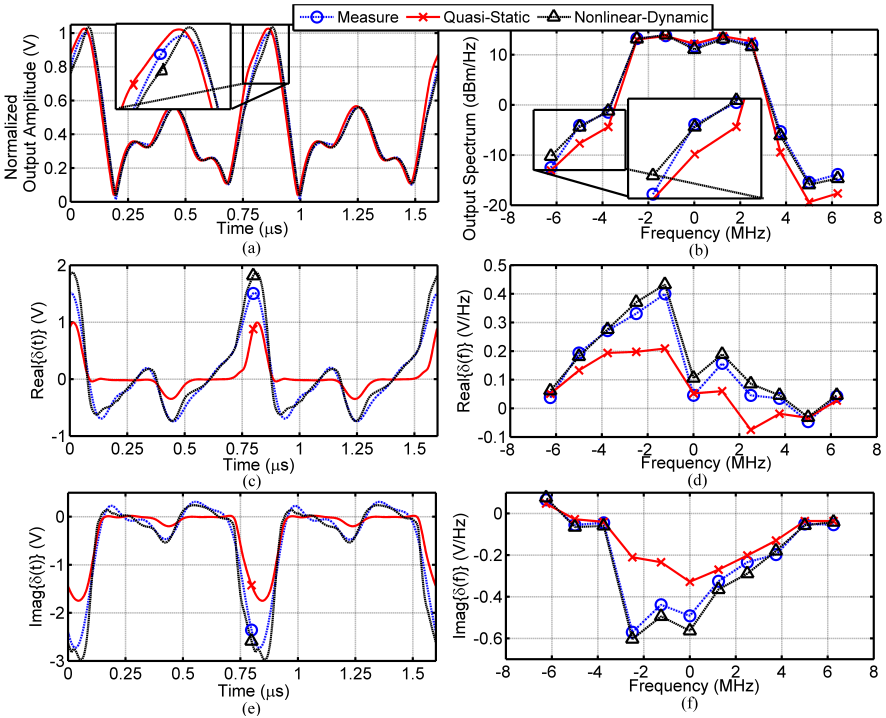


Figure 4.11: Measured and modeled  $b_2(t)$  under concurrent modulated supply ( $V_3^{(0)} = 5$  V,  $V_{3pp} = 2$  V) and RF input (5-tone, 5 MHz, PAPR = 8 dB,  $\Delta f = 1.25$  MHz ( $T = 1.6 \mu$  s),  $P_{in} = 4$  dBm) versus time (a) and frequency (b). (c) Time-domain and (d) frequency-domain of  $\Re\{\delta(t)\}$ . (e) Time-domain and (f) frequency-domain of  $\Im\{\delta(t)\}$ .

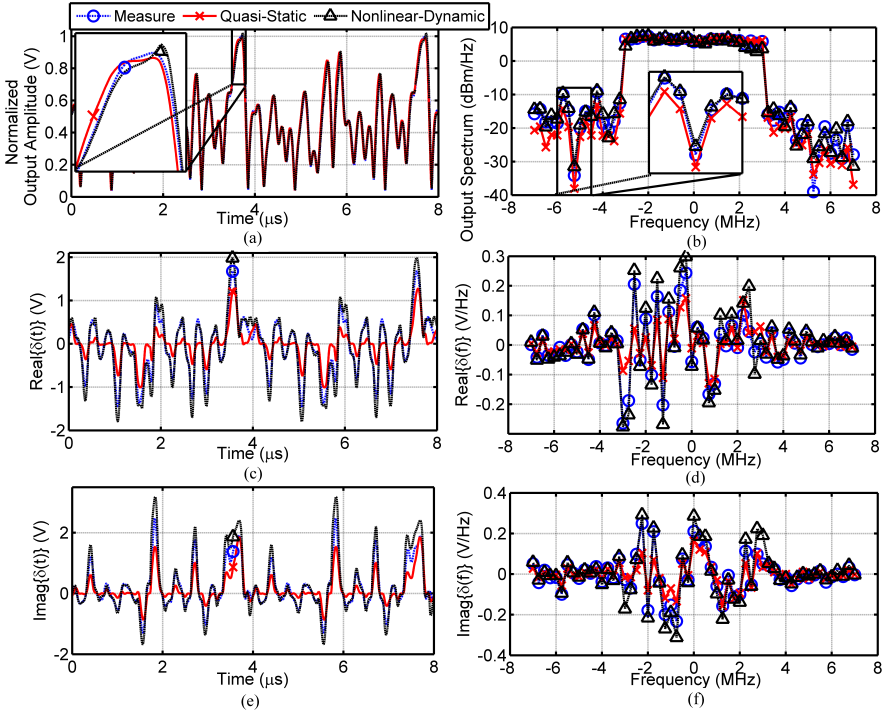


Figure 4.12: Measured and modeled  $b_2(t)$  under concurrent modulated supply ( $V_3^{(0)} = 5 \text{ V}$ ,  $V_{3pp} = 2 \text{ V}$ ) and RF input (25-tone, 5 MHz, PAPR=10.2 dB,  $\Delta f = 250 \text{ kHz}$  ( $T = 4 \mu \text{ s}$ ),  $P_{in} = 4 \text{ dBm}$ ) versus time (a) and frequency (b). (c) Time-domain and (d) frequency-domain of  $\Re\{\delta(t)\}$ . (e) Time-domain and (d) frequency-domain of  $\Im\{\delta(t)\}$ .

the quasi-static approximation, while  $PAE_{DYN}(t)$  is the one calculated with the nonlinear dynamic one. The error prediction  $\Delta PAE$ , calculated over the signal period with the formula in (4.52) either using  $PAE_{QS}(t)$  or  $PAE_{DYN}(t)$ , has also been reported in Table 4.2. In all tests, the PAE calculated through the nonlinear dynamic model formulation gives better predictions than the quasi-static approximation.

Table 4.2: Experimental results for the PA under concurrent RF and supply random multi-tone modulation

Excitation signals			NMSE (dB)		$\langle \{\Delta i_3 / i_3\} \rangle$ (%)		$\langle \text{PAE} \rangle$	$\Delta \text{PAE}$ (%)	
$^1 P_{in}$ (dBm)	$V_3^{(0)}$ (V)	$^2 V_{3pp}$ (V)	$\delta_{QS}(t)$	$\delta_{DYN}(t)$	$i_{QS}(t)$	$i_{DYN}(t)$	(%)	$\text{PAE}_{QS}(t)$	$\text{PAE}_{DYN}(t)$
$^3$ 5 MHz, 5-tone supply modulation									
1.1	3	0.8	-7.9	-8.4	12.4	6.2	19.3	1.6	1.6
4.0	3	1.0	-9.9	-10.5	16.0	5.4	28.2	3.5	3.2
1.1	4	1.2	-5.4	-8.9	9.6	5.8	14.7	0.6	0.6
4.0	4	1.4	-7.0	-10.3	11.1	6.0	22.6	2.9	1.5
1.1	5	1.2	-5.1	-7.6	8.3	4.9	11.1	0.3	0.2
4.0	5	1.8	-6.5	-10.4	9.2	6.5	18.0	1.2	0.9
$^4$ 5 MHz, 25-tone signal									
1.0	3	1.0	-7.3	-8.3	14.7	8.1	18.1	1.9	1.9
4.0	3	1.2	-10.1	-10.5	18.5	8.7	26.8	5.9	2.6
1.0	4	1.3	-5.1	-9.1	11.8	7.8	13.8	0.7	0.5
4.0	4	1.8	-6.9	-9.6	14.6	10.3	21.3	3.3	1.3
1.0	5	1.2	-4.9	-8.1	10.0	7.0	10.6	0.4	0.1
4.0	5	2.2	-6.5	-9.8	12.9	10.7	17.0	1.6	0.7

<sup>1</sup> Average RF input power of the multi-tone modulated signal; <sup>2</sup> Voltage swing resulting by the multi-tone modulation of the supply port; <sup>3</sup> The 5-tone signal has PAPR  $\simeq$  8 dB, and is applied at both the RF input and the supply port by the vector signal generator baseband output, through the low-frequency bias tee; <sup>4</sup> The 25-tone signal has PAPR  $\simeq$  10 dB, and is applied at both the RF input and the supply port by the vector signal generator baseband output, through the low-frequency bias tee.

## 4.6 Linearization technique

In this section, it will be shown how the three-port model presented in the previous sections can be used for the linearization of supply-modulated PAs. In particular, a model inversion algorithm [188], as well as some guidelines for the implementation of the digital implementation, will be given. The formulation of the proposed technique has been tested on the model previously extracted. The predistortion technique proposed here aims to account for the mutual dynamic dependency of both the RF input and the supply voltage. It should be noted, in fact, that single-input single-output behavioral models are typically used in the literature. Only a few works [202], [198] take also into account the dynamic dependency on  $v(t) = v_3(t)$ , which is considered dependent on the RF input envelope  $a(t) = a_1(t)$  by means of a function called *shaping table*, to be characterized beforehand. The digital predistortion (DPD) based on such models is typically obtained through a feedback of the downconverted RF output, and designed by minimizing the RF output error with respect to an optimal condition. A major drawback of this method, however, is the limited linearity and bandwidth of the feedback loop. The predistorter coefficients are obtained with a local optimization on a sample RF input waveform, thus must be often updated to achieve the performance. In addition, especially if the modulated supply voltage is not considered, the best combination of control signals  $v(t)$  and  $a(t)$  for optimal ET operation may not be reached. Instead, the availability of a three-port model allows considering the  $a(t)$  and  $v(t)$  as independent inputs. Section 4.6.1 is dedicated to the three-port model inversion algorithm, while sections 4.6.2 and 4.6.3 report, respectively, a few indications for the implementation of the algorithms and the results achieved in the inversion of the model of section 4.3.

### 4.6.1 Model inversion algorithm

The three-port model of section 4.3 has been defined through continuous time-domain signals. Here, as the aim is digital predistortion, the model is evaluated for the sampled input-output signals  $a(k) = a(t_0 + kT)$  and  $b(k) = b(t_0 + kT)$ , where  $T$  is the sampling period and  $t_0$  a generic time instant. The reflected waves will not be considered, so the port subscripts can be omitted. Moreover, to the extent of this inversion algorithm, the equation of the drain current is discarded. Although the nonlinear dynamic modeling of the current proposed in (4.14) is compatible with the proposed inversion, its consideration to maximize PAE requires further investigation, and it is out of the scope of this dissertation.

The discrete time formulation of the model can be written as:

$$b(k) = H[v(k), a(k)] + \Delta(k) \quad (4.53)$$

where  $v(k) = v(t_0 + kT)$  is the dynamic supply voltage, and  $H[v(k), a(k)] = H_S[v(k), |a(k)|] a(k)$ , being  $H_S$  the function already proposed in (4.14). One can also write:

$$H[v(k), a(k)] = H_A[v(k), |a(k)|] e^{j\{\angle\{a(k)\} + H_\phi[v(k), |a(k)|]\}} \quad (4.54)$$

where:

$$H_A[v(k), |a(k)|] = |H_S[v(k), |a(k)|]| |a(k)| \quad (4.55)$$

is the AM/AM characteristic, and

$$H_\phi[v(k), |a(k)|] = \angle\{H_S[v(k), |a(k)|]\} \quad (4.56)$$

is the AM/PM characteristic of the considered PA. The term  $\Delta(k)$  in (4.53) represents the sum of all dynamic deviations involved. As from (4.14), we have:

$$\Delta(k) = \Delta_{21}(k) + \Delta_{23}(k) \quad (4.57)$$

where

$$\begin{aligned} \Delta_{21}(k) = & \sum_{m=1}^M h_{21}[v(k), |a(k)|, m] \{a(k-m) - a(k)\} \\ & + a^*(k)^2 \sum_{m=1}^M \tilde{h}_{21}^*[v(k), |a(k)|, m] \{a^*(k-m) - a^*(k)\} \end{aligned} \quad (4.58)$$

takes into account the dynamic effects due to the RF input modulation, and

$$\Delta_{23}(k) = a(k) \sum_{m=1}^M h_{23}[v(k), |a(k)|, m] \{v(k-m) - v(k)\} \quad (4.59)$$

includes the dynamic deviations with respect to the modulated supply voltage. The variable  $M$  represents the maximum modeled memory length, while  $h_{21}$ ,  $\tilde{h}_{21}$  and  $h_{23}$  are the dynamic deviations kernels extensively discussed in section 4.3. It should be noted that only the kernels that impact the RF output are

considered. By introducing a vectorial notation, one can express (4.53) in terms of a generic input sequence  $\mathbf{a} = \{a(1), \dots, a(k), \dots\}$ , a generic output sequence  $\mathbf{b} = \{b(1), \dots, b(k), \dots\}$ , and a generic supply voltage sequence  $\mathbf{v} = \{v(1), \dots, v(k), \dots\}$ . As from (4.53), one obtains:

$$\mathbf{b} = \mathbf{H}[\mathbf{v}, \mathbf{a}] + \mathbf{\Delta}[\mathbf{v}, \mathbf{a}] \quad (4.60)$$

where two new sequences are defined as follows:

$$\begin{aligned} \mathbf{\Delta}[\mathbf{v}, \mathbf{a}] &\doteq \{\Delta(1), \dots, \Delta(k), \dots\} \\ \mathbf{H}[\mathbf{v}, \mathbf{a}] &\doteq \{H[v(1), a(1)], \dots, H[v(k), a(k)], \dots\}. \end{aligned} \quad (4.61)$$

For PA linearization by means of DPD, (4.53) must be solved so that the optimal predistorted sequence  $\hat{\mathbf{a}}$  should be retrieved for any target output sequence  $\hat{\mathbf{b}}$ . This can be obtained by iterative approximation procedures like the *fixed point* algorithm [208]. Such a method states that a nonlinear equation of the type  $\mathbf{x} = \mathbf{F}[\mathbf{x}]$  can be solved by formulating an iterative procedure

$$\mathbf{x}_{n+1} = \mathbf{F}[\mathbf{x}_n] \quad (4.62)$$

where  $n = 1, 2, \dots, N$  is the iteration index. Applying (4.62) to (4.53) leads to:

$$\mathbf{a}_{n+1} = \mathbf{H}^{-1}[\mathbf{v}, \hat{\mathbf{b}} - \mathbf{\Delta}[\mathbf{v}, \mathbf{a}_n]] \quad (4.63)$$

where

$$\begin{aligned} \mathbf{H}^{-1}[\mathbf{v}, \mathbf{b} - \mathbf{\Delta}[\mathbf{v}, \mathbf{a}_n]] &= \\ &= \{H^{-1}[v(1), \hat{b}(1) - \Delta(1)], \dots, H^{-1}[v(k), \hat{b}(k) - \Delta(k)], \dots\} \end{aligned} \quad (4.64)$$

is a sequence obtained by inverting the quasi-static input-output characteristic of the PA. In fact, each term of the sequence in (4.64) can be retrieved by mathematical manipulations of (4.53):

$$H^{-1}[v(k), \hat{b}(k) - \Delta(k)] = H_A^{-1}[v(k), |\hat{b}(k) - \Delta(k)|] e^{j\{\angle\{\hat{b}(k) - \Delta(k)\} - H_\phi[v(k), |a(k)|]\}}. \quad (4.65)$$

The term  $H_A^{-1}$  is the inversion of the quasi-static AM-AM characteristic  $H_A$ , which normally is a one-to-one relationship, thus analytically invertible with respect to the RF input, as already discussed in section 4.3. Equation (4.63) represents an iterative procedure which, if convergent, allows calculating the

optimal RF predistorted input sequence  $\hat{\mathbf{a}}$  for a targeted RF output sequence  $\hat{\mathbf{b}}$ . The principle of *contraction mapping* [208], used to linearize nonlinear dynamic systems also in [209], states that the fixed-point iteration algorithm in (4.63) converges if a constant  $L < 1$  exists such that,  $\forall(\mathbf{a}', \mathbf{a}'')$ :

$$\frac{\|\mathbf{H}^{-1}[\Delta[\mathbf{a}'']] - \mathbf{H}^{-1}[\Delta[\mathbf{a}']]\|}{\|\mathbf{a}'' - \mathbf{a}'\|} \leq L. \quad (4.66)$$

It also states that the smaller the value of  $L$ , the faster will be the convergence. Only the dependency on  $\mathbf{a}$ , upon which the inversion (and the DPD) is performed, is explicitly indicated in (4.66). A suitable norm operator  $\|\cdot\|$  to be used for the finite-power signals involved here can be defined as:

$$\|\mathbf{a}\| = \lim_{K \rightarrow \infty} \frac{1}{2K+1} \sum_{k=-K}^K |a(k)|^2. \quad (4.67)$$

From (4.66), one obtains two separate contributions:

$$\begin{aligned} & \frac{\|\mathbf{H}^{-1}[\Delta[\mathbf{a}'']] - \mathbf{H}^{-1}[\Delta[\mathbf{a}']]\|}{\|\mathbf{a}'' - \mathbf{a}'\|} = \\ & = \frac{\|\mathbf{H}^{-1}[\Delta[\mathbf{a}'']] - \mathbf{H}^{-1}[\Delta[\mathbf{a}']]\|}{\|\Delta[\mathbf{a}''] - \Delta[\mathbf{a}']\|} \frac{\|\Delta[\mathbf{a}''] - \Delta[\mathbf{a}']\|}{\|\mathbf{a}'' - \mathbf{a}'\|} \leq L_S L_M = L, \end{aligned} \quad (4.68)$$

$L_S$  being a boundary for the contribution due to the quasi-static nonlinear inversion, while  $L_M$  bounds the effects due to dynamic phenomena. In fact, the nonlinear quasi-static output can be bounded as follows:

$$\max \left\{ \frac{\|\mathbf{H}^{-1}[\Delta[\mathbf{a}'']] - \mathbf{H}^{-1}[\Delta[\mathbf{a}']]\|}{\|\Delta[\mathbf{a}''] - \Delta[\mathbf{a}']\|} \right\} \leq \frac{1}{\min\{G_\delta[\mathbf{a}'', \mathbf{a}']\}} = L_{NL} \quad (4.69)$$

where  $G_\delta[\mathbf{a}'', \mathbf{a}'] = \frac{\|\mathbf{H}[\mathbf{a}''] - \mathbf{H}[\mathbf{a}']\|}{\|\mathbf{a}'' - \mathbf{a}'\|}$ ,  $\forall(\mathbf{a}', \mathbf{a}'')$  is an incremental quasi-static gain, which is directly linked to the PA compression characteristic. The minimum value of  $G_\delta$ , so the convergence speed, can be controlled by tuning the supply voltage. At the same time:

$$\lim_{BW \rightarrow 0} \frac{\|\Delta[\mathbf{a}''] - \Delta[\mathbf{a}']\|}{\|\mathbf{a}'' - \mathbf{a}'\|} = 0, \quad \text{thus: } L_M \rightarrow 0 \text{ for } BW \rightarrow 0, \quad (4.70)$$

$BW$  being the maximum input modulated bandwidth involved. The result in (4.70) is a direct consequence of the fact that  $\Delta \rightarrow 0$  for  $BW \rightarrow 0$  [187]. Indeed, the slower is the input modulation, the smaller the dynamic effects involved, up to the limit of a quasi-static behavior entirely modeled by  $H$  in (4.53). According to (4.69) and (4.70), the iterative method will converge when,

for a given  $\min\{G_\delta\}$ , the dynamic deviations are small enough (i.e., the signal  $BW$  is not too large with respect to the PA memory duration). In the next section, it will be shown that this approach is particularly tailored for real-time DPD.

### 4.6.2 Real-time processing technique

While the majority of the available approaches features the identification of an inverted model and its feedback adaptation, the algorithm presented here does not include any analytical predistorter parameter fitting, while it only relies on the behavioral model of the PA and on the computation capabilities of the hardware. As such, it does not require the feeding of any additional PA data nor its RF output. As a consequence, once the model is extracted, it can be implemented as a fully pre-processing technique. If  $N$  is the number of iterations needed to compute the optimal predistorted input signal for a targeted  $\hat{\mathbf{b}}$  with the proposed algorithm, the architecture of the predistorter will consist of a cascade of  $N$  blocks, each of which computes  $\mathbf{a}_{n+1}$  at the  $n$ -th iteration (Fig. 4.13). At each iteration (Fig. 4.14), first  $\Delta(k)$  is computed (block A), and then the quasi-static functions  $H_A^{-1}$  and  $H_\phi$  (block B) are evaluated. A possible architecture to calculate the nonlinear convolutions in (4.58) and

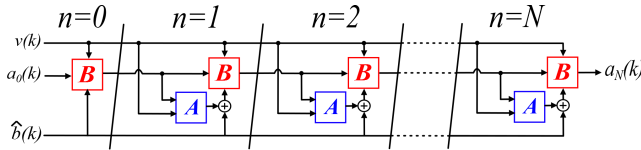


Figure 4.13: Functional scheme for the implementation of the iterative procedure, where the first iteration ( $n = 0$ ) is a simple quasi-static inversion (A and B blocks in Fig. 4.14).

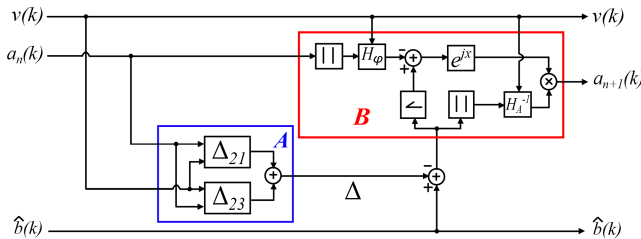


Figure 4.14: Processing at each iteration stage. A: Calculation of  $\Delta(k)$ . B: Quasi-static model inversion.

(4.59) consists of digital filters whose nonlinear coefficients  $h[v(k), |a(k)|, m]$  are stored in two-dimensional look-up tables (2D-LUTs) and evaluated at run-time (Fig. 4.15). Indeed, this is not the only possible architecture [119]. One should choose the processing architecture that best fits the available hardware. The complex operations necessary to calculate  $\Delta_{21}(k)$  and  $\Delta_{23}(k)$  at each  $n$ -th step with the schematic of Fig. 4.15 are reported in Table 4.3.

### 4.6.3 Results

The proposed iterative procedure is applied to the empirically identified three-port model of the GaAs-based hand-set PA. As already discussed in section 4.3, the model of a GaAs handset PA has been extracted over the maximum LSNA available RF bandwidth (20 MHz) for  $v(k) \in [2, 6]$  V and  $P_{TN}^{RF} \in [-20, 13]$  dBm.

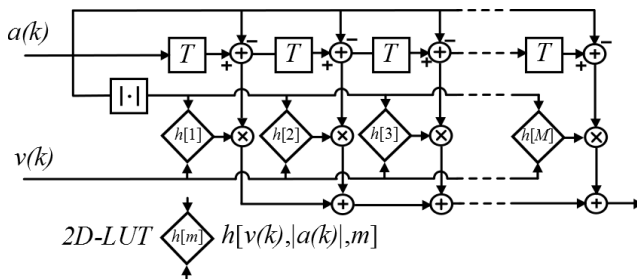


Figure 4.15: Architecture for the digital implementation of a nonlinear convolution, necessary to calculate the terms in (4.58) and (4.59) (within block A in Fig. 4.13).

Operation	$\Delta_{21}$	$\Delta_{23}$
T	2M	M
+	2M-1	M-1
-	2M	M
*	2M+1	M+1
$()^*$	1	0
$(\cdot)^2$	1	0
$ \cdot $	1	1
LUT access	2M	M

Table 4.3: Complex operations to calculate  $\Delta_{21}$  and  $\Delta_{31}$  with the scheme in Fig. 4.15.

We consider a set of predetermined voltages  $v(k) = S[|\hat{b}(k)|]$  (Fig. 4.16) for progressively higher power-added efficiency (PAE). Then, the predistorted  $\mathbf{a}_N$ , optimal for the chosen  $\mathbf{v}$ , is obtained as the output of the iterative inversion (4.63), which inherently accounts for the mutual dynamic interactions. It should be noted that this approach differs not only from works such as [202], where the modulated supply voltage is a quasi-static function of the RF input, but also from [210], where the mapping of various shaping tables to the RF output is evaluated, but no dynamic mutual dependency is accounted for to obtain the RF predistorted input. Results of RF output spectra, normalized mean square error (NMSE) and adjacent channel power ratio (ACPR) for a 6 MHz 25-tone signal are shown in Figs. 4.17-4.18 for the supply voltage waveforms reported in Fig. 4.16. As shown in Fig. 4.20, the higher the PAE, the more iterations

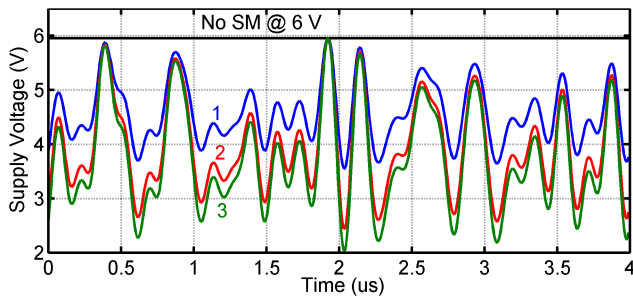


Figure 4.16: Applied supply voltage time-domain modulation waveforms (SM) corresponding to different average PAE. No SM: 12.4% PAE, SM 1: 18.2% PAE, SM 2: 21.8% PAE, SM 3: 23.4% PAE.

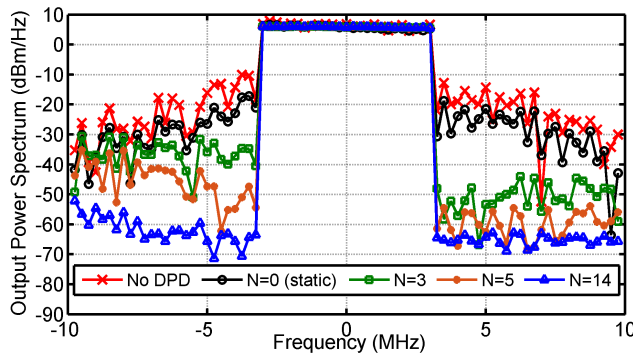


Figure 4.17: Spectrum of the RF output for a random-phase 25-tone RF input test signal with peak-to-average power ratio (PAPR) = 8 dB under the supply modulation (SM) 1 reported in Fig. 4.16. Linearized gain: 15 dB.

will be needed to guarantee the linearity target.

## 4.7 Conclusion

This Chapter was dedicated to the presentation of a three-port nonlinear dynamic behavioral model applicable to supply-modulated RF PAs. A mathematical formulation based on the modified Volterra series, truncated at the first order, was suitably derived and extended to include the dynamic deviations with respect to both the RF input as well as the dynamic supply voltage. Moreover, the model is extended to also predict the dynamic current obtained due to the dynamic variations of the inputs. Thus, the model entails the prediction of the dynamic PAE dependent on the two controlling signals

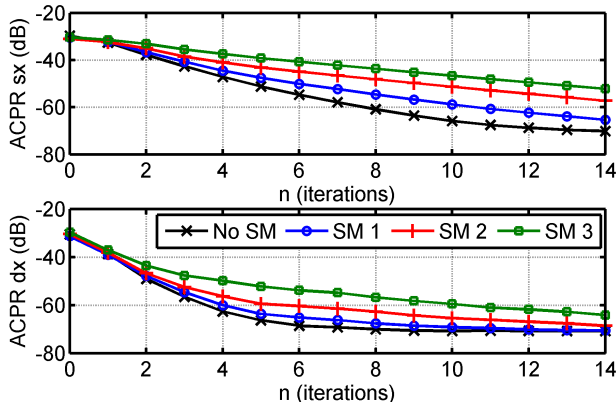


Figure 4.18: Left (top) and right (bottom) ACPR vs. iteration number  $n$  for the supply voltages in Fig. 4.16. RF input test signal as in Fig. 4.17.

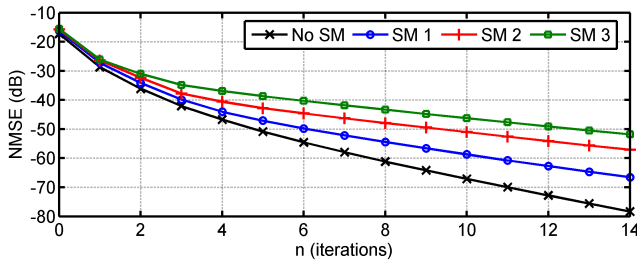


Figure 4.19: Output NMSE vs. iteration number  $n$  with the supply voltages of Fig. 4.16. RF input test signal as in Fig. 4.17.

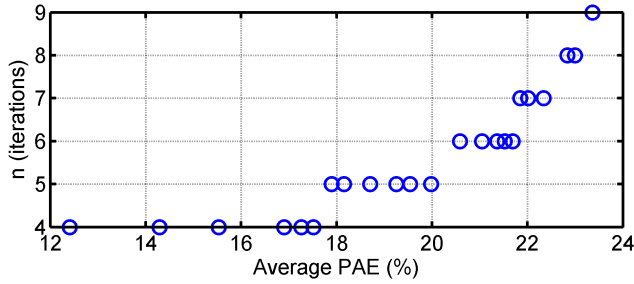


Figure 4.20: Number of iterations needed to guarantee  $\max\{\text{ACPR}\} < -45$  dBc. RF test signal as in Fig. 4.17.

of the supply-modulated PA. An analytical identification procedure has been described in detail and mathematically derived in the frequency domain. Such an extraction technique is suitable for an orthogonal measurement of the kernels by means of small signal excitations around large signal operating points. The approach has been implemented to obtain the three-port behavioral model of an handset PA by using the LF-LSNA set-up. Analysis of the function kernel revealed a nonlinear dependency of the transfer functions, despite the limitation of the set-up of measuring 20 MHz of bandwidth. The model suitably increase the accuracy of predictions for random multi-sine excitations applied at both the RF input and at the supply ports, enabling system simulations and easier interfacing with supply modulators, which have been shown to be far from ideal, especially in the MHz range. The Chapter is concluded with a straightforward yet general iterative procedure for linearizing supply-modulated PAs with RF power and supply modulated voltage as independent inputs. This technique features the three-port model inversion through an algorithm directly implementable in a digital architecture for real-time predistortion. The approach, tested on the extracted three-port model, has shown excellent linearization capabilities within a limited number of iterations, whilst taking into account the mutual nonlinear dynamic effects due to the RF input and the supply modulation.



# Chapter 5

## Conclusion

### 5.1 Main achievements

Although large-signal characterization is a well established field, the hardware platforms for performing nonlinear measurements are progressively evolving to higher frequencies, more accuracy and flexibility, providing further possibilities as well as exposing to new challenges. In fact, while this allows to gain more precise and controlled information on the DUT, advanced modeling techniques must be suitably formulated in order to exploit the measurement data for a precise application. On the other hand, some specific application requirements often request a tailored customization of the set-up capabilities, establishing a permanent feedback between set-up developments and modeling techniques. During the Ph.D. research, such a way of operating was adopted for the characterization and modeling of nonlinear and dynamics effects both at the device and PA levels.

With respect to device characterization, the focus has been on investigating the behavior of charge trapping effects in HEMT devices. The activity, mostly done at University of Bologna and in cooperation with the local group, began with the customization of the LF pulsed IV set-up and produced the following results:

- the implementation of the double-pulse excitation by means of suitable programming the arbitrary generator channels. The technique, published in [127], was then used for characterizing charge trapping effects in GaN HEMTs, and resulted to be a suitable way of obtaining isodynamic

IV characteristics, i.e., with a fixed charge trapping state at a fixed yet programmable pre-condition. These results have been reported in [128],[129];

- the definition of lag functions, which allow to identify directly the mutual dependencies between dynamic voltage excitations and the dynamic drain current, as well as to define trap-related performance parameters useful for process improvements [130],[131];
- a compact modeling approach for the GaN LF operation based on the DPiV characteristics, which takes advantage of the nonlinear lag function for defining a state equation describing the trap dynamics [132].

At PA level, the subject of research was the characterization and modeling of PAs operating under supply modulation. This involved the dynamic characterization of the supply port, and the inclusion of the dynamic supply voltage into a nonlinear behavioral model. Since no commercial set-up was readily available for such kind of measurements under application-like ET operation, the main efforts have been spent on the LF-LSNA, which, although not being a tailored set-up for supply-modulated PAs, it allowed the calibrated and synchronized measurements of the signals at both RF and at the supply port. In parallel, other set-ups have been developed as described in section 3.3 [174]. The activity allowed reaching the following results:

- an empirical method for the characterization of impedance-like nonlinear functions to characterize the non-idealities of PA and of the supply modulator under large-signal and wideband modulation [149], [150]. This also involved an experiment to assess PA linearity and efficiency under load-pull of the supply port [152];
- a measurement-based approach for modeling the self-heating effects in PAs, which leverage on a pulsed RF excitation and the external imposition of the PA case temperature [153];
- the formulation, identification and validation of a nonlinear dynamic three-port behavioral model applicable to supply-modulated PAs. Such a model is based on the modified Volterra series formulation, suitably extended to account for the dynamic supply voltage and also providing the dynamic current as well as dynamic PAE prediction. The approach was published in [187].
- An algorithm, yet unpublished, for the behavioral model inversion, and the validation of a predistortion method applicable to two independent inputs, i.e., the RF modulated input and the dynamic supply voltage,

while accounting for their mutual dynamic interactions affecting the RF modulated output.

## 5.2 Future challenges

### 5.2.1 Compact modeling of GaN HEMTs

Despite the results obtained, many challenges related to the Ph.D. research remain yet to be investigated, both at the device and PA levels. With respect to GaN compact device modeling, it should be noted that the model proposed is bias-dependent, and it has been developed for class AB operation. However, many PA applications striving for high-efficiency, as for example in telecommunications, necessitate to bias the PA at threshold and sub-threshold to obtain class B, C, etc. operation. Unfortunately, as already pointed out in section 2.6, the behavior of charge trapping effects sharply changes when the transistor is turned off. As a consequence, it is not straightforward to extend the modeling capabilities for a multi-bias compact model, and much effort should still be invested in the topic. Moreover, it should be recalled that, to the aim of the work proposed here, the identification of the nonlinear capacitances has been performed by means of multi-bias  $S$ -parameters characterization. Such a method, indeed, discards the trapping effects on the displacement current. Although, in first instance, such an approximation has been found acceptable, new methods taking into account the nonlinear charge trapping phenomena should be included in coherency with the resistive part of the model.

### 5.2.2 PA behavioral modeling and predistortion

Also the PA behavioral modeling activity opens opportunities for research developments. Indeed, it would be interesting to assess the capabilities of the model over larger bandwidths and on PAs based on different technologies or topologies, which would thus present different nonlinear dynamics. Moreover, it would be worth building a rather general PA measurement bench including multi-tone load-pull capabilities both at RF and at the supply port. With such a set-up, in fact, one could test the PA behavior under arbitrary (possibly active) termination at the supply, as to emulate realistic supply modulation and to compatibly compensate for non-idealities. In particular, the capabilities should include wideband multi-harmonic load-pull, i.e., not only featuring a limited number of harmonics as in many commercial set-ups, but allowing the impedance synthesis over the full bandwidth of the signal. This would allow

correlating the operating conditions of the PA with the distortion mechanisms corrupting the transmitted signal over the bandwidth of interest, in presence of various kind of mismatches (e.g., due to the antenna, the supply path, etc.). Such kind of measurements ultimately enables the effective co-design of hardware components and signal processing compensation techniques. From the modeling point of view, an interesting field of research would consist of leveraging on the results obtained on GaN HEMTs at the device level to formulate behavioral modeling approaches tailored for GaN-based PAs. In fact, as discussed in section 1.3, GaN is not yet the technology of choice for the high power telecommunication infrastructure. On the other hand, the inevitable trend towards higher frequencies and larger bandwidths must rely on a reliable technology for developing highly efficient and sufficiently linear PAs. A behavioral modeling approach accounting for nonlinear charge trapping would enhance the design of complex, yet demandingly linear, RF systems. Effective DPD techniques may, in turn, compensate for the nonlinear dispersive phenomena that nowadays prevent the mainstream diffusion of GaN.

# Bibliography

- [1] T. Rappaport, S. Sun, R. Mayzus, H. Zhao, Y. Azar, K. Wang, G. Wong, J. Schulz, M. Samimi, and F. Gutierrez, “Millimeter wave mobile communications for 5G cellular: It will work!,” *IEEE Access*, vol. 1, pp. 335–349, May 2013. pages 1
- [2] “3GPP LTE-Advanced.” <http://www.3gpp.org/LTE-Advanced>. Datasheet. pages 1
- [3] Agilent Technologies, “Introducing LTE-Advanced.” White Paper, Mar. 2011. pages 1
- [4] L. Sorensen and K. E. Skouby, “User scenarios 2020,” tech. rep., Wireless World Research Forum, 2009. pages 2
- [5] J. Andrews, S. Buzzi, W. Choi, S. Hanly, A. Lozano, A. Soong, and J. Zhang, “What will 5G be?,” *IEEE Journal on Selected Areas in Communications*, vol. 32, pp. 1065–1082, Jun. 2014. pages 2
- [6] F. Boccardi, R. Heath, A. Lozano, T. Marzetta, and P. Popovski, “Five disruptive technology directions for 5G,” *IEEE Communications Magazine*, vol. 52, pp. 74–80, Feb. 2014. pages 2
- [7] D. Muirhead, M. Imran, and K. Arshad, “Insights and approaches for low-complexity 5G small-cell base-station design for indoor dense networks,” *IEEE Access*, vol. 3, pp. 1562–1572, Sept. 2015. pages 2
- [8] C. Han, T. Harrold, S. Armour, I. Krikidis, S. Videv, P. M. Grant, H. Haas, J. Thompson, I. Ku, C.-X. Wang, T. A. Le, M. Nakhai, J. Zhang, and L. Hanzo, “Green radio: radio techniques to enable energy-efficient wireless networks,” *IEEE Communications Magazine*, vol. 49, pp. 46–54, Jun. 2011. pages 3
- [9] Commission of the European Communities, “Addressing the roadmap for moving to a low-carbon economy in 2050.” Report, Mar. 2011. pages 3

- [10] H. Holtkamp, G. Auer, S. Bazzi, and H. Haas, "Minimizing base station power consumption," *IEEE Journal on Selected Areas in Communications*, vol. 32, pp. 297–306, Feb. 2014. pages 3
- [11] O. Blume, D. Zeller, and U. Barth, "Approaches to energy efficient wireless access networks," in *Proc. 4th International Symposium on Communications, Control and Signal Processing (ISCCSP)*, pp. 1–5, Mar. 2010. pages 3
- [12] G. Auer, V. Giannini, C. Desset, I. Godor, P. Skillermark, M. Olsson, M. Imran, D. Sabella, M. Gonzalez, O. Blume, and A. Fehske, "How much energy is needed to run a wireless network?," *IEEE Wireless Communications*, vol. 18, pp. 40–49, Oct. 2011. pages 3
- [13] A. Carrol and G. Heiser, "An analysis of power consumption in a smartphone," in *Proc. USENIX Ann. Technical Conf. (USENIXATC)*, Jun. 2010. pages 4
- [14] J. Deng and L. E. Larson, "Multi-mode power amplifiers for wireless handset applications," in *Circuits and Systems for Future Generations of Wireless Communications* (A. Tasic, W. A. Serdijn, L. E. Larson, and G. Setti, eds.), Springer, 2009. pages 4
- [15] Z. Wang, *Envelope Tracking Power Amplifiers for Wireless Communications*. Artech House, 2014. pages 4, 15
- [16] P. Roblin and H. Rohdin, *High-Speed Heterostructure Devices: From Device Concepts to Circuit Modeling*. Cambridge University Press, 2002. pages 4
- [17] S. Oliver, "Optimize a power scheme for these transient times." <http://electronicdesign.com/>, Sept. 2014. pages 4
- [18] S. Emami, R. Wisser, E. Ali, M. Forbes, M. Gordon, X. Guan, S. Lo, P. McElwee, J. Parker, J. Tani, J. Gilbert, and C. Doan, "A 60 GHz CMOS phased-array transceiver pair for multi-Gb/s wireless communications," in *IEEE International Solid-State Circuits Conference Digest*, pp. 164–166, Feb. 2011. pages 5
- [19] S. Theeuwien and J. Qureshi, "LDMOS technology for RF power amplifiers," *IEEE Transactions on Microwave Theory and Techniques*, vol. 60, pp. 1755–1763, Jun. 2012. pages 5
- [20] F. van Rijs, "Status and trends of silicon LDMOS base station pa technologies to go beyond 2.5 GHz applications," in *IEEE Radio and Wireless Symposium Digest*, pp. 69–72, Jan. 2008. pages 5

- [21] R. Pengelly, S. Wood, J. Milligan, S. Sheppard, and W. Pribble, "A review of GaN on SiC High Electron-Mobility Power Transistors and MMICs," *IEEE Transactions on Microwave Theory and Techniques*, vol. 60, pp. 1764–1783, Jun. 2012. pages 5, 9
- [22] D. Floriot, V. Brunel, M. Camiade, C. Chang, B. Lambert, Z. Ouarch-Provost, H. Blanck, J. Grunenputt, M. Hosch, H. Jung, J. Spletstober, and U. Meiners, "GH25-10: New qualified power GaN HEMT process from technology to product overview," in *Proceedings of the European Microwave Integrated Circuit Conference*, pp. 225–228, Oct. 2014. pages 6, 29
- [23] Qorvo, "Foundry service booklet." <http://www.qorvo.com/foundry/>. pages
- [24] C. Lanzieri, A. Pantellini, P. Romanini, F. Crispoldi, A. Nanni, and R. Graffitti, "Selex ES GaN technology: Improvements, results and r&d approach for 0.5  $\mu\text{m}$  and 0.25  $\mu\text{m}$  process," in *Proceedings of the European Microwave Integrated Circuit Conference*, pp. 229–232, Sept. 2014. pages 6, 29
- [25] Wolfspeed, "Foundry service booklet." <http://www.wolfspeed.com/RF/Foundry-Services/MMICs/>. pages 6
- [26] P. Miaja, A. Rodriguez, and J. Sebastian, "Buck-derived converters based on gallium nitride devices for envelope tracking applications," *IEEE Transactions on Power Electronics*, vol. 30, pp. 2084–2095, Apr. 2015. pages 6
- [27] M. Ishida, T. Ueda, T. Tanaka, and D. Ueda, "GaN on Si technologies for power switching devices," *IEEE Transactions on Electron Devices*, vol. 60, pp. 3053–3059, Oct. 2013. pages 6
- [28] G. Kompa, *Basic Properties of III-V devices - Understanding mysterious trapping phenomena*. Kassel University Press, 2014. pages 6, 7
- [29] G. Meneghesso, G. Verzellesi, R. Pierobon, F. Rampazzo, A. Chini, U. K. Mishra, C. Canali, and E. Zanoni, "Surface-related drain current dispersion effects in AlGaN-GaN HEMTs," *IEEE Transactions on Electron Devices*, vol. 51, pp. 1554–1561, Oct. 2004. pages 7
- [30] B. Green, K. Chu, E. Chumbes, J. Smart, J. Shealy, and L. Eastman, "The effect of surface passivation on the microwave characteristics of undoped AlGaN/GaN HEMTs," *IEEE Electron Device Letters*, vol. 21, pp. 268–270, Jun. 2000. pages 7

- [31] G. Meneghesso, G. Verzellesi, F. Danesin, F. Rampazzo, F. Zanon, A. Tazzoli, M. Meneghini, and E. Zanoni, "Reliability of GaN High-Electron-Mobility Transistors: State of the art and perspectives," *IEEE Transactions on Device and Materials Reliability*, vol. 8, pp. 332–343, Jun. 2008. pages 7
- [32] S. Binari, P. Klein, and T. Kazior, "Trapping effects in GaN and SiC microwave FETs," *Proceedings of the IEEE*, vol. 90, pp. 1048–1058, Jun. 2002. pages 7
- [33] M. Faqir, G. Verzellesi, A. Chini, F. Fantini, F. Danesin, G. Meneghesso, E. Zanoni, and C. Dua, "Mechanisms of RF current collapse in AlGaN-GaN High Electron Mobility Transistors," *IEEE Transactions on Device and Materials Reliability*, vol. 8, pp. 240–247, Jun. 2008. pages 7
- [34] D. V. Lang, "Deep-level transient spectroscopy: A new method to characterize traps in semiconductors," *Journal of Applied Physics*, vol. 45, pp. 3023–3032, Jul. 1974. pages 7
- [35] C. Charbonniaud, J. Teyssier, and R. Quere, "Time-domain pulsed large-signal non-linear characterization of microwave transistors," in *Proceedings of the European Microwave Conference*, vol. 1, pp. 241–244 Vol.1, Oct. 2003. pages 7
- [36] R. Quere, R. Sommet, P. Bouysse, T. Reveyrand, D. Barataud, J. Teyssier, and J. Nebus, "Low frequency parasitic effects in RF transistors and their impact on power amplifier performances," in *IEEE Wireless and Microwave Technology Conference Digest*, pp. 1–5, Apr. 2012. pages 7
- [37] G. Koley, V. Tilak, L. F. Eastman, and M. G. Spencer, "Slow transients observed in AlGaN/GaN HFETs: effects of SiNx passivation and UV illumination," *IEEE Transactions on Electron Devices*, vol. 50, pp. 886–893, Apr. 2003. pages 7
- [38] J. Brinkhoff and A. Parker, "Charge trapping and intermodulation in hemts," in *IEEE MTT-S International Microwave Symposium Digest*, vol. 2, pp. 799–802 Vol.2, Jun. 2004. pages 8
- [39] S. Binari, K. Ikossi, J. Roussos, W. Kruppa, D. Park, H. B. Dietrich, D. D. Koleske, A. Wickenden, and R. L. Henry, "Trapping effects and microwave power performance in AlGaN/GaN HEMTs," *IEEE Transactions on Electron Devices*, vol. 48, pp. 465–471, Mar. 2001. pages 8
- [40] G. Meneghesso, F. Zanon, M. Uren, and E. Zanoni, "Anomalous kink effect in GaN High Electron Mobility Transistors," *IEEE Electron Device Letters*, vol. 30, pp. 100–102, Feb. 2009. pages 8

- [41] M. Wang and K. Chen, "Kink effect in AlGa<sub>N</sub>/Ga<sub>N</sub> HEMTs induced by drain and gate pumping," *IEEE Electron Device Letters*, vol. 32, pp. 482–484, Apr. 2011. pages 8
- [42] G. Crupi, A. Raffo, Z. Marinkovic, G. Avolio, A. Caddemi, V. Markovic, G. Vannini, and D.-P. Schreurs, "An extensive experimental analysis of the kink effects in  $s_{22}$  and  $h_{21}$  for a Ga<sub>N</sub> HEMT," *IEEE Transactions on Microwave Theory and Techniques*, vol. 62, pp. 513–520, Mar. 2014. pages 8
- [43] S. Mertens, "Status of the Ga<sub>N</sub> HEMT standardization effort at the Compact Model Coalition," in *IEEE Compound Semiconductor Integrated Circuit Symposium Digest*, pp. 1–4, Oct. 2014. pages 8
- [44] A. Darwish, A. Bayba, and H. Hung, "Thermal resistance calculation of AlGa<sub>N</sub>/Ga<sub>N</sub> on SiC devices," in *IEEE MTT-S International Microwave Symposium Digest*, vol. 3, pp. 2039–2042 Vol.3, Jun. 2004. pages 9
- [45] C. Florian, A. Santarelli, R. Cignani, and F. Filicori, "Characterization of the nonlinear thermal resistance and pulsed thermal dynamic behavior of AlGa<sub>N</sub>-Ga<sub>N</sub> HEMTs on SiC," *IEEE Transactions on Microwave Theory and Techniques*, vol. 61, pp. 1879–1891, May 2013. pages 9, 58, 98, 101
- [46] L. Dunleavy, C. Baylis, W. Curtice, and R. Connick, "Modeling Ga<sub>N</sub>: Powerful but challenging," *IEEE Microwave Magazine*, vol. 11, pp. 82–96, Oct. 2010. pages 9
- [47] D. Root, J. Verspecht, D. Sharrit, J. Wood, and A. Cognata, "Broad-band poly-harmonic distortion (PHD) behavioral models from fast automated simulations and large-signal vectorial network measurements," *IEEE Transactions on Microwave Theory and Techniques*, vol. 53, pp. 3656–3664, Nov. 2005. pages 9, 25, 117
- [48] J. Leckey, "A scalable  $X$ -parameter model for GaAs and Ga<sub>N</sub> FETs," in *Proceedings of the European Microwave Integrated Circuits Conference*, pp. 13–16, Oct. 2011. pages 9
- [49] O. Jardel, F. De Groote, T. Reveyrand, J.-C. Jacquet, C. Charbonniaud, J.-P. Teyssier, D. Floriot, and R. Quere, "An electrothermal model for AlGa<sub>N</sub>/Ga<sub>N</sub> power HEMTs including trapping effects to improve large-signal simulation results on high VSWR," *IEEE Transactions on Microwave Theory and Techniques*, vol. 55, pp. 2660–2669, Dec. 2007. pages 9, 33, 35, 48
- [50] J. Xu, R. Jones, S. Harris, T. Nielsen, and D. Root, "Dynamic FET model - DynaFET - for Ga<sub>N</sub> transistors from NVNA active source injection

- measurements,” in *IEEE MTT-S International Microwave Symposium Digest*, pp. 1–3, Jun. 2014. pages 9, 52
- [51] I. Angelov, H. Zirath, and N. Rosman, “A new empirical nonlinear model for HEMT and MESFET devices,” *IEEE Transactions on Microwave Theory and Techniques*, vol. 40, pp. 2258–2266, Dec. 1992. pages 9
- [52] V. Camarchia, F. Cappelluti, M. Pirola, S. Guerrieri, and G. Ghione, “Self-consistent electrothermal modeling of class A, AB, and B power GaN HEMTs under modulated RF excitation,” *IEEE Transactions on Microwave Theory and Techniques*, vol. 55, pp. 1824–1831, Sept. 2007. pages 9
- [53] J. Deng, W. Wang, S. Halder, W. Curtice, J. Hwang, V. Adivarahan, and M. Khan, “Temperature-dependent RF large-signal model of GaN-based MOSHFETs,” *IEEE Transactions on Microwave Theory and Techniques*, vol. 56, pp. 2709–2716, Dec. 2008. pages 9
- [54] I. Angelov, V. Desmaris, K. Dynefors, P. Nilsson, N. Rorsman, and H. Zirath, “On the large-signal modelling of AlGaIn/GaN HEMTs and SiC MESFETs,” in *Proceedings of the European Gallium Arsenide and Other Semiconductor Application Symposium*, pp. 309–312, Oct. 2005. pages 9
- [55] P. Cabral, J. Pedro, and N. Carvalho, “Nonlinear device model of microwave power GaN HEMTs for high power-amplifier design,” *IEEE Transactions on Microwave Theory and Techniques*, vol. 52, pp. 2585–2592, Nov. 2004. pages 9
- [56] A. Platzker, A. Palevsky, S. Nash, W. Struble, and Y. Tajima, “Characterization of GaAs devices by a versatile pulsed I-V measurement system,” in *IEEE MTT-S International Microwave Symposium Digest*, pp. 1137–1140 vol.3, May 1990. pages 9, 33
- [57] S. Trassaert, B. Boudart, C. Gaquiere, D. Theron, Y. Crosnier, F. Huet, and M. Poisson, “Trap effects studies in GaN MESFETs by pulsed measurements,” *Electronics Letters*, vol. 35, pp. 1386–1388, Aug. 1999. pages 9, 33
- [58] J. King and T. Brazil, “Nonlinear electrothermal GaN HEMT model applied to high-efficiency power amplifier design,” *IEEE Transactions on Microwave Theory and Techniques*, vol. 61, pp. 444–454, Jan. 2013. pages 9
- [59] I. Angelov, G. Avolio, and D. Schreurs, “Large-signal time-domain waveform-based transistor modeling,” in *Microwave De-embedding: From theory to applications* (G. Crupi and D. Schreurs, eds.), Academic Press, 2013. pages 10

- [60] A. Raffo, V. Vadala, D. Schreurs, G. Crupi, G. Avolio, A. Caddemi, and G. Vannini, "Nonlinear dispersive modeling of electron devices oriented to GaN power amplifier design," *IEEE Transactions on Microwave Theory and Techniques*, vol. 58, pp. 710–718, Apr. 2010. pages 10
- [61] E. Higham, "GaN technology in base stations - why and when?," in *IEEE Compound Semiconductor Integrated Circuit Symposium Digest*, pp. 1–4, Oct. 2014. pages 10
- [62] S. C. Cripps, *Advanced Techniques in RF Power Amplifier Design*. Artech House, 2002. pages 10, 11, 13
- [63] F. Raab, P. Asbeck, S. Cripps, P. Kenington, Z. Popovic, N. Pothecary, J. Sevic, and N. Sokal, "Power amplifiers and transmitters for RF and microwave," *IEEE Transactions on Microwave Theory and Techniques*, vol. 50, pp. 814–826, Mar. 2002. pages 10
- [64] "3GPP." <http://www.3gpp.org/>. Datasheet. pages 11
- [65] F. Raab, "High-efficiency linear amplification by dynamic load modulation," in *IEEE MTT-S International Microwave Symposium Digest*, vol. 3, pp. 1717–1720 vol.3, Jun. 2003. pages 11
- [66] W. Neo, Y. Lin, X. dong Liu, L. de Vreede, L. Larson, M. Spirito, M. Pelk, K. Buisman, A. Akhnoukh, A. de Graauw, and L. Nanver, "Adaptive multi-band multi-mode power amplifier using integrated varactor-based tunable matching networks," *IEEE Journal of Solid-State Circuits*, vol. 41, pp. 2166–2176, Sept. 2006. pages 11
- [67] H. Nemati, H. Cao, B. Almgren, T. Eriksson, and C. Fager, "Design of highly efficient load modulation transmitter for wideband cellular applications," *IEEE Transactions on Microwave Theory and Techniques*, vol. 58, pp. 2820–2828, Nov. 2010. pages 11
- [68] H. Chireix, "High power outphasing modulation," *Proceedings of the Institute of Radio Engineers*, vol. 23, pp. 1370–1392, Nov. 1935. pages 11
- [69] W. Doherty, "A new high efficiency power amplifier for modulated waves," *Proceedings of the Institute of Radio Engineers*, vol. 24, pp. 1163–1182, Sept. 1936. pages 11, 13
- [70] J. Qureshi, M. Pelk, M. Marchetti, W. Neo, J. Gajadharsing, M. van der Heijden, and L. de Vreede, "A 90-W peak power GaN outphasing amplifier with optimum input signal conditioning," *IEEE Transactions on Microwave Theory and Techniques*, vol. 57, pp. 1925–1935, Aug. 2009. pages 12

- [71] P. Lavrador, T. Cunha, P. Cabral, and J. Pedro, "The linearity-efficiency compromise," *IEEE Microwave Magazine*, vol. 11, pp. 44–58, Aug. 2010. pages 12, 15
- [72] R. Langridge, T. Thornton, P. Asbeck, and L. Larson, "A power re-use technique for improved efficiency of outphasing microwave power amplifiers," *IEEE Transactions on Microwave Theory and Techniques*, vol. 47, pp. 1467–1470, Aug. 1999. pages 12
- [73] B. Kim, J. Kim, I. Kim, and J. Cha, "The Doherty power amplifier," *IEEE Microwave Magazine*, vol. 7, pp. 42–50, Oct. 2006. pages 13
- [74] F. Raab, "Efficiency of Doherty RF power-amplifier systems," *IEEE Transactions on Broadcasting*, vol. BC-33, pp. 77–83, Sept. 1987. pages 13
- [75] B. Kim, I. Kim, and J. Moon, "Advanced Doherty architecture," *IEEE Microwave Magazine*, vol. 11, pp. 72–86, Aug. 2010. pages 13
- [76] L. Piazzon, R. Giofre, R. Quaglia, V. Camarchia, M. Pirola, P. Colantonio, F. Giannini, and G. Ghione, "Effect of load modulation on phase distortion in Doherty power amplifiers," *IEEE Microwave and Wireless Components Letters*, vol. 24, pp. 505–507, Jul. 2014. pages 13
- [77] D. Gustafsson, J. Cahuana, D. Kuylenstierna, I. Angelov, and C. Fager, "A GaN MMIC modified Doherty PA with large bandwidth and reconfigurable efficiency," *IEEE Transactions on Microwave Theory and Techniques*, vol. 62, pp. 3006–3016, Dec. 2014. pages 13
- [78] R. Giofre, L. Piazzon, P. Colantonio, and F. Giannini, "An ultra-broadband GaN Doherty amplifier with 83% of fractional bandwidth," *IEEE Microwave and Wireless Components Letters*, vol. 24, pp. 775–777, Nov. 2014. pages 13
- [79] B. Kim, J. Kim, D. Kim, J. Son, Y. Cho, J. Kim, and B. Park, "Push the envelope: Design concepts for envelope-tracking power amplifiers," *IEEE Microwave Magazine*, vol. 14, no. 3, pp. 68–81, 2013. pages 13, 16, 107
- [80] L. Kahn, "Single-sideband transmission by envelope elimination and restoration," *Proceedings of the IRE*, vol. 40, pp. 803–806, July 1952. pages 13
- [81] J. Jeong, D. Kimball, M. Kwak, P. Draxler, C. Hsia, C. Steinbeiser, T. Landon, O. Krutko, L. Larson, and P. Asbeck, "High-efficiency WCDMA envelope tracking base-station amplifier implemented with GaAs HVHBTs," *IEEE Journal of Solid-State Circuits*, vol. 44, pp. 2629–2639, Oct. 2009. pages 13, 14

- [82] J. Pedro, J. Garcia, and P. Cabral, "Nonlinear distortion analysis of polar transmitters," *IEEE Transactions on Microwave Theory and Techniques*, vol. 55, pp. 2757–2765, Dec. 2007. pages 14
- [83] N. Wang, X. Peng, V. Yousefzadeh, D. Maksimovic, S. Pajic, and Z. Popovic, "Linearity of x-band class-e power amplifiers in eer operation," *IEEE Transactions on Microwave Theory and Techniques*, vol. 53, pp. 1096–1102, Mar. 2005. pages 14
- [84] K. Bumman, M. Junghwan, and K. Ildu, "Efficiently amplified," *IEEE Microwave Magazine*, vol. 11, pp. 87–100, Aug. 2010. pages 15
- [85] E. McCune, "Operating modes of dynamic power supply transmitter amplifiers," *IEEE Transactions on Microwave Theory and Techniques*, vol. 62, pp. 2511–2517, Nov. 2014. pages 15, 86, 107
- [86] J. Pelaz, J.-M. Collantes, N. Otegi, A. Anakabe, and G. Collins, "Combined control of drain video bandwidth and stability margins in power amplifiers for envelope tracking applications," in *IEEE MTT-S International Microwave Symposium Digest*, pp. 1–4, 2014. pages 15
- [87] M. Rodriguez, P. Fernandez-Miaja, A. Rodriguez, and J. Sebastian, "A multiple-input digitally controlled buck converter for envelope tracking applications in radiofrequency power amplifiers," *IEEE Transactions on Power Electronics*, vol. 25, pp. 369–381, Feb. 2010. pages 16
- [88] M. Vasic, O. Garcia, J. Oliver, P. Alou, D. Diaz, and J. Cobos, "Multilevel power supply for high-efficiency RF amplifiers," *IEEE Transactions on Power Electronics*, vol. 25, pp. 1078–1089, Apr. 2010. pages
- [89] C. Florian, T. Cappello, R. Paganelli, D. Niessen, and F. Filicori, "Envelope tracking of an RF high power amplifier with an 8-level digitally controlled GaN-on-Si supply modulator," *IEEE Transactions on Microwave Theory and Techniques*, vol. 63, pp. 2589–2602, Aug. 2015. pages 16
- [90] L. Mathe, D. Kimball, J. Archambault, and W. Haley, "Apparatus and method for efficiently amplifying wideband envelope signals," Oct. 9 2001. US Patent 6,300,826. pages 16
- [91] J. Choi, D. Kang, D. Kim, and B. Kim, "Optimized envelope tracking operation of Doherty power amplifier for high efficiency over an extended dynamic range," *IEEE Transactions on Microwave Theory and Techniques*, vol. 57, pp. 1508–1515, Jun. 2009. pages 16

- [92] D. Kang, B. Park, D. Kim, J. Kim, Y. Cho, and B. Kim, "Envelope-tracking cmos power amplifier module for LTE applications," *IEEE Transactions on Microwave Theory and Techniques*, vol. 61, pp. 3763–3773, Oct. 2013. pages 16
- [93] OpenET Alliance, "ET enabled products." <http://www.open-et.org/>. pages 16
- [94] Qualcomm, "QFE1100: The world's first envelope tracking technology for 3G/4G LTE devices." <https://www.qualcomm.com>. Brochure. pages 16
- [95] J. Kim, J. Son, S. Jee, S. Kim, and B. Kim, "Optimization of envelope tracking power amplifier for base-station applications," *IEEE Transactions on Microwave Theory and Techniques*, vol. 61, pp. 1620–1627, Apr. 2013. pages 16
- [96] D. Kimball, J. Jeong, C. Hsia, P. Draxler, S. Lanfranco, W. Nagy, K. Linthicum, L. Larson, and P. Asbeck, "High-efficiency envelope-tracking W-CDMA base-station amplifier using GaN HFETs," *IEEE Transactions on Microwave Theory and Techniques*, vol. 54, pp. 3848–3856, Nov. 2006. pages 16
- [97] J. Pedro and N. Borges Carvalho, *Intermodulation distortions in microwave and wireless circuits*. Artech House, 2003. pages 17, 68, 128, 130
- [98] D. Schreurs, M. O'Droma, A. A. Goacher, and M. Gadringer, *RF power amplifier behavioral modeling*. Cambridge University Press, 2009. pages 17, 18, 19, 21
- [99] J. Pedro and S. Maas, "A comparative overview of microwave and wireless power-amplifier behavioral modeling approaches," *IEEE Transactions on Microwave Theory and Techniques*, vol. 53, pp. 1150–1163, Apr. 2005. pages 18, 19, 20, 107, 124
- [100] T. Liu, S. Boumaiza, and F. Ghannouchi, "Dynamic behavioral modeling of 3G power amplifiers using real-valued time-delay neural networks," *Microwave Theory and Techniques, IEEE Transactions on*, vol. 52, pp. 1025–1033, Mar. 2004. pages 18
- [101] A. Saleh, "Frequency-independent and frequency-dependent nonlinear models of TWT amplifiers," *IEEE Transactions on Communications*, vol. 29, pp. 1715–1720, Nov. 1981. pages 19
- [102] C. Rapp, "Effects of HPA-nonlinearity on a 4-DPSK/OFDM-signal for a digital sound broadcasting signal," in *Proceedings of the Second European*

- Conference on Satellite Communications*, vol. 1, pp. 179–184, 1991. pages 19
- [103] H. Poza, Z. Sarkozy, and H. Berger, “A wideband data link computer simulation model,” in *Proceedings of the National Aerospace and Electronics Conference*, vol. 1, pp. 71–78, 1975. pages 19
- [104] P. Asbeck, H. Kobayashi, M. Iwamoto, G. Hanington, S. Nam, and L. Larson, “Augmented behavioral characterization for modeling the nonlinear response of power amplifiers,” in *IEEE MTT-S International Microwave Symposium Digest*, vol. 1, pp. 135–138, 2002. pages 19, 107
- [105] H. Ku, M. McKinley, and J. Kenney, “Quantifying memory effects in RF power amplifiers,” *IEEE Transactions on Microwave Theory and Techniques*, vol. 50, pp. 2843–2849, Dec. 2002. pages 19
- [106] N. De Carvalho and J. Pedro, “A comprehensive explanation of distortion sideband asymmetries,” *IEEE Transactions on Microwave Theory and Techniques*, vol. 50, pp. 2090–2101, Sep. 2002. pages 19
- [107] M. Schetzen, *The Volterra and Wiener theories of nonlinear systems*. John Wiley & Sons, 1980. pages 20, 64
- [108] E. G. Lima, T. R. Cunha, H. M. Teixeira, M. Pirola, and J. C. Pedro, “Base-band derived Volterra series for power amplifier modeling,” in *IEEE MTT-S International Microwave Symposium Digest*, pp. 1361–1364, IEEE, 2009. pages 21
- [109] S. Boyd, Y. Tang, and L. Chua, “Measuring Volterra kernels,” *IEEE Transactions on Circuits and Systems*, vol. 30, pp. 571–577, Aug. 1983. pages 21, 109
- [110] A. Zhu, M. Wren, and T. J. Brazil, “An efficient Volterra-based behavioral model for wideband RF power amplifiers,” in *IEEE MTT-S International Microwave Symposium Digest*, vol. 2, pp. 787–790, Jun. 2003. pages 21
- [111] A. Zhu and T. J. Brazil, “Behavioral modeling of RF power amplifiers based on pruned Volterra series,” *IEEE Microwave and Wireless Components Letters*, vol. 14, pp. 563–565, Dec. 2004. pages 21
- [112] L. Ding, G. T. Zhou, D. R. Morgan, Z. Ma, J. S. Kenney, J. Kim, and C. R. Giardina, “A robust digital baseband predistorter constructed using memory polynomials,” *IEEE Transactions on Communications*, vol. 52, pp. 159–165, Jan. 2004. pages 22

- [113] D. R. Morgan, Z. Ma, J. Kim, M. G. Zierdt, and J. Pastalan, "A generalized memory polynomial model for digital predistortion of RF power amplifiers," *IEEE Transactions on Signal Processing*, vol. 54, pp. 3852–3860, Oct. 2006. pages 22
- [114] F. Filicori, G. Vannini, and V. Monaco, "A nonlinear integral model of electron devices for hb circuit analysis," *IEEE Transactions on Microwave Theory and Techniques*, vol. 40, pp. 1456–1465, Jul. 1992. pages 22, 23
- [115] D. Mirri, G. Iuculano, F. Filicori, G. Pasini, G. Vannini, and G. Pellegrini Gualtieri, "A modified Volterra series approach for nonlinear dynamic systems modeling," *IEEE Transactions on Circuits and Systems I: Fundamental Theory and Applications*, vol. 49, pp. 1118–1128, Aug. 2002. pages 22, 23, 109, 110
- [116] N. Le Gallou, E. Ngoya, H. Buret, D. Barataud, and J. Nebus, "An improved behavioral modeling technique for high power amplifiers with memory," in *IEEE MTT-S International Microwave Symposium Digest*, vol. 2, pp. 983–986 vol.2, May 2001. pages 23, 113
- [117] A. Soury, E. Ngoya, and J.-M. Nebus, "A new behavioral model taking into account nonlinear memory effects and transient behaviors in wideband SSPAs," in *IEEE MTT-S International Microwave Symposium Digest*, vol. 2, pp. 853–856, Jun. 2002. pages 74
- [118] D. Mirri, F. Filicori, G. Iuculano, and G. Pasini, "A nonlinear dynamic model for performance analysis of large-signal amplifiers in communication systems," *IEEE Transactions on Instrumentation and Measurement*, vol. 53, pp. 341–350, Apr. 2004. pages 23, 25, 110, 113, 117, 118, 120
- [119] A. Zhu, J. C. Pedro, and T. J. Brazil, "Dynamic deviation reduction-based Volterra behavioral modeling of RF power amplifiers," *IEEE Transactions on Microwave Theory and Techniques*, vol. 54, pp. 4323–4332, Dec. 2006. pages 23, 113, 142
- [120] J. Wood, "A glimpse of the future," *IEEE Microwave Magazine*, vol. 13, pp. 60–69, Nov. 2012. pages 24
- [121] A. S. Tehrani, J. Chani, T. Eriksson, and C. Fager, "Investigation of parameter adaptation in RF power amplifier behavioral models," *arXiv preprint arXiv:1410.8127*, 2014. pages 24
- [122] H. Cao, H. Nemati, A. Tehrani, T. Eriksson, J. Grahn, and C. Fager, "Linearization of efficiency-optimized dynamic load modulation transmitter architectures," *IEEE Transactions on Microwave Theory and Techniques*, vol. 58, pp. 873–881, Apr. 2010. pages 24

- [123] P. Roblin, D. Root, J. Verspecht, Y. Ko, and J. Teyssier, "New trends for the nonlinear measurement and modeling of high-power RF transistors and amplifiers with memory effects," *IEEE Transactions on Microwave Theory and Techniques*, vol. 60, pp. 1964–1978, Jun. 2012. pages 25, 52
- [124] D. E. Root, J. Verspecht, J. Horn, and M. Marcu, *X-Parameters: Characterization, Modeling, and Design of Nonlinear RF and Microwave Components*. Cambridge University Press, 2013. pages 25, 77
- [125] J. M. Horn, J. Verspecht, D. Gunyan, L. Betts, D. E. Root, and J. Eriksson, "X-parameter measurement and simulation of a GSM handset amplifier," in *Proceedings of the European Microwave Integrated Circuit Conference*, pp. 135–138, Oct. 2008. pages 25
- [126] J. Verspecht, J. Horn, L. Betts, D. Gunyan, R. Pollard, C. Gillease, and D. E. Root, "Extension of X-parameters to include long-term dynamic memory effects," in *IEEE MTT-S International Microwave Symposium Digest*, pp. 741–744, Jun. 2009. pages 25, 74, 98, 113
- [127] A. Santarelli, R. Cignani, G. Gibiino, D. Niessen, P. Traverso, C. Florian, D. Schreurs, and F. Filicori, "A double-pulse technique for the dynamic I/V characterization of GaN FETs," *IEEE Microwave and Wireless Components Letters*, vol. 24, pp. 132–134, Feb 2014. pages 29, 34, 35, 147
- [128] G. P. Gibiino, R. Cignani, D. Niessen, D. Schreurs, A. Santarelli, and F. Filicori, "Thermal characterization of nonlinear charge trapping effects in GaN-FETs," in *Proceedings of the International Workshop on Integrated Nonlinear Microwave and Millimetre-wave Circuits*, pp. 1–4, Apr. 2014. pages 44, 148
- [129] A. Santarelli, R. Cignani, G. P. Gibiino, D. Niessen, P. A. Traverso, C. Florian, C. Lanzieri, A. Nanni, D. Schreurs, and F. Filicori, "Nonlinear charge trapping effects on pulsed I/V characteristics of GaN FETs," in *Proceedings of the Microwave Integrated Circuits Conference*, pp. 404–407, Oct. 2013. pages 38, 148
- [130] A. Santarelli, R. Cignani, D. Niessen, G. P. Gibiino, P. A. Traverso, V. Di Giacomo, C. Chang, D. Floriot, D. Schreurs, and F. Filicori, "Evaluation of GaN FET power performance reduction due to nonlinear charge trapping effects," in *Proceedings of the European Microwave Integrated Circuit Conference*, pp. 198–201, Sept. 2014. pages 46, 47, 148
- [131] A. Santarelli, R. Cignani, D. Niessen, G. P. Gibiino, P. Traverso, D. Schreurs, and F. Filicori, "Multi-bias nonlinear characterization of

- GaN FET trapping effects through a multiple pulse time domain network analyzer,” in *Proceedings of the European Microwave Integrated Circuits Conference*, pp. 1–3, Sept. 2014. pages 29, 49, 148
- [132] A. Santarelli, D. Niessen, R. Cignani, G. P. Gibiino, P. A. Traverso, C. Florian, D. Schreurs, and F. Filicori, “GaN FET nonlinear modeling based on double pulse characteristics,” *IEEE Transactions on Microwave Theory and Techniques*, vol. 62, pp. 3262–3273, Dec. 2014. pages 30, 48, 59, 148
- [133] J.-C. Nallatamby, R. Sommet, S. Laurent, M. Prigent, R. Quere, and O. Jardel, “A microwave modeling oxymoron?: Low-frequency measurements for microwave device modeling,” *IEEE Microwave Magazine*, vol. 15, pp. 92–107, Jun. 2014. pages 30
- [134] J. Scott, J. G. Rathmell, A. Parker, and M. Sayed, “Pulsed device measurements and applications,” *IEEE Transactions on Microwave Theory and Techniques*, vol. 44, pp. 2718–2723, Aug. 1996. pages 30
- [135] Auriga Microwave, “Pulsed IV/RF system.” <http://www.aurigamicrowave.com>. Datasheet. pages 30
- [136] Focus Microwave, “Modular pulsed iv system.” <http://www.focus-microwaves.com>. Datasheet. pages
- [137] AMCAD Engineering, “PIV/PLP family of pulsed IV system.” <http://www.amcad-engineering.fr>. Datasheet. pages 30
- [138] D. Niessen, “Nonlinear characterization and modelling of GaN HEMTs for microwave power amplifier applications,” *Ph.D. thesis*, 2013. pages 31, 32
- [139] A. Santarelli, R. Cignani, D. Niessen, P. A. Traverso, and F. Filicori, “New pulsed measurement setup for GaN and GaAs FETs characterization,” *International Journal of Microwave and Wireless Technologies*, vol. 4, pp. 387–397, Jun. 2012. pages 31, 33, 34, 41
- [140] O. Jardel, F. De Groote, C. Charbonniaud, T. Reveyrand, J.-P. Teyssier, R. Quere, and D. Floriot, “A drain-lag model for AlGaIn/GaN power HEMTs,” in *IEEE MTT-S International Microwave Symposium Digest*, pp. 601–604, Jun. 2007. pages 33
- [141] S. Albahrani, J. G. Rathmell, A. E. Parker, *et al.*, “Characterizing drain current dispersion in GaN HEMTs with a new trap model,” in *Proceedings of the European Microwave Conference*, pp. 1692–1695, Sept. 2009. pages 33

- [142] A. Raffo, G. Bosi, V. Vadala, and G. Vannini, "Behavioral modeling of GaN FETs: A load-line approach," *IEEE Transactions on Microwave Theory and Techniques*, vol. 62, pp. 73–82, Jan. 2014. pages 52
- [143] G. Dambrine, A. Cappy, F. Heliodore, and E. Playez, "A new method for determining the fet small-signal equivalent circuit," *IEEE Transactions on Microwave Theory Techniques*, vol. 36, pp. 1151–1159, Jul. 1988. pages 53, 59
- [144] K. Kurokawa, "Power waves and the scattering matrix," *IEEE Transactions on Microwave Theory and Techniques*, vol. 13, pp. 194–202, Jan. 1965. pages 63
- [145] W. Van Moer and Y. Rolain, "A large-signal network analyzer: Why is it needed?," *IEEE Microwave Magazine*, vol. 7, pp. 46–62, Nov. 2006. pages 64, 65
- [146] W. Van Moer and L. Gomme, "NVNA versus LSNA: enemies or friends?," *IEEE Microwave Magazine*, vol. 11, pp. 97–103, Feb. 2010. pages 64
- [147] J. Verspecht, F. Verbeyst, M. Vanden Bossche, *et al.*, "Network analysis beyond  $S$ -parameters: Characterizing and modeling component behaviour under modulated large-signal operating conditions," in *Proceedings of the European Microwave Conference*, vol. 30, pp. 373–376, Oct. 2000. pages 64, 65
- [148] P. Blockley, D. Gunyan, and J. B. Scott, "Mixer-based, vector-corrected, vector signal/network analyzer offering 300khz-20ghz bandwidth and traceable phase response," in *IEEE MTT-S International Microwave Symposium Digest*, pp. 1–4, Jun. 2005. pages 64, 72
- [149] G. P. Gibiino, G. Avolio, D. Schreurs, and A. Santarelli, "Nonlinear characterization of microwave power amplifiers with supply modulation," in *International Workshop on Integrated Nonlinear Microwave and Millimetre-wave Circuits*, pp. 1–3, Apr. 2014. pages 64, 88, 148
- [150] G. P. Gibiino, G. Avolio, D. Schreurs, A. Santarelli, and F. Filicori, "Mixer-like modeling with dynamic baseband characterization for supply-modulated pas," in *Proceedings of the European Microwave Integrated Circuit Conference*, Sept. 2014. pages 64, 88, 148
- [151] G. P. Gibiino, J. Couvidat, G. Avolio, D. Schreurs, and A. Santarelli, "Supply-terminal 40 MHz BW characterization of impedance-like nonlinear functions for envelope tracking PAs," in *ARFTG Microwave Measurement Conference Digest*, May 2016. pages 64, 87

- [152] G. P. Gibiino, G. Avolio, S. Schafer, D. Schreurs, Z. Popovic, A. Santarelli, and F. Filicori, "Active baseband drain-supply terminal load-pull of an X-band GaN MMIC PA," in *Proceedings of the European Microwave Conference*, Sept. 2015. pages 65, 95, 97, 148
- [153] G. P. Gibiino, T. Cappello, D. Niessen, D. M.-P. Schreurs, A. Santarelli, and F. Filicori, "An empirical behavioral model for RF PAs including self-heating," in *Proceedings of the International Workshop on Integrated Nonlinear Microwave and Millimetre-wave Circuits*, pp. 1–3, Oct. 2015. pages 65, 148
- [154] C. Nader, W. Van Moer, K. Barbe, N. Bjorsell, and P. Handel, "Harmonic sampling and reconstruction of wideband undersampled waveforms: Breaking the code," *IEEE Transactions on Microwave Theory and Techniques*, vol. 59, pp. 2961–2969, Nov. 2011. pages 65, 66
- [155] NMDG (National Instruments) and Maury Microwave, "Large-Signal Network Analyzer (MT4463)." <http://www.nmdg.be/>. Datasheet. pages 66
- [156] S. Vandenplas, J. Verspecht, F. Verbeyst, E. Vandamme, and M. Vanden Bossche, "Calibration issues for the large signal network analyzer (lsna)," in *ARFTG Fall Conference Digest*, pp. 99–106, Dec. 2002. pages 68
- [157] P. Roblin, *Nonlinear RF circuits and nonlinear vector network analyzers: interactive measurement and design techniques*. Cambridge University Press, 2011. pages 68, 118
- [158] F. De Groote, P. Roblin, Y.-S. Ko, C.-K. Yang, S. J. Doo, M. Vanden Bossche, and J.-P. Teyssier, "Pulsed multi-tone measurements for time domain load pull characterizations of power transistors," in *ARFTG Microwave Measurement Conference Digest*, pp. 1–4, Jun. 2009. pages 68
- [159] F. Verbeyst and M. Vanden Bossche, "Real-time and optimal PA characterization speeds up PA design," in *Proceedings of the European Microwave Conference*, Oct. 2004. pages 68
- [160] D. Williams, J. Leckey, and P. Tasker, "A study of the effect of envelope impedance on intermodulation asymmetry using a two-tone time domain measurement system," in *IEEE MTT-S International Microwave Symposium Digest*, vol. 3, pp. 1841–1844, Jun. 2002. pages 69, 96
- [161] M. Spirito, M. J. Pelk, F. Van Rijs, S. J. Theeuwens, D. Hartskeerl, and L. C. De Vreede, "Active harmonic load-pull for on-wafer out-of-band

- device linearity optimization,” *IEEE Transactions on Microwave Theory and Techniques*, vol. 54, pp. 4225–4236, Dec. 2006. pages 69
- [162] G. Avolio, G. Paillancy, D. Schreurs, M. Vanden Bossche, and B. Nauwelaers, “On-wafer LSNA measurements including dynamic-bias,” in *Proceedings of the European Microwave Conference*, pp. 930–933, Sept. 2009. pages 69
- [163] G. Avolio, “Combined low-and high-frequency nonlinear characterization and modeling (gecombineerd laag-en hoog-frequent niet-lineaire karakterisatie en modellering),” *Ph.D. thesis*, 2012. pages 70, 71
- [164] Keysight Technologies, “PNA-X Microwave Network Analyzer.” <http://literature.cdn.keysight.com/>. Datasheet. pages 72, 73
- [165] R. E. Shoulders and L. C. Betts, “Pulsed signal device characterization employing adaptive nulling and IF gating,” Mar. 4 2008. US Patent 7,340,218. pages 73
- [166] Keysight Technologies, “Active-device characterization in pulsed operation using the PNA-X,” 2014. Application Note. pages 74, 75
- [167] Keysight Technologies, “Pulsed-RF S-parameter measurements with the PNA microwave network analyzers using wideband and narrowband detection,” 2014. Application Note. pages 74
- [168] Keysight Technologies, “Infiniivision oscilloscope probes and accessories.” <http://literature.cdn.keysight.com/>. Datasheet. pages 76, 102
- [169] Keysight Technologies, “Infiniivision 6000l series low-profile oscilloscopes.” <http://literature.cdn.keysight.com/>. Datasheet. pages 76
- [170] G. P. Gibiino, F. F. Tafuri, T. S. Nielsen, D. Schreurs, and A. Santarelli, “Pulsed NVNA measurements for dynamic characterization of RF PAs,” in *IEEE International Microwave and RF Conference Digest*, pp. 92–95, Dec. 2014. pages 76, 77
- [171] Texas Instruments, “LM3290-91.” <http://www.ti.com/>. Product Brief. pages 78
- [172] Tektronix, “Arbitrary/function generators AFG3022B.” <http://www.tek.com/>. Datasheet. pages 78, 87, 94, 125
- [173] N. Instruments, “Vector signal transceiver PXIe-5645.” <http://www.ni.com/vst/>. Datasheet. pages 81, 102

- [174] J. Couvidat, G. P. Gibiino, G. Pailloncy, M. Vanden Bossche, A. Ghiotto, and D. Schreurs, "A compact measurement set-up for envelope-tracking RF PAs with calibrated sensing of baseband V/I at the supply terminal," in *ARFTG Fall Conference Digest*, Dec. 2015. pages 82, 83, 85, 94, 148
- [175] M. Thorsell and K. Andersson, "A new baseband measurement system for characterization of memory effects in nonlinear microwave devices," in *ARFTG Microwave Measurement Conference Digest*, pp. 1–3, Jun. 2012. pages
- [176] S. Schafer and Z. Popovic, "Multi-frequency measurements for supply modulated transmitters," *IEEE Transactions on Microwave Theory and Techniques*, vol. 63, pp. 2931–2941, Aug. 2015. pages 85, 94
- [177] J. Santiago, J. Portilla, and T. Fernández, "Nonlinear and memory characterization of gaas fet devices and fet-based power amplifier circuits," in *Proceedings of the European Microwave Integrated Circuits Conference*, pp. 99–102, Sept. 2006. pages 88
- [178] S. Schafer, M. Litchfield, A. Zai, Z. Popovic, and C. Campbell, "X-band MMIC GaN power amplifiers designed for high-efficiency supply-modulated transmitters," in *IEEE MTT-S International Microwave Symposium Digest*, pp. 1–3, Jun. 2013. pages 89
- [179] S. Boyd, "Multitone signals with low crest factor," tech. rep., DTIC Document, 1986. pages 90
- [180] N. De Carvalho and J. Pedro, "Large- and small-signal imd behavior of microwave power amplifiers," *IEEE Transactions on Microwave Theory and Techniques*, vol. 47, pp. 2364–2374, Dec. 1999. pages 96
- [181] J. Brinkhoff and A. E. Parker, "Effect of baseband impedance on fet intermodulation," *IEEE Transactions on Microwave Theory and Techniques*, vol. 51, pp. 1045–1051, Apr. 2003. pages 96
- [182] B. Bunz, A. Ahmed, and G. Kompa, "Influence of envelope impedance termination on RF behaviour of GaN HEMT power devices," in *Proceedings of the Gallium Arsenide and Other Semiconductor Application Symposium*, pp. 649–652, Oct. 2005. pages 96
- [183] M. Akmal, J. Lees, S. Bensmida, S. Woodington, V. Carrubba, S. Cripps, J. Benedikt, K. Morris, M. Beach, J. McGeehan, *et al.*, "The effect of baseband impedance termination on the linearity of GaN HEMTs," in *Proceedings of the European Microwave Conference*, pp. 1046–1049, Sept. 2010. pages 96

- [184] J. H. Vuolevi, T. Rahkonen, and J. Manninen, "Measurement technique for characterizing memory effects in RF power amplifiers," *IEEE Transactions on Microwave Theory and Techniques*, vol. 49, pp. 1383–1389, Aug. 2001. pages 98
- [185] C. Mazière, A. Soury, E. Ngoya, and J.-M. Nebus, "A system level model of solid state amplifiers with memory based on a nonlinear feedback loop principle," in *Proceedings of the European Microwave Conference*, vol. 1, pp. 4–pp, Oct. 2005. pages 98
- [186] J. Mazeau, R. Sommet, D. Caban-Chastas, E. Gatard, R. Quéré, and Y. Mancuso, "Behavioral thermal modeling for microwave power amplifier design," *IEEE Transactions on Microwave Theory and Techniques*, vol. 55, pp. 2290–2297, Nov. 2007. pages 98
- [187] G. P. Gibiino, G. Avolio, D. Schreurs, A. Santarelli, and F. Filicori, "A three-port, nonlinear dynamic behavioral model for supply-modulated RF PAs," *IEEE Transactions on Microwave Theory and Techniques*, vol. 64, pp. 133–147, Jan. 2016. pages 107, 140, 148
- [188] G. P. Gibiino, A. Santarelli, D. Schreurs, and F. Filicori, "Two-input nonlinear dynamic model inversion for the linearization of envelope-tracking RF PAs," *IEEE Microwave and Wireless Components Letters*, under review. pages 107, 137
- [189] J. Jeong, D. F. Kimball, M. Kwak, C. Hsia, P. Draxler, and P. M. Asbeck, "Wideband envelope tracking power amplifiers with reduced bandwidth power supply waveforms and adaptive digital predistortion techniques," *IEEE Transactions on Microwave Theory and Techniques*, vol. 57, pp. 3307–3314, Dec. 2009. pages 107
- [190] J. Hoversten, S. Schafer, M. Roberg, M. Norris, D. Maksimović, and Z. Popović, "Codesign of PA, supply, and signal processing for linear supply-modulated RF transmitters," *IEEE Transactions on Microwave Theory and Techniques*, vol. 60, pp. 2010–2020, Jun. 2012. pages 107
- [191] J. Jeong, D. F. Kimball, M. Kwak, C. Hsia, P. Draxler, and P. M. Asbeck, "Modeling and design of RF amplifiers for envelope tracking WCDMA base-station applications," *IEEE Transactions on Microwave Theory and Techniques*, vol. 57, pp. 2148–2159, Sept. 2009. pages
- [192] J. Kim, D. Kim, Y. Cho, D. Kang, B. Park, K. Moon, and B. Kim, "Analysis of envelope-tracking power amplifier using mathematical modeling," *IEEE Transactions on Microwave Theory and Techniques*, vol. 62, pp. 1352–1362, Jun. 2014. pages

- [193] H. Cao, H. M. Nemat, A. S. Tehrani, T. Eriksson, and C. Fager, "Digital predistortion for high efficiency power amplifier architectures using a dual-input modeling approach," *IEEE Transactions on Microwave Theory and Techniques*, vol. 60, pp. 361–369, Feb. 2012. pages 107, 108
- [194] H. Jang, A. Zai, T. Reveyrand, P. Roblin, Z. Popovic, and D. E. Root, "Simulation and measurement-based  $X$ -parameter models for power amplifiers with envelope tracking," in *IEEE MTT-S International Microwave Symposium Digest*, pp. 1–4, Jun. 2013. pages 107
- [195] A. S. Tehrani, H. Cao, S. Afsardoost, T. Eriksson, M. Isaksson, and C. Fager, "A comparative analysis of the complexity/accuracy tradeoff in power amplifier behavioral models," *IEEE Transactions on Microwave Theory and Techniques*, vol. 58, pp. 1510–1520, Jun. 2010. pages 107
- [196] A. Zhu, P. Draxler, C. Hsia, T. Brazil, D. Kimball, and P. Asbeck, "Digital predistortion for envelope-tracking power amplifiers using decomposed piecewise Volterra series," *IEEE Transactions on Microwave Theory and Techniques*, vol. 56, pp. 2237–2247, Oct. 2008. pages 107, 108
- [197] F. M. Ghannouchi and O. Hammi, "Behavioral modeling and predistortion," *IEEE Microwave Magazine*, vol. 10, pp. 52–64, Dec. 2009. pages 108
- [198] P. L. Gilabert and G. Montoro, "Look-up table implementation of a slow envelope dependent digital predistorter for envelope tracking power amplifiers," *IEEE Microwave and Wireless Components Letters*, vol. 22, pp. 97–99, Feb. 2012. pages 107, 108, 137
- [199] D. Kim, D. Kang, J. Choi, J. Kim, Y. Cho, and B. Kim, "Optimization for envelope shaped operation of envelope tracking power amplifier," *IEEE Transactions on Microwave Theory and Techniques*, vol. 59, pp. 1787–1795, Jul. 2011. pages 107
- [200] I. Kim, Y. Y. Woo, S. Hong, and B. Kim, "High efficiency hybrid EER transmitter for WCDMA application using optimized power amplifier," in *Proceedings of the European Microwave Conference*, pp. 182–185, Oct. 2007. pages
- [201] C. Hsia, D. F. Kimball, and P. M. Asbeck, "Effect of maximum power supply voltage on envelope tracking power amplifiers using GaN HEMTs," in *Proceedings of the IEEE Topical Conference on Power Amplifiers for Wireless and Radio Applications*, pp. 69–72, Jan. 2011. pages 107, 108
- [202] F. F. Tafuri, D. Sira, T. S. Nielsen, O. K. Jensen, J. H. Mikkelsen, and T. Larsen, "Memory models for behavioral modeling and digital

- predistortion of envelope tracking power amplifiers,” *Microprocessors and Microsystems*, vol. 39, Nov. 2015. pages 108, 137, 143
- [203] A. Soury, E. Ngoya, J.-M. Nebus, and T. Reveyrand, “Measurement based modeling of power amplifiers for reliable design of modern communication systems,” in *IEEE MTT-S International Microwave Symposium*, vol. 2, pp. 795–798, Jun. 2003. pages 113, 118
- [204] M. Myslinski, F. Verbeyst, M. Bossche, and D. Schreurs, “*S*-functions extracted from narrow-band modulated large-signal network analyzer measurements,” in *ARFTG Microwave Measurement Conference Digest*, pp. 1–8, Nov. 2009. pages 117
- [205] C. Florian, F. Filicori, D. Mirri, T. Brazil, and M. Wren, “CAD identification and validation of a non-linear dynamic model for performance analysis of large-signal amplifiers,” in *IEEE MTT-S International Microwave Symposium Digest*, vol. 3, pp. 2125–2128, Jun. 2003. pages 118
- [206] M. Thorsell, K. Andersson, G. Pailloncy, and Y. Rolain, “Extending the best linear approximation to characterize the nonlinear distortion in GaN HEMTs,” *IEEE Transactions on Microwave Theory and Techniques*, vol. 59, pp. 3087–3094, Oct. 2011. pages 119
- [207] W. Van Moer and Y. Rolain, “Measuring the sensitivity of microwave components to bias variations,” *IEEE Transactions on Instrumentation and Measurement*, vol. 53, pp. 787–791, Jun. 2004. pages 132
- [208] L. O. Chua and P. Y. Lin, *Computer-aided analysis of electronic circuits: algorithms and computational techniques*. Prentice Hall, 1975. pages 139, 140
- [209] P. A. Traverso, G. Pasini, A. Raffo, D. Mirri, G. Iuculano, and F. Filicori, “On the use of the discrete-time convolution model for the compensation of non-idealities within digital acquisition channels,” *Measurement*, vol. 40, pp. 527–536, Sept. 2007. pages 140
- [210] N. Giovannelli, T. Vlasits, A. Cidronali, and G. Manes, “Efficiency and linearity enhancements with envelope shaping control in wideband envelope tracking gaas pa,” in *Proceedings of the International Workshop on Integrated Nonlinear Microwave and Millimetre-Wave Circuits*, pp. 1–4, Apr. 2011. pages 143



# Curriculum Vitae

Gian Piero Gibiino received the B.Sc. and the M.Sc in electrical engineering, both with honors, from University of Bologna, Bologna, Italy, in 2008 and 2011, respectively. From September 2010 until March 2011 he was exchange student at KU Leuven, Leuven, Belgium, for the development of the master thesis. He also received a postgraduate MBA from Collège des Ingénieurs, Paris, France, in 2012. Since October 2012 he has been Ph.D. student at both University of Bologna and KU Leuven on a dual Ph.D. programme. His research interests include RF device and circuit characterization and modeling, microwave nonlinear measurements, and linearization techniques.



# List of Publications

## International Journals

1. **G. P. Gibiino**, G. Avolio, D. Schreurs, A. Santarelli and F. Filicori, "A Three-port Nonlinear Dynamic Behavioral Model for Supply-Modulated RF PAs," *IEEE Transactions on Microwave Theory and Techniques*, vol. 64, no. 1, pp.133-147, Jan. 2016
2. **G. P. Gibiino**, A. Santarelli, D. Schreurs, and F. Filicori, "Two-Input Nonlinear Dynamic Model Inversion for the Linearization of Envelope-Tracking RF PAs" *IEEE Microwave and Wireless Components Letters*, under review
3. P. Barmuta, D. C. Alcobia Ribeiro, K. Wang , G. Avolio, M. Rajabi, A. Lewandowski, **G. P. Gibiino**, J. Szatkowski, D. Schreurs, P. Hale, K. Remley, and D. Williams, "Comparing LSNA Calibrations," *IEEE Microwave Magazine*, vol.17, no. 2, pp. 59-64, Feb. 2016
4. P. Barmuta, F. Ferranti, **G. P. Gibiino**, A. Lewandowski, D. Schreurs, "Compact Behavioral Models of Nonlinear Active Devices Using Response Surface Methodology," *IEEE Transactions on Microwave Theory and Techniques*, vol.63, no.1, pp.56-64, Jan. 2015
5. A. Santarelli, D. Niessen, R. Cignani, **G. P. Gibiino**, P.A. Traverso, C. Florian, D. Schreurs, and F. Filicori, "GaN FET Nonlinear Modeling Based on Double Pulse  $I/V$  Characteristics," *IEEE Transactions on Microwave Theory and Techniques*, vol.62, no.12, pp.3262-3273, Dec. 2014
6. A. Santarelli, R. Cignani, **G.P. Gibiino**, D. Niessen, P.A. Traverso, C. Florian, D. Schreurs, F. Filicori, "A Double-Pulse Technique for the Dynamic  $I/V$  Characterization of GaN FETs," *IEEE Microwave and Wireless Components Letters*, vol.24, no.2, pp.132-134, Feb. 2014

## International Conferences

1. **G.P. Gibiino**, J. Couvidat, D. Schreurs, and A. Santarelli, "Supply-Terminal 40 MHz BW Characterization of Impedance-like Nonlinear Functions for Envelope Tracking PAs", to be presented at the *ARFTG Microwave Measurement Conference*, San Francisco (United States), May 2016
2. **G.P. Gibiino**, P. Barmuta, R. Cignani, A. Lewandowski, L. Dobrzanski, D. Schreurs, and A. Santarelli, "Double-pulse characterization of GaN-on-Sapphire FETs for technology development", to be presented at the *International Conference on Microwaves, Radar and Wireless Communications (MIKON)*, Krakow (Poland), May 2016
3. **G.P. Gibiino**, T. Cappello, D. Niessen, D. Schreurs, A. Santarelli, and F. Filicori, "An empirical behavioral model for RF PAs including self-heating", *Proceedings of the International Workshop on Integrated Nonlinear Microwave and Millimetre-wave Circuits (INMMiC)*, pp.1-3, Taormina (Italy), Oct. 2015
4. **G.P. Gibiino**, G. Avolio, S. Schafer, D. Schreurs, Z. Popovic, A. Santarelli, and F. Filicori, "Active Baseband Drain-Supply Terminal Load-Pull of an X-Band GaN MMIC PA", *Proceedings of the European Microwave Conference (EuMC)*, pp. 1204–1207, Paris (France), Sept. 2015
5. **G.P. Gibiino**, F. F. Tafuri, T.S. Nielsen, D. Schreurs, and A. Santarelli, "Pulsed NVNA measurements for dynamic characterization of RF PAs," *IEEE International Microwave and RF Conference Digest*, pp.92-95, Bangalore (India), Dec. 2014
6. **G.P. Gibiino**, G. Avolio, D. Schreurs, A. Santarelli, and F. Filicori, "Mixer-like modeling with dynamic baseband characterization for supply-modulated PAs," *Proceedings of the European Microwave Conference (EuMC)*, pp.1313-1316, Rome (Italy), Oct. 2014
7. **G.P. Gibiino**, G. Avolio, D. Schreurs, and A. Santarelli, "Nonlinear characterization of microwave power amplifiers with supply modulation," *Proceedings of the International Workshop on Integrated Nonlinear Microwave and Millimetre-wave Circuits (INMMiC)*, pp.1-3, Leuven (Belgium), Apr. 2014
8. **G.P. Gibiino**, R. Cignani, D. Niessen, D. Schreurs, A. Santarelli, and F. Filicori, "Thermal characterization of nonlinear charge trapping effects in GaN-FETs," *Proceedings of the International Workshop on Integrated Nonlinear Microwave and Millimetre-wave Circuits (INMMiC)*, pp.1-3, Leuven (Belgium), Apr. 2014

9. **G.P. Gibiino**, A. Santarelli, S. Farsi, M. Myslinski, G. Avolio, and D. Schreurs, "S-functions mixer modeling for linearization purposes," *Proceedings of the European Microwave Integrated Circuits Conference (EuMIC)*, pp.490-493, Manchester (United Kingdom), Oct. 2011
10. D. Niessen, **G.P. Gibiino**, R. Cignani, A. Santarelli, D. Schreurs and F. Filicori, "Iso-thermal and Iso-dynamic Direct Charge Function Characterization of GaN FET with Single Large-Signal Measurement", *IEEE MTT-S International Microwave Symposium (IMS) Digest*, pp.1-3, San Francisco (United States), May 2016
11. J. Couvidat, **G.P. Gibiino**, G. Pailloney, M. Vanden Bossche, A. Ghiotto, and D. Schreurs, "A compact measurement set-up for envelope-tracking RF PAs with calibrated sensing of baseband V/I at the supply terminal", *ARFTG Microwave Measurement Conference Digest*, Atlanta (United States), Dec. 2015
12. A. Santarelli, R. Cignani, D. Niessen, **G.P. Gibiino**, P.A. Traverso, D. Schreurs, and F. Filicori, "Multi-Bias Nonlinear Characterization of GaN FET Trapping Effects Through a Multiple Pulse Time Domain Network Analyzer", *Proceedings of the European Microwave Integrated Circuit Conference (EuMIC)*, pp. 81-84, Paris (France), Sept. 2015
13. A. Santarelli, R. Cignani, D. Niessen, **G.P. Gibiino**, P.A. Traverso, V. Di Giacomo, C. Chang, D. Floriot, D. Schreurs, and F. Filicori, "Evaluation of GaN FET power performance reduction due to nonlinear charge trapping effects," *Proceedings of the European Microwave Integrated Circuit Conference (EuMIC)*, pp.198-201, Rome (Italy), Oct. 2014
14. A. Santarelli, D. Niessen, R. Cignani, **G.P. Gibiino**, P.A. Traverso, C. Florian, D. Schreurs, and F. Filicori, "Large-signal GaN transistor characterization and modeling including charge trapping nonlinear dynamics," *IEEE MTT-S International Microwave Symposium (IMS) Digest*, pp.1-3, Tampa (United States), Jun. 2014
15. P. Barmuta, **G.P. Gibiino**, F. Ferranti, A. Lewandowski, and D. Schreurs, "Nonlinear behavioral models of HEMTs using response surface methodology," *Proceedings of the International Conference on Numerical Electromagnetic Modeling and Optimization for RF, Microwave, and Terahertz Applications (NEMO)*, pp.1-4, Pavia (Italy), May 2014
16. A. Santarelli, R. Cignani, **G.P. Gibiino**, D. Niessen, P.A. Traverso, C. Florian, C. Lanzieri, A. Nanni, D. Schreurs, and F. Filicori, "Nonlinear charge trapping effects on pulsed I/V characteristics of GaN FETs," *Proceedings of the European Microwave Conference (EuMC)*, pp.1375-1378, Nuremberg (Germany), Oct. 2013





